

**Mathematical modelling of the effect of low-dose radiation on the
G2/M transition and survival fraction via the ATM-Chk2
pathway**

by

Carlos Contreras

A thesis submitted in partial fulfillment of the requirements for the degree of

Doctor of Philosophy

in

Applied Mathematics

Department of Mathematical and Statistical Sciences
University of Alberta

© Carlos Contreras, 2020

Abstract

Radiation therapy is an important component of cancer treatment. It consists of applying ionizing radiation to kill cells by damaging their DNA and reducing their ability to reproduce and survive. It is reasonable to think that more radiation causes more damage and kills more cells. However, in the low-dose range (less than 1 Gy radiation dose), some cell lines experience counter-intuitive experimental behaviour: at about 0.3 Gy, more radiation less cells. This phenomenon, known as hyper radio-sensitivity and increased radioresistance (HRS/IRR), has intrigued radiobiologists for the last two decades. Below 0.3 Gy, cells are very sensitive to radiation; but above 0.3 Gy, they gain some resistance to radiation. Eventually, for higher dose, radiation damage becomes too much for the cell to bear. In the search for an effective radiation therapy that maximizes the damage on cancer cells and minimizes the damage on normal cells, the understanding of this phenomenon may improve the efficiency of radiation therapy.

One hypothesis that explains the HRS/IRR phenomenon is that activation of the G2 checkpoint, a mechanism that controls cell cycle progression to mitosis, occurs around the 0.3 Gy threshold. The G2 checkpoint activation provides extra time to repair DNA damage instead of carrying it to mitosis and compromising the integrity of daughter cells. However, testing this hypothesis experimentally is challenging. Mathematical modelling can provide insight into the validity of this hypothesis and the improve understanding of the underlying mechanisms governing HRS/IRR.

The effect of radiation on cells is commonly assessed through the cell survival fraction, which measures the ability of a culture of cells to reproduce several days after ionizing radiation application. The Linear Quadratic (LQ) model is the simplest

model to describe survival fraction data. However, the LQ model fails to describe HRS/IRR data, which is better described by the Induced Repair (IR) model, a variation of the LQ model. Although these are widely acceptable models, they fail to explain why HRS/IRR occurs. In recent years, attempts to explain HRS/IRR with survival fraction models have included more details of the molecular and cellular networks governing the cell dynamics. However, the question as to what is the involvement of the G2 checkpoint on the HRS/IRR phenomenon remains open.

In this thesis, I study the effect of radiation on the cell cycle and the survival fraction. For this purpose, I model the problem at two levels, the effect of radiation on the cell cycle at the individual level, and the effect of radiation on cells at the population level. At the individual level, I model the kinetic pathway triggered by radiation, namely, the activation of ATM and Chk2 proteins by radiation-induced Double Strand Breaks (DSBs); and the cell cycle, characterized by proteins MPF, Wee1, and Cdc25 and the G2-phase. The model for the cell cycle and radiation pathway consists of a system of differential equations, which involve Law of Mass Action and Goldbeter-Koshland kinetics. At the population level, I model lethal lesions for the cells based on the count of DSBs remaining during mitosis (obtained at the individual level), a distribution of a cell population over the cell cycle, and Poisson's Law for lethal events.

I use this mathematical modelling to study the role of the G2-phase in the survival fraction. I establish numerical and theoretical arguments to support the hypothesis that the G2/M transition plays a major role in the HRS/IRR phenomenon. Moreover, I provide a biological and mechanistic interpretation of the parameters in the IR model. The methodology presented in this thesis provides meaningful insights into the understanding of the effect of radiation on the G2/M transition and can be used to study the role that other radiation-induced pathways play in the cell cycle dynamics.

Preface

Chapter 2 of this thesis has been published as Contreras, C., Carrero, G., and de Vries, G. (2019), “A Mathematical Model for the Effect of Low-Dose Radiation on the G2/M Transition”, *Bulletin of Mathematical Biology*. I was the leading researcher responsible the conceptual ideas, numerical simulation, and writing of the manuscript. G. de Vries and G. Carrero were the supervisory authors involved in the conceptualization and editing of the manuscript.

Dedicated to Gabriel and David,
whose life should not have ended so soon.

Acknowledgements

I am thankful for the financial support I received through a PIMS Student Training Acceleration Award, a University of Alberta Doctoral Recruitment Scholarship, and a Pundit RD Sharma Memorial Graduate Award.

I am grateful for my supervisors Dr. Gerda de Vries and Dr. Gustavo Carrero. You both have been the best academic and personal mentors I could ask for. Your guidance and support were fundamental for my Ph.D. program and the culmination of this thesis. Your teachings, though, have not been limited to mathematics, academia, pedagogy and writing. Gerda, from you, I learned the importance of patience, altruism, and serenity. Gustavo, from you, I learned the importance of passion, mindfulness, and compromise.

I also want to thank those who have contributed to the development of this thesis. Dr. Michael Hendzel, who introduced me to the topic of research of this thesis, and Dr. David Murray, who served as an examiner in my candidacy and provided crucial feedback. Dr. John Tyson, who advised me in the mathematical modelling of the cell cycle, the central component in this thesis. Dr. Jonathan Rubin, who served as an examiner in my final exam and contributed towards the foundation of Chapter 4.

Thank you to the Mathbio Journal Club for your feedback and support. It is so fundamental for a graduate student to be part of such an amazing group of young and senior researchers. Special thanks to Dr. Thomas Hillen, who I consider my third supervisor, for being an excellent teacher and mentor. Thank you also to Dr. Jay Newby and Dr. Hassan Safouhi, for being examiners in the final exam and candidacy exam. To my colleagues and academic bothers for listening and sharing thoughts (especially Andreas, Victor and Samuel). I am thankful for the support

received from Tara Schuetz-Zawaduk and the rest of the staff at the Department of Mathematical and Statistical Sciences.

I am incredibly grateful for the support of my friends and family. Jody, Dean and Philippe, I am so happy for the time we spend together as first-year students taking courses and the subsequent years of unconditional support. Wafa, my best and first friend in Edmonton, I knew from the first time I met you that this friendship was long-lasting. Angela and Kirsten, whom I consider my Canadian family, for being so caring and comforting. My Venezuelan-Canadian family, Luis, Ivan, Catalina, Marcotulio, Desiree, and Jorge, I have no words to describe how happy I feel for having you in my life. I love you all.

This thesis is dedicated to my family. My brother Daniel, I wish that happiness, health and prosperity be with you, Mariana, Piero Daniel and Gabriel Fabricio. I only think about the time when we meet again and I meet my nephews for the first time. Mom, every achievement, every success, every moment of happiness, is all thanks to you. I love you so much. And last but not least, my friend, partner, lover, and wife, Mariangel, thank you for being exactly who you are. You are my everything. Te mi.

Table of Contents

1	Introduction	1
1.1	Motivation	1
1.2	Outline of the thesis	4
2	Effect of low-dose radiation on the G2 checkpoint through the ATM-Chk2 pathway	6
2.1	Introduction	7
2.2	Model for the cell cycle and radiation pathway in mammalian cells .	10
2.2.1	Cell cycle module	13
2.2.2	Radiation pathway module	15
2.2.3	Model parameter values	17
2.3	Results	18
2.3.1	Effect of radiation pulse intensity on the G2/M transition . .	22
2.3.2	Effect of radiation pulse timing on the G2/M transition . . .	23
2.3.3	No effect of radiation pulse on the G2/M transition	24
2.3.4	Overall effect of radiation pulse on the G2 checkpoint activation	26
2.4	Analysis of the G2/M transition and definition of G2 checkpoint . .	28
2.5	Discussion	35

2.A	Appendix: parameters values	39
3	Effect of low-dose radiation on the survival fraction through the ATM-Chk2 pathway: a numerical approach	44
3.1	Lethal DSBs	46
3.2	Survival fraction	50
3.3	Results	54
3.3.1	Uniform distribution	57
3.3.2	Von Mises distribution	58
3.3.3	Effect at very low-dose caused by ATM dynamics	61
3.4	Lethal DSBs and time available for repair	64
3.5	Discussion	67
3.A	Table of parameter values	69
4	Carryover of a saddle-node bifurcation after transformation of a parameter into a variable	73
4.1	One-dimensional case	77
4.2	n -dimensional case	91
4.3	Discussion	97
5	Reduction of the Cell Cycle model to one-dimension around the SNIC bifurcation	101
5.1	Introduction	102
5.2	G2 module: saddle-node bifurcation driven by cell mass	111
5.2.1	Translation of a steady state to the origin	115
5.2.2	Nondimensionalization and approximation	119
5.2.3	Change of coordinates	124

5.2.4	Reduction to one-dimensional form	132
5.3	G2 module with variable cell mass: saddle-node bifurcation driven by V_{c2}	135
5.4	G2 and M modules combined with variable cell mass and resetting condition: SNIC bifurcation driven by V_{c2}	140
5.5	Normal form for the SNIC bifurcation driven by V_{c2} : describing the G2/M transition	143
5.6	Discussion	146
5.A	Power series expansions of the Goldbeter-Koshland kinetics	148
5.B	Normal form for the saddle-node bifurcation	149
5.C	Parameters	151
6	Effect of low-dose radiation on the survival fraction through the ATM- Chk2 pathway: a theoretical approach	154
6.1	Summary of the previous chapters	156
6.2	Normal form for the cell cycle during the G2/M transition with the radiation pathway	161
6.3	Average number of lethal lesions due to G2 checkpoint failure	166
6.3.1	Time available for repair prior to the G2/M transition	167
6.3.2	Time available for repair during the G2/M transition	168
6.3.3	Combined average number of lethal lesions due to G2 check- point failure away and during the G2/M transition	172
6.4	Understanding the effect of an impulse $g(t)$ on the phase model	173
6.5	Discussion	178
6.A	Phase model for the normal form of the SNIC bifurcation	180
6.B	Goldbeter-Koshland kinetics	183

6.C Table of parameter values	186
7 Discussion and future work	191
7.1 Summary and discussion	191
7.2 Future work	196
7.3 Final remarks	201
Bibliography	201

List of Figures

1.1	Survival fraction curve showing the HRS/IRR phenomenon.	2
2.1	Schematic diagram of the cell cycle.	9
2.2	Diagram of the cell cycle and radiation pathway.	12
2.3	Numerical solutions (left) and one-parameter bifurcation diagrams with respect to \tilde{V}_{c2} as the bifurcation parameter (right).	19
2.4	Effect of a radiation pulse at very low dose.	25
2.5	Diagram of the overall effect of radiation, as a function of the dose and timing of the radiation pulse, on the G2/M transition by the ATM-Chk2 pathway.	29
2.6	Bifurcation diagrams.	32
2.7	Cell cycle progression and G2 checkpoint activation.	35
3.1	Survival fraction showing HRS/IRR.	45
3.2	Colour map for the number of lethal DSBs at M-phase.	51
3.3	Survival curve data from asynchronous and synchronous cells.	56
3.4	Numerical survival fraction with uniform distribution.	58
3.5	Numerical survival fraction with Von Mises distribution for cells enriched in G1-phase.	61

3.6	Numerical survival fraction with Von Mises distribution for cells enriched in S-phase.	62
3.7	Numerical survival fraction with Von Mises distribution for cells enriched in G2-phase.	63
3.8	Numerical survival fraction with Von Mises distribution for cells enriched in G2-phase and fixed ATM concentration.	64
3.9	Colour map for the time available for repair of DSBs.	66
4.1	A bifurcation curve Γ and its corresponding bifurcation boundary $h(\mu_1, \mu_2) = 0$ (projection onto the (μ_1, μ_2) -plane). Modified from Figure 8.1 in Kuznetsov [48].	80
4.2	Bifurcation diagrams for Example 4.1.1.	89
4.3	Bifurcation diagrams for Example 4.1.2.	92
4.4	Bifurcation diagrams for Example 4.2.1.	98
5.1	Numerical solution of the cell cycle model (5.1)–(5.2).	104
5.2	Cell cycle model diagram.	105
5.3	Construction of the branched manifold.	106
5.4	Bifurcation diagram for V_{e2}	108
5.5	Bifurcation diagram of the G2 module (5.4) with mass as varying parameter.	113
5.6	Two-parameter bifurcation diagram for the G2 module (5.4) with mass and V_{e2} as bifurcation parameters.	136
5.7	Bifurcation diagram of the G2 module with variable mass (5.35) with V_{e2} as varying parameter.	139
5.8	Bifurcation diagram of the G2 and M modules with variable mass (5.39) with V_{e2} as varying parameter.	142

5.9	Bifurcation diagram of the normal form (5.41) of the saddle-node bifurcation.	144
5.10	Diagram of the one-dimensional approximation of the cell cycle model around the $\text{SNIC}_{V_{e2}}$ bifurcation.	145
6.1	Diagram of structure of the thesis.	155
6.2	Linear representation of the cell cycle.	161
6.3	Solution of the normal form and radiation pathway model.	163
6.4	Numerical time available for repair.	166
6.5	Solution of the phase model.	170
6.6	Diagram of Goldbeter-Koshland kinetics	183
6.7	Goldbeter-Koshland function.	186

List of Tables

2.1	Name and description of variables in the cell cycle and radiation pathway model.	13
2.2	Parameter values.	40
3.1	Name and description of variables in Eqs. (3.1a)–(3.1j). All variables represent concentration, except <i>Mass</i> and <i>DSB</i>	48
3.2	Concentrations, times, and percentages.	60
3.3	Parameter values.	69
5.1	Name and description of variables in Eqs. (5.1a)–(5.1g). All variables represent concentration, except for the cell mass.	103
5.2	Parameter values.	151
6.1	Name and description of variables in Eqs. (6.1a)–(6.1j). All variables represent concentration, except <i>Mass</i> and <i>DSB</i>	157
6.2	Description of variable and parameters new to the normal form with radiation pathway model (6.15) and other parameter used the simulations.	165
6.3	Parameter values.	187

Chapter 1

Introduction

1.1 Motivation

Hyper-radiosensitivity and increased radioresistance (HRS/IRR) is a phenomenon in radiation biology in which cells are very sensitive to low-dose radiation and become resistant as radiation increases (see Figure 1.1) [39]. This phenomenon is mostly observed in laboratory experiments using tumour cells but has a great potential for clinical applications [92]. Although there have been significant advances in the understanding of the HRS/IRR phenomenon in the recent years, the underlying mechanisms behind HRS/IRR are still unclear [39, 3]. Marples et al. [58] hypothesize that the G2/M checkpoint of the cell cycle is responsible for the HRS/IRR effect observed in some cell lines. The G2/M checkpoint is a cell regulatory mechanism which prevents cell cycle progression in the presence of DNA damage [65].

The cell survival curve reflects the ability of cells to reproduce after a given dose of radiation [1]. Many models have been developed to describe survival curves [51, 52, 19, 12, 18, 30, 93], but the Linear Quadratic (LQ) model [40, 41] remains the most popular and simple cell survival model [101]. The LQ model is defined in

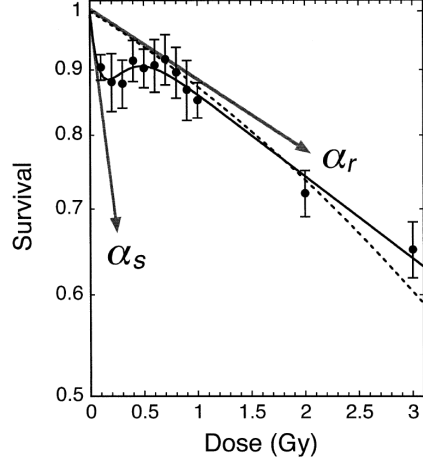


Figure 1.1: Survival curve as a function dose showing hyper-radiosensitivity (HRS) and increased radioresistance (IRR). Below 0.25 Gy, the survival fraction decreases fast with dose. Between 0.25 Gy and 1 Gy, cells become resistant to radiation and increase their survival probability. Both Linear-Quadratic (dotted) and Induced Repair (solid) models are fit to data. Taken from Marples et al. [58].

terms of the *yield of lesions* (terminology adopted from Rossi and Zaider [82])

$$\lambda_{LQ}(D) = -\ln(S_{LQ}(D)) = \alpha D + \beta D^2, \quad (1.1)$$

where D is the total dose delivered, and α and β are constants. Despite many attempts to interpret the LQ model [12, 91, 14, 76, 7, 35], there is not a clear mechanistic interpretation for the parameters in this model [29, 6]. The LQ model is widely used in clinical studies[103, 23, 101]; however, some concerns have been raised with this regard [43, 9]. Ultimately, the LQ model fails to describe cell survival data exhibiting HRS/IRR due to its non-monotonic shape at low dose.

The Induced Repaired (IR) model [49] is suitable for cell survival data exhibiting HRS/IRR [92]. The yield of lesions of the model reads

$$\lambda_{IR}(D) = -\ln(S_{IR}(D)) = \left(\alpha_r + (\alpha_s - \alpha_r)e^{-\frac{D}{d_c}} \right) D + \beta D^2, \quad (1.2)$$

where α_s describes the slope for low dose, α_r describes the slope for high dose, and d_c is the dose at which radio resistance is induced (see Figure 1.1). As in the LQ model, there is no clear mechanistic interpretation for the parameters in the IR model [60, 6].

In the recent years, there has been a modern approach to model the cell survival with regulatory and organizational components of the cell [6]. Bodgi and Foray [5] developed a cell survival model based on nucleo-shuttling of ATM (protein kinase involved in the repair of DNA damage) that provides a biological explanation of HRS/IRR and an interpretation of the IR model. However, this approach does not explain the participation of the G2/M checkpoint of the cell cycle on the HRS/IRR phenomenon [59]. Olobatuyi et al. [78] developed a compartmental model for the population of cells in G2-phase to provide a biological interpretation of the IR model in terms of the cell cycle. However, they do not investigate how radiation affects the cell cycle or why it is the G2/M checkpoint in particular that produces the HRS/IRR phenomenon.

In this thesis, I explore the involvement of the G2/M checkpoint in the HRS/IRR phenomenon by adding a radiation pathway to the mathematical model of the cell cycle developed by Novák and Tyson Novák and Tyson [71]. Over two decades, they built a framework to model regulatory and signalling pathways in the cell using Law of Mass Action, Michaelis-Menten kinetics, and Goldbeter-Koshland kinetics [99, 86]. In their extensive research, they have been able to explain characteristics of the cell cycle from a mathematical perspective, such as checkpoints, cell cycle progression, growth and division [95]. Based on the hypothesis that the G2/M checkpoint is the determinant component of the HRS/IRR phenomenon [58], I am interested in modelling the G2/M transition of the cell cycle.

1.2 Outline of the thesis

In this thesis, I study the effect of radiation on the G2/M transition and survival fraction using mathematical modelling. Several questions arise from this approach:

1. What is the signalling pathway between radiation and the cell cycle, and how to model it?
2. Would modelling the radiation pathway in the cell cycle result in a significant influence on the G2/M transition?
3. How to extend this study to obtain a model for the survival fraction?
4. Can the radiation pathway modelling result in a survival fraction exhibiting HRS/IRR?

In Chapter 2, I study the effect of radiation on the G2/M transition and address questions 1 and 2. I use Novák and Tyson's mathematical framework to model the cell cycle with focus on the G2/M transition, and model the signalling pathway of Double Strand Breaks (DSBs) and kinases ATM and Chk2 in connection with the cell cycle model. I show that radiation triggers the G2/M checkpoint under dose and temporal conditions, and that the checkpoint is governed by a saddle-node on an invariant circle (SNIC) bifurcation. Moreover, I identify an interesting relationship between the SNIC bifurcation studied here, and a different SNIC bifurcation studied by Novák et al. [74]. The latter motivates the theoretical study in Chapters 4 and 5. Chapter 2 has been published as [13].

In Chapter 3, I study the effect of radiation on the survival fraction. I develop a model for the survival fraction based on the number of DSBs reaching mitosis and on the cell cycle model and radiation pathway studied in Chapter 2. I use numerical

simulations to show that this approach results in an HRS/IRR effect in the survival fraction. In this chapter, I partially address questions 3 and 4. This motivates a further theoretical study on the effect of radiation on the survival fraction via the ATM-Chk2 pathway, which is done in Chapter 6 using the calculations carried out in Chapter 5.

In Chapter 4, I introduce and study a theoretical problem in dynamical systems: the manifestation of a saddle-node bifurcation after transforming the bifurcation parameter into a variable. We call this problem the carryover of a saddle-node bifurcation. I show that this is possible under additional singularity and transversality conditions. This result is used in Chapter 5.

In Chapter 5, I reduce the cell cycle model used in Chapter 2 to the normal form for the saddle-node bifurcation. This normal form is used to define the G2/M transition in mathematical terms and is used as well later in Chapter 6.

In Chapter 6, I study the effect of radiation on the survival fraction via the ATM-Chk2 pathway, following the framework in Chapter 3, but now on a theoretical basis. I show that, under certain simplifications, our formulation of the survival fraction is equivalent to the IR model (1.2). This provides a novel kinetic and mechanistic interpretation of the IR model.

In Chapter 7, I summarize and discuss the results, and propose future work.

Chapter 2

Effect of low-dose radiation on the G2 checkpoint through the ATM-Chk2 pathway

Abstract

We develop a mathematical model to study the immediate effect of low-dose radiation on the G2 checkpoint and the G2/M transition of the cell cycle via a radiation pathway (the ATM-Chk2 pathway) of an individual mammalian cell. The model consists of a system of nonlinear differential equations describing the dynamics of a network of regulatory proteins that play key roles in the G2/M transition, cell cycle oscillations, and the radiation pathway. We simulate the application of a single pulse of low-dose radiation at different intensities ($\sim 0\text{--}0.4$ Gy) and timing during the latter part of the G2-phase. We use bifurcation analysis to characterize the effect of radiation on the G2/M transition via the ATM-Chk2 pathway. We show that radiation between 0.1–0.3 Gy can delay the G2/M transition, and radiation higher than 0.3

Gy can fully activate the G2 checkpoint. Also, our results show that radiation can be low enough to neither delay the G2/M transition nor activate the G2 checkpoint (~ 0.1 Gy). Our model supports the idea that the cell response to radiation during G2-phase explains hyper-radiosensitivity and increased radioresistance (HRS/IRR) observed at low dose.

2.1 Introduction

The cell cycle is the essential process for cell growth and reproduction. The elaborate control mechanisms that regulate the cell cycle can be easily compromised by ionizing radiation. One such control mechanism is the G2 checkpoint, a protective mechanism that ensures that the transition from G2-phase to M-phase is carried out with healthy DNA (see Fig. 2.1) [34]. Low-dose radiation can cause DNA lesions that may not fully trigger G2 checkpoint activation [39]. Failure to activate the G2 checkpoint in the presence of DNA damage can result in a variety of outcomes affecting cell survival, including cell cycle arrest, apoptosis and mitotic catastrophe [36, 102, 62]. A better understanding of the mechanisms underlying the effect of low-dose radiation on cells is key to improving radiation therapy on cancer cells [68]. To help understand the effect of low-dose radiation on mammalian cells, we model the dynamics of the proteins involved in the regulation of the cell cycle. The starting point for this work is the modelling regulatory networks of Tyson et al. [99].

The effect of radiation is closely connected to how it affects the cell cycle and checkpoint control mechanisms [62]. For instance, it has been shown that the G2-phase and the G2 checkpoint of the cell cycle play a significant role in the hyper-radiosensitivity and increased radioresistance (HRS/IRR) phenomenon observed at low-dose [60]. HRS/IRR is characterized by a first range of radiation

dose (between 0 and 0.3 Gy) where cells are very sensitive (a small increase in the dose greatly decreases cell survival), and a second range of radiation dose (between 0.3 and 0.6 Gy) where cells gain radioresistance to radiation (cells are no longer hypersensitive and rather increase their survival as radiation dose increases) [60]. Understanding the hyper-radiosensitivity part of HRS/IRR may greatly improve radiation therapy. For instance, the application of multiple pulses of low-dose radiation (typically < 1 Gy) has already shown positive *in-vivo* and clinical results [104, 64]. However, the molecular mechanisms behind the HRS/IRR phenomenon remains unclear. Although cancer cells differ from normal cells in various aspects, understanding the HRS/IRR phenomenon in the latter is a first step in discovering the potential use of HRS/IRR in radiation therapy. In this study, we focus on low-dose radiation (~ 0 – 0.4 Gy) to understand its effect on the G2 checkpoint and the G2/M transition of normal mammalian cells.

Unfortunately, observing the cell response to radiation in experiments is particularly difficult. For this reason, mathematical modelling becomes a powerful tool to simulate experiments, make predictions, and gain insight into the mechanisms underlying the effect of radiation on the cell cycle. We assume that the cell response to radiation determines the fate of the cell and that of future generations. Under this assumption, we show that understanding of the mechanisms that affect the G2/M transition has implications for the understanding of the HRS/IRR phenomenon.

The G2 checkpoint activation after radiation is mediated by DSB sensor kinase ATM and checkpoint kinase Chk2 [56]. However, it is unclear how this ATM-Chk2 pathway can cause HRS/IRR in the survival fraction. The aim of this work is to explore the effect of the ATM-Chk2 pathway on the G2/M transition on normal mammalian cells. For this purpose, we propose a mathematical model that incorporates the effect of radiation on the cell cycle. In Section 2.2, we introduce

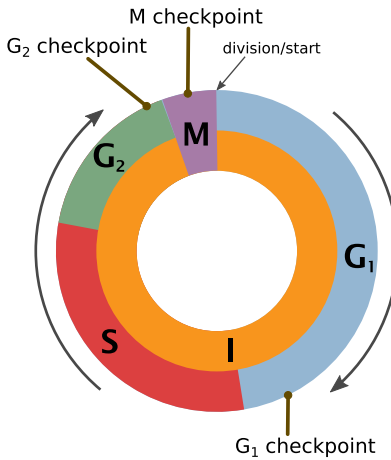


Figure 2.1: Schematic diagram of the cell cycle. Interphase (I) (which consists of the G₁-phase, Synthesis (S) and G₂-phase) and M-phase (M), with G₁ (start), G₂, and M (spindle) checkpoints. Adapted from image by Zephyris.

the two components of the mathematical model, namely, the cell cycle module and the radiation pathway. In Section 2.3, we simulate numerically the application of a radiation pulse at different intensities (0–0.4 Gy) and times during the latter part of the G₂-phase, and study the effect of the pulse on the G₂/M transition. We also apply bifurcation analysis to understand the simulation results in terms of the dynamical changes in the system. We show that there are dose- and time-dependent thresholds, arising from the radiation pathway, that affect the G₂/M transition. More precisely, the G₂ checkpoint requires sufficiently high dose (> 0.2 Gy) and appropriate timing for mitotic entry to be triggered successfully. In Section 2.4, we analyze the G₂ checkpoint further using two-parameter bifurcation analysis and explore the reasons behind our findings. In Section 2.5, we conclude with a discussion of our results.

2.2 Model for the cell cycle and radiation pathway in mammalian cells

The foundation of the proposed mathematical model is Novák and Tyson's work on the regulation of the cell cycle [71, 98, 96]. We extend a basic version of their model for the cell cycle with the ATM-Chk2 pathway. Although most of Novák and Tyson's research has been conducted on frog eggs extracts, fission yeast and budding yeast, the similarities in the G2/M transition between yeast and mammalian cells allow us to use their modelling approach for mammalian cells with confidence.

Our model consists of three interconnected modules, namely the interphase, the M-phase, and the radiation pathway, as shown in Fig. 2.2. The model accounts for the G2/M transition, cell division, and radiation. Each module captures the interactions between the proteins playing an essential role. The interphase module describes the G2/M transition, the M-phase module closes the cell cycle, and the radiation pathway module keeps track of the number of Double Strand Breaks (DSBs). The model variables are listed in Table 2.1. The resulting biological network is modelled with the following system of differential equations:

$$\begin{aligned} \frac{dMPF}{dt} = & k_{m0}Mass - (k_{m2} + k_{m2a}Wee1)MPF \\ & + (k_{m1} + k_{m1a}Cdc25)MPF_P - (k_{m3} + k_{m3a}APC)MPF, \end{aligned} \quad (2.1a)$$

$$\begin{aligned} \frac{dMPF_P}{dt} = & (k_{m2} + k_{m2a}Wee1)MPF - (k_{m1} + k_{m1a}Cdc25)MPF_P \\ & - (k_{m3} + k_{m3a}APC)MPF_P, \end{aligned} \quad (2.1b)$$

$$\frac{dWee1}{dt} = V_{w1} \frac{Wee1_T - Wee1}{J_{w1} + (Wee1_T - Wee1)} - k_{w2}(MPF + \alpha MPF_P) \frac{Wee1}{J_{w2} + Wee1}, \quad (2.1c)$$

$$\begin{aligned} \frac{dCdc25}{dt} = & k_{c1}(MPF + \alpha MPF_P) \frac{Cdc25_T - Cdc25}{J_{c1} + (Cdc25_T - Cdc25)} \\ & - (V_{c2} + k_{c2a}Chk2) \frac{Cdc25}{J_{c2} + Cdc25}, \end{aligned} \quad (2.1d)$$

$$\frac{dIE}{dt} = k_{i1}(MPF + \alpha MPF_P) \frac{IE_T - IE}{J_{i1} + (IE_T - IE)} - V_{i2} \frac{IE}{J_{i2} + IE}, \quad (2.1e)$$

$$\frac{dAPC}{dt} = k_{a1}IE \frac{APC_T - APC}{J_{a1} + (APC_T - APC)} - V_{a2} \frac{APC}{J_{a2} + APC}, \quad (2.1f)$$

$$\frac{dMass}{dt} = \mu Mass \left(1 - \frac{Mass}{K_{Mass}} \right), \quad (2.1g)$$

$$\frac{dChk2}{dt} = k_{h1}ATM DSB \frac{Chk2_T - Chk2}{J_{h1} + (Chk2_T - Chk2)} - V_{h2} \frac{Chk2}{J_{h2} + Chk2}, \quad (2.1h)$$

$$\frac{dATM}{dt} = k_{t1}DSB \frac{ATM_T - ATM}{J_{t1} + (ATM_T - ATM)} - V_{t2} \frac{ATM}{J_{t2} + ATM}, \quad (2.1i)$$

$$\frac{dDSB}{dt} = k_{d1}\dot{D}(t) - k_{d2}ATM DSB, \quad (2.1j)$$

subject to the resetting condition

$$\text{if } MPF(t) = \theta_M \text{ and } \frac{dMPF}{dt}(t) < 0 \implies Mass(t) \leftarrow \frac{Mass(t)}{2}, \quad (2.2)$$

where parameters are described in Table 2.2 in the Appendix. The model is fully explained below. In Section 2.2.1, we explain Eqs. (2.1a)–(2.2) pertaining to the interphase and M-phase modules in Fig. 2.2, which together comprise the cell cycle module. The cell cycle module has been taken from Novák and Tyson’s work [96]. In Section 2.2.2, we explain Eqs. (2.1h)–(2.1j) pertaining to the radiation pathway, which is newly introduced in this work. In Section 2.2.3, we describe the choice of the parameters values that we use in our simulations.

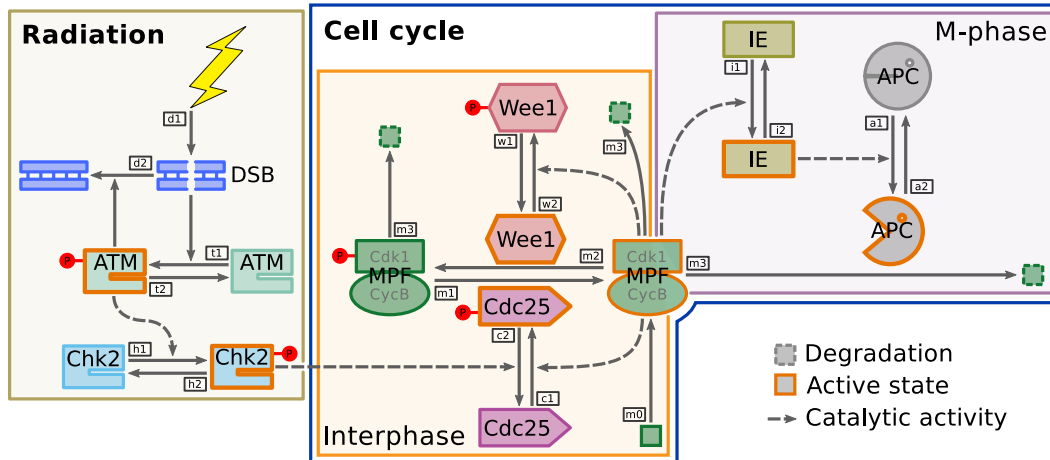


Figure 2.2: Diagram of the cell cycle and radiation pathway. The model for the cell cycle and radiation pathway consists of three modules: interphase, M-phase, and radiation. The interphase and M-phase modules together make the cell cycle module. The Mitotic Promoting Factor (MPF) is central for the progression of the cell cycle. The interphase module (in orange) is characterized by MPF and the two positive feedback loops with Wee1 and Cdc25 that control MPF activity. The M-phase (in purple) is mainly characterized by MPF, a hypothetical intermediary enzyme (IE), Anaphase Promoting Complex (APC), and the negative feedback loop that degrades MPF. The radiation pathway is characterized by DSBs, ATM, and Chk2 after a radiation input. Solid arrows represent activation, inactivation, synthesis, and degradation depending on the case. Dashed arrows represent catalytic activity. Labels in the small white boxes refer to the parameter subscripts appearing in the corresponding equations. Shapes with a dashed boundary represent degraded proteins; shapes with an orange boundary represent the active state. Based on Fig.3 in [96].

Table 2.1: Name and description of variables in Eqs. (2.1a)–(2.1j). All variables represent concentration, except DSB , which represents a number.

Symbol	Description
MPF	Active Cdk1-cyclin B complex (Mitotic Promoting Factor)
MPF_P	Inactive, phosphorylated form of MPF
$Wee1$	Active dephosphorylated form of kinase Wee1 (MPF inactivator)
$Cdc25$	Active phosphorylated form of the phosphatase Cdc25C (MPF activator)
IE	Active form of an intermediate enzyme [94]
APC	Active phosphorylated form of APC (Anaphase Promoting Complex)
$Chk2$	Active phosphorylated form of Chk2 (Checkpoint kinase 2)
ATM	Active phosphorylated, monomerized and recruited form of ATM
DSB	Recognized Double Strand Brakes formed by Ionizing Radiation
$Mass$	Mass of the cell

2.2.1 Cell cycle module

The interphase and M-phase modules represented in the diagram in Fig. 2.2 are sufficient to explain cell cycle dynamics with emphasis on mitotic entry and exit. This module is developed and explained in detail by Novák and Tyson [71] and in their subsequent publications (see Tyson and Novák [96] for a review). The radiation module is excluded from this section by simply setting the variable Chk2 (Checkpoint kinase 2) to zero in Eq. (2.1d). The Mitotic Promoting Factor (MPF) (also known as Maturation or M-phase Promoting Factor) is the central protein necessary for both G2/M and M/G1 transitions. MPF is a complex formed by the Cyclin-dependent kinase 1 (Cdk1) and the M-phase promoting Cyclin B protein (CycB). In eukaryotic cells, and particularly in mammals, there are other cyclin-CDK complexes involved in the cell cycle progression [65]. However, these are not involved in the G2/M transition and we therefore do not consider their role in this work for the sake of simplicity.

Note that we consider two forms of MPF depending on its phosphorylation on

the Thr-15 residue. The MPF variable in Eq. (2.1a) represents the more active form when it is unphosphorylated, and the MPF_P variable in Eq. (2.1b) represents the less active form when it is phosphorylated. Whenever we mention the activity of MPF, we refer to the concentration of the active form of MPF, that is, the MPF variable. The MPF reactions are modelled with mass action kinetics. MPF is formed when cell mass promotes synthesis of CycB subunit and this binds to free Cdk1 at rate k_{m0} (first term of Eq. 2.1a). MPF is always formed unphosphorylated, but both the phosphorylated and unphosphorylated forms of MPF can be destroyed by degradation of CycB, at rate k_{m3} . Phosphorylation of MPF is controlled by the regulatory enzymes Wee1 and Cdc25 through two positive feedback loops (as shown in the interphase module in Fig. 2.2). The active form of MPF deactivates Wee1, which in turn deactivates MPF. Similarly, the active form of MPF activates Cdc25, which in turn activates MPF. These interactions are positive feedback loops since the net effect on MPF is favourable for its activation. In each case, the activity of the catalytic enzyme (either Wee1 or Cdc25) is added to a basal value of phosphorylation (k_{m2}) or dephosphorylation (k_{m1}).

The Wee1 and Cdc25 reactions are modelled with Goldbeter-Koshland kinetics in Eqs. (2.1c) and (2.1d), respectively [27]. Under these kinetics, the first and second terms on the right-hand side of the equations are the activation and inactivation rate, respectively, while the total concentration remains constant. For example, denoting the total concentration of Wee1 as $Wee1_T$, the term $Wee1_T - Wee1$ is the concentration of inactive Wee1. Note that MPF_P also plays a minor role (encoded in the 5% value of the parameter α) in the inactivation of $Wee1$ and the activation of $Cdc25$.

MPF activity fluctuates throughout the cell cycle between low and high activity. During the interphase, MPF activity stays low due to Wee1 inactivation, until the

two positive feedback loops quickly increase MPF activity. High MPF activity determines the end of the G2-phase and the start of mitosis. At high concentration, MPF is responsible for the assembly of mitotic spindles, chromosomes alignment, and phosphorylation and activation of Anaphase Promoting Complex (APC) through its activating subunit Cdc20. Active APC degrades MPF by targeting its cyclin B subunit (with rate k_{m3a} ; see Eqs. (2.1a) and (2.1b)) [65]. In Eqs. (2.1e) and (2.1f), delayed APC activation is modelled through a hypothetical ‘intermediary enzyme’ (IE) (possibly Plk1). Both APC and IE are modelled with Goldbeter-Koshland kinetics (see Fig. 2.2) [94]. The negative feedback loop for MPF (activation of its inactivator) and the delayed APC activation cause the subsequent decay in MPF activity after mitotic entry. Low concentration of MPF marks the end of cytokinesis and the start of another round of the cell cycle.

In the model, cell division is defined as an event that divides mass in half, and occurs when the concentration of MPF falls below a threshold value for mitosis, θ_M (see Eq. (2.2)). Moreover, mass is modelled with logistic growth in Eq. (2.1g), where μ is the growth rate, and K_{Mass} is the maximum mass. The use of the logistic equation has two advantages: it prevents cells from growing unrealistically in the case of a prolonged checkpoint, and it describes cell growth with both exponential and linear profiles. This last point reconciles the debate on linear versus exponential cell growth [26].

2.2.2 Radiation pathway module

The radiation pathway involves two main proteins called ATM and Checkpoint kinase 2 (Chk2), as shown in Fig. 2.2 [61, 17]. Following radiation, monomerized ATM is recruited inside the cell nucleus around Double Strand Breaks (DSBs)

and autophosphorylated to become active [45]. ATM activates Chk2 in a catalytic manner, and Chk2 in turn inhibits Cdc25 [2]. Thus, in the presence of active Chk2, the inactivation rate of Cdc25 increases. Since Cdc25 is involved in a positive feedback loop with MPF, its inactivation affects the G2/M transition.

Formation and repair of DSBs are modelled in Eq. (2.1j). In response to radiation, the rate of DSBs formation is linearly dependent on the dose rate [83]. We denote the external dose rate applied to the cell as $\dot{D}(t)$. Notice that the total radiation applied during the radiation treatment is

$$D = \int_0^{t_f} \dot{D}(t) dt, \quad (2.3)$$

where t_f is the time at the end of the treatment.

After formation of DSBs, ATM foci are formed around the DSBs to promote their repair. The product term $ATM \cdot DSB$ in Eq. (2.1j) is the number of ATM foci, i.e., the proportion of DSBs that are recognized and being repaired. Activation of ATM is important for DSBs repair during late interphase [28]. Provided ATM is active, we model repair of DSBs to depend linearly on DSBs. This linear dependence has been validated by Taleei and Nikjoo [90]. Since we focus on the G2-phase, the repair mechanism in Eq. 2.1j accounts primarily for homologous recombination (HR), which is known to be slower than non-homologous end joining (NHEJ) [89].

We consider ATM to be active after it has been monomerized, recruited inside the cell nucleus around DSBs, and phosphorylated. We assume that ATM activation and inactivation are fast and very sensitive to a few DSBs [10, 83, 45]. We model ATM fast activity into one kinetic equation, Eq. (2.1i), with Golbeter-Koshland kinetics, where ATM activation is promoted by the presence of DSBs. Active ATM in turn catalyzes Chk2 activation by phosphorylation, which we also model with

Goldbeter-Koshland kinetics in Eq. (2.1h). In both ATM and Chk2 equations, we use Goldbeter-Koshland kinetics as it models ultrasensitive activation. As mentioned in Section 2.2.1, the radiation pathway module connects with the cell cycle module through the catalytic effect of Chk2 on Cdc25 inactivation (see Eq. (2.1d)).

As mentioned before, we focus on the effect of radiation on the G2/M transition, i.e., how radiation triggers the G2 checkpoint and to what extent DNA damage is carried into M-phase. DSBs carried into M-phase can result in a variety of unfavourable outcomes during cell division, including mitotic catastrophe, senescence, and aneuploid/polyploid cells [102]. To avoid this complexity, the current form of the radiation pathway in the model does not keep track of DSBs after M-phase. Thus, when considering a radiation input, the model is limited to the next mitotic entry.

2.2.3 Model parameter values

Most of the parameters values in the radiation pathway are taken from the literature, when available, from similar cell lines. When not available in the literature, parameter values are chosen to accommodate the cell cycle dynamics, cell cycle length and radiation response. For example, the parameter values for the Goldbeter-Koshland kinetics of Chk2 and ATM in Eqs. (2.1h)–(2.1i) are chosen to reproduce the results related to the dose threshold for DSBs recognition observed by Rothkamm and Löbrich [83] (this dose threshold is presented in Section 2.3.3) and the threshold for unrepaired DSBs observed by Deckbar et al. [16] for G2 checkpoint activation and maintenance (this threshold is presented in Section 2.3.4). Similarly, the parameter values of μ and k_{m0} in Eqs. (2.1g) and (2.1a), respectively, have been chosen to accommodate a cell cycle length of approximately 24 hr. Parameter values are

summarized in Table 2.2.

Given the size (ten variables and over forty parameters) and the complex non-linearity of the model, numerical methods become a powerful tool to analyze the system. In the next section, we use numerical simulations and bifurcations to study and explain the effect of radiation on the G2 checkpoint. All numerical simulations are performed in Julia language and the Differential Equations suite [4, 81].

2.3 Results

When no radiation is applied, the model exhibits a stable oscillation (limit cycle). The numerical solution for this *control* case is shown in Fig. 2.3a. We observe the most important features of the cell cycle explained in the previous section, namely low MPF activity during interphase followed by a quick increase and decrease in its activity during M-phase, Wee1 activation during interphase, and APC activation during M-phase. MPF determines M-phase entry (exit) when its concentration increases above (decreases below) the threshold for mitosis, θ_M [25]. In the model, the cell mass divides in half on M-phase exit when MPF activity falls below θ_M . Having a threshold for mitosis is important to obtain some of our conclusions, but one should note the specific value ($\theta_M = 0.2$) is not important to describe the qualitative behaviour of the system in response to radiation.

Since the radiation pathway affects cell cycle dynamics through the inactivation of Cdc25, our analysis is focused on the total inactivation rate in Eq. (2.1d),

$$\tilde{V}_{c2} = V_{c2} + k_{c2a}Chk2. \quad (2.4)$$

This value is constant and equal to the *basal value* V_{c2} when radiation is not present

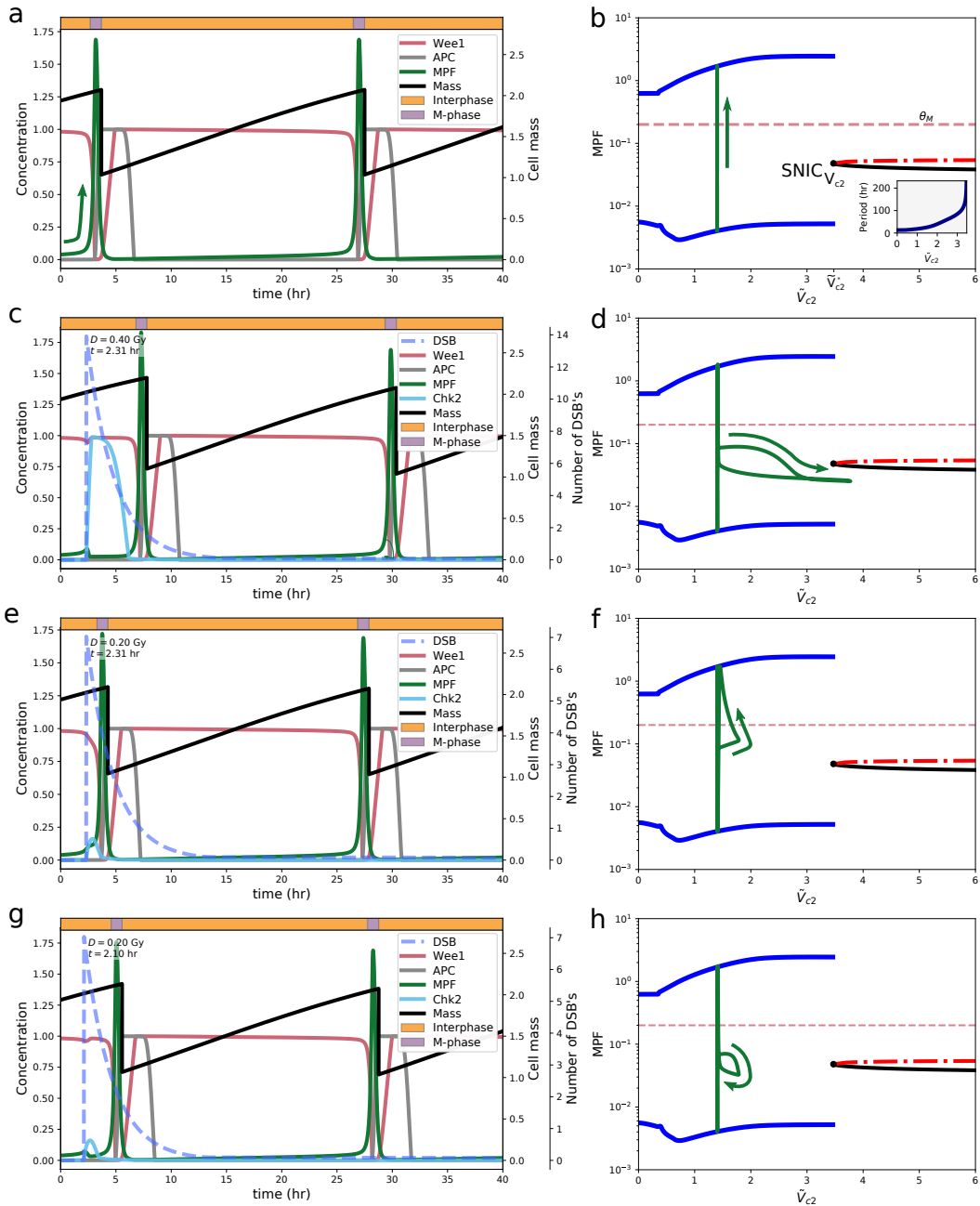


Figure 2.3: Numerical solutions (left) and one-parameter bifurcation diagrams with respect to \tilde{V}_{c2} as the bifurcation parameter (right). a) Plot of the dynamics of MPF, Wee1, APC and cell mass for one full cell cycle. The top bar indicates the phase of the cell cycle, either interphase or M-phase. G2/M transition is indicated with a green arrow. b) The SNIC $_{V_{c2}}$ bifurcation point ($\tilde{V}_{c2}^* = 3.47$) divides the diagram into two parts: cell cycle oscillation to the left (the blue curves are the maximum
(continued)

Figure 2.3 (*continued*): and minimum values of MPF) and G2 checkpoint to the right (the solid black and dot-dashed curves represent a stable node and saddle, respectively). For the basal value of \tilde{V}_{c2} , the superimposed full trajectory of MPF from a) shows the cell cycle oscillations, and the green arrow indicates the G2/M transition as the concentration of MPF crosses the threshold for M-phase $\theta_M = 0.2$. The inset shows the period of the oscillation (length of the cell cycle) as the parameter changes; the period becomes infinity at the $\text{SNIC}_{V_{c2}}$ bifurcation point. c–h) Similar to a) and b), when a single pulse of radiation is applied (total dose and time of application are indicated in the top left corners). Note that c), e), and g) include curves representing the number of DSBs and the activity of Chk2. The total dose D is computed using Eq. (2.3).

and Chk2 remains fully inactive.

In Fig. 2.3b, we plot the one-parameter bifurcation diagram using \tilde{V}_{c2} as the bifurcation parameter. The bifurcation diagram shows how the dynamics of the system changes as the parameter \tilde{V}_{c2} increases. To the left of $\tilde{V}_{c2}^* \approx 3.47$, the system exhibits a stable limit cycle (the cell cycle). The maximum and minimum values of the concentration of MPF on the limit cycle are represented with the blue curves, and are found numerically by collecting the minimum and maximum values of MPF in the limit cycle solution for each value of $\tilde{V}_{c2} < V_{c2}^*$. To the right of \tilde{V}_{c2}^* , there are a saddle and a stable node, represented with dot-dashed red and solid black curves, respectively. These were generated by using numerical continuation from a stable steady state for some $\tilde{V}_{c2} > V_{c2}^*$, and where the limit point $V_{c2}^* \approx 3.47$ was identified numerically. At \tilde{V}_{c2}^* , there is a saddle-node on an invariant circle bifurcation point ($\text{SNIC}_{V_{c2}}$, with subscript V_{c2} to distinguish it from another SNIC encountered later), which divides the bifurcation diagram into an oscillatory region to the left and a non-oscillatory region to the right [22]. The $\text{SNIC}_{V_{c2}}$ bifurcation is associated with an infinite-period limit cycle. The period of the limit cycle as a function of the bifurcation parameter \tilde{V}_{c2} is shown in the inset.

In Fig. 2.3b, the solution shown in Fig. 2.3a has been superimposed (green

curve). Note that this trajectory corresponds to the control case where no radiation is applied and the bifurcation parameter \tilde{V}_{c2} is equal the basal value V_{c2} . The G2/M transition (green arrow) occurs when MPF crosses the threshold for mitosis θ_M (horizontal dashed red line) from below.

When radiation is applied, Chk2 activity increases, thereby increasing the value of the bifurcation parameter \tilde{V}_{c2} . This forces the trajectory to move to the right on the bifurcation diagram, that is, towards the $\text{SNIC}_{V_{c2}}$ bifurcation. When the value of \tilde{V}_{c2} is greater than \tilde{V}_{c2}^* , the limit cycle is lost and trajectories are attracted to the stable node.

Under certain conditions (depending on radiation dose and time, explored in the subsections below), the detour of the trajectory to the right corresponds with an effect on the G2/M transition. We understand that the G2/M transition can be affected in one of two ways. On the one hand, the M-phase can be delayed if the trajectory remains in the oscillatory region. Because the dynamics still are oscillatory, the G2/M transition is inevitable. On the other hand, the G2 checkpoint can be activated if the trajectory detours into the non-oscillatory region (a refined definition of G2 checkpoint in the context of our mathematical model is provided in Section 2.4). In such case, the G2 checkpoint is inactivated when the trajectory comes back to the oscillatory region. Further understanding of the M-phase delay and G2 checkpoint activation is presented in Section 2.4. The overall message for now is that G2 checkpoint activation is possible via an increase in \tilde{V}_{c2} , that is, via an increase in the total inactivation rate of Cdc25.

The radiation scheme in our simulations is a single radiation pulse applied for one minute ($t_f - t_0 = 1$ min) at a constant radiation dose rate and at different times during the G2-phase. In the sections below, we illustrate that both the total radiation dose and the radiation timing are important when it comes to characterize

the effect of radiation on the G2/M transition. In Section 2.3.1, we vary the intensity of radiation and show that there is a Chk2-activation threshold that determines G2 checkpoint activation. In Section 2.3.2, we vary the timing of the radiation pulse, and show that there is a time-dependent threshold that determines the ability of the cell to postpone entry to M-phase. In Section 2.3.3, we show that there is no effect on the G2/M transition for extremely low doses of radiation. In Section 2.3.4, we synthesize the results obtained in the previous sections to characterize the overall effect of radiation on the G2/M transition.

Our study focuses on the simple case of a single radiation pulse. Studying the effect of a radiation pulse suffices to show how the cell cycle network changes dynamically in a short period of time. If we wanted to study the effect of fractionation and protraction on the G2 checkpoint activation, it would be necessary to consider explicitly other response pathways in the model, as there could be a cross response effect between the pathways. This is beyond the scope of this paper, therefore we do not study applications of such radiation schemes.

2.3.1 Effect of radiation pulse intensity on the G2/M transition

To illustrate the importance of the intensity of the radiation pulse, we simulate the application of two different intensities of low-dose radiation (0.4 and 0.2 Gy) about one hour before mitotic entry. For a radiation dose of 0.4 Gy (Fig. 2.3c), the cell is arrested in the G2 checkpoint until most of the DNA damage is repaired (only a couple DSBs remain). In this particular case, the oscillations are temporarily lost for few hours. This happens because Chk2 becomes active and the total inactivation rate of Cdc25, \tilde{V}_{c2} , is high enough to compromise the two positive feedback loops with MPF and block MPF activation. When Chk2 becomes inactive again, \tilde{V}_{c2} returns

to its basal value and the cell exits the G2 checkpoint to resume its cycle. In the bifurcation diagram of Fig. 2.3d, we observe that the solution makes an excursion into the non-oscillatory region as a result of the dynamic changes in \tilde{V}_{c2} .

For a lower radiation dose of 0.2 Gy, mitotic entry is not affected by DNA damage (see Fig. 2.3e), and most DSBs are able to pass through mitosis without being repaired. In the bifurcation diagram in Fig. 2.3f, we observe that the solution trajectory remains in the oscillatory region and the concentration of MPF continues to increase. Note that mitotic entry is not delayed even though we observe that the superimposed solution from Fig. 2.3e makes an excursion to the right. Thus, when radiation is applied close to mitotic entry, the number of DSBs caused by radiation has to be sufficiently high to successfully activate Chk2 and the G2 checkpoint, otherwise DSBs will be carried to the next M-phase.

2.3.2 Effect of radiation pulse timing on the G2/M transition

To illustrate the importance of timing of the radiation pulse, we use the application of 0.2 Gy in the previous section as a reference and simulate its application at an earlier time (Fig. 2.3g). In this case, mitotic entry is delayed until most DNA damage is repaired (only a couple DSBs remain). Compare Figs. 2.3e–2.3f, where there is not enough time for the response to delay mitosis, to Figs. 2.3g–2.3h (radiation pulse applied twelve minutes (0.2 hr) earlier), where there is enough time for the response to delay M-phase. We conclude that the ATM-Chk2 pathway requires some time for the G2/M transition to be affected successfully.

2.3.3 No effect of radiation pulse on the G2/M transition

In this section, we examine the model for radiation doses of 0.1 Gy and below. We show that there is no evidence of delayed G2/M transition or G2 checkpoint activation after a radiation pulse of 0.1 Gy or lower. This observation matches experimental results reported by Deckbar et al. [15]. We also demonstrate that the model exhibits an ATM-activation threshold of DSB at extremely low radiation. This threshold has been observed experimentally by Rothkamm and Löbrich [83] at approximately 2 mGy. The purpose of this section is to validate our modelling of the radiation pathway and parameter values therein independently of the cell cycle model.

Fig. 2.4a shows that Chk2 is completely inactive with the application of a radiation pulse of 0.1 Gy a few hours before mitosis. This observation is independent of the timing of radiation in terms of the cell cycle. Chk2 is not active because there are not enough ATM foci, which in turn is due to the low number of DSBs. Since Chk2 activation is necessary for G2 checkpoint activation or delay in the G2/M transition, we can conclude that there is no effect of radiation on the G2/M transition for doses below 0.1 Gy. Note that ATM is still active at this dose and targets DSBs for repair.

In Figs. 2.4b–2.4d, we simulate the application of a radiation pulse at extremely low dose (20, 5.0 and 1.2 mGy) with fixed dose rate of 50 mGy per minute and track the formation and repair of DSBs. ATM activation is necessary for the formation of ATM foci, given by the product $ATM \cdot DSB$, where DSBs are repaired. In Figs. 2.4b and 2.4c, we show that DSB repair follows minutes after the application of radiation at doses of 20 and 5 mGy, respectively, but stops when the average number of DSBs reaches approximately 0.1 (1 DSB every 10 cells). DSBs are no longer

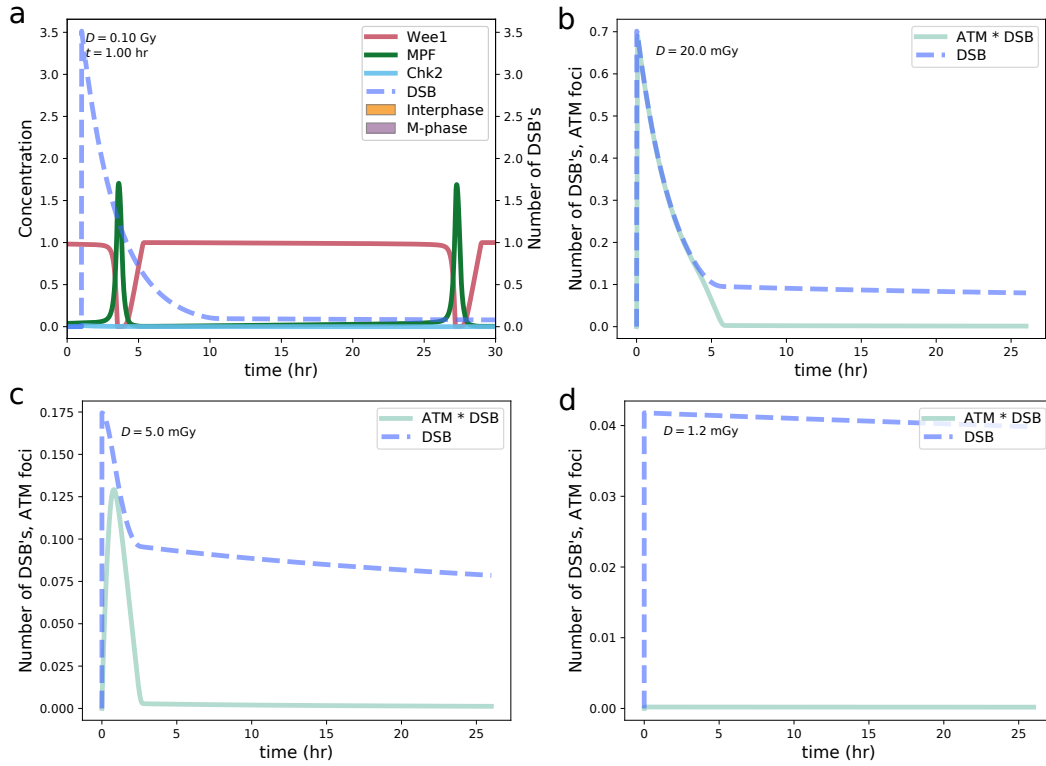


Figure 2.4: Effect of a radiation pulse at very low dose. a) Radiation pulse of 0.1 Gy. Chk2 is not activated below this dose, thus the cell cycle is not affected by radiation. b–d) ATM foci formation following radiation pulses of 20, 5 and 1.2 mGy, respectively. The product $ATM \cdot DSB$ is the number ATM foci, i.e., the number of recognized DSBs. Whenever the number of DSBs is below 0.1 (on average), ATM becomes inactive and the DSBs are no longer targeted for repair and remain unrepaired. At dose 1.2 mGy (d), the number of DSBs is too small to activate ATM.

repaired because there are too few of them to maintain activation of ATM. At 1.2 mGy, there is no evidence of ATM activation or DSB repair, as shown in Fig. 2.4d. We conclude that there is an ATM-activation threshold around 1-5 mGy. This ATM-activation threshold is governed by the Goldbeter-Koshland kinetics included in Eq. (2.1h).

Note that the application of radiation in Figs. 2.4b–d, where dose rate is fixed and duration varies, is different from that in Figs. 2.3 and 2.4a, where duration is fixed and dose rate varies. We have fixed the dose rate in Figs. 2.4b–2.4d in order to match the experimental set-up used by Rothkamm and Löbrich [83] in their Figure 3 (our model does not include their reported background level of ≈ 0.05 DSBs per cell). Results do not change if we fix the duration instead.

2.3.4 Overall effect of radiation pulse on the G2 checkpoint activation

The examples in the previous sections show how the G2/M transition can remain unaffected, be delayed, or blocked in response to a radiation pulse. The outcome depends on the radiation intensity and the moment of the cell cycle when the radiation is applied. Note that the moment and time of the cell cycle are ambiguous terms, for example, when cell cycle progression has been delayed. Thus, we prefer to use the *phase of the cell* to refer to the cell cycle progression relative to the control cell [54]. That is, phase of the cell is equivalent to time for the control cell when time $t = 0$ is at the start of the cell cycle (immediately after cell division).

The Chk2-activation dependent threshold occurs between 0.1 and 0.2 Gy, and is caused primarily by the activation of Chk2. At 0.1 Gy (see Fig. 2.4a), Chk2 is completely inactive and the G2/M transition remains unaffected. At 0.2 Gy (see

Fig. 2.3g), Chk2 is partially active and able to delay the G2/M transition. At 0.4 Gy (see Fig. 2.3c), Chk2 is fully active and the G2 checkpoint is active for a short period of time while DSBs are repaired. The difference between the delay of the G2/M transition at 0.2 Gy and the full G2 checkpoint activation at 0.4 Gy can be seen in the corresponding bifurcation diagrams. In the first case, the solution trajectory remains in the oscillatory region (see Figs. 2.3h) so that the G2/M transition is still possible. In the second case, the solution trajectory moves into the non-oscillatory region (see Fig. 2.3d) so that G2/M transition is not possible.

The phase-dependent threshold occurs some time before M-phase, and determines when radiation should be applied in order to affect the G2/M transition (compare Fig. 2.3e to Figs. 2.3c and 2.3g). This suggests that the closer the radiation pulse is to the mitotic entry, the higher the radiation intensity needs to be in order to affect the G2/M transition. Therefore, G2 checkpoint activation is the result of sufficiently high radiation applied enough time before M-phase.

The Chk2-activation and phase-dependent thresholds are summarized in Fig. 2.5. The four regions in the dose-phase plane determine the effectiveness of the radiation response that ultimately affects the collective cell survival. Radiation in region I is sufficiently high and early enough to trigger a G2 checkpoint activation that prevents damage from progressing to the M-phase. Radiation in region II is early enough to trigger a response but only high enough to cause a delay in the G2/M transition. Both regions I and II are beneficial for the cell and contribute to cell survival. Radiation in region III is too late to prevent damage from progressing into the M-phase. Radiation in region IV is too low to trigger any response. Both region III and IV are unfavourable for the cell and contribute to cell death and anomalies. This shows that G2 checkpoint activation is a fast mechanism but sensitive to dose and phase conditions to be triggered and maintained (region I) or partially induced

(region II). Recall from Fig. 2.3d that G2 checkpoint activation is deactivated when the value of \tilde{V}_{c_2} decreases below the critical value $V_{c_2}^*$. We can observe in Fig. 2.3c that this happens when the number of DSBs falls below 6 to 12 breaks and Chk2 becomes inactive. The number of DSBs at which the G2 checkpoint is deactivated agrees with experimental observations made by Deckbar et al. [16]. The location of the Chk2-activation threshold in Fig. 2.5 was obtained from the steady-state value of Chk2 in Eq. (2.1h) given by the Goldbeter-Koshland function. The shape and the location of the phase-dependent threshold are approximate and qualitative, based on numerical experimentation with several values of intensity and time of radiation pulse (details are not provided in this manuscript).

In the context of the HRS/IRR phenomenon reported by Marples and Joiner [57], we identify HRS with region IV and IRR with region II, respectively. That is, cells are hypersensitive to very low doses of radiation due to lack of response, but increasingly gain resistance to radiation when the response becomes active above the Chk2-activation threshold. For higher radiation (~ 0.3 Gy), cell cycle delay is replaced by successful G2 checkpoint activation. For radiation higher than 0.6 Gy, other pathways that affect cell survival would play a more significant role, such as pro-apoptotic signals and necrosis [68].

2.4 Analysis of the G2/M transition and definition of G2 checkpoint

In Section 2.3, we showed how radiation intensity and timing can result in G2 checkpoint activation. In this section, we analyze the G2/M transition in terms of the model using bifurcation theory. In particular, we show the relation between the

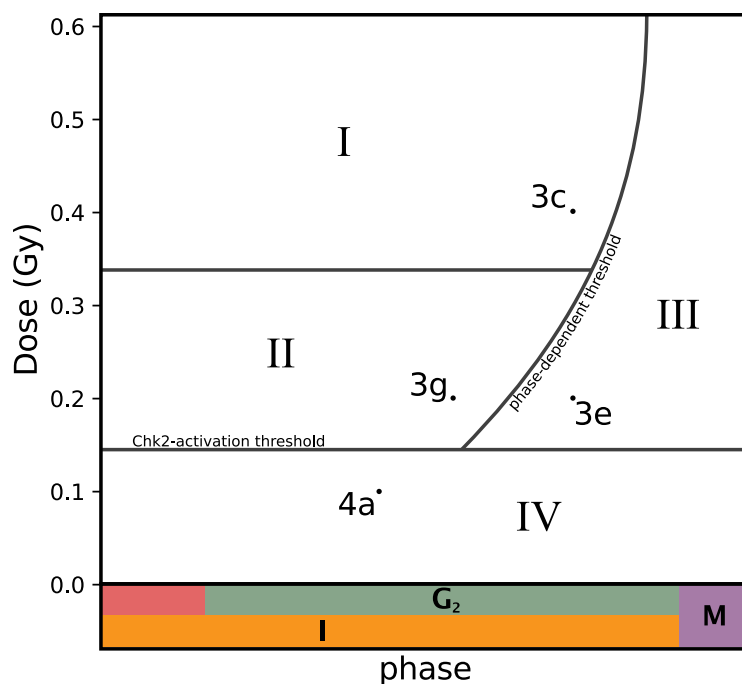


Figure 2.5: Diagram of the overall effect of radiation, as a function of the dose and timing of the radiation pulse, on the G2/M transition by the ATM-Chk2 pathway. Only a portion of the cell cycle, focusing on the G2-phase, is shown on the horizontal axis. 'Phase indicates the moment at which the radiation pulse is applied relative to the control cell. The intensity and timing of the radiation pulse applied in Figs. 2.3c, 2.3e, 2.3g, and 2.4a are indicated in the diagram with a dot symbol. The diagram is divided into four regions: region I, G2 checkpoint activation; region II, delay of mitotic entry; region III, G2 checkpoint is not possible and delay is very limited; and region IV, DSBs have no effect on the cell cycle.

SNIC $_{V_{c2}}$ bifurcation in Fig. 2.3 and a different SNIC bifurcation responsible for the G2/M transition and driven by mass as presented by Novák et al. [74]. This relation is determined by the ability of the radiation pathway to counteract the influence that cell mass has on the G2/M transition. To further explore this idea, we consider in this section only Eqs. (2.1a)–(2.1f), and treat both cell mass (variable $Mass$ in Eq. (2.1a)) and total inactivation rate of Cdc25 (\tilde{V}_{c2} in Eq. 2.4 and thereby in Eq. 2.1d) as bifurcation parameters.

First, we consider the bifurcation diagram with cell mass as a parameter under default conditions (no radiation), shown in Fig. 2.6a. The diagram is divided into a non-oscillatory region and an oscillatory region by a SNIC bifurcation, which we label as SNIC $_{Mass}$ to distinguish it from the already mentioned SNIC $_{V_{c2}}$. The non-oscillatory region is to the left of SNIC $_{Mass}$; the oscillatory region is to the right. The stable node in the non-oscillatory region, represented by the black curve, corresponds to the action of Wee1 blocking MPF activity. Therefore, the non-oscillatory region is identified with the interphase of the cell cycle. As cell mass increases, the stable node disappears at the SNIC $_{Mass}$ bifurcation when it coalesces with the saddle, represented by the lower branch of the red curve. To the right of SNIC $_{Mass}$, the concentration of active MPF is oscillatory. This oscillation is a consequence of the negative feedback loop of MPF with APC and is responsible for the increase and decrease of MPF during M-phase [73]. Therefore, the oscillatory region of the bifurcation diagram is identified with the M-phase of the cell cycle. In essence then, it is when the cell mass passes through the SNIC $_{Mass}$ bifurcation point that the G2/M transition is triggered [71]. The superimposed trajectory from Fig. 2.3a (green curve) shows the evolution of active MPF during the cell cycle in relation to the bifurcation structure of the model. Note that the concentration of active MPF first increases as the cell enters M-phase, followed by a decrease in

concentration that eventually determines cell division (mass splits in two).

When Chk2 is fully active ($\text{Chk2} \sim 1$), \tilde{V}_{c2} reaches a maximum value of 3.8 (see Table 2.2 in the Appendix) and the bifurcation diagram in Fig. 2.6a transforms into that of Fig. 2.6b. Note that the original bifurcation diagram is included in transparent colour, for reference. As \tilde{V}_{c2} changes dynamically, so does the bifurcation diagram. In particular, as \tilde{V}_{c2} increases, the SNIC_{Mass} bifurcation point moves to the right. At the maximum value of \tilde{V}_{c2} , note that the SNIC_{Mass} bifurcation point has moved just to the right of the K_{Mass} value, indicated by the dashed grey vertical line.

In Fig. 2.6b, we have superimposed a portion of the solution from Fig. 2.3c (from time 2.3 hr to 15.0 hr, shown in green) obtained in the presence of a radiation pulse (administered at 2.3 hr). At first, the phase point is in the oscillatory region, and both cell mass and active MPF are increasing. Also, the radiation pathway is activated causing an increase in \tilde{V}_{c2} , in turn causing the SNIC_{Mass} bifurcation point to move to the right. A little while later, the SNIC_{Mass} bifurcation point overtakes the phase point such that the trajectory is caught in the basin of attraction of the stable node. For this particular simulation, this is associated with a decrease in active MPF. Eventually, due to repair of damaged DNA, the radiation pathway becomes inactive, causing the SNIC_{Mass} bifurcation point to move back to the left of the phase point. At this point, the G2/M transition proceeds and the cell cycle resumes.

Now, keeping track of the SNIC_{Mass} bifurcation point while varying the total inactivation rate of Cdc25, \tilde{V}_{c2} , we obtain the two-parameter bifurcation curve shown in red in Fig. 2.6c. Note that this curve separates the interphase (non-oscillatory region) from the M-phase (oscillatory region), and crossing it from left to right describes the G2/M transition. The cell cycle oscillation shown in Fig. 2.6a (green curve) corresponds to the green horizontal line that crosses back and forth between

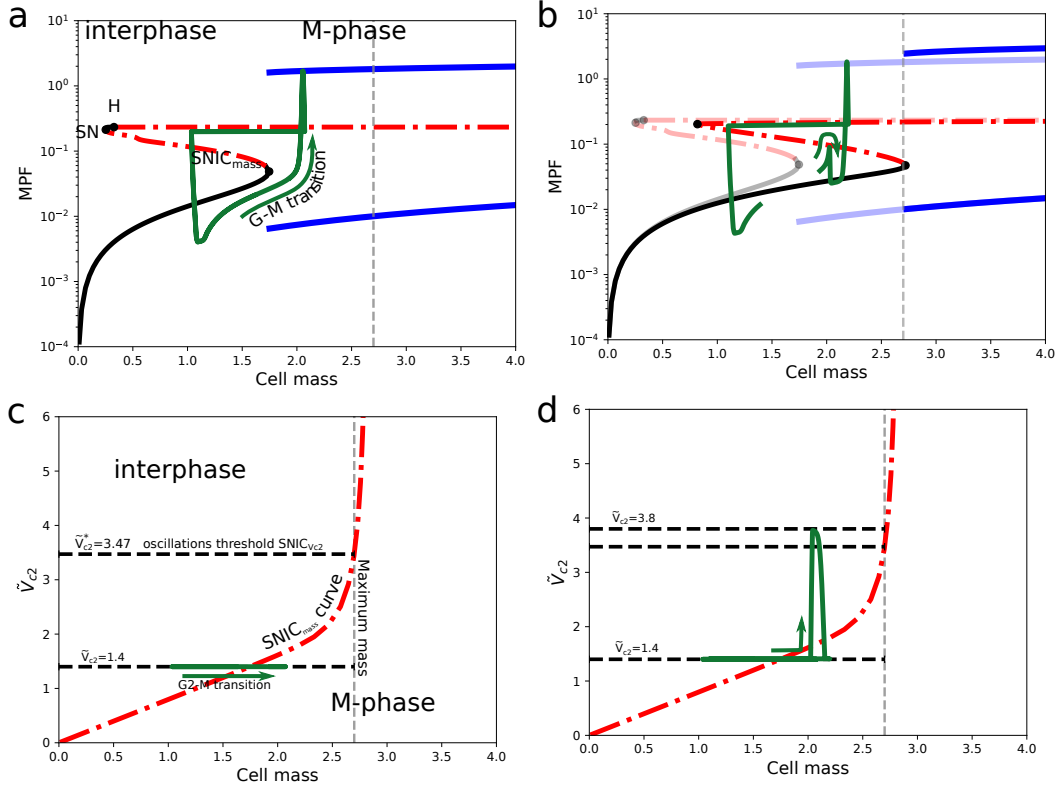


Figure 2.6: Bifurcation diagrams. a) One-parameter bifurcation diagram with respect to cell mass when *Chk2* is inactive ($\tilde{V}_{c2} = V_{c2} = 1.4$). The $SNIC_{Mass}$ divides the diagram into interphase to the left and M-phase to the right. The interphase is governed by steady states, with the stable branch of the $SNIC_{Mass}$ (solid black) determining the concentration of MPF. The Hopf (H) and saddle-node (SN) bifurcation points that appear on the left side do not affect the dynamics of the cell cycle. The M-phase is governed by oscillations (minimum and maximum in solid blue) that make possible an increase and a decrease of the concentration of MPF. The MPF solution trajectory (solid green) from Fig. 2.3a is superimposed on the diagram to show how the $SNIC_{Mass}$ point determines the bistable switch from G2-phase to M-phase (G2/M transition). b) One-parameter bifurcation diagram with respect to cell mass when *Chk2* is fully active ($\tilde{V}_{c2} = V_{c2} + k_{c2a} = 3.8$). The bifurcation diagram in A is shown in transparent colour, for reference. The portion of the MPF trajectory from Fig. 2.3c representing the first 14 hours after radiation is superimposed to show how the saddle node is relocated in front of the trajectory, which will be now attracted to the stable node. When *Chk2* becomes inactive again, the bifurcation diagram returns to the original state (shown as transparent) and the cell cycle resumes. This allows the cell to enter the first M-phase shown in Fig. 2.3c. c) Two-parameter bifurcation diagram with respect to cell mass and total inactivation
(continued)

Figure 2.6 (*continued*): rate of Cdc25, \tilde{V}_{c2} . The SNIC_{Mass} curve (dot-dashed red) is the continuation of the SNIC_{Mass} point found in a, and divides the diagram into interphase and M-phase. The solution trajectory (solid green) from Fig. 2.3a superimposes as a horizontal line and shows that the G2/M transition occurs when it crosses the SNIC_{Mass} curve from left to right. For a fixed value of \tilde{V}_{c2} , the segment of possible values of cell mass (dashed black) determines the range (between 0 and K_{Mass}) in which a solution oscillates back and forth between interphase and M-phase. Cell cycle oscillations are lost at $\tilde{V}_{c2} = \tilde{V}_{c2}^* = 3.47$ when the cell mass segment no longer intersects the SNIC_{Mass} curve. d) Similar to c, but with the trajectory solution from B superimposed. The green arrow indicates the detour the solution trajectory has taken after the radiation pulse.

the interphase region and the M-phase region in Fig. 2.6c (note that it corresponds to the green vertical line shown in Fig. 2.3b).

Due to the logistic growth in Eq. (2.1g), the possible values for the cell mass are between 0 and $K_{Mass} = 2.7$. The K_{Mass} value is indicated in the diagram with a vertical dashed gray line. The mass range for the default value of \tilde{V}_{c2} (control conditions; no radiation) is represented in Fig. 2.6c with the lower horizontal dashed line segment. As \tilde{V}_{c2} increases, the segment moves upwards. There is a value of \tilde{V}_{c2} for which the mass-range-segment first lies entirely in the interphase region. This value of \tilde{V}_{c2} corresponds to the value $\tilde{V}_{c2}^* \approx 3.47$ where the $\text{SNIC}_{V_{c2}}$ takes place in Fig. 2.3b. Thus, if \tilde{V}_{c2} is larger than the bifurcation value \tilde{V}_{c2}^* , the G2/M transition is no longer possible. The cell cycle oscillations are lost and the cell remains in the interphase. In other words, the $\text{SNIC}_{V_{c2}}$ bifurcation point shown in Fig. 2.3b is the loss of the SNIC_{Mass} bifurcation point shown in Fig. 2.6a within the cell mass range values.

The solution superimposed in Fig. 2.6b appears in the two-parameter bifurcation diagram as shown in Fig. 2.6d. After the radiation pulse, the value of \tilde{V}_{c2} increases and the solution trajectory moves upwards in this diagram. This motion is associated with the decrease in MPF in Fig. 2.6b. Note that the solution trajectory crosses the

upper mass-range-segment where cell cycle oscillations are lost. With DNA repair, the value of \tilde{V}_{c2} decreases back to the basal value and the trajectory resumes the cell cycle oscillations.

In the context of the mathematical model, we view delay on the G2/M transition as any detour of the solution trajectory either to the right in the one-parameter bifurcation diagram in Fig. 2.3b or upwards in the two-parameter bifurcation diagram in Fig. 2.6c (provided there is enough time before M-phase for a proper response). Moreover, we view G2 checkpoint activation to take place when the trajectory crosses the $\text{SNIC}_{V_{c2}}$ bifurcation point in Fig. 2.3b or, equivalently, when the trajectory crosses the mass-range oscillations in Fig. 2.6c. The G2 checkpoint can be sustained as long as the phase point remains in the non-oscillatory region.

We illustrate the appearance of the G2/M transition in control conditions (no radiation) on the familiar schematic diagram of the cell cycle in Fig. 2.7a. The figure shows six snapshots of a cell as it progresses through the cell cycle. We represent the G2 checkpoint with the black U-shaped curve. The fourth snapshot, where the U-shaped curve touches the schematic diagram of the cell cycle, represents the SNIC_{Mass} bifurcation. The G2 checkpoint controls the transition in an irreversible switch-like manner as cell mass increases. The G2 checkpoint can be seen as a control ‘gate’ that is lifted (indicated by the movement of the U-shaped curve in the direction of the arrow) to enable the G2/M transition as cell mass increases.

The interplay between the effects of cell growth and radiation is illustrated in Figs. 2.7b–2.7d. Radiation counteracts the effect of cell growth by activating the G2 checkpoint (moving the U-shaped curve in the opposite direction) and blocking the G2/M transition towards the end of the interphase. G2 checkpoint activation is possible as long as the saddle node can be dynamically positioned ahead of the current state of the cell, as shown in Fig. 2.7b where the checkpoint is activated.

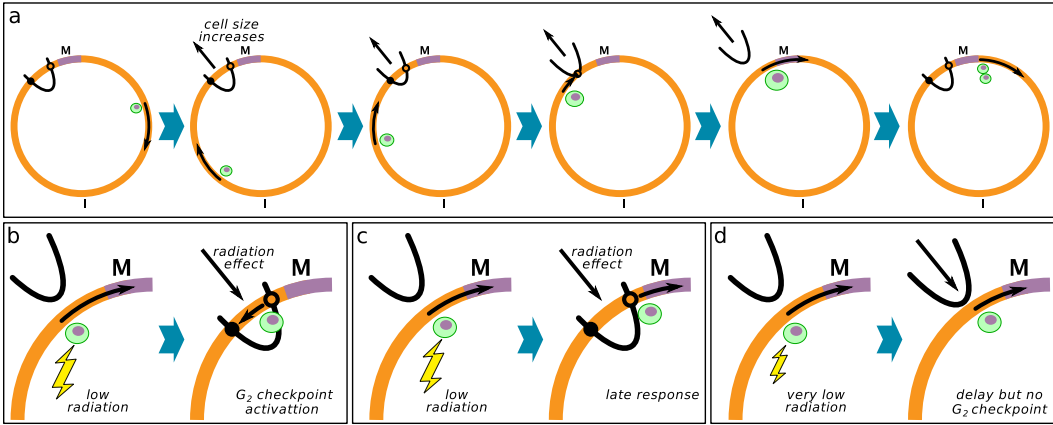


Figure 2.7: Cell cycle progression and G2 checkpoint activation. a) A control cell (represented in green with purple nucleus) progresses through the cell cycle and makes the G2/M transition as cell mass increases. The saddle and node branches of the SNIC_{Mass} in Fig. 2.6a are represented with open and solid circles on the U-shape curve, respectively. b-d) Closeup of the G2/M transition showing the effect of radiation on the U-shape curve for different G2 checkpoint scenarios: b) effective activation, c) late activation, and d) no activation.

If the cell already committed to enter mitosis, G2 checkpoint activation fails, as shown in Fig. 2.7c, where the cell skips the checkpoint. Finally, if Chk2 is not fully activated, the G2/M transition is not blocked; however, delay is still possible, as shown in Fig. 2.7d. The three cases correspond to regions I, II, and III presented in Fig. 2.5. Using the gate analogy, radiation lowers down the gate, but the position of the cell (relative to the gate) determines if it passes through before the gate closes. If radiation is not high enough to fully close the gate, the cell slows down but eventually passes towards mitosis.

2.5 Discussion

The effect of radiation on cells is far more complex than simply stating ‘radiation causes DNA damage and kills cells’. Several events that follow radiation influence the fate of cells and future generations, including repair mechanisms, checkpoint

failure, apoptosis, mitotic catastrophe, etc. Although the final effect of radiation is a decrease in the survival fraction, investigating the immediate effect and the cascade of numerous pathways that follow is critical to understand the overall effect of radiation. This is not an easy task given the difficulty in tracking intracellular protein dynamics in radiation experiments. After decades of research, we have clues on the mechanisms that follow radiation, yet the exact mechanisms remain unclear. In this work, we have studied one of these mechanisms from a kinetic perspective. Specifically, we studied the effect of radiation on the G2/M transition through the ATM-Chk2 pathway.

We extended a mathematical model of the cell cycle, based on the work of Tyson and Novák [96], by including the radiation pathway. Our resulting model, given by Eqs. (2.1a)–(2.1j), consists of modules for the interphase, M-phase, and the radiation pathway, describing the interactions between the main proteins involved. The radiation module, characterized by the ATM–Chk2 pathway, becomes active after formation of DSBs. The parameter values in the model were taken and adapted from different sources to represent observed values for the cell cycle length, cell mass growth, DSBs formation/repair rates, and threshold of activation for mammalian cells.

By considering single radiation pulses, we were able to analyze the effect of the radiation intensity and timing on the G2/M transition. Our results show that the effect depends on the ability of cells to delay the G2/M transition so that DNA damage can be repaired before mitosis. In particular, we identified a qualitative change in the dynamics of the cell cycle as radiation dose varies. Below 0.1 Gy, the G2/M transition is not affected by radiation; between 0.1 and 0.3 Gy, the G2/M transition is delayed; and above 0.3 Gy, the G2 checkpoint is fully activated. We conjecture that the first and second ranges are responsible for the hyper-radiosensitivity (HRS) and

increased radioresistance (IRR), respectively, which supports the hypothesis that the trade-off between increasing DNA damage and G2 checkpoint failure/success is responsible for the HRS/IRR phenomenon [60]. It is worthwhile to mention that these dynamical changes are the result of incorporating the ‘fast but insensitive’ activation of Chk2 observed in experiments [16] into our model.

We also identified a phase-dependent threshold, describing the time when the application of a radiation pulse does not leave enough time to delay or arrest the cell. In other words, the phase-dependent threshold refers to the time when the cell has already committed to enter M-phase. Thus, DSBs initiated after this threshold will enter mitosis and potentially affect the cell or future generations. This threshold may contribute to HRS/IRR as well as mitotic catastrophe.

Other mathematical modelling approaches and signalling pathways have been used to explain HRS/IRR. The Induced-Repair model is the simplest model to capture HRS/IRR [88]. The model is phenomenological; it does not provide a mechanistic explanation for it. Other models capturing the underlying mechanisms for the HRS/IRR with alternate pathways include a kinetic model for the interaction between nucleo-shuttling of ATM and DSBs [5], and a reaction-diffusion model for bystander effect [77]. However, these models do not explain the relationship between the HRS/IRR and the G2-phase. Olobatuyi et al. [78] use a population-based model with the cell phases as compartments to capture HRS/IRR and classify cell lines by their HRS profile. It would be interesting to derive a survival fraction model from our kinetic and cell cycle approach, and relate it to the previously mentioned models. However, this derivation is beyond the scope of this paper and is left for future research.

There are other radiation pathways not included in the model (such as those mediated by p53) that could have an effect after the ATM pathway. These different

pathways may result in the two different G2 checkpoints discussed by Marples [59]: one dose and ATM dependent (presented here), and one slow and ATM independent (presumably p53 dependent). Also, there are aspects in the radiation pathway not considered in our model that could play an important role in the G2/M transition, such as ATM nucleo-shuttling [6], ATM phosphorylation and signalling [32, 20], different repair mechanisms (non-homologous end joining, for example) [28], repairable/irreparable DSBs rates, DSB types [90], and ATR-Chk1-p53 pathway [2]. It would be interesting as well to extend the model to incorporate these aspects.

The qualitative analysis of our model not only reveals the effect of radiation on the cell cycle dynamics, but also has the potential to provide insight on the dynamical differences between healthy and cancer cells. For example, one of the characteristics of cancer cells is their insensitivity to anti-growth signals [33], which can be thought of as causing cancer cells to increase their mass uncontrollably beyond their carrying capacity. In the context of the bifurcation diagram in Fig. 2.6b, this would result in the loss of the $\text{SNIC}_{V_{c2}}$ bifurcation in Fig. 2.3b, and thereby compromise proper G2 checkpoint activation in response to radiation. Similarly, changes in the values of other parameters could also be used to describe dynamical differences between healthy and cancer cells.

In conclusion, incorporating the ATM-Chk2 pathway in a model of the cell cycle and carrying out a detailed bifurcation analysis have allowed us to describe the G2/M transition and the nature of its delay caused by radiation. We distinguish mathematically between a delay that does not compromise the oscillatory behaviour of the cell dynamics but may (or may not) be sufficient for a successful repair of DNA damage, and a larger delay that is associated with the temporary loss of oscillatory behaviour of the cell dynamics due to the increased inactivation rate of

Cdc25. It is this latter delay that we identify with activation of the G2 checkpoint. Our theoretical work, based on the effect of radiation on the control mechanisms that regulate the cell cycle, contributes to a more detailed understanding of the G2/M transition and G2 checkpoint activation after radiation.

2.A Appendix: parameters values

The Goldbeter-Koshland kinetics model for protein activation is given by

$$\frac{dx}{dt} = v_1 \frac{1-x}{J_1 + 1-x} - v_2 \frac{x}{J_2 + x},$$

where x is the normalized concentration of the active form of the protein, $1-x$ is the concentration of the inactive form of the protein, v_1 is the maximum activation rate, v_2 is the maximum inactivation rate, and J_1 and J_2 are the Michaelis constants. The smaller the Michaelis constants the faster the activation/inactivation switch is. It can be shown that the activation of x is obtained when

$$\frac{v_1}{v_2} > 1.$$

Ultrasensitivity refers to a fast switch in activity when v_1 is close to v_2 and the Michaelis constants are small. Parameter values in the radiation pathway module, such as activation/inactivation rate and Michaelis constants, are carefully chosen so that our simulations match experimental results (see Table 2.2).

Table 2.2: Parameter values. Most parameter values have been taken from Gérard et al. [25] or adapted to match cell cycle length in mammalian cells. Parameters related to the radiation pathway come from different sources or were cautiously chosen on the basis of numerical simulations. Details are provided in the footnotes that are referenced in the Source column. Parameters with no units are dimensionless.

Symbol	Definition	Value	Units	Source
k_{m0}	Rate of synthesis of Cdk-cyclin fusion protein, MPF	0.2	hr ⁻¹	¹
k_{m1}	Rate constant for the dephosphorylation of MPF	0.4	hr ⁻¹	²
k_{m1a}	Rate constant for the dephosphorylation of MPF by Cdc25	20.0	hr ⁻¹	2
k_{m2}	Rate constant for the phosphorylation of MPF	0.4	hr ⁻¹	2
k_{m2a}	Rate constant for the phosphorylation of MPF by Wee1	50.0	hr ⁻¹	1
k_{m3}	Rate constant for the degradation of MPF and MPF _P	0.2	hr ⁻¹	2
k_{m3a}	Rate constant for the degradation of MPF and MPF _P by APC	6.35	hr ⁻¹	2
V_{w1}	Maximum activation rate, by dephosphorylation, of Wee1	1.0	hr ⁻¹	2
k_{w2}	Rate constant for activation of Wee1 by MPF	5.3	hr ⁻¹	2
J_{w1}	Michaelis constant for Wee1 activation	0.01		³

continued...

¹Taken from Gérard et al. [25]; slightly modified to accommodate the correct G2/M transition dynamics.

²Taken from Gérard et al. [25]; scaling factor of 8.5 needed to rescale the length of the cell cycle to approximately 24 hrs.

³Taken from Gérard et al. [25].

...continued

Symbol	Definition	Value	Units	Source
J_{w2}	Michaelis constant for Wee1 inactivation	0.01		3
k_{c1}	Rate constant for Cdc25 phosphorylation by MPF	8.5	hr ⁻¹	2
V_{c2}	Maximum inactivation rate, by dephosphorylation, of Cdc25	1.4	hr ⁻¹	1
k_{c2a}	Rate constant for the inactivation of Cdc25 by Chk2	2.4	hr ⁻¹	4
J_{c1}	Michaelis constant for Cdc25 activation	0.01		3
J_{c2}	Michaelis constant for Cdc25 inactivation	0.01		3
k_{i1}	Rate constant for the activation of IE by MPF	1.7	hr ⁻¹	2
V_{i2}	Maximum inactivation rate of IE	0.4	hr ⁻¹	2
J_{i1}	Michaelis constant for IE activation	0.001		3
J_{i2}	Michaelis constant for IE inactivation	0.001		3
k_{a1}	Rate constant for the activation, by phosphorylation, of APC by IE	6.8	hr ⁻¹	2
V_{a2}	Maximum inactivation rate, by phosphorylation, of APC	1.7	hr ⁻¹	2
J_{a1}	Michaelis constant for APC activation	0.001		3
J_{a2}	Michaelis constant for APC inactivation	0.001		3
k_{h1}	Rate constant for the activation, by phosphorylation, of Chk2 by ATM	0.32	hr ⁻¹	5

continued...

⁴Educated guess.

⁵Chosen to fit activation time presented by Buscemi et al. [11].

...continued

Symbol	Definition	Value	Units	Source
V_{h2}	Maximum inactivation rate, by dephosphorylation, of Chk2	1.9	hr^{-1}	6
J_{h1}	Michaelis constant for Chk2 activation	0.01		4
J_{h2}	Michaelis constant for Chk2 inactivation	0.01		4
k_{t1}	Rate constant for the activation (recruitment and autophosphorylation) of ATM around DSB repair foci	30	$\text{dsb}^{-1}\text{hr}^{-1}$	7
V_{t2}	Maximum inactivation rate of ATM	3.8	hr^{-1}	2
J_{t1}	Michaelis constant for ATM auto-phosphorylation	0.01		4
J_{t2}	Michaelis constant for ATM deactivation	0.01		4
k_{d1}	Rate constant for DSBs damage formation	35.0	$\text{dsb} \cdot \text{Gy}^{-1}$	8
k_{d2}	Rate constant for DSBs repair	0.4	hr^{-1}	9
α	Partial activity of MPF _P	0.05		2
μ	Growth rate of the cell	0.07	hr^{-1}	10
K_{Mass}	Maximum cell mass	2.7		4
$Wee1_T$	Total concentration of kinase Wee1	1.0		2
$Cdc25_T$	Total concentration of phosphatase Cdc25	1.0		2
IE_T	Total concentration of intermediate enzyme IE	1.0		2

continued...

⁶Chosen to fit Chk2 activation threshold after radiation [37].

⁷Taken from Kozlov et al. [45].

⁸Taken from Rothkamm and Löbrich [83].

⁹Taken from Scott [85].

¹⁰Informed by Park et al. [80].

...continued

Symbol	Definition	Value	Units	Source
APC_T	Total concentration of protein APC	1.0		2
$Chk2_T$	Total concentration of Checkpoint kinase 2	1.0		4
ATM_T	Total concentration of ATM	1.0		4

Chapter 3

Effect of low-dose radiation on the survival fraction through the ATM-Chk2 pathway: a numerical approach

In Chapter 2, we studied the effect of radiation on the G2/M transition through the ATM-Chk2 pathway. In this chapter, we extend our study by investigating the effect of radiation on the cell survival of a population of cells. We show that including the dynamics of the ATM/Chk2 pathway with the cell cycle, as modelled in Chapter 2, can produce the hyper-radiosensitivity and increased radioresistance (HRS/IRR) phenomenon observed in the cell survival fraction at low doses of radiation [58].

The cell survival curve is one of the most important tools to study the effect of radiation on a population of cells. It shows the relationship between the absorbed dose of radiation and the ability of cells to reproduce. HRS/IRR is a phenomenon observed in survival fraction curves at low dose of radiation (< 0.1 Gy) in which

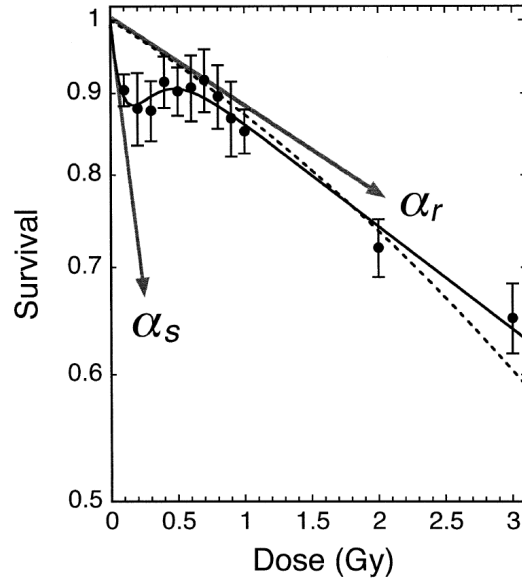


Figure 3.1: Survival fraction showing HRS/IRR. Hyper-radiosensitive (HRS) is observed for low radiation dose until approximately 0.2 Gy, and increased radioresistance (IRR) is observed for radiation ranging 0.2 to 0.5 Gy. Figure taken from Marples et al. [58]

cells can be hypersensitive to radiation at low dose but surprisingly gain resistance for higher dose (see Figure 3.1) [57]. This counterintuitive phenomenon can be used to make radiation therapy more effective [64].

In Chapter 2, we conjectured that the hyper-radiosensitive portion of the survival fraction curve is caused by the inability of cells to activate the G2 checkpoint while the increased radioresistance portion is caused by increased activation of the G2 checkpoint. This conjecture is made on the basis of the ATM and Chk2 pathways activated by radiation and resulting in changes in the G2/M transition. These ideas are consistent with the hypothesis of Marples [59] that the G2 checkpoint plays a mayor role in HRS/IRR based on experimental evidence that HRS/IRR is more pronounced when cells are synchronized in G2-phase. The question left to answer is how the effect of radiation on the G2/M transition studied in the previous chapter

translates to the HRS/IRR phenomenon in the survival fraction curve. The goal for this chapter is to establish the connection between radiation and survival fraction, using numerical simulations on the cell cycle and radiation pathway model studied in Chapter 2.

This chapter is structured as follows. In Section 3.1, we focus on single cells and introduce the concept of lethal Double Strand Breaks (DSBs) caused by the effect of radiation on the G2/M transition, which we assume are crucial to determine the fate of a cell and future generations. In Section 3.2, we extend our study to a population of cells and propose a model for the cell survival fraction based on lethal DSBs. In Section 3.3, we simulate the proposed survival fraction model for asynchronous cells and synchronous cells enriched in G1-, G2-, and M-phase. Our simulated cell survival curves show an HRS/IRR response more observable in G2 cells. In Section 3.4, we investigate ways to derive a theoretical expression for the proposed survival fraction model. In Section 3.5, we discuss our preliminary results and the limitations of our numerical procedure to fit survival fraction curve data. This discussion opens the opportunity to investigate a more practical theoretical formulation which will be introduced in Chapter 6.

3.1 Lethal DSBs

In Chapter 2, we studied the effect of radiation on the G2/M transition via the ATM-Chk2 pathway. We used a regulatory network consisting of the following system of differential equations:

$$\frac{dMPF}{dt} = k_{m0}Mass - (k_{m2} + k_{m2a}Wee1)MPF$$

$$+ (k_{m1} + k_{m1a}Cdc25)MPF_P - (k_{m3} + k_{m3a}APC)MPF, \quad (3.1a)$$

$$\begin{aligned} \frac{dMPF_P}{dt} &= (k_{m2} + k_{m2a}Wee1)MPF - (k_{m1} + k_{m1a}Cdc25)MPF_P \\ &\quad - (k_{m3} + k_{m3a}APC)MPF_P, \end{aligned} \quad (3.1b)$$

$$\frac{dWee1}{dt} = V_{w1} \frac{Wee1_T - Wee1}{J_{w1} + (Wee1_T - Wee1)} - k_{w2}(MPF + \alpha MPF_P) \frac{Wee1}{J_{w2} + Wee1}, \quad (3.1c)$$

$$\begin{aligned} \frac{dCdc25}{dt} &= k_{c1}(MPF + \alpha MPF_P) \frac{Cdc25_T - Cdc25}{J_{c1} + (Cdc25_T - Cdc25)} \\ &\quad - (V_{c2} + k_{c2a}Chk2) \frac{Cdc25}{J_{c2} + Cdc25}, \end{aligned} \quad (3.1d)$$

$$\frac{dIE}{dt} = k_{i1}(MPF + \alpha MPF_P) \frac{IE_T - IE}{J_{i1} + (IE_T - IE)} - V_{i2} \frac{IE}{J_{i2} + IE}, \quad (3.1e)$$

$$\frac{dAPC}{dt} = k_{a1}IE \frac{APC_T - APC}{J_{a1} + (APC_T - APC)} - V_{a2} \frac{APC}{J_{a2} + APC}, \quad (3.1f)$$

$$\frac{dMass}{dt} = \mu Mass \left(1 - \frac{Mass}{K_{Mass}} \right), \quad (3.1g)$$

$$\frac{dChk2}{dt} = k_{h1}ATM DSB \frac{Chk2_T - Chk2}{J_{h1} + (Chk2_T - Chk2)} - V_{h2} \frac{Chk2}{J_{h2} + Chk2}, \quad (3.1h)$$

$$\frac{dATM}{dt} = k_{t1}DSB \frac{ATM_T - ATM}{J_{t1} + (ATM_T - ATM)} - V_{t2} \frac{ATM}{J_{t2} + ATM}, \quad (3.1i)$$

$$\frac{dDSB}{dt} = k_{d1}\dot{D}(t) - k_{d2}ATM DSB, \quad (3.1j)$$

subject to the resetting condition

$$\text{if } MPF(t) = \theta_M \text{ and } \frac{dMPF}{dt}(t) < 0 \implies Mass(t) \leftarrow \frac{Mass(t)}{2}, \quad (3.2)$$

where the variables denote the concentration of the most important proteins involved in the G2/M transition and the ATM-Chk2 pathway, the number of DSBs, and the mass of the cell (see Table 3.1). The parameters denote the average rate of reactions between given proteins, cell growth, carrying capacity, and other average rates (see Table 3.3).

Table 3.1: Name and description of variables in Eqs. (3.1a)–(3.1j). All variables represent concentration, except $Mass$ and DSB .

Symbol	Description
MPF	Active Cdk1-cyclin B complex (Mitotic Promoting Factor)
MPF_P	Inactive, phosphorylated form of MPF
$Wee1$	Active dephosphorylated form of kinase Wee1 (MPF inactivator)
$Cdc25$	Active phosphorylated form of the phosphatase Cdc25C (MPF activator)
IE	Active form of an intermediate enzyme [94]
APC	Active phosphorylated form of APC (Anaphase Promoting Complex)
$Chk2$	Active phosphorylated form of Chk2 (Checkpoint kinase 2)
ATM	Active phosphorylated, monomerized and recruited form of ATM
DSB	Recognized Double Strand Brakes formed by Ionizing Radiation
$Mass$	Mass of the cell

We showed that radiation affects the G2/M transition by triggering the G2 checkpoint in coordination with two thresholds:

- Radiation needs to be above a *dose-dependent threshold* to affect the G2/M transition, either by delaying entry to mitosis or activating the checkpoint. In other words, sufficient radiation is necessary to cause sufficient DNA damage that signals changes in the cell cycle progression during the G2-phase.
- Above the dose-dependent threshold, the G2 checkpoint can be activated depending on how much the cell has progressed in the cell cycle by the moment of the radiation. With sufficient time before M-phase, the cell can activate the G2 checkpoint to repair the DNA damage. However, there is *phase-dependent threshold* after which it is too late to activate the G2 checkpoint.

The combination of these two thresholds determines a region in the dose-phase plane where cells cannot repair DNA damage before entering M-phase. DNA damage is not repaired either because radiation is too low to affect the G2/M transition or because the damage happened too late to activate the G2 checkpoint. We can

visualize such region and the thresholds if we count the number of DSB at M-phase entry. For that purpose, we first define a few concepts.

We assume that the *radiation scheme* $\dot{D}(t)$ in Eq (3.1j) starts at time t_0 and ends at time t_f . Thus, the *total dose* is defined as

$$D = \int_{t_0}^{t_f} \dot{D}(u) du.$$

Choices for \dot{D} that match experiments are single or successive copies of the Dirac delta and window functions. In either case, we can use the time of radiation t_0 and the total dose D to characterize the radiation scheme. In this chapter, we use a single radiation pulse at time t_0 for the simulations, which we approximate with the Dirac delta function at time t_0 , i.e.,

$$\dot{D}(t) = D\delta(t - t_0).$$

The start of the radiation scheme can happen at any moment of the cell cycle $[0, T]$, where T is the length of the cell cycle and $t = 0$ is the exact time after cell division. However, in simulations, we apply a pulse of radiation anytime during the interphase $[0, t_M]$, where t_M is the moment when MPF reaches the threshold for mitosis $\theta_M = 0.2$ from below in the no-radiation case, that is, $MPF(t_M) = \theta_M$ and $\frac{d}{dt}MPF(t_M) > 0$. As shown in Section 2.3, the time of M-phase entry t_M varies depending on the radiation start time t_0 and the radiation scheme \dot{D} . Thus, when there is radiation, we write $t_M(t_0, D)$; and when there is no radiation we simply have $t_M = t_M(0, 0)$.

We are interested in the number of *lethal DSBs* at M-phase entry $t_M(t_0, D)$,

which we define as

$$DSB_{\text{lethal}}(t_0, D) = DSB(t_M(t_0, D)), \quad (3.3)$$

provided $t_0 \in [0, t_M]$ and $D \geq 0$. We can compute the number of lethal DSBs by evaluating the solution to equation (3.1j) at the time of M-phase entry. This is plotted in Figure 3.2 as a function of time of radiation t_0 during the interphase and low-dose of radiation D (< 1 Gy). In this figure, we observe the region mentioned above in which cells cannot repair DNA damage before entering M-phase. DSBs during cell division lead to a loss in the reproductivity and therefore reduce the survival probability.

The definition of lethal DSBs above applies to a single average cell in a population of cells, i.e., an average number of DSB remain at M-phase entry (given by $DSB_{\text{lethal}}(t_0, D)$) when one cell is irradiated t_0 hours after the start of the cell cycle with total dose D . However, survival fraction curves take place at the population level and with the sole dependence on radiation dose D . We address these points in the next section, where we introduce the population of cells and remove the time dependence in the lethal DSBs.

3.2 Survival fraction

We assume that the population of cells has a distribution $f(t)$ of cells over the cell cycle. That is, a synchronous population of cells corresponds to a distribution $f(t)$ with modes, and an asynchronous population of cells corresponds to a constant $f(t)$. Cells synchronized in G2-phase could be described with a distribution with mean value and mode in the G2-phase, for example, with a Gaussian distribution

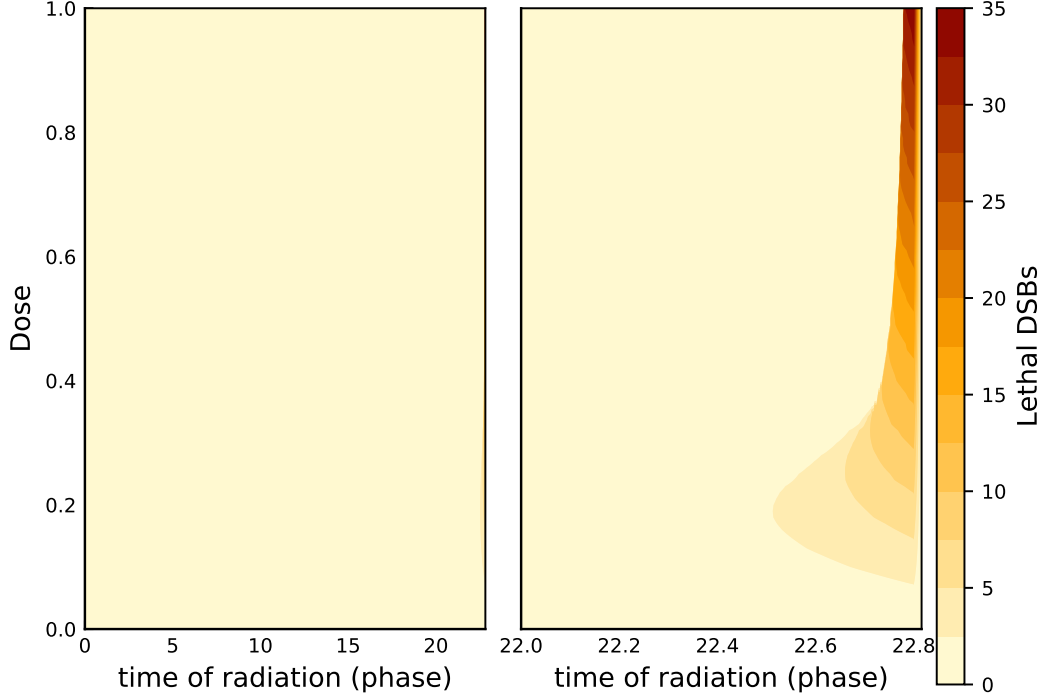


Figure 3.2: Colour map for the number of lethal DSBs at M-phase (3.3). Every point in the plot is the number of DSBs remaining at the exact moment of M-phase entry after a pulse of D Gy of radiation was applied at phase time t_0 . This figure was obtained numerically by discretizing time ($[0, t_M]$) and dose ($[0, 1]$ Gy) domains, simulating the cell cycle model with the radiation scheme at each point, and stopping at M-phase entry to measure the number of DSBs. The radiation scheme used here is a radiation pulse with dose rate D (Gy/min) for one minute, starting at t_0 . Left: colour map for the full interphase. Right: focus on the last 0.8 hours of the interphase.

wrapped around the cell cycle, also known as von Mises distribution. Choices of $f(t)$ are developed further in Section 3.3. Introducing a distribution of cell allows us to investigate the strong HRS/IRR phenomenon observed in cells synchronized in G2-phase [57].

Given a distribution $f(t)$, we define the *average number of lethal DSBs in a population of cells in interphase*, $\widehat{DSB}_{\text{lethal}}$, as the weighted average of DSB_{lethal} over t_0

$$\widehat{DSB}_{\text{lethal}}(D) = \frac{1}{t_M} \int_0^{t_M} DSB_{\text{lethal}}(t_0, D) \frac{f(t_0)}{c_M} dt_0, \quad (3.4)$$

where t_M is the length of the interphase of a control cell and

$$c_M = \int_0^{t_M} f(t)dt < 1.$$

is the fraction of the population in interphase. Note that by integrating over t_0 , we have that $\widehat{DSB}_{\text{lethal}}$ does not depend on t_0 . Examining Figure 3.2, we expect the average number of lethal DSBs to be higher when $f(t)$ has a higher density towards the end of the G2-phase.

DSBs during the M-phase (between t_M and T) are much more difficult to study because it is not clear how DSBs are passed after cell division to daughter cells or affect the G2/M transition in the next generation. In any case, we assume the DSBs during M-phase have no significant contribution to the survival fraction via the G2/M checkpoint.

Survival fractions curves are usually collected several generations after irradiation (6–12 generations) [1, 49]. It is also known that DSBs during M-phase produce subsequent events that affect the survival fraction several generations after radiation, such as polyploid nucleus, aneuploid cells, and mitotic death [102]. Thus, we take into account the effect of several generations by assuming that the *average number of lethal events due to G2 checkpoint failure* is proportional to the weighted average number of lethal DSBs in the first generation, i.e.,

$$\lambda_{G2/M}(D) = \gamma \widehat{DSB}_{\text{lethal}}(D) = \frac{\alpha_0}{t_M} \int_0^{t_M} DSB_{\text{lethal}}(t_0, D) f(t_0) dt_0, \quad (3.5)$$

where γ is a proportionality constant, and $\alpha_0 = \frac{\gamma}{c_M}$. This means that one lethal DSB can cause more than one lethal event downstream. We expect that the average number of lethal DSBs in equation (3.4) underestimates the average number of lethal

events in equation (3.5), i.e., $\gamma \geq 1$ thus $\alpha_0 \geq 1$. Therefore, γ accounts for both the population of cell in interphase and the effect that the affected first generation has on subsequent generations.

Now we consider all other lethal events that are not related to G2 checkpoint failure (such as radiation-induced apoptotic signals) but decrease the survival fraction. We assume that the the average number of such lethal events, which we denote as the *average number of other lethal events*, has a linear-quadratic form

$$\lambda_{\text{other}}(D) = \hat{\alpha}D + \hat{\beta}D^2, \quad (3.6)$$

for positive constants $\hat{\alpha}$ and $\hat{\beta}$. This assumption is reasonable since the Linear-Quadratic (LQ) model (1.1) is an appropriate model for most survival fraction curves [8].

The above definitions of average number of lethal events is consistent in the sense that equations (3.5) and (3.6) do not count a lethal events twice. Thus, we can define the *total average number of lethal events* as

$$\begin{aligned} \lambda(D) &= \lambda_{\text{other}}(D) + \lambda_{G2/M}(D) \\ &= \hat{\alpha}D + \hat{\beta}D^2 + \frac{\alpha_0}{t_M} \int_0^{t_M} DSB_{\text{lethal}}(t_0, D)f(t_0)dt_0. \end{aligned} \quad (3.7)$$

Note that the term $\lambda_{G2/M}(D)$ might also include linear and quadratic terms. Therefore, the notation $\hat{\alpha}$ and $\hat{\beta}$ is to indicate that these parameter might be underestimation of the corresponding parameters in the LQ model.

Having expression (3.7) and assuming Poisson's Law for the number of lethal lesions k , we can now find the survival fraction given by the probability that there

are no lethal lesions in the cell

$$S(D) = P(k = 0; \lambda(D)) = e^{-\lambda(D)} = e^{-\lambda_{G2/M}(D)} e^{-\lambda_{\text{other}}(D)}, \quad (3.8)$$

where P is the probability density function of the Poisson distribution with parameter $\lambda(D)$.

We believe that the most general model for the survival fraction $S(D)$ is based on the “*yield of lesions*”

$$\lambda(D) = -\ln(S(D)) = \underbrace{\alpha D + \beta D^2}_{\lambda_{\text{other and } \lambda_{G2/M}}} + \underbrace{o(D^2)}_{\lambda_{G2/M}}, \quad (3.9)$$

and that modelling specific phenomena might lead to higher other terms not present in the LQ model. In particular, the average number of lethal lesions due to G2 checkpoint failure might lead to higher other terms not present in the LQ model but necessary for the the HRS/IRR phenomenon (see Figure 3.1).

In the next section, we use numerical simulations of the cell cycle model (3.1) to explore the potential of the survival fraction (3.8) with total average number of lethal events (3.7) to produce the HRS/IRR phenomenon.

3.3 Results

In this section, we simulate cell survival fraction curves according to equation (3.8). In all our simulations, we use the start of the cell cycle as initial condition and the parameter values in Table 3.3. The radiation scheme consists of a pulse of radiation of intensity D at the time of radiation t_0 . This is done numerically by redefining the value of DSBs at t_0 to $DSB(t_0) = k_{d1}D$ (see (3.1j)) and continue the simulation

until MPF reaches the threshold for mitosis $\theta_M = 0.2$ from below. The simulations are carried out in three steps.

1. We solve the system of equations corresponding to the cell cycle and radiation pathway (3.1) using parameter values in Table 3.3 and save the state immediately after the resetting condition (3.2), which corresponds to the start of the cell cycle. This is the initial condition used in the next step. Note that the simulation has to run long enough in order to guarantee that the stable limit cycle has been reached.
2. We discretize the radiation domain $D \in [0, 2]$ and time of radiation domain $t_0 \in [0, t_M]$, with finer resolution at the end of the time domain. Then, we solve the cell cycle and radiation pathway from the start of the cell cycle and find the number of lethal DSBs in equation (3.3) for the different values of radiation dose D and start of radiation t_0 . This is illustrated in Figure 3.2. Note that the finer resolution at the end of the time domain is necessary to obtain the graph on the right of this figure.
3. We use these values of lethal DSBs and a given distribution $f(t)$ to calculate numerically the average number of lethal events due to G2 checkpoint failure (3.5) using the trapezoidal rule. Then, we compute the cell survival fraction (3.8) based on the total average number of lethal events (3.7). This step is applied for four distributions of cells $f(t)$ over the cell cycle to show the importance of G2-phase cells on the cell survival fraction curve.

Marples showed that cells synchronized in G2-phase have a more prominent HRS/IRR effect while asynchronous cells have a small HRS/IRR effect (see Figure 3.3) [59]. Cells synchronized in G1- and S-phase, on the other hand, do not

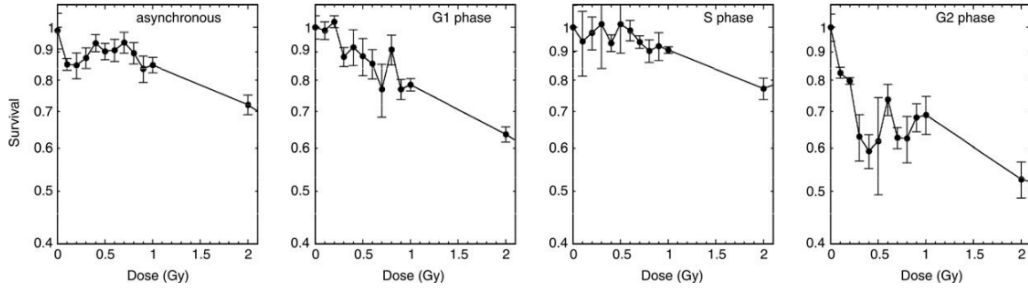


Figure 3.3: Survival curve data from asynchronous (G1=70%, S=15%, and G2=15%) and synchronous cells in G1- (~90%), S- (~60%), and G2-phase (~80%) of V79 cells. Taken from Marples [59].

have an evident HRS/IRR response. To account for the importance of the synchronization component of these experiments, we choose four distributions $f(t)$ in (3.7), corresponding to the four distributions of cells over the cell cycle shown in Figure 3.3: uniform distribution, and cell populations enriched in G1-, S-, and G2-phase. We use the uniform distribution on the $[0, T]$ domain for the asynchronous case, and the Von Mises distribution for the synchronous cases. In the following numerical experiments, we replicate the survival fraction curves in Figure 3.3 using the distributions mentioned above.

For the values of $\hat{\alpha}$ and $\hat{\beta}$ in equation (3.6), we use the values estimated in Tables II and III in Marples and Joiner [57], $\hat{\alpha} = 0.17$ and $\hat{\beta} = 0.04$. These values were chosen to have referential order of magnitude and α/β -ratio. For the α_0 value in equation (3.5), we use $\alpha_0 = 15$. This value was chosen to obtain similar survival fraction curves to those in Figure 3.3.

3.3.1 Uniform distribution

The probability density function for the *uniform distribution* (see Figure 3.4a) is given by

$$f(t|T) = \frac{1}{T},$$

where T is the length of the cell cycle.

Using the uniform distribution and the number of lethal DSBs obtained numerically (see Figure 3.2), we compute the average number of lethal events due to G2 checkpoint failure $\lambda_{G2/M}(D)$ in Figure 3.4b, according to equation (3.5). Each horizontal cross section of the graph of Figure 3.2 produces a point in Figure 3.4b. The survival fraction $S(D)$ in Figure 3.4c is then computed according to equation (3.8). In this figure, we can observe a moderate HRS/IRR effect in the survival fraction. Our results show a less pronounced effect, compared to the experimental results (Figure 3.3).

The spike observed at very low-dose in Figure 3.4 is caused by the dynamics of ATM activation at very low dose. According to the quasi-steady state of the Goldbeter-Koshland kinetics (refer to Appendix 2.A), ATM is activated when

$$\frac{k_{t1}DSB}{V_{t2}} > 1, \implies DSB > \frac{V_{t2}}{k_{t1}} = \frac{3.8}{30} = 0.127,$$

that is, when the number of DSBs is larger than 0.127. In terms of the radiation pulse, this is equivalent to

$$k_{d1}D = DSB > 0.127 \implies D > \frac{0.127}{k_{d1}} = \frac{0.127}{35} = 0.003619,$$

or 3 mGy. Therefore, for radiation dose less than 3 mGy, DSBs are not recognized and therefore not repaired; for radiation dose equal to 3 mGy, ATM becomes

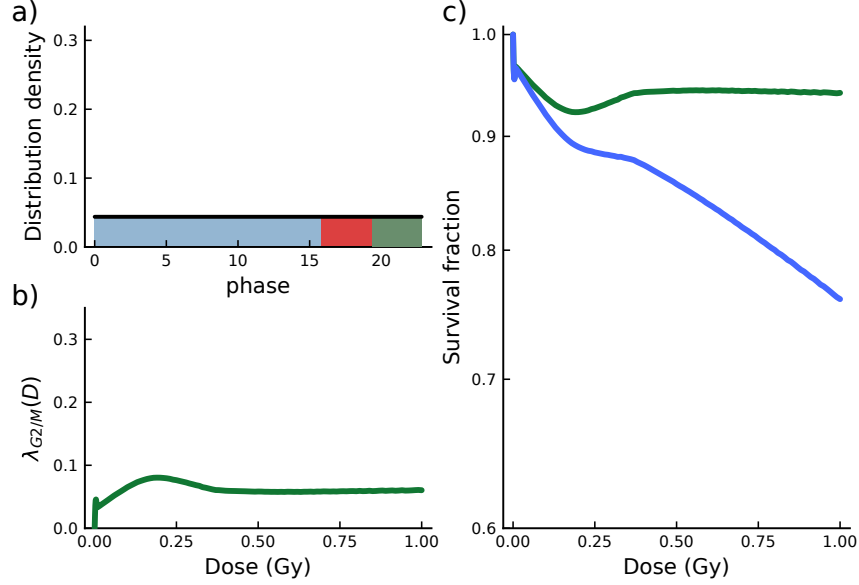


Figure 3.4: Numerical survival fraction with uniform distribution. a) Probability density function for the uniform distribution. The colours represent each phase of the cell cycle: G1 (blue), S (red), and G2 (green). Refer to Section 3.3.2 for details on the colouring. b) Average number of lethal events (3.5). c) Survival fraction curves: effect of radiation of the G2/M transition $e^{-\lambda_{G2/M}(D)}$ (green), and combined effect of radiation of the G2/M transition with the linear and quadratic terms as expressed in equation (3.8) (blue).

partially active and the average number of lethal events reaches a peak; and for radiation dose larger than 3 mGy, ATM becomes fully active which activates DSB repair mechanisms. We conjecture that ATM dynamics at very low dose causes the ultra-sensitive initial slope (α_s in Figure 3.1). We postpone a further discussion of the effect of ATM dynamics to Section 3.3.3.

3.3.2 Von Mises distribution

The probability density function for the *Von Mises distribution* is given by

$$f(t|\mu, \kappa) = \frac{e^{\kappa \cos(2\pi(t-\mu)/T)}}{TI_0(\kappa)},$$

where μ is the mean value (location parameter) and peak of the distribution, κ is a measure of the concentration ($1/\kappa$ is analogous to dispersion σ in the Gaussian distribution), and $I_0(\kappa)$ is the modified Bessel function of order 0. We assume that the Von Mises distribution replicates the distribution of synchronized population of cells.

To determine the value of the location parameter μ , we first find the maximum concentration thresholds of MPF for G1- and S-phases so that percentage of each phase under the uniform distribution matches the experimental percentages for the asynchronous case presented in Figure 3.3. The resulting values for the concentration threshold, time, and percentage for each phase are summarized in Table 3.2. These values are used to colour the different stages in Figure 3.4a. Second, we modify the value of the location parameter μ to resemble the experimental percentages in Figure 3.3 for the asynchronous cases. The resulting values for location parameter and percentage for each phase are summarized in Table 3.2. We use a relatively high value for the scale parameter $\kappa = 8$ (small dispersion).

Case 1: Von Mises distribution with mean in the G1 phase.

To account for a population of cells enriched in G1-phase, we use the Von Mises distribution with $\mu = 14.3$ hrs. The percentage of cells in each stage is shown in Table 3.2, and the probability density function is shown in Figure 3.5a. The average number of lethal events due to G2 checkpoint failure in Figure 3.5b is small, resulting in a survival fraction in Figure 3.5c with no HRS/IRR effect. This is consistent with the results of Marples in Figure 3.3.

Case 2: Von Mises distribution with mean in the S phase.

To account for a population of cells enriched in S-phase, we use the Von Mises distribution with $\mu = 16.4$ hrs. The percentage of cells in each stage is shown in

Table 3.2: Concentrations, times, and percentages. MPF maximum concentration thresholds refer to the MPF values that characterize each stage. These values were selected to match the percentage of asynchronous cells reported in Figure 3.3. More specifically, the MPF maximum thresholds for G1 and S were chosen to reach 70% and 15% in the asynchronous cells to match these values reported by Marples [59], while the MPF maximum thresholds for G2 is taken from Gérard et al. [25]. Using the same MPF concentration threshold found in the previous step, the value of the parameter μ in the Von Mises distribution was selected to match the percentage of synchronous cells mentioned in Figure 3.3.

	G1	S	G2
MPF maximum threshold	0.0274	0.0363	0.2
Duration of phase (hrs)	15.9985	3.437	3.381
Asynchronous cells	70 %	15 %	15 %
Synchronous G1-phase ($\mu = 14.3$ hr)	90 %	10 %	0 %
Synchronous S-phase ($\mu = 16.4$ hr)	38 %	60 %	2 %
Synchronous G2-phase ($\mu = 21.1$ hr)	10 %	10 %	80 %

Table 3.2, and the probability density function is shown in Figure 3.6a. As in the previous case, the average number of lethal events due to G2 checkpoint failure in Figure 3.6b is small, resulting in a survival fraction in Figure 3.6c with no HRS/IRR effect. This is also consistent with the results of Marples in Figure 3.3.

Case 3: Von Mises distribution with mean in the G2 phase.

To account for a population of cells enriched in G2-phase, we use the Von Mises distribution with $\mu = 21.1$ hrs. as shown in Figure 3.7a. The percentage of cells in each stage is shown in Table 3.2, and the probability density function is shown in Figure 3.7a. As opposed to the previous two cases, the average number of lethal events due to G2 checkpoint failure in Figure 3.7b is more pronounced (with a particular bump) around 0.2 Gy, resulting in a survival fraction in Figure 3.7c with a distinct HRS/IRR effect. This is also consistent with the results of Marples in Figure 3.3.

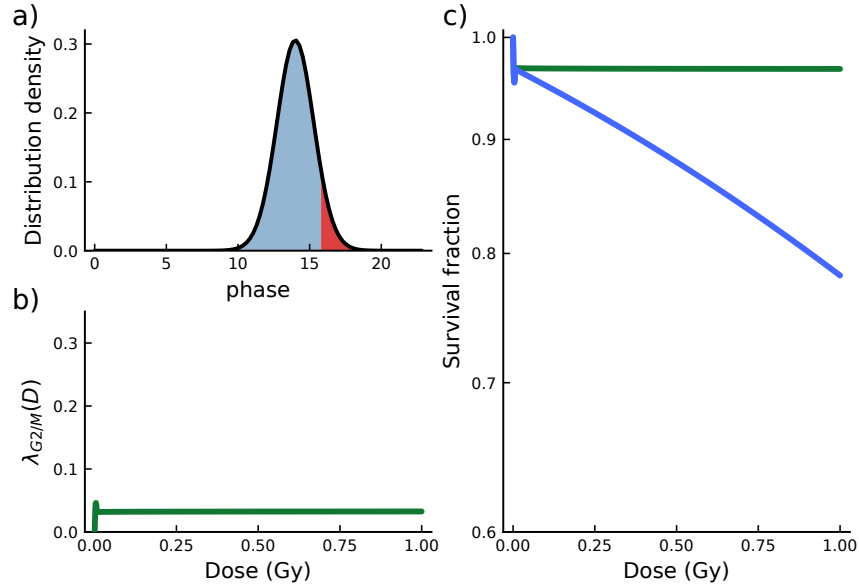


Figure 3.5: Numerical survival fraction with Von Mises distribution for cells enriched in G1-phase. a) Probability density function for the Von Mises distribution with $\mu = 14.3$. The colours represent the each phase of the cell cycle: G1 (blue), S (red), and G2 (green). b) Average number of lethal events (3.5). c) Survival fraction curves: effect of radiation of the G2/M transition $e^{-\lambda_{G2/M}(D)}$ (green), and combined effect of radiation of the G2/M transition with the linear and quadratic terms as expressed in equation (3.8) (blue).

3.3.3 Effect at very low-dose caused by ATM dynamics

In Figures 3.4–3.7, we observe a “hump” or “spike” in the average number of lethal events and survival fraction curves at very low-dose (< 1 cGy). We already stated that this is caused by the effect of ATM activation in the model (see equation (3.1i)) at very low-dose (refer to Section 2.3.3 for more details about the activation pathway of ATM). A minimum of number DSBs is required for ATM activation, which in turn is necessary for DSBs repair. Consequently, when ATM is inactive, there is no repair of DSBs and the average number of DSBs during M-phase entry is maximal. This causes a steep slope in the average number of lethal events and the survival fraction.

We predict that ATM activation causes a similar hyper-radiosensitive effect at

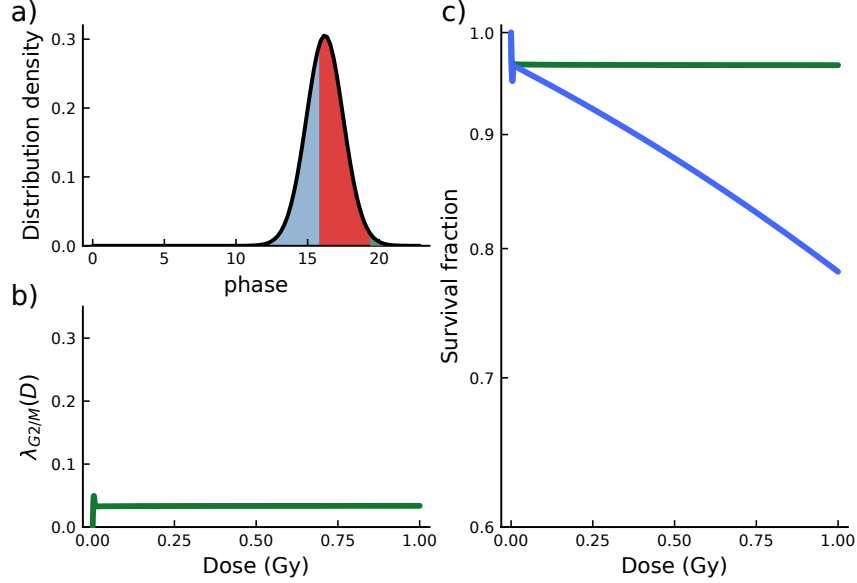


Figure 3.6: Numerical survival fraction with Von Mises distribution for cells enriched in S-phase. a) Probability density function for the Von Mises distribution with $\mu = 16.4$. The colours represent the each phase of the cell cycle: G1 (blue), S (red), and G2 (green). b) Average number of lethal events (3.5). c) Survival fraction curves: effect of radiation of the G2/M transition $e^{-\lambda_{G2/M}(D)}$ (green), and combined effect of radiation of the G2/M transition with the linear and quadratic terms as expressed in equation (3.8) (blue).

very low-dose (< 1 mGy) to that of Chk2 activation at low-dose (~ 0.1 Gy). However, the former is not enough to activate the G2 checkpoint since Chk2 is necessary to inhibit Cdc25 activity [16]. HRS/IRR response at very low-dose has already been reported in by [92] and Joiner et al. [39].

To show that the spiking effect at very low-dose observed in Figures 3.4–3.7 is caused by the activation ATM, we reproduce Figure 3.7 without the dynamics of ATM. To eliminate ATM activation dynamics, we remove equation (3.1i) from the cell cycle and radiation pathway model and set ATM to be active ($ATM = 1$). The resulting average number of lethal events and survival fraction curve is shown in Figure 3.8. Here, we observe that there is no spiking effect at very low-dose, yet the HRS/IRR at low-dose remains. The same result, no spike at very low-dose, is

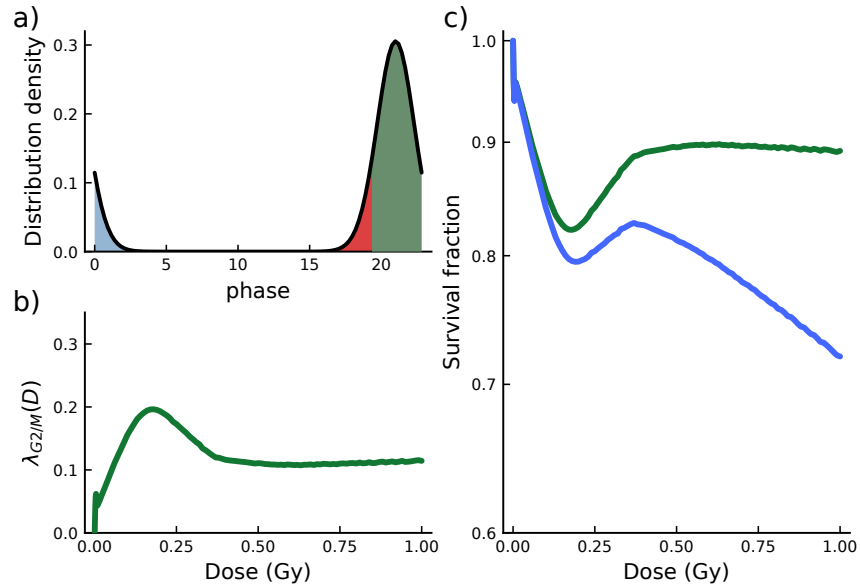


Figure 3.7: Numerical survival fraction with Von Mises distribution for cells enriched in G2-phase. a) Probability density function for the Von Mises distribution with $\mu = 21.1$. The colours represent the each phase of the cell cycle: G1 (blue), S (red), and G2 (green). b) Average number of lethal events (3.5). c) Survival fraction curves: effect of radiation of the G2/M transition $e^{-\lambda_{G2/M}(D)}$ (green), and combined effect of radiation of the G2/M transition with the linear and quadratic terms as expressed in equation (3.8) (blue).

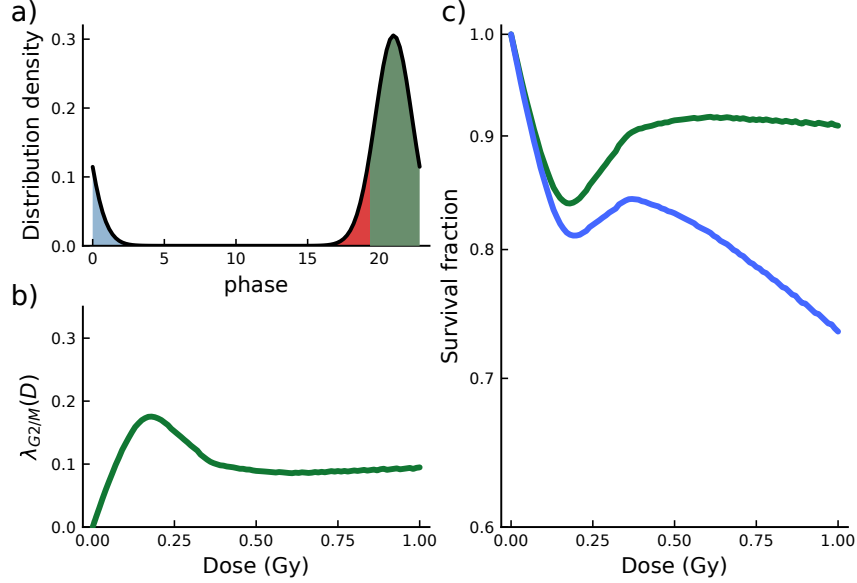


Figure 3.8: Numerical survival fraction with Von Mises distribution for cells enriched in G2-phase and fixed ATM concentration. a) Probability density function for the Von Mises distribution with $\mu = 21.1$. The colours represent the each phase of the cell cycle: G1 (blue), S (red), and G2 (green). b) Average number of lethal events (3.5). c) Survival fraction curves: effect of radiation of the G2/M transition $e^{-\lambda_{G2/M}(D)}$ (green), and combined effect of radiation of the G2/M transition with the linear and quadratic terms as expressed in equation (3.8) (blue).

obtained in the asynchronous cells and synchronous cells in G1 and S cases (results not shown here).

3.4 Lethal DSBs and time available for repair

We have shown with numerical simulations that DSBs at the moment of M-phase, defined as lethal DSBs in equation (3.3), produce a HRS/IRR phenomenon in the survival fraction (defined by equation (3.8)). However, we should note that the equation for DSBs (3.1j) can be explicitly solved if we assume that ATM is always active ($ATM = 1$). Recall from Figure 2.4 that ATM is active for radiation dose above 5 mGy and that this activation is maintained above 0.1 DSBs (in average).

Thus, the assumption of active ATM is valid for relevant low-dose radiation above 0.05 Gy. In such case, equation (3.1j) becomes

$$\frac{dDSB}{dt} = k_{d1}\dot{D}(t) - k_{d2}DSB.$$

For a radiation pulse of intensity D at time t_0

$$\dot{D}(t) = D\delta(t - t_0),$$

and zero DSBs at t_0 (initial condition), the equation above has solution

$$DSB(t) = k_{d1}De^{-k_{d2}(t-t_0)}, \quad t \geq t_0.$$

Using the definition of lethal DSBs (3.3), we get

$$DSB_{\text{lethal}}(t_0, D) = k_{d1}De^{-k_{d2}(t_M(t_0, D)-t_0)}, \quad (3.10)$$

where $t_M(t_0, D)$ is the time of M-phase entry. Although the number of DSB can be found explicitly without the cell cycle model, the number of lethal DSBs is highly dependent on the cell cycle through $t_M(t_0, D)$.

In the exponent in equation (3.10), we identify a time difference with a very important biological meaning, namely the length of time between the moment of radiation t_0 and the M-phase entry $t_M(t_0, D)$. We define this value as the time available for repair,

$$t_R(t_0, D) = t_M(t_0, D) - t_0. \quad (3.11)$$

Figure 3.9, shows the time available for repair $t_R(t_0, D)$ using the cell cycle model and radiation pathway, in the same way that the number of lethal DSBs in Figure 3.2

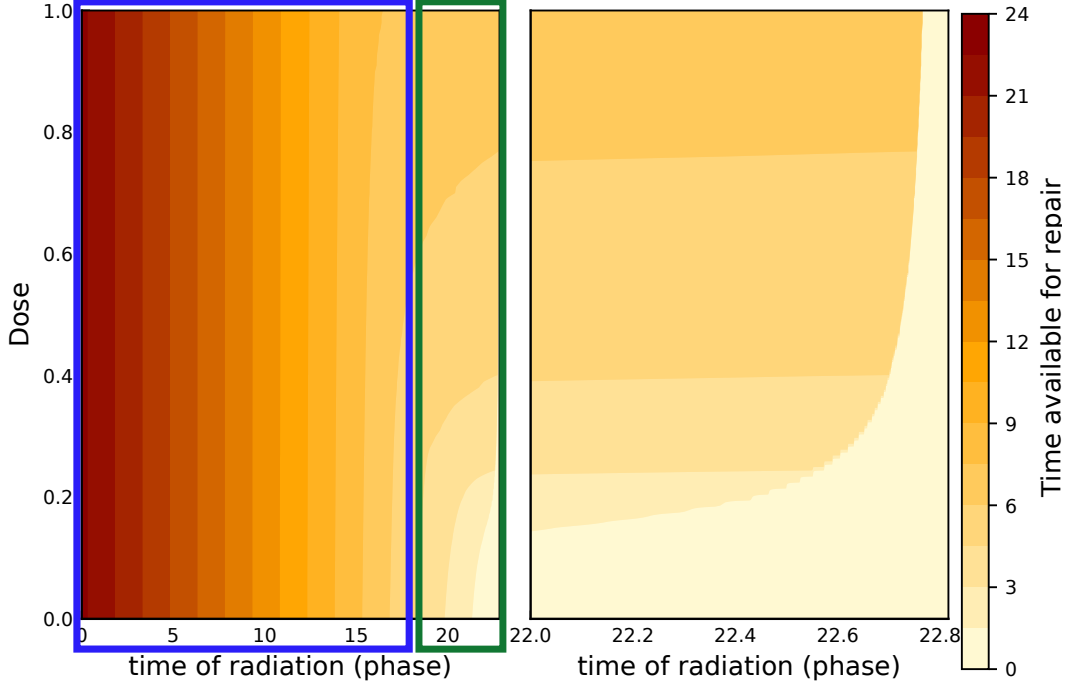


Figure 3.9: Colour map for the time available for repair of DSBs (3.11). The colour bar represents the time available for repair. Left: colour map for the full cell cycle $[0, T]$. Right: zoom in the last 0.8 hours of the cell cycle. This figure was obtained numerically by discretizing the time ($[0, T]$) and dose domains ($[0, 1]$ Gy), simulating the cell cycle model with the radiation scheme at each point, and stopping at M-phase entry to measure the number of DSBs. The radiation scheme used here is a radiation pulse with dose rate D (Gy/min) for one minute, starting at t_0 .

was obtained. Note that, alternatively, we can obtain Figure 3.2 by evaluating $t_R(t_0, D)$ in Figure 3.9 into the expression of DSB_{lethal} (3.10).

In Figure 3.9, we observe two regions, one region away from the G2/M transition (before approximately 17 hrs and indicated within a blue box) where the time available for repair is primarily constant with respect to t_0 (vertical cross sections), and one region around the G2/M transition (after approximately 17 hrs and indicated with a green box) where the time available for repair is more complex. We conjecture that this second region is dictated by the $\text{SNIC}_{V_{c2}}$ bifurcation studied in Chapter 2.

Moreover, we hypothesize that we should be able to approximate the time available for repair with an explicit formula if we approximate the cell cycle model around the G2/M transition with the SNIC bifurcation normal form. Characterization of t_R in these two regions could allow us to find an explicit expression for the average number of lethal events due to G2 checkpoint failure (3.5). This is the subject of Chapter 6.

3.5 Discussion

We defined a survival fraction model (3.8) considering the effect of radiation on the G2/M transition in a population of cells. This survival fraction model accounts for the average number of lethal events due to G2 checkpoint failure (3.5) based on average number of DSBs entering M-phase (3.4). Other lethal events affecting the survival fraction that are not related to the G2/M transition, such as radiation-induced apoptosis and necrosis [69], are lumped into linear and quadratic terms in (3.6), inspired by the Linear-Quadratic model. Investigating lethal event accounting explicitly for mechanisms like apoptosis and necrosis is part of future work.

To show that the effect of radiation of the G2/M transition produces an HRS/IRR effect on the survival fraction curve, we simulated the survival fraction model using the cell cycle and radiation pathway model and assumed different distribution of population of cells over the cell cycle. First, we simulated the cell cycle and radiation pathway model for a pulse of radiation starting at different moments of the cell cycle and different values of total dose, and recorded the number of DSB at the moment of M-phase. Then, we used four distributions that replicate experiments on a population of cells—uniform distribution (asynchronous cells), Von Mises distribution with mean in the G1-phase (cells enriched in G1), Von Mises distribution with mean

in the S-phase (cells enriched in S), and Von Mises distribution with mean in the G2-phase (cells enriched in G2)—to produce cell survival curves.

Since DSBs during M-phase affect the fate of cells and their ability to reproduce [102], we assumed that DSBs become lethal entering M-phase. In our simulations, we assumed that this happens when the MPF concentration reaches the threshold $\theta_M = 0.2$, which initiates mitosis. For a control cell, this happens t_M hours after cell division, but for an irradiated cell this happens at a later time.

In our results, G1- and S-enriched cells do not show an HRS/IRR effect, asynchronous cells show little to no HRS/IRR effect, and G2-enriched cells show a pronounced HRS/IRR effect in the cell survival fraction curve. This is consistent with experimental results [59].

Moreover, we identify that ATM threshold activation causes a similar hyper-radiosensitivity effect at very low-dose. This effect causes a steep slope in the survival fraction at very low-dose. We hypothesize that inactivity of ATM is responsible for the initial slope of hyper-radioresistance, and that Chk2 activation during late G2 combined with the SNIC driven by V_{c2} are responsible for the HRS/IRR phenomenon. HRS/IRR response to very low-dose radiation has been reported and attributed to exposure time to radiation in connection to ATM-mediated recognition of DSBs [92]. Their results are consistent with ours, although we do not include exposure time to radiation in our experiments.

We also identified the time available for repair (3.11) as an important quantity to compute the number of lethal DSBs (3.3) explicitly. The subject of Chapter 6 is to compute theoretically the time available for repair based on a one-dimensional reduction of the cell cycle model around the $\text{SNIC}_{V_{c2}}$ bifurcation discussed in Chapter 2. Such reduction to one-dimension is the goal of Chapter 5, and is based on a theoretical general result presented in Chapter 4.

3.A Table of parameter values

Table 3.3: Parameter values. Most parameter values have been taken from Gérard et al. [25] or adapted to match the cell cycle length in mammalian cells. Parameters related to the radiation pathway come from different sources or were cautiously chosen on the basis of numerical simulations. Details are provided in the footnotes that are referenced in the Source column. Parameters with no units are dimensionless.

Symbol	Definition	Value	Units	Source
k_{m0}	Rate of synthesis of Cdk-cyclin fusion protein, MPF	0.2	hr ⁻¹	¹
k_{m1}	Rate constant for the dephosphorylation of MPF	0.4	hr ⁻¹	²
k_{m1a}	Rate constant for the dephosphorylation of MPF by Cdc25	20.0	hr ⁻¹	²
k_{m2}	Rate constant for the phosphorylation of MPF	0.4	hr ⁻¹	²
k_{m2a}	Rate constant for the phosphorylation of MPF by Wee1	50.0	hr ⁻¹	¹
k_{m3}	Rate constant for the degradation of MPF and MPF _P	0.2	hr ⁻¹	²
k_{m3a}	Rate constant for the degradation of MPF and MPF _P by APC	6.35	hr ⁻¹	²
V_{w1}	Maximum activation rate, by dephosphorylation, of Wee1	1.0	hr ⁻¹	²
k_{w2}	Rate constant for activation of Wee1 by MPF	5.3	hr ⁻¹	²

continued...

¹Taken from Gérard et al. [25]; slightly modified to accommodate the correct G2/M transition dynamics.

²Taken from Gérard et al. [25]; scaling factor of 8.5 needed to rescale the length of the cell cycle to approximately 24 hrs.

...continued

Symbol	Definition	Value	Units	Source
J_{w1}	Michaelis constant for Wee1 activation	0.01		³
J_{w2}	Michaelis constant for Wee1 inactivation	0.01		3
k_{c1}	Rate constant for Cdc25 phosphorylation by MPF	8.5	hr ⁻¹	2
V_{c2}	Maximum inactivation rate, by dephosphorylation, of Cdc25	1.4	hr ⁻¹	1
k_{c2a}	Rate constant for the inactivation of Cdc25 by Chk2	2.4	hr ⁻¹	⁴
J_{c1}	Michaelis constant for Cdc25 activation	0.01		3
J_{c2}	Michaelis constant for Cdc25 inactivation	0.01		3
k_{i1}	Rate constant for the activation of IE by MPF	1.7	hr ⁻¹	2
V_{i2}	Maximum inactivation rate of IE	0.4	hr ⁻¹	2
J_{i1}	Michaelis constant for IE activation	0.001		3
J_{i2}	Michaelis constant for IE inactivation	0.001		3
k_{a1}	Rate constant for the activation, by phosphorylation, of APC by IE	6.8	hr ⁻¹	2
V_{a2}	Maximum inactivation rate, by phosphorylation, of APC	1.7	hr ⁻¹	2
J_{a1}	Michaelis constant for APC activation	0.001		3
J_{a2}	Michaelis constant for APC inactivation	0.001		3

continued...

³Taken from Gérard et al. [25].

⁴Educated guess.

...continued

Symbol	Definition	Value	Units	Source
k_{h1}	Rate constant for the activation, by phosphorylation, of Chk2 by ATM	0.32	hr ⁻¹	5
V_{h2}	Maximum inactivation rate, by dephosphorylation, of Chk2	1.9	hr ⁻¹	6
J_{h1}	Michaelis constant for Chk2 activation	0.01		4
J_{h2}	Michaelis constant for Chk2 inactivation	0.01		4
k_{t1}	Rate constant for the activation (recruitment and autophosphorylation) of ATM around DSB repair foci	30	dsb ⁻¹ hr ⁻¹	7
V_{t2}	Maximum inactivation rate of ATM	3.8	hr ⁻¹	2
J_{t1}	Michaelis constant for ATM auto-phosphorylation	0.01		4
J_{t2}	Michaelis constant for ATM deactivation	0.01		4
k_{d1}	Rate constant for DSBs damage formation	35.0	dsb · Gy ⁻¹	8
k_{d2}	Rate constant for DSBs repair	0.4	hr ⁻¹	9
α	Partial activity of MPF _p	0.05		2
μ	Growth rate of the cell	0.07	hr ⁻¹	10
K_{Mass}	Maximum cell mass	2.7		4
$Wee1_T$	Total concentration of kinase Wee1	1.0		2

continued...

⁵Chosen to fit activation time presented by Buscemi et al. [11].

⁶Chosen to fit Chk2 activation threshold after radiation [37].

⁷Taken from Kozlov et al. [45].

⁸Taken from Rothkamm and Löbrich [83].

⁹Taken from Scott [85].

¹⁰Informed by Park et al. [80].

...continued

Symbol	Definition	Value	Units	Source
$Cdc25_T$	Total concentration of phosphatase gCdc25	1.0		2
IE_T	Total concentration of intermediate enzyme IE	1.0		2
APC_T	Total concentration of protein APC	1.0		2
$Chk2_T$	Total concentration of Checkpoint kinase 2	1.0		4
ATM_T	Total concentration of ATM	1.0		4

Chapter 4

Carryover of a saddle-node bifurcation after transformation of a parameter into a variable

In this chapter, we are interested in the conditions such that a saddle-node bifurcation for the system

$$\dot{z} = f(z; \mu_1, \mu_2), \quad (4.1)$$

where $z \in \mathbb{R}^n$ and $\mu_1, \mu_2 \in \mathbb{R}$, manifests itself after we extend the system by transforming one of the parameters, for example, μ_1 , into a variable. This defines the extended system

$$\begin{aligned} \dot{z} &= f(z, \mu_1; \mu_2), \\ \dot{\mu}_1 &= g(\mu_1; \mu_2), \end{aligned} \quad (4.2)$$

where a saddle-node bifurcation occurs and $g(\mu_1; \mu_2)$ is the vector field of the new variable μ_1 . We call this saddle-node the carryover of a saddle-node bifurcation in the original system (4.1) to the extended system (4.2). Note that the function g does

not depend on z . The case where g depends on z is beyond the scope of this chapter, but we briefly discuss this case in Section 4.3.

Saddle-node bifurcations in \mathbb{R}^n are characterized by three conditions: singularity, nondegeneracy, and transversality conditions. They guarantee the creation (or destruction) of two equilibria as one parameter crosses the bifurcation value. This is summarized in the following results taken from Meiss [63, Ch. 8].

Theorem 4.0.1 (saddle node). *Let $f \in C^2(\mathbb{R}^n \times \mathbb{R}^k, \mathbb{R}^n)$, and suppose that $f(z; \mu)$ satisfies*

$$f(0; 0) = 0, \quad \text{spec}(D_z f(0; 0)) = \{0, \lambda_2, \lambda_3, \dots, \lambda_n : \lambda_k \neq 0, k \neq 1\}. \quad (4.3)$$

Choose coordinates so that $D_z f(0; 0)$ is diagonal in the zero eigenvalue and set $z = (x, y)$ where $x \in \mathbb{R}^1$ corresponds to the zero eigenvalue and $y \in \mathbb{R}^{n-1}$ are the remaining coordinates. Then

$$\begin{aligned} \dot{x} &= f_1(x, y; \mu), \\ \dot{y} &= My + f_2(x, y; \mu), \end{aligned} \quad (4.4)$$

where $f_1(0, 0; 0) = 0$, $f_2(0, 0; 0) = 0$, $D_x f_1(0, 0; 0) = 0$, $D_x f_2(0, 0; 0) = 0$, and M is an invertible matrix. Suppose that

$$D_{xx} f_1(0, 0; 0) = c \neq 0. \quad (4.5)$$

Then there exists an interval $I(\mu)$ containing 0, functions $y = \eta(x; \mu)$ and extremal value $m(\mu) = \text{Ext}_{x \in I(\mu)}[f_1(x; \eta(\mu); \mu)]$, and a neighborhood of $\mu = 0$ such that if $m(\mu)c > 0$ there are no equilibria and if $m(\mu)c < 0$ there are two. Suppose that M has a u -dimensional unstable space and an $(n - u - 1)$ -dimensional stable space.

Then, when there are two equilibria, one has a u -dimensional unstable manifold and an $(n - u)$ -dimensional stable manifold and the other has a $(u + 1)$ -dimensional unstable manifold and an $(n - u - 1)$ -dimensional stable manifold.

Equations (4.3) and (4.5) are the singularity and nondegeneracy conditions, respectively. They are necessary conditions for the function f_1 to be zero up to the zero- and first-order approximations about the bifurcation point, but nonzero in the second-order approximation. The function $y = \eta(x; \mu)$ allows us to reduce the dynamics in a neighborhood of the bifurcation point to one-dimension, i.e.,

$$\dot{x} = f_1(x, \eta(x; \mu); \mu).$$

The extremal value function $m(\mu)$ determines a single condition on the parameters, $m(\mu) = 0$, along which two equilibria are created (or destroyed). Having one condition on the parameters means that the bifurcation that takes place has codimension-one. In order to be a saddle-node bifurcation, the equilibria need to be created as a some combination of the parameters crosses the bifurcation point. This can be guaranteed with a simple condition.

Corollary 4.0.1. *If μ_1 is a single parameter such that*

$$D_{\mu_1} f_1(0, 0; 0) \neq 0, \tag{4.6}$$

then a saddle-node bifurcation takes place when μ_1 crosses zero.

Equation (4.6) is the transversality condition that guarantees that $m(\mu) = 0$ is crossed transversally as μ_1 crosses zero. Note that μ_1 is an arbitrary parameter, and that the transversality condition can hold for several parameters at the same time.

We only consider saddle-node bifurcations that take place as a single parameter crosses the bifurcation point.

In the context of this chapter, we only consider two parameters for the sake of simplicity, i.e., $\mu = (\mu_1, \mu_2) \in \mathbb{R}^2$. We show that as long as a saddle-node bifurcation takes place in system (4.1) for at least one of the parameters, the extended system (4.2) also has a saddle-node bifurcation for the other parameter (the extended variable does not have to be a bifurcation parameter in the original system) under some singularity and transversality conditions.

The Implicit Function Theorem is an essential tool in this chapter and in the study of saddle-node bifurcations in general. For example, the function $y = \eta(x; \mu)$ in Theorem 4.0.1 is consequence of this theorem. The following form of the Implicit Function Theorem is taken from Meiss [63, Ch. 8].

Theorem 4.0.2 (implicit function). *Let U be an open set in $\mathbb{R}^n \times \mathbb{R}^k$ and $F \in C^r(U, \mathbb{R}^n)$ with $r \geq 1$. Suppose there is a point $(x_0, \mu_0) \in U$ such that $F(x_0; \mu_0) = c$ and $D_x F(x_0; \mu_0)$ is a nonsingular matrix. Then there are open sets $V \subset \mathbb{R}^n$ and $W \subset \mathbb{R}^k$ and a unique C^r function $\xi(\mu) : W \mapsto V$ for which $x_0 = \xi(\mu_0)$ and $F(\xi(\mu); \mu) = c$.*

This chapter is structured as follows. In Section 4.1, we look at the case where system (4.1) is one dimensional, in which case we replace $z \in \mathbb{R}^n$ with $x \in \mathbb{R}^1$. We find conditions such that the two-dimensional extended system (4.2) has a saddle-node bifurcation. Moreover, we provide a graphical way to easily verify such conditions: the nullcline of the new equation ($g = 0$ in the extended system (4.2)) has to intersect transversally the two-parameter bifurcation curve of the original system (4.1). Then, we apply our results to a few illustrative examples. In Section 4.2, we expand our results to the n -dimensional case and apply our results

to one illustrative example. Finally, in Section 4.3, we discuss our results and further research.

4.1 One-dimensional case

In this section, we focus on the case where the variable z in the system (4.1) is one-dimensional, i.e., the system

$$\dot{x} = f(x; \mu_1, \mu_2), \quad (4.7)$$

where $x \in \mathbb{R}$, $\mu_1, \mu_2 \in \mathbb{R}$, and f is a sufficiently smooth function on (x, μ_1, μ_2) . This system is extended by transforming one of the parameters, for example, μ_1 , into a variable to define the extended system

$$\begin{aligned} \dot{x} &= f(x, \mu_1; \mu_2), \\ \dot{\mu}_1 &= g(\mu_1; \mu_2), \end{aligned} \quad (4.8)$$

where $g(\mu_1; \mu_2)$ is the sufficiently smooth vector field of the new variable μ_1 . We want to find conditions for the carryover of a saddle-node bifurcation in the original (4.7) to the extended system (4.8).

Suppose, without loss of generality, that the saddle-node bifurcation for (4.7) occurs at the origin as one parameter, μ_1 , crosses zero. That is, f at $(x, \mu_1, \mu_2) = (0, 0, 0)$ satisfies the singularity conditions

$$\begin{cases} f(x; \mu_1, \mu_2) = 0, \\ D_x f(x; \mu_1, \mu_2) = 0, \end{cases} \quad (4.9)$$

and the nondegeneracy and transversality conditions

$$\begin{cases} D_{xx}f(x; \mu_1, \mu_2) \neq 0, \\ D_{\mu_1}f(x; \mu_1, \mu_2) \neq 0. \end{cases} \quad (4.10)$$

Note that system (4.9) has two equations in \mathbb{R}^3 with coordinates (x, μ_1, μ_2) and Jacobian

$$J = \begin{pmatrix} D_x f & D_{\mu_1} f & D_{\mu_2} f \\ D_{xx} f & D_{x\mu_1} f & D_{x\mu_2} f \end{pmatrix} = \begin{pmatrix} 0 & D_{\mu_1} f & D_{\mu_2} f \\ D_{xx} f & D_{x\mu_1} f & D_{x\mu_2} f \end{pmatrix}.$$

This matrix has full rank since

$$\det \begin{pmatrix} D_x f & D_{\mu_1} f \\ D_{xx} f & D_{x\mu_1} f \end{pmatrix} = \det \begin{pmatrix} 0 & D_{\mu_1} f \\ D_{xx} f & D_{x\mu_1} f \end{pmatrix} = -D_{\mu_1} f D_{xx} f \neq 0,$$

by conditions (4.9) and (4.10). The Implicit Function Theorems 4.0.2 guarantees the existence of an interval I and unique functions

$$\begin{aligned} x &= \mathcal{X}(\mu_2), \\ \mu_1 &= \mathcal{M}(\mu_2), \end{aligned} \quad (4.11)$$

for $\mu_2 \in I$, such that

$$\mathcal{X}(0) = 0, \quad \mathcal{M}(0) = 0,$$

and the singularity condition (4.9) is satisfied. This defines a smooth one-dimensional curve Γ that follows the bifurcation point $(x, \mu_1, \mu_2) = (0, 0, 0)$ and is parameterized

by μ_2 , i.e.,

$$\Gamma = \{(x, \mu_1, \mu_2) : x = \mathcal{X}(\mu_2), \mu_1 = \mathcal{M}(\mu_2), \mu_2 \in I\}, \quad (4.12)$$

and points in Γ satisfy (4.9).

By continuity, we can start from $(x, \mu_1, \mu_2) = (0, 0, 0)$ and follow the points that satisfy the singularity conditions (4.9) and the nondegeneracy and transversality conditions (4.10) to extend Γ . If the transversality condition is violated at some point, $D_{\mu_1}f = 0$, but the same condition is satisfied for the other parameter, $D_{\mu_2}f \neq 0$, we apply similar arguments to parameterize Γ by μ_1 in that section. Hence, we can extend Γ from the bifurcation point $(x, \mu_1, \mu_2) = (0, 0, 0)$ beyond the interval I as long as the transversality condition is satisfied for at least one of the parameters (see Figure 4.1). The projection of the extended Γ onto the (μ_1, μ_2) -plane, given by $\pi : (x, \mu_1, \mu_2) \mapsto (\mu_1, \mu_2)$, defines an implicit function

$$h(\mu_1, \mu_2) = 0,$$

known as *bifurcation boundary*, commonly found numerically using continuation (for example, the curve in Figure 2.6c that follows the $\text{SNIC}_{\text{Mass}}$ bifurcation). Note that, although Γ is a smooth curve, $h(\mu_1, \mu_2) = 0$ is not necessarily smooth at every point. For more details on two-parameter bifurcations see Kuznetsov [48].

If the extended system (4.8) has a saddle-node bifurcation that is the carryover of the saddle-node bifurcation of interest in original system (4.7), then this bifurcation must take place on Γ as it is the set of points satisfying the conditions for a saddle-node bifurcation.

Proposition 4.1.1. *Consider the system (4.7). Suppose $f(x; \mu_1, \mu_2) \in C^2(\mathbb{R} \times$*

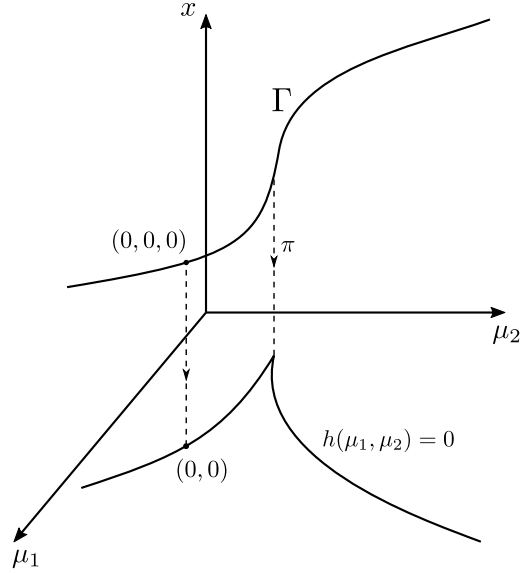


Figure 4.1: A bifurcation curve Γ and its corresponding bifurcation boundary $h(\mu_1, \mu_2) = 0$ (projection onto the (μ_1, μ_2) -plane). Modified from Figure 8.1 in Kuznetsov [48].

\mathbb{R}^2, \mathbb{R}) with a nonhyperbolic equilibrium at the origin, $f(0; 0, 0) = 0$, $D_x f(0; 0, 0) = 0$, and satisfying the nondegeneracy condition

$$D_{xx}f(0; 0, 0) \neq 0,$$

and transversality condition for either μ_1 or μ_2

$$D_{\mu_1}f(0; 0, 0) \neq 0 \quad \text{or} \quad D_{\mu_2}f(0; 0, 0) \neq 0,$$

i.e., the system (4.7) has a saddle-node bifurcation where either μ_1 or μ_2 is the bifurcation parameter. This defines a one-dimensional smooth curve $\Gamma \subset \mathbb{R}^3$ in a neighbourhood of $(x, \mu_1, \mu_2) = (0, 0, 0)$ in which f satisfies the singularity and nondegeneracy conditions.

Consider the extended system (4.8) by transforming parameter μ_1 into a variable, where $f \in C^2(\mathbb{R}^2 \times \mathbb{R}, \mathbb{R})$ and $g \in C^2(\mathbb{R} \times \mathbb{R}, \mathbb{R})$. If there is a point $(x, \mu_1, \mu_2) = (x^*, \mu_1^*, \mu_2^*) \in \Gamma$ such that $g(\mu_1; \mu_2)$ satisfies the singularity conditions

$$g(\mu_1^*; \mu_2^*) = 0, \quad D_{\mu_1}g(\mu_1^*; \mu_2^*) = b \neq 0, \quad (4.13)$$

and the transversality condition

$$\det \begin{pmatrix} D_{\mu_1}f & D_{\mu_1}g \\ D_{\mu_2}f & D_{\mu_2}g \end{pmatrix} = D_{\mu_1}f D_{\mu_2}g - D_{\mu_1}g D_{\mu_2}f \neq 0, \quad (4.14)$$

at $(x, \mu_1, \mu_2) = (x^*, \mu_1^*, \mu_2^*)$, then the extended system (4.8) has a saddle-node bifurcation at $(x, \mu_1) = (x^*, \mu_1^*)$ as μ_2 crosses μ_2^* .

Moreover, there exists a unique function $\mu_1 = \nu(\mu_2)$ such that $\mu_1^* = \nu(\mu_2^*)$, and the extended system is reduced to one dimension around (x^*, μ_1^*)

$$\dot{\xi} = f\left(\xi + \frac{a}{b}(\nu(\mu_2) - \mu_1^*) + x^*, \nu(\mu_2); \mu_2\right) - \frac{a}{b}g(\nu(\mu_2); \mu_2),$$

where $\xi = x - x^* - \frac{a}{b}(\mu_1 - \mu_1^*)$ and $a = D_{\mu_1}f(x^*, \mu_1^*; \mu_2^*)$.

Proof. Let $z = (x, \mu_1)^T$ and $F(z; \mu_2) = F(x, \mu_1; \mu_2) = (f(x, \mu_1; \mu_2), g(\mu_1; \mu_2))^T$. By definition of Γ , the singularity conditions ($f = 0$ and $D_x f = 0$), the nondegeneracy condition ($D_{xx}f \neq 0$), and one of the transversality conditions ($D_{\mu_1}f \neq 0$ or $D_{\mu_2}f \neq 0$) are satisfied at the point $(z^*, \mu_2^*) = (x^*, \mu_1^*, \mu_2^*) \in \Gamma$. Since $g(\mu_1^*; \mu_2^*) = 0$, we also have $F(x^*, \mu_1^*; \mu_2^*) = 0$ (first singularity condition for

F). The Jacobian of F evaluated at z^* is

$$A = D_z F(x^*, \mu_1^*, \mu_2^*) = \left(\begin{array}{cc} D_x f & D_{\mu_1} f \\ D_x g & D_{\mu_1} g \end{array} \right) \Big|_{z=z^*} = \begin{pmatrix} 0 & a \\ 0 & b \end{pmatrix},$$

where $a = D_{\mu_1} f(x^*, \mu_1^*, \mu_2^*)$ and $b = D_{\mu_1} g(\mu_1^*, \mu_2^*) \neq 0$, by assumption (4.13).

Since $\det(A) = 0$ and $\text{tr}(A) = b \neq 0$, the eigenvalues of A are $\lambda_1 = 0$ and $\lambda_2 = b \neq 0$ with corresponding eigenvectors

$$v_{\lambda_1} = \begin{pmatrix} 1 \\ 0 \end{pmatrix}, \quad v_{\lambda_2} = \begin{pmatrix} a \\ b \end{pmatrix}.$$

Note that condition $D_{\mu_1} g \neq 0$ is needed to guarantee only one zero eigenvalue.

Thus, $D_z F$ is singular with only one zero eigenvalue (second singularity condition for F).

The diagonalization matrix P and its inverse are given by

$$P = \begin{pmatrix} 1 & a \\ 0 & b \end{pmatrix}, \quad P^{-1} = \frac{1}{b} \begin{pmatrix} b & -a \\ 0 & 1 \end{pmatrix}.$$

Let the new shifted coordinates be defined by

$$\begin{pmatrix} \xi \\ v \end{pmatrix} = P^{-1} \begin{pmatrix} x - x^* \\ \mu_1 - \mu_1^* \end{pmatrix} = \begin{pmatrix} x - x^* - \frac{a}{b}(\mu_1 - \mu_1^*) \\ \frac{1}{b}(\mu_1 - \mu_1^*) \end{pmatrix}.$$

Then the corresponding extended system is given by

$$\begin{aligned} \dot{\xi} &= f(\xi + av + x^*, bv + \mu_1^*, \mu_2) - \frac{a}{b}g(bv + \mu_1^*, \mu_2^*), \\ \dot{v} &= \frac{1}{b}g(bv + \mu_1^*, \mu_2^*). \end{aligned}$$

Define

$$f_1(\xi, v; \mu_2) = f(\xi + av + x^*, bv + \mu_1^*; \mu_2) - \frac{a}{b}g(bv + \mu_1^*; \mu_2^*), \quad (4.15)$$

and define $f_2(v; \mu_2)$ such that

$$\frac{1}{b}g(bv + \mu_1^*; \mu_2^*) = bv + f_2(v; \mu_2).$$

Then,

$$\begin{aligned} \dot{\xi} &= f_1(\xi, v; \mu_2), \\ \dot{v} &= bv + f_2(v; \mu_2). \end{aligned} \quad (4.16)$$

Note that the singularity conditions are satisfied by construction,

$$\begin{aligned} f_1(0, 0; \mu_2^*) &= f_2(0; \mu_2^*) = 0, \\ D_\xi f_1(0, 0; \mu_2^*) &= D_v f_1(0, 0; \mu_2^*) = D_\xi f_2(0; \mu_2^*) = D_v f_2(0; \mu_2^*) = 0. \end{aligned} \quad (4.17)$$

The nondegeneracy condition for f_1 is satisfied since

$$D_{\xi\xi} f_1(0, 0; \mu_2^*) = D_{xx} f(x^*, \mu_1^*; \mu_2^*) \neq 0.$$

The transversality condition for f_1 follows from dividing the determinant in (4.14)

by $-b \neq 0$ and the definition of f_1 (4.15)

$$\begin{aligned} & \left(\cancel{D_{\mu_1} f(x^*, \mu_1^*; \mu_2^*)} \xrightarrow{a} D_{\mu_2} g(\mu_1^*; \mu_2^*) - \cancel{D_{\mu_1} g(\mu_1^*; \mu_2^*)} \xrightarrow{b} D_{\mu_2} f(x^*, \mu_1^*; \mu_2^*) \right) \neq 0, \\ \implies & D_{\mu_2} f(x^*, \mu_1^*; \mu_2^*) - \frac{a}{b} D_{\mu_2} g(\mu_1^*; \mu_2^*) = D_{\mu_2} f_1(0, 0; \mu_2^*) \neq 0. \end{aligned}$$

Then, by Theorem 4.0.1 and Corollary 4.0.1, the transformed system (4.16) has a

saddle-node bifurcation point at $(0, 0)$ as μ_2 crosses μ_2^* .

Transforming back to the variable z , we have that the extended system (4.8) has a saddle-node bifurcation point at (x^*, μ_1^*) as μ_2 crosses μ_2^* .

Now, denote

$$F_2(v; \mu_2) = bv + f_2(v; \mu_2) = 0.$$

Note that $D_v F_2(0; \mu_2^*) = b \neq 0$, by equation (4.17). By the Implicit Function Theorem 4.0.2, there is a neighbourhood of $\mu_2 = \mu_2^*$ where there exists a unique function $v = \hat{v}(\mu_2)$ such that $\hat{v}(\mu_2^*) = 0$ and $F_2(\hat{v}(\mu_2), \mu_2) = 0$. Then, equation (4.16) reduces to

$$\dot{\xi} = f_1(\xi, \hat{v}(\mu_2); \mu_2).$$

Changing back to μ_1 , we have

$$\begin{aligned} v &= \frac{1}{b}(\mu_1 - \mu_1^*) \\ \implies \mu_1 &= bv + \mu_1^* = b\hat{v}(\mu_2) + \mu_1^*. \end{aligned}$$

Define $\mu_1 = \nu(\mu_2) = b\hat{v}(\mu_2) + \mu_1^*$, then $\nu(\mu_2^*) = b\hat{v}(\mu_2^*) + \mu_1^* = \mu_1^*$. Finally, using the definition of $f_1(\xi, \nu, \mu_2)$, we have

$$\begin{aligned} \dot{\xi} &= f_1(\xi, \nu(\mu_2); \mu_2) \\ &= f_1(\xi, \frac{1}{b}(\nu(\mu_2) - \mu_1^*); \mu_2) \\ &= f(\xi + \frac{a}{b}(\nu(\mu_2) - \mu_1^*) + x^*, \nu(\mu_2); \mu_2) - \frac{a}{b}g(\nu(\mu_2); \mu_2) \\ &= f(\xi + \frac{a}{b}(\nu(\mu_2) - \mu_1^*) + x^*, \nu(\mu_2); \mu_2) - \frac{a}{b}g(\nu(\mu_2); \mu_2). \end{aligned}$$

□

This theorem provides a way to extend the scalar system (4.7) where a saddle-

node occurs by transforming any parameter, μ_1 for convenience, into a variable to obtain the extended system (4.2) where a saddle-node bifurcation now occurs as the other parameter, μ_2 , passes through some bifurcation value μ_2^* . Note that the transformed parameter, μ_1 , does not need to be the original bifurcation parameter. Thus, we say that the saddle-node bifurcation in the extended system is the carryover of the saddle-node bifurcation in the original system. Also note that Proposition 4.1.1 requires that $g(\mu_1; \mu_2)$ does not depend explicitly on x . This makes the conditions of this proposition easy to verify with graphical and numerical tools.

Proposition 4.1.2. *Under the conditions of Proposition (4.1.1), let $h(\mu_1, \mu_2) = 0$ be the projection of Γ onto the (μ_1, μ_2) -plane. If $h(\mu_1, \mu_2)$ is differentiable at (μ_1^*, μ_2^*) , then conditions (4.14) and (4.13) are equivalent to*

1. $g(\mu_1; \mu_2) = 0$ intersects $h(\mu_1, \mu_2) = 0$ transversally at a point (μ_1^*, μ_2^*) , and
2. the tangent line to $g(\mu_1; \mu_2) = 0$ at (μ_1^*, μ_2^*) is not parallel to the μ_1 -axis,

respectively.

This proposition says that in order to find the saddle-node bifurcation points for the extended system, we plot the two-parameter bifurcation diagram of the smaller system, superimpose the nullclines of the new equation in the extended system, and look for transverse intersections between the saddle-node bifurcation curve and the nullclines. This is enough to verify the singularity and transversality conditions in the extended system.

Proof of Proposition 4.1.2. Note that (μ_1^*, μ_2^*) satisfies $g = 0$. Now, two vectors $u, v \in \mathbb{R}^2$ are transverse (parallel) if and only if the determinant of the matrix

formed by them is non-zero (is zero), i.e.,

$$\det(u, v) = u_1v_2 - v_1u_2 = |u||v|\sin(\theta) \neq 0 \iff \theta \neq 0, \pi.$$

Recall that $h(\mu_1, \mu_2) = 0$ is defined by the projection of Γ onto the (μ_1, μ_2) -plane, given by $(x, \mu_1, \mu_2) \mapsto (\mu_1, \mu_2)$. Since at least one of $D_{\mu_1}f$ or $D_{\mu_2}f$ is non-zero, points on Γ have a unique correspondence to points on $h(\mu_1, \mu_2) = 0$. Thus, a point (μ_1^*, μ_2^*) at which $g = 0$ and $h = 0$ intersect has a unique corresponding point $(z^*, \mu_2^*) = (x^*, \mu_1^*, \mu_2^*) \in \Gamma$.

Assume $D_{\mu_1}f \neq 0$ at $(z^*; \mu_2^*)$. Then, by the Implicit Function Theorem 4.0.2, we can parameterize Γ by μ_2 with functions $x = \mathcal{X}(\mu_2)$ and $\mu_1 = \mathcal{M}(\mu_2)$ such that $x^* = \mathcal{X}(\mu_2^*)$ and $\mu_1^* = \mathcal{M}(\mu_2^*)$ (see equation (4.11)). Implicit differentiation of $f(x, \mu_1; \mu_2) = 0$ with respect to μ_2 gives

$$D_x f \mathcal{X}' + D_{\mu_1} f \mathcal{M}' + D_{\mu_2} f = 0.$$

At z^* , $D_x f = 0$ and we have

$$\mathcal{M}' = -\frac{D_{\mu_2} f}{D_{\mu_1} f}.$$

Implicit differentiation of $h(\mu_1, \mu_2) = 0$ with respect to μ_2 gives

$$D_{\mu_1} h \mathcal{M}' + D_{\mu_2} h = 0.$$

Evaluating at z^* , substituting the \mathcal{M}' and multiplying by $-D_{\mu_1} f$, we obtain

$$D_{\mu_1} h D_{\mu_2} f - D_{\mu_2} h D_{\mu_1} f = 0.$$

This means that vectors $(D_{\mu_1} f, D_{\mu_2} f)^T$ and $(D_{\mu_1} h, D_{\mu_2} h)^T$ are multiple of each

other at z^* . Note that this is also true if $D_{\mu_1}f = 0$ since we must have $D_{\mu_2}f \neq 0$ and similar arguments follow. Thus, $(D_{\mu_1}h, D_{\mu_2}h)^T$ and $(D_{\mu_1}g, D_{\mu_2}g)^T$ are transverse if and only if $(D_{\mu_1}f, D_{\mu_2}f)^T$ and $(D_{\mu_1}g, D_{\mu_2}g)^T$ are transverse, which is equivalent to saying that the transversality condition (4.14) holds.

Finally, the condition that the tangent line of $g(\mu_1; \mu_2) = 0$ at (μ_1^*, μ_2^*) is not parallel to the μ_1 -axis is clearly equivalent to $D_{\mu_1}g(\mu_1^*, \mu_2^*) \neq 0$. \square

In the previous propositions, it is possible to generalize the arguments of the new scalar field, $g(\mu_1; \mu_2)$, to include dependence on x , i.e., $g(x, \mu_1; \mu_2)$, provided Γ and $g = 0$ intersect in the (x, μ_1, μ_2) -space. However, in the case of $g(\mu_1; \mu_2)$, the conditions of Proposition 4.1.1 are easy to verify with graphical and numerical tools.

In order to illustrate the application of Propositions 4.1.1 and 4.1.2, we introduce the following examples, where we consider a one-dimensional system with two parameters, a and b ,

$$\dot{x} = f(x; a, b),$$

and transform the parameter a into a variable to obtain the extended system

$$\dot{x} = f(x, a; b),$$

$$\dot{a} = g(a; b).$$

Example 4.1.1. Consider $f(x; a, b) = -a - b - x^2$. Since $D_x f = -2x = 0$ at $x = 0$, $D_{xx}f = -2 \neq 0$, and $D_a f = -1 \neq 0$, there is a saddle-node bifurcation at $x = 0$ as a crosses zero and $b = 0$. Furthermore, since $D_b f = -1 \neq 0$, b could be also taken as bifurcation parameter when $a = 0$. The bifurcation boundary is given by $h(a, b) = -a - b = 0$. Figure 4.2a shows the two-parameter bifurcation

diagram along with the following three choices for $g(a; b)$.

1. If $g(a; b) = a + b$, then $g = 0$ overlaps $h = 0$ and they are never transverse. Indeed, the extended system does not have a saddle-node bifurcation since it always has a unique steady state at $(x, a) = (0, -b)$, for all values of b .
2. If $g(a; b) = -a + b$, then $g = 0$ intersects $h = 0$ transversally at $(a, b) = (0, 0)$. According to Proposition 4.1.2, the extended system has a saddle-node bifurcation at $(x, a) = (0, 0)$ as b crosses $b = 0$. Indeed, there are two steady states, $(x, a) = (\pm\sqrt{-2b}, b)$ when $b < 0$, and they collide and disappear as b becomes positive. Figure 4.2b shows the bifurcation diagram for the extended system.
3. If $g(a; b) = a^2 - b$, then $g = 0$ intersects $h = 0$ transversally at $(a, b) = (0, 0)$ and $(a, b) = (-1, 1)$, but the tangent line of $g(a; b) = 0$ at $(a, b) = (0, 0)$ is parallel to the a -axis. Proposition 4.1.2 guarantees the saddle-node bifurcation at $(x, a, b) = (0, -1, 1)$, but not at $(x, a, b) = (0, 0, 0)$. In fact, at $(x, a, b) = (0, 0, 0)$, there is a Bogdanov-Takens (double-zero) bifurcation (see Section 8.4 in Kuznetsov [48]), since $D_a g = 0$ implies that there are two zero eigenvalues. When $b = 0$, there is a single steady state at $(x, a) = (0, 0)$. When $0 < b < 1$, two steady states emerge from the origin, a stable node $(x, a) = (\sqrt{\sqrt{b} - b}, -\sqrt{b})$, and saddle $(x, a) = (-\sqrt{\sqrt{b} - b}, -\sqrt{b})$. When $b = 1$ there is a saddle-node bifurcation at $(x, a) = (0, -1)$ as the two steady states collide and $D_a g \neq 0$. Figure 4.2c shows the bifurcation diagram for the extended system.

Example 4.1.2. Consider $f(x; a, b) = b^2 + 1 - a - x^2$. Since $D_x f = -2x = 0$ at $x = 0$, $D_{xx} f = -1 \neq 0$, and $D_a f = -1 \neq 0$, there is a saddle-node bifurcation at

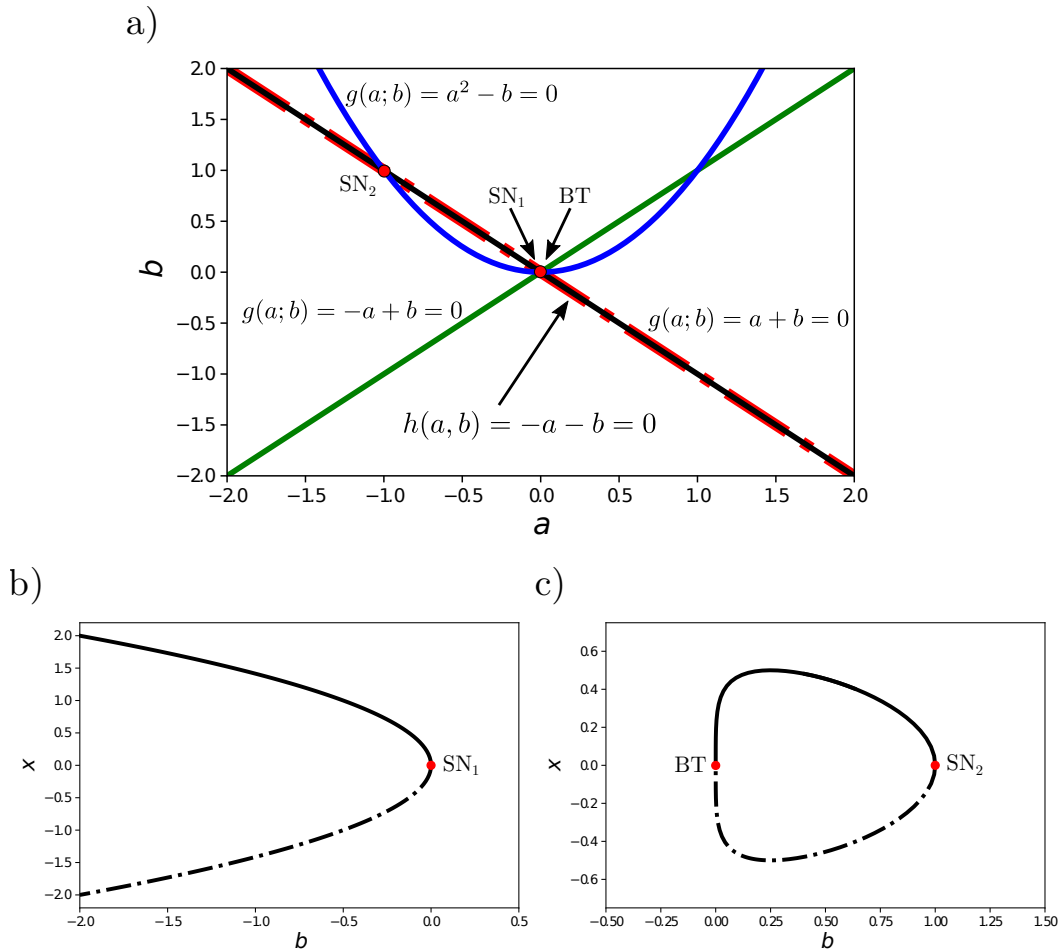


Figure 4.2: Bifurcation diagrams for Example 4.1.1 where $f(x; a, b) = -a - b - x^2$. a) Two-parameter bifurcation boundary (red dash-dotted line) for f with a and b as bifurcation parameters, and nullclines for three choices of $g(a; b)$: $g(a; b) = a + b$ (black) nullcline is never transverse; $g(a; b) = -a + b$ (green) nullcline is transverse at $(a, b) = (0, 0)$; and $g(a; b) = a^2 + b$ (blue) nullcline is transverse at $(a, b) = (-1, 1)$ and $(a, b) = (0, 0)$ but $D_a g(0, 0) = 0$. b) Bifurcation diagram when $g(a; b) = -a + b$. A saddle-node bifurcation (SN_1) occurs at $(x, a, b) = (0, 0, 0)$. c) Bifurcation diagram when $g(a; b) = a^2 - b$. A saddle-node bifurcation (SN_2) occurs at $(x, a, b) = (0, 1, 1)$ and a Bogdanov-Takens (double-zero) bifurcation (BT) occurs at $(x, a, b) = (0, 0, 0)$.

$x = 0$ as a crosses 1 and $b = 0$. However, since $D_b f = 2b = 0$ at $b = 0$, there is no saddle-node bifurcation at $(x, a, b) = (0, 1, 0)$ if b is taken as bifurcation parameter. The bifurcation boundary is given by $h(a, b) = b^2 + 1 - a = 0$. Figure 4.3a shows the two-parameter bifurcation diagram along with the following three choices for $g(b; a)$. Moreover, there is a saddle-node bifurcation at $x = 0$ as a crosses $b^2 + 1$, for fixed b .

1. If $g(a; b) = -a + 2$, then $g = 0$ intersects $h = 0$ transversally twice, at $(a, b) = (2, \pm 1)$. Thus, by Proposition 4.1.2, the extended system undergoes two saddle-node bifurcations at $(x, a) = (0, 2)$, one as b crosses $b = -1$ from the left where the two steady states, $(x, a) = (\pm\sqrt{b^2 - 1}, 2)$, collide and disappear, and one as b crosses $b = 1$ from the left where the two steady states, $(x, a) = (\pm\sqrt{b^2 - 1}, 2)$, emerge. Figure 4.3b shows the bifurcation diagram for the extended system.
2. If $g(a; b) = -a + 1$, then $g = 0$ is tangential to $h = 0$ at $(a, b) = (1, 0)$. No saddle-node bifurcation occurs since the two steady states $(x, a) = (\pm\sqrt{b^2}, 1) = (\pm|b|, 1)$ collide and bounce back, as seen in Figure 4.3c. In fact, at $(x, a, b) = (0, 1, 0)$, the extended system satisfies the singularity conditions $(\lambda = 0, -1)$ and nondegeneracy condition $(D_{xx}f = -2 \neq 0)$, but not the transversality condition $(D_a f D_b g - D_a g D_b f = -2b|_{b=0} = 0)$. Note that this is not a transcritical bifurcation since the steady states $(|b|, 1)$ and $(-|b|, 1)$ are a stable node (two negative eigenvalues) and a saddle point (eigenvalues with opposite sign), respectively, for all b . In other words, they do not exchange stability when they collide, instead they touch and bounce back preserving their stability.
3. If $g(a; b) = b - a + 1$, then $g(a; b) = 0$ is transverse at $(a, b) = (1, 0)$ and

$(a, b) = (2, 1)$. Moreover, the tangent line to $g(a, b) = 0$ at $(1, 0)$ and $(2, 1)$ is not parallel to the a -axis since $D_a g(a; b) = -1$. Thus, as in the first case ($g(a; b) = -a + 2$), two saddle-node bifurcations occur, one as b crosses $b = 0$ from the left where two steady states $(x, a) = (\pm\sqrt{b(b-1)}, b+1)$ collide and disappear, and one as b crosses $b = 1$ where two steady states $(x, a) = (\pm\sqrt{b(b-1)}, b+1)$ emerge. Figure 4.3d shows the bifurcation diagram for the extended system. This case is interesting because at $(a, b) = (1, 0)$, the transversality condition is not satisfied for the original system with respect to b , i.e., $D_b f(0; 1, 0) = 0$. In other words, even if b is not a bifurcation parameter in the original system at (x^*, μ^*) , b becomes a bifurcation parameter in the extended system at the same point.

4. If we extend the parameter b instead using $\hat{b} = g(b; a) = b - a + 1$, it follows from the previous case that two saddle-node bifurcations occur at $(x, a, b) = (0, 1, 0)$ and $(x, a, b) = (0, 2, 1)$, as seen in Figure 4.3e. However, note that b is not a bifurcation parameter in the original system at $(x, a, b) = (0, 1, 0)$ yet transforming b into a variable there is a carryover of the saddle-node bifurcation that occurs in the original system with a as bifurcation parameter.

4.2 n -dimensional case

In the previous section, we showed the carryover of a saddle-node bifurcation in the one-dimensional case. In this section, we show that this result also holds in the n -dimensional case. In short, this is true because the saddle-node bifurcations can be reduced to one-dimension around the bifurcation point.

Suppose that f in the original system (4.1) satisfies the conditions of Theo-

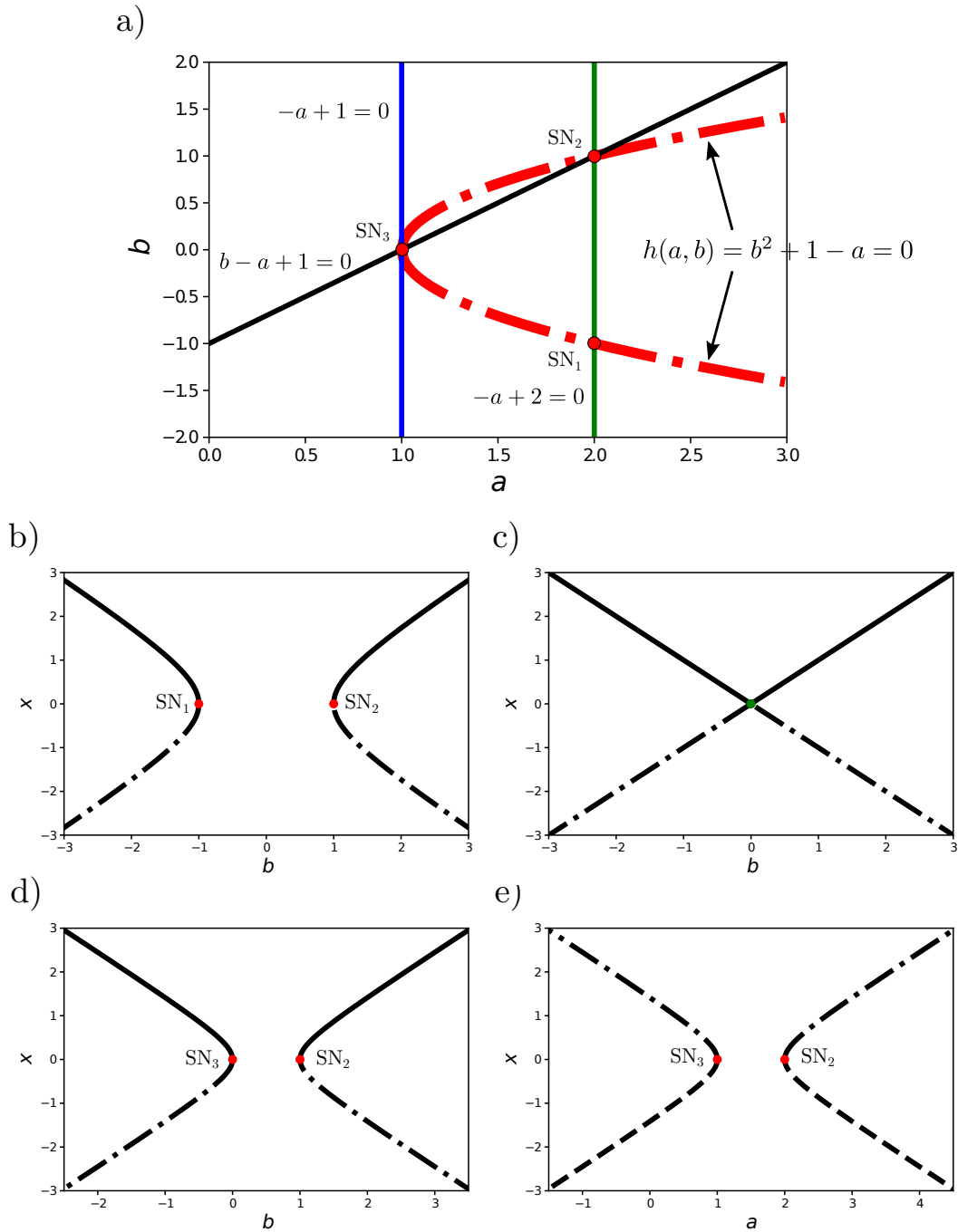


Figure 4.3: Bifurcation diagrams for Example 4.1.2 where $f(x; a, b) = b^2 + 1 - a - x^2$. a) Two-parameter bifurcation boundary (red dash-dotted curve) for f with a and b as bifurcation parameters, and nullclines for three choices of $g(a; b)$: $g(a; b) = -a + 2$ (green) nullcline is transverse at $(a, b) = (2, -1)$ and $(a, b) = (2, 1)$; (continued)

Figure 4.3 (*continued*): $g(a; b) = -a + 1$ (blue) is tangential at $(a, b) = (1, 0)$; and $g(a; b) = b - a + 1$ (black) nullcline is transverse at $(a, b) = (1, 0)$ and $(a, b) = (2, 1)$. b) Bifurcation diagram when $g(a; b) = -a + 2$. Two saddle-node bifurcations occur at $(x, a, b) = (0, 2, \pm 1)$. c) Bifurcation diagram when $g(a; b) = -a + 1$. No bifurcation occurs because the steady states collide but do not disappear. d) Bifurcation diagram when $g(a; b) = b - a + 1$. Two saddle-node bifurcations occur at $(x, a, b) = (0, 1, 0)$ and $(x, a, b) = (0, 1, 1)$. e) Bifurcation diagram when $\dot{b} = g(a; b) = b - a + 1$. Two saddle-node bifurcations occur at $(x, a, b) = (0, 1, 0)$ and $(x, a, b) = (0, 2, 1)$.

rem 4.0.1. Then, we can reduce the system to one-dimensional form

$$\dot{x} = f_1(x, \eta(x; \mu_1, \mu_2); \mu_1, \mu_2),$$

where functions $f_1(x, y; \mu_1, \mu_2)$ and $y = \eta(x; \mu_1, \mu_2)$ are given by the theorem, in a neighbourhood of $(x, y, \mu) = (0, 0, 0)$ in regards to the saddle-node bifurcation. Now, suppose that f_1 satisfies the transversality condition of Corollary 4.0.1 for either μ_1 or μ_2 . Then, in a similar fashion as in the one-dimensional case, the Implicit Function Theorem 4.0.2 guarantees the existence of an interval I and unique functions \mathcal{X} and \mathcal{M} such x and μ_1 can be parameterized in terms of μ_2 (for example), i.e.,

$$x = \mathcal{X}(\mu_2), \mu_1 = \mathcal{M}(\mu_2), \mu_2 \in I, \quad \text{and} \quad \mathcal{X}(0) = 0, \mathcal{M}(0) = 0.$$

This defines the smooth one-dimensional bifurcation curve

$$\Gamma = \{(z, \mu_1, \mu_2) : z = (x, y) = (\mathcal{X}(\mu_2), \eta(\mathcal{X}(\mu_2); \mathcal{M}(\mu_2), \mu_2)), \\ \mu_1 = \mathcal{M}(\mu_2), \mu_2 \in I\}. \quad (4.18)$$

To extend Γ in this case, we take a point in Γ , different from $(x, y, \mu) = (0, 0, 0)$,

and apply again Theorem 4.0.1 (after some appropriate translation) followed by the Implicit Function Theorem 4.0.2 as shown above. Note that functions f_1 , \mathcal{X} , and \mathcal{M} do not need to be the same as before. By continuity we can apply this process repetitive times and further extend Γ as long as the transversality condition holds for either μ_1 and μ_2 at each step. Finally, the bifurcation boundary, $h(\mu_1, \mu_2) = 0$, is defined by the projection of extended Γ onto the (μ_1, μ_2) -plane, given by $\pi(z, \mu_1, \mu_2) \mapsto (\mu_1, \mu_2)$. Thus, the definition of Γ and $h(\mu_1, \mu_2) = 0$ is similar to the one-dimensional case.

Proposition 4.2.1. *Let $f(z; \mu_1, \mu_2) \in C^2(\mathbb{R}^n \times \mathbb{R}^2, \mathbb{R}^n)$ and suppose that the hypotheses of Theorem 4.0.1 are satisfied at $(z, \mu_1, \mu_2) = (0, 0, 0)$. Suppose also that the transversality condition in Corollary 4.0.1 is satisfied for either μ_1 or μ_2 . Let $m(\mu_1, \mu_2)$ be the extremal value defined in Theorem 4.0.1. This defines a one-dimensional smooth curve $\Gamma \subset \mathbb{R}^{n+2}$ in a neighbourhood of (z, μ_1, μ_2) that satisfies the singularity and nondegeneracy conditions.*

Consider the extended system (4.2) by transforming parameter μ_1 into a variable, where $f \in C^2(\mathbb{R}^{n+1} \times \mathbb{R}, \mathbb{R}^n)$ and $g \in C^2(\mathbb{R} \times \mathbb{R}, \mathbb{R})$. If there is a point $(z, \mu_1, \mu_2) = (z^, \mu_1^*, \mu_2^*) \in \Gamma$ such that $g(\mu_1; \mu_2)$ satisfies*

$$g(\mu_1^*; \mu_2^*) = 0, \quad b = D_{\mu_1}g(\mu_1^*; \mu_2^*) \neq 0, \quad (4.19)$$

and the transversality condition

$$\det \begin{pmatrix} D_{\mu_1}m & D_{\mu_1}g \\ D_{\mu_2}m & D_{\mu_2}g \end{pmatrix} = D_{\mu_1}hD_{\mu_2}g - D_{\mu_1}gD_{\mu_2}h \neq 0, \quad (4.20)$$

is satisfied at $(z, \mu_1, \mu_2) = (z^, \mu_1^*, \mu_2^*)$, then (4.2) has a saddle-node bifurcation at*

$(z, \mu_1) = (z^*, \mu_1^*)$ as μ_2 crosses μ_2^* .

Proof. First, we translate the point z^* to the origin using a new variable $\zeta = z - z^*$ to obtain the translated system

$$\dot{\zeta} = f(\zeta + z^*; \mu_1, \mu_2),$$

that satisfies all the conditions of Theorem 4.0.1 at $\zeta = 0$. By Theorem 4.0.1, we choose new translated coordinates $x \in \mathbb{R}$ and $y \in \mathbb{R}^{n-1}$ such that

$$\begin{aligned}\dot{x} &= f_1(x, y; \mu_1, \mu_2), \\ \dot{y} &= My + f_2(x, y; \mu_1, \mu_2),\end{aligned}$$

where $f_1 = 0$, $f_2 = 0$, $D_x f_1 = 0$, $D_x f_2 = 0$, $D_y f_1 = 0$, $D_y f_2 = 0$, and $D_{xx} f_1 \neq 0$ at $(x, y; \mu_1, \mu_2) = (0, 0; \mu_1^*, \mu_2^*)$, and M is invertible. Moreover, there is an interval $I(\mu_1, \mu_2)$ of 0 and function $y = \eta(x; \mu_1, \mu_2)$ where the extremal value $m(\mu_1, \mu_2) = \text{Ext}_{x \in I(\mu_1, \mu_2)} [f_1(x, \eta(x; \mu_1, \mu_2); \mu_1, \mu_2)]$ is defined. Therefore, the system is reduced to one equation $\dot{x} = f_3(x; \mu_1, \mu_2) = f_1(x, \eta(x; \mu_1, \mu_2); \mu_1, \mu_2)$ in a neighborhood of $(\zeta, \mu_1, \mu_2) = (0, \mu_1^*, \mu_2^*)$ where the singularity and nondegeneracy conditions are satisfied. Then, the extended system (4.2) can be reduced to

$$\begin{aligned}\dot{x} &= f_3(x, \mu_1; \mu_2) = f_1(x, \eta(x; \mu_1, \mu_2); \mu_1, \mu_2), \\ \dot{\mu}_1 &= g(\mu_1; \mu_2),\end{aligned}$$

in a neighborhood of $(\zeta, \mu_1, \mu_2) = (0, \mu_1^*, \mu_2^*)$. By assumption, the transversality condition, $D_{\mu_i} f_1 \neq 0$, is satisfied for either μ_1 or μ_2 . Then, by Proposition 4.1.1, this system has a saddle-node bifurcation at $(x, \mu_1) = (0, \mu_1^*)$ as μ_2 crosses μ_2^* . It follows that the extended system (4.2) has a saddle-node bifurcation at $(z, \mu_1) = (0, \mu_1^*)$ as

μ_2 crosses μ_2^* .

□

As we might expect, Proposition 4.1.2 also applies to the n -dimensional case. The proof follows similar arguments to the one-dimensional case.

Proposition 4.2.2. *Under the conditions of Proposition (4.2.1), let $h(\mu_1, \mu_2) = 0$ be the projection of Γ onto the (μ_1, μ_2) -plane. If $h(\mu_1, \mu_2)$ is differentiable at (μ_1^*, μ_2^*) , then conditions (4.20) and (4.19) are equivalent to:*

1. $g(\mu_1; \hat{\mu}, \nu) = 0$ intersects $h(\mu_1, \mu_2) = 0$ transversally at a point (μ_1^*, μ_2^*) , and
2. the tangent line to $g(\mu_1; \mu_2) = 0$ at (μ_1^*, μ_2^*) is not parallel to the μ_1 -axis,

respectively.

Example 4.2.1. *Consider the system*

$$\dot{x} = \mu - x^2 + xy - xy^2,$$

$$\dot{y} = \lambda - y - x^2 + x^2y,$$

taken from Meiss [63, p. 292]. There is a saddle-node bifurcation at the origin as μ crosses zero. The two-parameter bifurcation diagram starting from this bifurcation point is shown in Figure 4.4a. Now, consider the extended system

$$\dot{x} = \mu - x^2 + xy - xy^2,$$

$$\dot{y} = \lambda - y - x^2 + x^2y,$$

$$\dot{\mu} = g(\mu; \lambda) = \mu - \frac{1}{2}.$$

The μ -nullcline is transverse to the two-parameter bifurcation diagram in two points near $\lambda = 0.5$ and $\lambda = 1.1$ (see Figure 4.4a). Since the tangent line of $g(\mu; \lambda)$ is not parallel to the μ -axis at neither intersection, two saddle-node bifurcations are

inherited with λ as bifurcation parameter. Indeed, the bifurcation diagrams for x and y are shown in Figures 4.4b and 4.4c, respectively. The corresponding bifurcation points are found to be

$$(x, u, \mu; \lambda) \approx (-0.6792, 0.0604, 0.5; 0.4940),$$

$$(x, u, \mu; \lambda) \approx (-0.8429, 1.2069, 0.5; 1.0599).$$

4.3 Discussion

Given a system with a saddle-node bifurcation, we studied the manifestation of the saddle-node bifurcation when transforming one parameter into a variable. We call this property the carryover of a saddle-node bifurcation. We focused on the case where the new differential equation associated with the new variable does not depend on the rest of the variables. We showed that additional singularity and transversality conditions are sufficient for the carryover of the saddle-node bifurcation. We also find that such conditions can be verified graphically with a two-parameter bifurcation diagram.

In Section 4.1, we studied the scalar case, that is, the scalar system (4.7) has a saddle-node bifurcation at the origin as either μ_1 or μ_2 cross zero. Such a saddle-node bifurcation is characterized by singularity and non-degeneracy conditions, and a transversality condition for either μ_1 and μ_2 [63]. By the Implicit Function Theorem 4.0.2, there exists a one-dimensional bifurcation curve $\Gamma \in \mathbb{R}^3$ in the neighborhood of zero where the singularity, non-degeneracy, and transversality conditions are satisfied [48]. If we transform μ_1 into a variable, we obtain the two-dimensional extended system (4.8). Any carryover of the saddle-node bifurcation to the extended system must take place in Γ . We proved that if 1) the μ_1 -nullcline intersects Γ

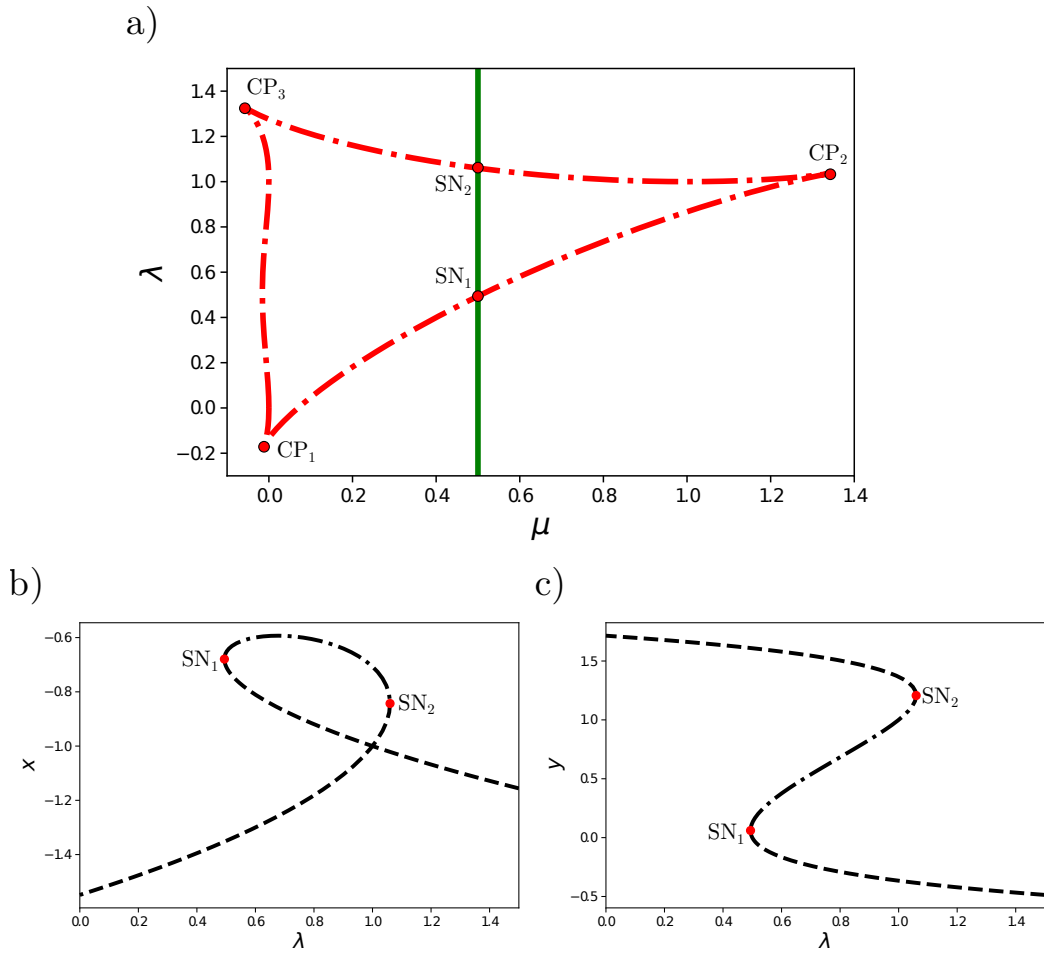


Figure 4.4: Bifurcation diagrams for Example 4.2.1. a) Two-parameter bifurcation boundary (red dashed-dotted curve) and nullcline for $g(\mu; \lambda) = \mu - \frac{1}{2}$ (green). Two saddle-node bifurcations (SN_1 and SN_2) occur at the transverse intersection between the g -nullcline and the bifurcation boundary. Note that there are cusp bifurcations (CP_1 , CP_2 , and CP_3) associated with the system at the intersection of two saddle-node bifurcations. b-c) Bifurcation diagrams for the extended system with λ as bifurcation parameter and variables x and y in the ordinate, respectively. The dashed lines indicate the unstable node with associated three-dimensional unstable manifold, while the dot-dashed lines indicate the saddle-node with associated one-dimensional stable manifold and two-dimensional unstable manifold.

transversally, and 2) the new equation does not add another zero eigenvalue at the intersection, then the extended system has a saddle-node bifurcation at the intersection. These are the additional transversality and singularity conditions for the extended system, respectively (see Proposition 4.1.1).

Moreover, we showed that the transversality and singularity conditions for the extended system can be easily verified in the two-parameter bifurcation diagram with μ_1 and μ_2 as bifurcation parameters. The two-parameter bifurcation curve is the projection of Γ onto the $\mu_1\mu_2$ -plane. By superimposing the μ_1 -nullcline on the two-parameter, we can verify 1) the transversality condition if the μ_1 -nullcline intersects the two-parameter bifurcation curve transversally, and 2) the singularity condition if the μ_1 -nullcline is not parallel to the μ_1 -axis at the intersection (see Proposition 4.1.2). This graphical result is the consequence of the fact that the new equation does not depend on the other variable ($g(\mu_1; \mu_2)$ does not depend on x). Thus, if the projection of Γ and the μ_1 -nullcline intersect as seen from the $\mu_1\mu_2$ -plane, then Γ and the μ_1 -nullcline also intersect in \mathbb{R}^3 .

Note that it is irrelevant which of the two parameters (or both) satisfies the transversality condition for the original system, we only need to start from a saddle-node bifurcation point and follow the bifurcation along Γ . In fact, Γ can be extended as long as the transversality condition is satisfied for at least one of the parameters. Interestingly, a carryover can happen at a point where either μ_1 (the transformed variable) or μ_2 (the remaining parameter) is a bifurcation parameter in the original system. These cases were illustrated with examples in the text. It is still left to show that a carryover can happen at a point where the bifurcation happens as both μ_1 and μ_2 change simultaneously (but not individually), separately, or when k parameters change simultaneously.

In Section 4.2, we extended our study to the n -dimensional case, that is, the

n -dimensional system (4.1) has a saddle-node bifurcation at the origin as either μ_1 or μ_2 cross zero and μ_1 is transformed into a variable. We showed that the same singularity and transversality conditions apply in the carryover of the saddle-node bifurcation for the n -dimensional case. To show this, we reduced the original system in a neighborhood of the bifurcation point to one-dimension and applied our results for the scalar case. The n -dimensional case is also illustrated with an example.

The case where the new differential equation depends on the other variables, i.e., $\dot{\mu}_1 = g(z, \mu_1; \mu_2)$, is not covered here. Assuming the bifurcation curve and the μ_1 -nullcline intersect in \mathbb{R}^n , an extra condition (or conditions) would be required to guarantee that the matrix A , as defined within the proof of Proposition (4.1.1), is invertible. We leave this case open for future research. We also leave open the interesting exploration of the carryover of other types of bifurcation (transcritical, pitchfork, Hopf, etc) as well as applications of the carryover of bifurcations.

The problem of the carryover of a saddle-node bifurcation was motivated by our results in Chapter 2, where we found an interesting, yet unclear, relationship between the $\text{SNIC}_{\text{Mass}}$ bifurcation and the $\text{SNIC}_{V_{c2}}$ bifurcation. In fact, studying Figure 2.6 motivated us to conjecture Proposition 4.2.2, which indeed applies to conclude that the $\text{SNIC}_{V_{c2}}$ (locally, saddle-node) bifurcation is the carryover of the $\text{SNIC}_{\text{Mass}}$ (locally, saddle-node) bifurcation after transforming Mass into a variable. In addition to clarifying the true origin of the $\text{SNIC}_{V_{c2}}$ bifurcation, our results from this chapter are used in the next chapter.

Chapter 5

Reduction of the Cell Cycle model to one-dimension around the SNIC bifurcation

In Chapter 2, we studied the effect of radiation on the G2/M transition of the cell cycle through the ATM and Chk2 pathway. We took a model from Novak and Tyson for the cell cycle and introduced a radiation pathway accounting for ATM and Chk2. We identified a saddle-node on an invariant circle (SNIC) bifurcation that arises from the effect of radiation on the G2/M transition through the ATM/Chk2 radiation pathway. We showed that this SNIC bifurcation, driven by the inactivation rate V_{c2} , is the loss of the SNIC bifurcation driven by the cell mass implicit in the system. In Chapter 2, the relationship between the two bifurcation points was illustrated and explained through bifurcation diagrams. In this chapter, we show theoretically how these two bifurcations are related using the results obtained in Chapter 4. In particular, we show that the SNIC bifurcation driven by V_{c2} is the carryover of the SNIC bifurcation driven by cell mass after the mass is transformed

into a state variable. Moreover, we are able to reduce the cell cycle model to a one-dimensional form around the SNIC bifurcation driven by V_{c2} . This form will be used, in Chapter 6, to approximate the time available for repair discussed in Chapter 3 and derive a theoretical form for the survival fraction based on the ATM-Chk2 pathway.

Before describing the structure of this chapter, we first review the results obtained in Chapter 2.

5.1 Introduction

In Chapters 2 and 3, we focused on the effect of the radiation pathway on the cell cycle model developed by Tyson and Novák (see Tyson and Novák [96] for a review). In this chapter, we detach the radiation pathway (variables DSB, ATM, and Chk2) to focus on the cell cycle dynamics. The cell cycle model is given by the set of differential equations

$$\begin{aligned} \frac{dMPF}{dt} = & k_{m0}Mass - (k_{m2} + k_{m2a}Wee1)MPF \\ & + (k_{m1} + k_{m1a}Cdc25)MPF_P - (k_{m3} + k_{m3a}APC)MPF, \end{aligned} \quad (5.1a)$$

$$\begin{aligned} \frac{dMPF_P}{dt} = & (k_{m2} + k_{m2a}Wee1)MPF - (k_{m1} + k_{m1a}Cdc25)MPF_P \\ & - (k_{m3} + k_{m3a}APC)MPF_P, \end{aligned} \quad (5.1b)$$

$$\begin{aligned} \frac{dWee1}{dt} = & V_{w1} \frac{Wee1_T - Wee1}{J_{w1} + (Wee1_T - Wee1)} \\ & - k_{w2}(MPF + \alpha MPF_P) \frac{Wee1}{J_{w2} + Wee1}, \end{aligned} \quad (5.1c)$$

$$\begin{aligned} \frac{dCdc25}{dt} = & k_{c1}(MPF + \alpha MPF_P) \frac{Cdc25_T - Cdc25}{J_{c1} + (Cdc25_T - Cdc25)} \\ & - V_{c2} \frac{Cdc25}{J_{c2} + Cdc25}, \end{aligned} \quad (5.1d)$$

Table 5.1: Name and description of variables in Eqs. (5.1a)–(5.1g). All variables represent concentration, except for the cell mass.

Symbol	Description
MPF	Active Cdk1-cyclin B complex (Mitotic Promoting Factor)
MPF_P	Inactive, phosphorylated form of MPF
$Wee1$	Active dephosphorylated form of kinase Wee1 (MPF inactivator)
$Cdc25$	Active phosphorylated form of the phosphatase Cdc25C (MPF activator)
IE	Active form of an intermediate enzyme [94]
APC	Active phosphorylated form of APC (Anaphase Promoting Complex)
$Mass$	Mass of the cell

$$\frac{dIE}{dt} = k_{i1}(MPF + \alpha MPF_P) \frac{IE_T - IE}{J_{i1} + (IE_T - IE)} - V_{i2} \frac{IE}{J_{i2} + IE}, \quad (5.1e)$$

$$\frac{dAPC}{dt} = k_{a1}IE \frac{APC_T - APC}{J_{a1} + (APC_T - APC)} - V_{a2} \frac{APC}{J_{a2} + APC}, \quad (5.1f)$$

$$\frac{dMass}{dt} = \mu Mass \left(1 - \frac{Mass}{K_{Mass}} \right), \quad (5.1g)$$

subject to the resetting condition

$$\text{if } MPF(t) = \theta_M \text{ and } \frac{dMPF}{dt}(t) < 0 \implies Mass(t) \leftarrow \frac{Mass(t)}{2}. \quad (5.2)$$

The model variables and parameters are listed in Tables 5.1 and 5.2, respectively. A typical numerical solution for some of the variables of the model that describe the oscillating behaviour of the cell cycle is shown in Figure 5.1.

As discussed in Section 2.2.1, the cell cycle model (5.1)–(5.2) can be broken down into two interconnected modules that describe the cell cycle dynamics; namely, the interphase and M-phase modules (see Figure (5.2)). The interface module is governed by equations (5.1a)–(5.1d). These equations model the transition from low to high concentration of MPF, which in turns determines the G2/M transition and the

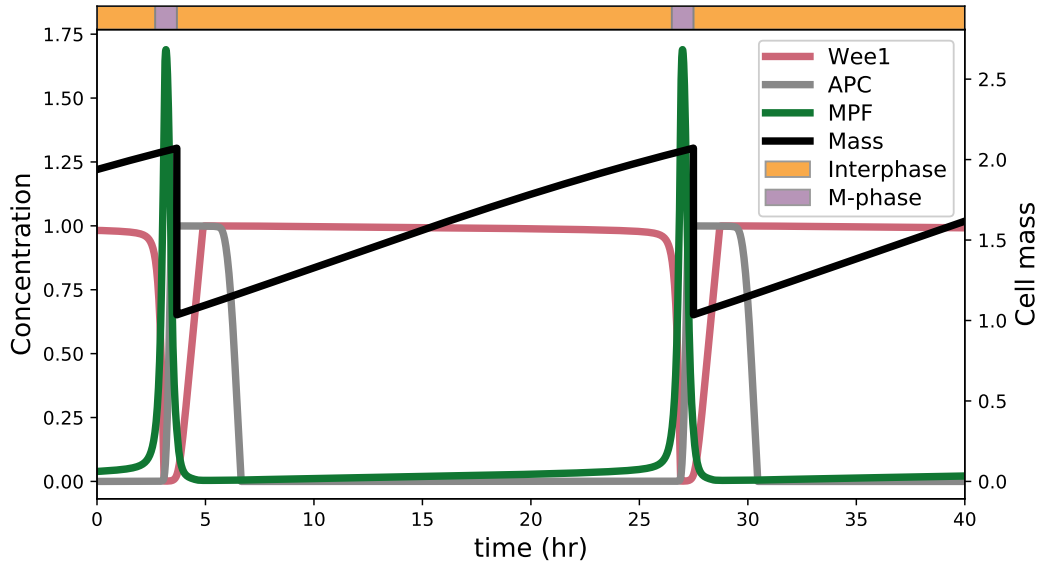


Figure 5.1: Numerical solution of the cell cycle model (5.1)–(5.2).

M-phase entry. This can be seen in Figure 5.1 with MPF concentration rising quickly above the threshold for M-phase ($\theta_M = 0.2$) at the end of the interphase. We note that the G1/S and S/G2 transitions in mammalian cells are not considered explicitly in this version of the cell cycle model, since they would require other proteins (different from MPF) to be modelled. Instead, the G1- and S-phases are implicitly accounted for by the parameters of the model to accommodate an interphase length of approximately 22 hrs. Thus, when we consider the interphase module alone it is more reasonable to refer to it as the G2 module since it only models the dynamics of the G2-phase. In this chapter, we focus on the G2 module and the G2/M transition.

The M-phase is mainly governed by equations (5.1a) and (5.1e)–(5.1f). These equations model the rapid increase and decrease in the concentration of MPF during the M-phase, as shown in Figure 5.1. The cell cycle oscillations are completed when the cell mass (governed by equation (5.1g)) is divided in half according to the resetting condition (5.2). This resetting event places solutions back in the interphase

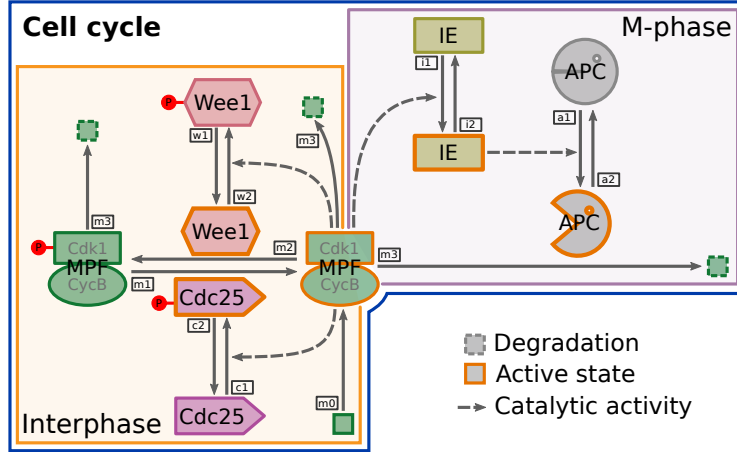


Figure 5.2: Cell cycle model diagram.

as explained in Section 2.4 (see Novák et al. [74] for further details).

The resetting event defines a discontinuous jump in the phase space of model (5.1), which can be viewed as a branched manifold. A branched manifold is a generalization of a differentiable manifold that allows special types of singularities, such as resetting conditions. Consider the differentiable manifold \mathcal{M} defined by the phase space of the model given by equations (5.1). The resetting condition in equation (5.2) maps trajectories reaching a submanifold N ($MPF = \theta_M$ and decreasing) in the M-phase to a submanifold $g(N)$ (cell mass is divided by two) in the G2-phase (see Figure 5.3). The branched manifold is given by folding the manifold and “gluing together” submanifolds N and $g(N)$ such that the resulting manifold is tangential at the connection [31]. The associated vector field is well-defined provided trajectories satisfy transversality conditions, which are discussed in Section 5.3. Thus, the cell cycle oscillation shown in Figure 5.1 belongs to the branched manifold where the discontinuous jump in the cell mass is well defined. Moreover, numerical simulations show that such cell cycle oscillation is a locally asymptotically stable limit cycle on the branched manifold.

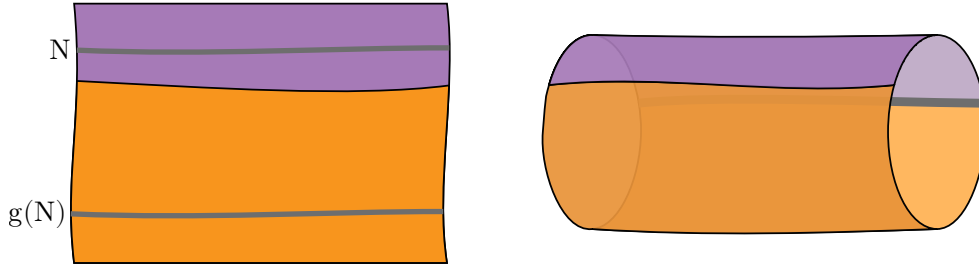


Figure 5.3: Construction of the branched manifold. The cell cycle model (5.1) (without resetting condition (5.2)) defines a manifold \mathcal{M} (left). Resetting condition (5.2) maps trajectories reaching submanifold N (upper grey curve) in the M-phase (purple) to submanifold $g(N)$ (lower grey curve) in the interphase (orange). The branched manifold (right) is constructed by tangentially gluing together submanifolds N and $g(N)$ (grey line). The black line separating the interphase and M-phase represents the threshold θ_M when MPF is increasing (see equation (5.2)).

If we take V_{c2} in Equation 5.1d as a varying parameter and increase its value, we observe that the cell cycle oscillations are lost in a saddle-node in an invariant circle (SNIC) bifurcation (see Figure 5.4). This provides an entrance to the G2 checkpoint defined by a stable node and a saddle point. In Section 2.3, we showed that G2 checkpoint activation can be caused by radiation as it increases the value of V_{c2} beyond the $\text{SNIC}_{V_{c2}}$ bifurcation point, $V_{c2}^* \approx 3.47$. The $\text{SNIC}_{V_{c2}}$ bifurcation point and corresponding eigenvalues (eigenvalues of the jacobian matrix of the

vector field evaluated at the steady state) found numerically are given by

$$V_{c2}^* \approx 3.471683, \quad \begin{bmatrix} MPF^* \\ MPF_P^* \\ Wee1^* \\ Cdc25_P^* \\ IE^* \\ APC^* \\ Mass^* \end{bmatrix} \approx \begin{bmatrix} 0.048044 \\ 2.650815 \\ 0.825999 \\ 0.007785 \\ 0.003287 \\ 0.000013 \\ 2.7 \end{bmatrix}, \quad \vec{\lambda} \approx \begin{bmatrix} 0 \\ -0.0700 \\ -0.2000 \\ -21.768 \\ -36.960 \\ -115.58 \\ -1655.6 \end{bmatrix}. \quad (5.3)$$

The $SNIC_{V_{c2}}$ bifurcation is represented in the illustration of the branched manifold in Figure 5.4.

In Section 2.4, we also showed how this $SNIC_{V_{c2}}$ bifurcation relates to the $SNIC_{Mass}$ bifurcation driven by Mass. In particular, we showed that the $SNIC_{V_{c2}}$ bifurcation is the loss of the $SNIC_{Mass}$ embedded in the cell cycle model. The $SNIC_{Mass}$ bifurcation, studied by [98], appears in the version of the cell cycle model where the cell mass is not a variable but a varying parameter and the bifurcation itself defines the G2/M transition. Besides the observed relationship between the two SNIC bifurcations, it was not clear what underpins this relationship mathematically. Moreover, the oscillations associated with these SNIC bifurcations have a completely different nature: the oscillation associated with the $SNIC_{Mass}$ arises from the negative feedback loop between MPF and APC in the M-phase module, while the oscillation associated with the $SNIC_{V_{c2}}$ is the ability to cycle between the G2- and M-phases. In this Chapter, we unravel the dynamical relationship between these two SNIC bifurcations. In particular, we show that the $SNIC_{V_{c2}}$ bifurcation is the carryover of the $SNIC_{Mass}$ bifurcation after the cell mass is turned into a

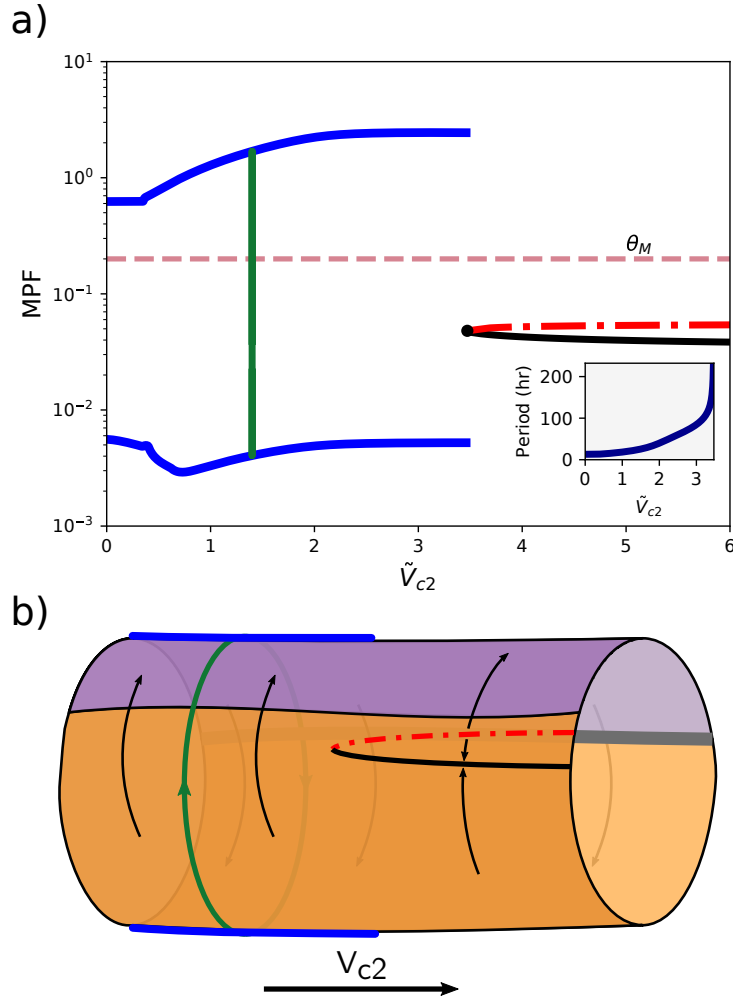


Figure 5.4: a) Bifurcation diagram for V_{c2} (top). b) Illustration of the bifurcation diagram drawn on the branched manifold. The arrows represent the vector field.

variable.

We are able to establish the theoretical connection between the two SNIC bifurcations by unfolding the branched manifold and focusing on the saddle-node component of the SNIC, that is, excluding oscillations. We show, using the results obtained in Chapter 4, that the saddle-node bifurcation associated with the $\text{SNIC}_{V_{c2}}$ bifurcation is the carryover of the saddle-node bifurcation associated with the SNIC_{Mass} bifurcation after the cell mass is transformed into variable.

In Chapter 3, we used numerical simulations to show that the $\text{SNIC}_{V_{c2}}$ bifurcation can produce a hyper-radiosensitivity and increased radioresistance (HRS/IRR) effect in the survival fraction. However, we also stated the importance of computing such survival fraction without extensive numerical calculations. We hypothesize that this is possible if we reduce the cell cycle model to one-dimensional form around the $\text{SNIC}_{V_{c2}}$ bifurcation. This one-dimensional reduction is the goal of this chapter, which is organized into the following sections:

5.2 G2 module: saddle-node bifurcation driven by cell mass. In this section, we decouple the G2 module from the cell cycle model corresponding to equations (5.1a)–(5.1d). We show that in this module, there is a saddle-node bifurcation with the cell mass as the bifurcation parameter. Under appropriate initial conditions, this means that the cell mass forces an abrupt increase in the concentration of MPF. Such change in the concentration of MPF determines the G2/M transition. Moreover, we reduce the G2 module to a one-dimensional system form as follows. First, we start with the G2 module, which we denote as

$$z' = f(z; p),$$

where $z \in \mathbb{R}^4$, and $p \in \mathbb{R}^{18}$ is the vector of associated parameters. Second, we translate a given steady state z^* to the origin using the transformation $\hat{z} = z - z^*$ and write the translated G2 module

$$\hat{z}' = f(\hat{z} + z^*; p),$$

with steady state at the origin, $\hat{z}^* = 0$. Third, we nondimensionalize to write

the G2 module as

$$\tilde{z}' = \tilde{f}(\tilde{z}; p).$$

Nondimensionalization helps us to simplify calculations. Fourth, we find conditions such that $(\tilde{z}; p) = (0, p^*)$ is a saddle-node bifurcation point and, following Theorem 4.0.1, we find new coordinates (ξ, ϕ) and write

$$\begin{aligned}\xi' &= f_1(\xi, \phi; p), \\ \phi' &= M\phi + f_2(\xi, \phi; p),\end{aligned}$$

where $\xi \in \mathbb{R}^1$ corresponds to the zero eigenvalue of the saddle-node bifurcation, and $\phi \in \mathbb{R}^3$ are the remaining coordinates. Theorem 4.0.1 guarantees the reduction to one-dimension in the form

$$\xi' = f_1(\xi, \eta(\xi); p),$$

in a neighborhood of the saddle-node bifurcation point $(0, p^*)$ and for some function $\phi = \eta(\xi)$.

5.3 G2 module with variable cell mass: saddle-node bifurcation driven by

V_{c2} . In this section, we add the cell mass as a dynamical state variable to the G2 module, and show that there is a saddle-node bifurcation with V_{c2} as the bifurcation parameter. This means that V_{c2} can prevent the G2/M transition forced by the new state variable $Mass$. Based on the theory developed in Chapter 4, we show that this new saddle-node bifurcation driven by V_{c2} is the carryover of the previous saddle-node bifurcation driven by cell mass, and

that the one-dimensional reduction in this case remains in the form

$$\xi' = f_1(\xi; p).$$

5.4 G2 and M modules combined with variable cell mass and resetting condition: SNIC bifurcation driven by V_{c2} . In this section, we add the M module and resetting condition to the G2 module with variable mass to fully recover the cell cycle model where a SNIC bifurcation driven by V_{c2} takes place. Analogously, we add a resetting condition to the one-dimensional form found in the in the previous sections to transform the associated saddle-node bifurcation into a SNIC bifurcation. We show that one-dimensional form approximates the cell cycle model around the SNIC bifurcation driven by V_{c2} .

5.2 G2 module: saddle-node bifurcation driven by cell mass

The G2 module consists of differential equations

$$\begin{aligned} \frac{dMPF}{dt} = & k_{m0}Mass - (k_{m2} + k_{m2a}Wee1)MPF \\ & + (k_{m1} + k_{m1a}Cdc25)MPF_P - (k_{m3} + k_{m3a}APC)MPF, \end{aligned} \quad (5.4a)$$

$$\begin{aligned} \frac{dMPF_P}{dt} = & (k_{m2} + k_{m2a}Wee1)MPF - (k_{m1} + k_{m1a}Cdc25)MPF_P \\ & - (k_{m3} + k_{m3a}APC)MPF_P, \end{aligned} \quad (5.4b)$$

$$\begin{aligned} \frac{dWee1}{dt} = & V_{w1} \frac{Wee1_T - Wee1}{J_{w1} + (Wee1_T - Wee1)} \\ & - k_{w2}(MPF + \alpha MPF_P) \frac{Wee1}{J_{w2} + Wee1}, \end{aligned} \quad (5.4c)$$

$$\begin{aligned} \frac{dCdc25}{dt} = & k_{c1}(MPF + \alpha MPF_P) \frac{Cdc25_T - Cdc25}{J_{c1} + (Cdc25_T - Cdc25)} \\ & - V_{c2} \frac{Cdc25}{J_{c2} + Cdc25}, \end{aligned} \quad (5.4d)$$

where variables and parameters are listed in Tables 5.1 and 5.2, respectively. Note that cell mass is a state variable in the cell cycle model (5.1), whereas it is a parameter in the G2 module. Also, variables IE and APC have been set to constant in the G2 module equal to their corresponding value at the $SNIC_{V_{c2}}$ bifurcation point (see equation 5.3), i.e., $IE \approx 0.003287$ and $APC \approx 0.000013$. This choice of constant values will become appropriate and relevant in the following sections.

Figure 5.5 shows the bifurcation diagram for (5.4) with $Mass$ as the bifurcation parameter. The G2 module has up to three steady states: one stable state with low activity of MPF, inactive Cdc25 and active Wee1; one stable steady state with high activity of MPF, active Cdc25 and inactive Wee1; and one intermediate unstable steady state. The lower stable steady state corresponds to G2-phase conditions, while upper the second stable steady state corresponds to M-phase conditions. When $Mass = Mass^* \approx 1.74$, a saddle-node bifurcation occurs: as mass increases through $Mass^*$ the G2-like steady state and the unstable steady state coalesce and disappear, leaving only the M-like steady state. We denote this saddle-node bifurcation as SN_{Mass} . Using numerical continuation, we find the value of this bifurcation point and associated eigenvalues to be

$$Mass^* \approx 1.7465, \quad \begin{bmatrix} MPF^* \\ MPF_P^* \\ Wee1^* \\ Cdc25_P^* \end{bmatrix} \approx \begin{bmatrix} 0.048606 \\ 1.697167 \\ 0.976645 \\ 0.040495 \end{bmatrix}, \quad \vec{\lambda} \approx \begin{bmatrix} 0.000005 \\ -0.200085 \\ -8.896248 \\ -56.244604 \end{bmatrix}. \quad (5.5)$$

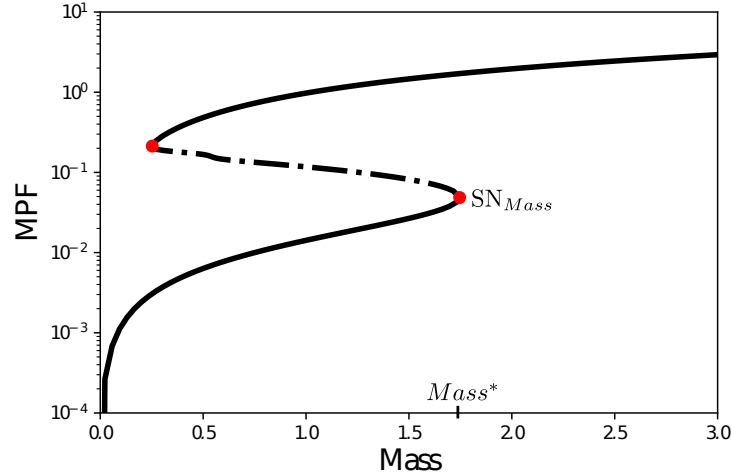


Figure 5.5: Bifurcation diagram of the G2 module (5.4) with mass as varying parameter.

The other saddle-node bifurcation on the left side of the bifurcation diagram does not play a significant role in the G2/M transition and is not considered in this chapter.

Novák and Tyson [72] identified the irreversible transition of the SN_{Mass} with the G2/M transition, which they hypothesize would be driven by the cell mass as more proteins are synthesized and formed, including the cyclin B subunit of MPF. Their hypothesis that cell mass causes cell cycle progression was later supported with experimental results on frog egg extracts [87]. Moreover, Tyson et al. [98] explain that checkpoints in general happen when the associated saddle-node bifurcation no longer occurs (e.g., if the bifurcation point is moved away in one direction).

In this section we focus on the existence of the SN_{Mass} bifurcation found numerically above. In particular, we apply Theorem 4.0.1 and Corollary 4.0.1, regarding saddle-node bifurcations in \mathbb{R}^n , to the G2 module. This allows us to reduce the 4-dimensional system of the G2 module (5.4) into a one-dimensional form in a neighborhood of the SN_{Mass} bifurcation provided the following three conditions hold:

C.1 Singularity condition: the bifurcation point of interest, which must be a steady state, has only one associated zero eigenvalue. We can choose coordinates such that one of the coordinates corresponds to the zero eigenvalue.

C.2 Nondegeneracy condition: in the new coordinates, the quadratic terms in the differential equation corresponding to the zero eigenvalue coordinate do not vanish at the bifurcation point.

C.3 Transversality condition: in the new coordinates, the first derivative of the differential equation corresponding to the zero eigenvalue with respect to the parameter of interest does not vanish at the bifurcation point.

If the conditions above are satisfied, then a saddle-node bifurcation takes place and the differential equation corresponding to the zero eigenvalue can be written in one-dimensional form

$$\dot{\xi} = f_1(\xi; p),$$

where ξ is a linear combination of the variables in the G2 module and function f_1 satisfies $f_1 = D_\xi f_1 = 0$ and $D_{\xi\xi} f_1 \neq 0$ at the bifurcation point.

Our main goal is to verify that the G2 module satisfies each of the conditions above. First, in Section 5.2.1, we translate the system by placing a generic steady state at the origin. Second, in Section 5.2.2, we nondimensionalize the system. Third, in Section 5.2.3, we apply a change of coordinates so that one coordinate corresponds to the zero eigenvalue. Finally, in Section 5.2.4 we verify the conditions in Theorem 4.0.1 and Corollary 4.0.1, which allows us to conclude the existence of the SN_{Mass} bifurcation. Due to the nonlinearity of the system (in particular, equations for Wee1 (5.4c) and Cdc25 (5.4d)) we use a combination of theoretical and numerical results.

5.2.1 Translation of a steady state to the origin

Adopting the short notation $z' = f(z; p)$, where $z \in \mathbb{R}^4$, $p \in \mathbb{R}^{20}$, and f is given by the right-hand side of system (5.4), we denote an equilibrium point as

$$z^* = \begin{bmatrix} MPF^* \\ MPF_P^* \\ Wee1^* \\ Cdc25^* \end{bmatrix}$$

and translate this equilibrium to the origin to write a translated system, i.e.,

$$\widehat{z} = \begin{bmatrix} \widehat{MPF} \\ \widehat{MPF}_P \\ \widehat{Wee1} \\ \widehat{Cdc25} \end{bmatrix} = z - z^* = \begin{bmatrix} MPF - MPF^* \\ MPF_P - MPF_P^* \\ Wee1 - Wee1^* \\ Cdc25 - Cdc25^* \end{bmatrix}, \quad \Rightarrow \quad \widehat{z}' = f(\widehat{z} + z^*, p).$$

Note that z^* depends implicitly on the parameters in the system, including *Mass*. Due to the nonlinearity of the system (in particular in the equations for Wee (5.4c) and Cdc25 (5.4d)), we rely on numerical methods to find the steady states. Also, it is important to mention some relevant properties of the steady states.

Properties of steady states

We look at the intersection of the nullclines (null surfaces) of MPF and MPF_P . Setting $\frac{d}{dt}MPF_P = 0$ in equation (5.4b), we obtain

$$MPF_P = \frac{k_{m2} + k_{m2a}Wee1}{k_{m1} + k_{m1a}Cdc25 + k_{m3}}MPF. \quad (5.6)$$

Similarly, setting $\frac{d}{dt}MPF = 0$ in equation (5.4a), we get

$$(k_{m2} + k_{m2a}Wee1 + k_{m3})MPF - (k_{m1} + k_{m1a}Cdc25)MPF_P = k_{m0}Mass. \quad (5.7)$$

Substituting equation (5.6) into equation (5.7), and we obtain that

$$\frac{k_{m3}(k_{m1} + k_{m1a}Cdc25 + k_{m2} + k_{m2a}Wee1 + k_{m3})}{k_{m1} + k_{m1a}Cdc25 + k_{m3}}MPF = k_{m0}Mass. \quad (5.8)$$

Using equations (5.6) and (5.8), we can solve for MPF and MPF_P in terms of $Wee1$ and $Cdc25$,

$$MPF = \frac{k_{m0}Mass}{k_{m3}} \frac{k_{m1} + k_{m1a}Cdc25 + k_{m3}}{k_{m1} + k_{m1a}Cdc25 + k_{m2} + k_{m2a}Wee1 + k_{m3}}, \quad (5.9)$$

and

$$MPF_P = \frac{k_{m0}Mass}{k_{m3}} \frac{k_{m2} + k_{m2a}Wee1}{k_{m1} + k_{m1a}Cdc25 + k_{m2} + k_{m2a}Wee1 + k_{m3}}. \quad (5.10)$$

At any steady state z^* , equations (5.9) and (5.10) satisfy

$$MPF^* + MPF_P^* = \frac{k_{m0}Mass}{k_{m3}}, \quad (5.11)$$

and

$$\begin{aligned} &MPF^* + \alpha MPF_P^* \\ &= \frac{k_{m0}Mass}{k_{m3}} \frac{k_{m1} + k_{m1a}Cdc25^* + \alpha(k_{m2} + k_{m2a}Wee1^*) + k_{m3}}{k_{m1} + k_{m1a}Cdc25^* + k_{m2} + k_{m2a}Wee1^* + k_{m3}}. \end{aligned} \quad (5.12)$$

The previous two equations will be used later in some calculations.

System after translation

Now we return to the G2 module 5.4 and rewrite it into its translated form

$$\hat{z}' = f(\hat{z} + z^*; p)$$

Using the change of variables $\hat{z} = z - z^*$ and equation (5.4a), we have

$$\begin{aligned} \frac{d\widehat{MPF}}{dt} &= k_{m0}Mass - (k_{m2} + k_{m2a}(\widehat{Wee1} + Wee1^*))(\widehat{MPF} + MPF^*) \\ &\quad + (k_{m1} + k_{m1a}(\widehat{Cdc25} + Cdc25^*))(\widehat{MPF}_P + MPF_P^*) \\ &\quad - k_{m3}(\widehat{MPF} + MPF^*) \\ &= \cancel{k_{m0}Mass} - \cancel{(k_{m2} + k_{m2a}Wee1^* + k_{m3})MPF^*} \\ &\quad + \cancel{(k_{m1} + k_{m1a}Cdc25^*)MPF_P^*} \\ &\quad - (k_{m2} + k_{m2a}Wee1^* + k_{m3})\widehat{MPF} + (k_{m1} + k_{m1a}Cdc25^*)\widehat{MPF}_P \\ &\quad - k_{m2a}MPF^*\widehat{Wee1} + k_{m1a}MPF_P^*\widehat{Cdc25} \\ &\quad - k_{m2a}\widehat{MPF}_P\widehat{Wee1} + k_{m1a}\widehat{MPF}_P\widehat{Cdc25}, \end{aligned}$$

where equation (5.7) has been used to cancel the first three terms. Similarly, using equation (5.4b), we have

$$\begin{aligned} \frac{d\widehat{MPF}_P}{dt} &= (k_{m2} + k_{m2a}(\widehat{Wee1} + Wee1^*))(\widehat{MPF} + MPF^*) \\ &\quad - (k_{m1} + k_{m1a}(\widehat{Cdc25} + Cdc25^*))(\widehat{MPF}_P + MPF_P^*) \\ &\quad - k_{m3}(\widehat{MPF}_P + MPF_P^*) \\ &= \cancel{(k_{m2} + k_{m2a}Wee1^*)MPF^*} - \cancel{(k_{m1} + k_{m1a}Cdc25^* + k_{m3})MPF_P^*} \\ &\quad + (k_{m2} + k_{m2a}Wee1^*)\widehat{MPF} - (k_{m1} + k_{m1a}Cdc25^* + k_{m3})\widehat{MPF}_P \end{aligned}$$

$$k_{m2a}MPF^*\widehat{Wee1} - k_{m1a}MPF_P^*\widehat{Cdc25},$$

where equation (5.7) has been used to cancel the first two terms. The $MPF + \alpha MPF_P$ term in the equations for $Wee1$ (5.4c) and $Cdc25$ (5.4d) can be written as

$$MPF + \alpha MPF_P = MPF^* + \alpha MPF_P^* + \widehat{MPF} + \alpha \widehat{MPF}_P.$$

Thus, the translated G2 module (5.4) becomes

$$\begin{aligned} \frac{d\widehat{MPF}}{dt} &= -(k_{m2} + k_{m2a}Wee1^* + k_{m3})\widehat{MPF} + (k_{m1} + k_{m1a}Cdc25^*)\widehat{MPF}_P \\ &\quad - k_{m2a}MPF^*\widehat{Wee1} + k_{m1a}MPF_P^*\widehat{Cdc25} \\ &\quad - k_{m2a}\widehat{MPF}_P\widehat{Wee1} + k_{m1a}\widehat{MPF}_P\widehat{Cdc25}, \end{aligned} \quad (5.13a)$$

$$\begin{aligned} \frac{d\widehat{MPF}_P}{dt} &= (k_{m2} + k_{m2a}Wee1^*)\widehat{MPF} - (k_{m1} + k_{m1a}Cdc25^* + k_{m3})\widehat{MPF}_P \\ &\quad - k_{m2a}MPF^*\widehat{Wee1} - k_{m1a}MPF_P^*\widehat{Cdc25} \\ &\quad - k_{m2a}\widehat{MPF}_P\widehat{Wee1} - k_{m1a}\widehat{MPF}_P\widehat{Cdc25} \end{aligned} \quad (5.13b)$$

$$\begin{aligned} \frac{d\widehat{Wee1}}{dt} &= V_{w1} \frac{Wee1_T - Wee1^* - \widehat{Wee1}}{J_{w1} + Wee1_T - Wee1^* - \widehat{Wee1}} \\ &\quad - k_{w2}(k_m + \widehat{MPF} + \alpha \widehat{MPF}_P) \frac{Wee1^* + \widehat{Wee1}}{J_{w2} + Wee1^* + \widehat{Wee1}}, \end{aligned} \quad (5.13c)$$

$$\begin{aligned} \frac{d\widehat{Cdc25}}{dt} &= k_{c1}(k_m + \widehat{MPF} + \alpha \widehat{MPF}_P) \frac{Cdc25_T - Cdc25^* - \widehat{Cdc25}}{J_{c1} + Cdc25_T - Cdc25^* - \widehat{Cdc25}} \\ &\quad - V_{c2} \frac{Cdc25^* + \widehat{Cdc25}}{J_{c2} + Cdc25^* + \widehat{Cdc25}}. \end{aligned} \quad (5.13d)$$

where

$$k_m = MPF^* + \alpha MPF_P^*$$

$$= \frac{k_{m0}Mass k_{m1} + k_{m1a}Cdc25^* + \alpha(k_{m2} + k_{m2a}Wee1^*) + k_{m3}}{k_{m3} k_{m1} + k_{m1a}Cdc25^* + k_{m2} + k_{m2a}Wee1^* + k_{m3}}. \quad (5.14)$$

Note that the last equality comes from equation (5.12) and the origin is now a steady state, denoted $\widehat{z}^* = 0$, for the translated system (5.13).

5.2.2 Nondimensionalization and approximation

To simplify our calculations, we nondimensionalize the translated G2 module (5.13) using the following transformation

$$x = \widehat{MPF}, \quad y = \widehat{MPFP}, \quad w = \frac{\widehat{Wee1}}{\widehat{Wee1}_T}, \quad u = \frac{\widehat{Cdc25}}{\widehat{Cdc25}_T}, \quad \tau = k_{m3}t. \quad (5.15)$$

Taking the derivative of x with respect to τ , we obtain

$$x' = \frac{d\widehat{MPF}}{dt} \frac{dt}{d\tau} = \frac{1}{k_{m3}} \frac{d\widehat{MPF}}{dt}.$$

Similarly,

$$y' = \frac{1}{k_{m3}} \frac{d\widehat{MPFP}}{dt}, \quad w' = \frac{1}{k_{m3}} \frac{d\widehat{Wee1}}{dt}, \quad u' = \frac{1}{k_{m3}} \frac{d\widehat{Cdc25}}{dt}.$$

After dividing every equation in (5.13) by k_{m3} , the translated and nondimensionalized G2 module becomes

$$x' = -(1+a)x + by - cw + du - \kappa_w xw + \kappa_u yu, \quad (5.16a)$$

$$y' = ax - (1+b)y + cw - du + \kappa_w xw - \kappa_u yu, \quad (5.16b)$$

$$w' = \beta_w \frac{1 - w^* - w}{\epsilon_1 + 1 - w^* - w} - \gamma_w (k_m + x + \alpha y) \frac{w^* + w}{\epsilon_2 + w^* + w}, \quad (5.16c)$$

$$u' = \gamma_u (k_m + x + \alpha y) \frac{1 - u^* - u}{\epsilon_3 + 1 - u^* - u} - \beta_u \frac{u^* + u}{\epsilon_4 + u^* + u}, \quad (5.16d)$$

where

$$\begin{aligned}
k_m &= MPF^* + \alpha MPF_P^*, \\
a &= \frac{k_{m2} + k_{m2a} Wee1^*}{k_{m3}}, \quad b = \frac{k_{m1} + k_{m1a} Cdc25^*}{k_{m3}}, \\
c &= \frac{k_{m2a} MPF^* Wee1_T}{k_{m3}}, \quad d = \frac{k_{m1a} MPF_P^* Cdc25_T}{k_{m3}}, \\
\kappa_w &= \frac{k_{m2a} Wee1_T}{k_{m3}}, \quad \kappa_u = \frac{k_{m1a} Cdc25_T}{k_{m3}}, \\
\beta_w &= \frac{V_{w1}}{k_{m3} Wee1_T}, \quad \gamma_w = \frac{k_{w2}}{k_{m3} Wee1_T}, \quad w^* = \frac{Wee1^*}{Wee1_T}, \\
\gamma_u &= \frac{k_{c1}}{k_{m3} Cdc25_T}, \quad \beta_u = \frac{V_{c2}}{k_{m3} Cdc25_T}, \quad u^* = \frac{Cdc25^*}{Cdc25_T}, \\
\epsilon_1 &= \frac{J_{w1}}{Wee1_T}, \quad \epsilon_2 = \frac{J_{w2}}{Wee1_T}, \quad \epsilon_3 = \frac{J_{c1}}{Cdc25_T}, \quad \epsilon_4 = \frac{J_{c2}}{Cdc25_T}.
\end{aligned} \tag{5.17}$$

The nonlinear functions associated with the Goldbeter-Koshland kinetics (in the equations for w and u) complicate any theoretical analysis on the system, but now that we have shifted the coordinates to a steady state, we can write an approximation of the system for small values of w and u . Using the power series expansion (5.48) (see Appendix 5.A), we write the second-order approximation of the normalized G2 module (5.16) for small values of x , y , w , and u , given by

$$x' = -(1 + a)x + by - cw + du - \kappa_w xw + \kappa_u yu, \tag{5.18a}$$

$$y' = ax - (1 + b)y + cw - du + \kappa_w xw - \kappa_u yu, \tag{5.18b}$$

$$w' = B_0 - Dx - \alpha Dy - Bw - D_2 xw - \alpha D_2 yw + B_2 w^2 + \text{h.o.t.}, \tag{5.18c}$$

$$u' = C_0 + Ex + \alpha Ey - Cu - E_2 xw - \alpha E_2 yw + C_2 w^2 + \text{h.o.t.}, \tag{5.18d}$$

where

$$\begin{aligned}
B_0 &= \frac{\beta_w(1-w^*)}{\epsilon_1+1-w^*} - \frac{\gamma_w k_m w^*}{\epsilon_2+w^*}, & B &= \frac{\beta_w \epsilon_1}{(\epsilon_1+1-w^*)^2} + \frac{\gamma_w k_m \epsilon_2}{(\epsilon_2+w^*)^2}, \\
B_2 &= -\frac{\beta_w \epsilon_1}{(\epsilon_1+1-w^*)^3} + \frac{\gamma_w k_m \epsilon_2}{(\epsilon_2+w^*)^3}, \\
D &= \frac{\gamma_w w^*}{\epsilon_2+w^*}, & D_2 &= \frac{\gamma_w w^*}{(\epsilon_2+w^*)^2}, \\
C_0 &= \frac{\gamma_u k_m(1-u^*)}{\epsilon_3+1-u^*} - \frac{\beta_u u^*}{\epsilon_4+u^*}, & C &= \frac{\gamma_u k_m \epsilon_3}{(\epsilon_3+1-u^*)^2} + \frac{\beta_u \epsilon_4}{(\epsilon_4+u^*)^2}, \\
C_2 &= \frac{\gamma_u k_m \epsilon_3}{(\epsilon_3+1-u^*)^3} + \frac{\beta_u \epsilon_4}{(\epsilon_4+u^*)^3}, \\
E &= \frac{\gamma_u(1-u^*)}{\epsilon_3+1-u^*}, & E_2 &= \frac{\gamma_u(1-u^*)}{(\epsilon_3+1-u^*)^2}.
\end{aligned} \tag{5.19}$$

Adopting the short notation $\tilde{z}' = \tilde{f}(\tilde{z}; p)$ for the nondimensionalized G2 module (5.16), the Jacobian matrix at the steady state $\tilde{z} = 0$ can be easily found from its second-order approximation (5.18)

$$J = D_{\tilde{z}} \tilde{f} \Big|_{\tilde{z}=0} = \begin{pmatrix} -(1+a) & b & -c & d \\ a & -(1+b) & c & -d \\ -D & -\alpha D & -B & 0 \\ E & \alpha E & 0 & -C \end{pmatrix}.$$

The characteristic polynomial of J is

$$P_J(\lambda) = \det(\lambda I - J) = \begin{vmatrix} \lambda + 1 + a & -b & c & -d \\ -a & \lambda + 1 + b & -c & d \\ D & \alpha D & \lambda + B & 0 \\ -E & -\alpha E & 0 & \lambda + C \end{vmatrix}$$

$$\begin{aligned}
&= \begin{vmatrix} \lambda + 1 + a & -b & c & -d \\ \lambda + 1 & \lambda + 1 & 0 & 0 \\ D & \alpha D & \lambda + B & 0 \\ -E & -\alpha E & 0 & \lambda + C \end{vmatrix} \\
&= \begin{vmatrix} \lambda + A & -b & c & -d \\ 0 & \lambda + 1 & 0 & 0 \\ (1 - \alpha)D & \alpha D & \lambda + B & 0 \\ -(1 - \alpha)E & -\alpha E & 0 & \lambda + C \end{vmatrix} \\
&= (\lambda + 1) [(\lambda + A)(\lambda + B)(\lambda + C) \\
&\quad - (1 - \alpha)(cD(\lambda + C) + dE(\lambda + B))],
\end{aligned}$$

where

$$A = 1 + a + b \quad (5.20)$$

For the zero eigenvalue singularity condition **C.1**, we require the characteristic polynomial above to be zero when $\lambda = 0$, i.e.,

$$P_J(0) = 0 \iff ABC = (1 - \alpha)(cCD + bBE). \quad (5.21)$$

We can verify that the singularity condition above holds for the bifurcation point $(z_{SN}^*; p^*)$ found numerically in (5.5). Indeed, using parameter definitions (5.17), (5.19) and (5.20), we obtain

$$313361.4433 \approx ABC = (1 - \alpha)(cCD + bBE) \approx 313362.2906 ,$$

which reflects a relative error with a magnitude of 10^{-5} . This error is due to the fact

that $(z_{SN}^*; p^*)$ is found numerically.

Using the zero eigenvalue singularity condition (5.21), the characteristic polynomial becomes

$$\begin{aligned}
P_J(\lambda) &= (\lambda + 1) [(\lambda + A)(\lambda + B)(\lambda + C) \\
&\quad - (1 - \alpha)(cD(\lambda + C) + dE(\lambda + B))] \\
&= (\lambda + 1) [\lambda^3 + (A + B + C)\lambda^2 + (AB + BC + CA)\lambda + ABC \\
&\quad - (1 - \alpha)(cD + dE)\lambda - \cancel{(1 - \alpha)(cDC + dEB)}] \\
&= \lambda(\lambda + 1) [\lambda^2 + (A + B + C)\lambda \\
&\quad + AB + BC + CA - (1 - \alpha)(cD + dE)],
\end{aligned}$$

Thus, the eigenvalues are given by

$$\lambda_1 = 0, \quad \lambda_2 = -1, \quad \lambda_{\pm} = \frac{-(A + B + C) \pm \sqrt{F}}{2},$$

where

$$F = (A + B + C)^2 - 4(AB + BC + CA) + 4(1 - \alpha)(cD + dE). \quad (5.22)$$

Using parameter definitions (5.17) and (5.19) and multiplying by the scaling factor $\frac{d\tau}{dt} = k_{m3} = 0.2$, we verify that the eigenvalues match the ones found numerically in (5.5)

$$\begin{aligned}
k_{m3}\lambda_1 &= 0, \\
k_{m3}\lambda_2 &= k_{m3}(-1) = -0.2, \\
k_{m3}\lambda_+ &= k_{m3} \frac{-(A + B + C) + \sqrt{F}}{2} = -8.8962,
\end{aligned}$$

$$k_{m3}\lambda_- = k_{m3} \frac{-(A+B+C) - \sqrt{F}}{2} = -56.2445.$$

For the single zero eigenvalue singularity condition **C.1**, we require that eigenvalues λ_+ and λ_- are real. This is true if F , defined in equation 5.22, is greater than 0, i.e.,

$$(A+B+C)^2 + 4(1-\alpha)(cD+dE) > 4(AB+BC+CA) > 0. \quad (5.23)$$

Note that these eigenvalues are negative if $(A+B+C)^2 > F$, i.e.,

$$(1-\alpha)(cD+dE) < AB+BC+CA. \quad (5.24)$$

The previous two equations provide conditions for negative real eigenvalues λ_+ and λ_- .

5.2.3 Change of coordinates

In this section, we apply the standard results on a saddle-node bifurcation in \mathbb{R}^n given by Theorem 4.0.1 and Corollary 4.0.1 in Chapter 4. These results required a change of coordinates that places one variable in the single zero eigenvalue. The standard method to find such change of coordinates is to find the eigenvectors, write the invertible matrix P of diagonalization, invert it, and define the new coordinates as $\zeta = P^{-1}\tilde{z}$. Unfortunately, the explicit inversion of this matrix P is too complicated. Instead, we propose the following change of coordinates that is not the canonical transformation, yet satisfies the conditions of Theorem 4.0.1

$$\xi = (aBC - cCD - dBE)x + ((1+a)BC - cCD - dBE)y$$

$$+ cCw - dBu, \quad (5.25a)$$

$$\psi = x + y, \quad (5.25b)$$

$$\begin{aligned} \omega &= (aBC - cCD - dBE)Gx + ((1 + a)BC - cCD - dBE)Gy \\ &\quad + (1 + cCG)w - dBGu, \end{aligned} \quad (5.25c)$$

$$\begin{aligned} v &= (aBC - cCD - dBE)Hx + ((1 + a)BC - cCD - dBE)Hy \\ &\quad + cCHw + (1 - dBH)u. \end{aligned} \quad (5.25d)$$

where

$$\begin{aligned} G &= \frac{(1 - \alpha)CD}{B^2C^2 - (1 - \alpha)(cC^2D - dB^2E)}, \\ H &= \frac{(1 - \alpha)BE}{B^2C^2 - (1 - \alpha)(cC^2D - dB^2E)}, \end{aligned} \quad (5.26)$$

and the following inequality holds

$$B^2C^2 - (1 - \alpha)(cC^2D - dB^2E) \neq 0. \quad (5.27)$$

The change of variables (5.25) is motivated from the calculations to obtain the eigenvectors, i.e., from the elementary row operations necessary to solve $(\lambda I - J)\mathbf{v} = \mathbf{v}$ for $\mathbf{v} \neq 0$ (calculations not shown here).

Constants G and H are the solution to the following equations

$$\begin{aligned} (1 - \alpha) \frac{BC - cCG - dBH}{BC} D + BG &= 0, \\ -(1 - \alpha) \frac{BC - cCG - dBH}{BC} E + CH &= 0, \end{aligned} \quad (5.28)$$

assuming (5.27) holds. These equations are the result of forcing the linear terms in the dervative of (5.25) to have the same structure as the linear terms in equation

(4.4) in the statement of Theorem 4.0.1, i.e., forcing that the linear terms in the derivatives of ω and v do not depend on ξ . In fact, equations (5.25c) and (5.25c) are the result of choosing $\omega = G\xi + w$ and $v = H\xi + u$, respectively. At the end of this section, we will see how enforcing the linear structure mentioned above results in equation (5.28).

The corresponding inverse transformation of the change of coordinates 5.25 is

$$x = -\frac{BC - cCG - dBH}{BC}\xi + \frac{(1+a)BC - cCD - dBE}{BC}\psi + \frac{c}{B}\omega - \frac{d}{C}v, \quad (5.29a)$$

$$y = \frac{BC - cCG - dBH}{BC}\xi - \frac{aBC - cCD - dBE}{BC}\psi - \frac{c}{B}\omega + \frac{d}{C}v, \quad (5.29b)$$

$$w = -G\xi + \omega, \quad (5.29c)$$

$$u = -H\xi + v. \quad (5.29d)$$

Taking derivatives of equation (5.25b), we have

$$\begin{aligned} \psi' &= x' + y' = -(1+a)x + by - cw + du - \kappa_w xw + \kappa_u yu \\ &\quad + ax - (1+b)y + cw - du + \kappa_w xw - \kappa_u yu \\ &= -(x + y) = -\psi. \end{aligned}$$

Equation (5.25a) can be written as

$$\xi = BCy + cCw - dBu + (aBC - cCD - dBE)\psi.$$

Differentiating and using equations (5.16b) and (5.18), we obtain

$$\xi' = BCy' + cCw' - dBu' + (aBC - cCD - dBE)\psi'$$

$$\begin{aligned}
&= aBC\bar{x} - (1+b)BCy + cBC\bar{w} - dBC\bar{u} + \kappa_w BCxw + \kappa_u BCyu \\
&\quad + cCB_0 - cC\bar{D}x - \alpha cCDy - cCB\bar{w} \\
&\quad\quad - cCD_2xw - \alpha cCD_2yw + cCB_2w^2 + \text{h.o.t.} \\
&\quad - dBC_0 - dBE\bar{x} - \alpha dBEy + dBC\bar{u} \\
&\quad\quad + dBE_2xu + \alpha dBEyu - dBC_2u^2 + \text{h.o.t.} \\
&\quad + (-aBC + cCD + dBE)x + (-aBC + cCD + dBE)y \\
&= cCB_0 - dBC_0 \\
&\quad + (-ABC + (1-\alpha)(cCD - dBE))y \\
&\quad\quad + (\kappa_w BC - cCD_2)xw + dBE_2xu - \alpha cCD_2yw \\
&\quad\quad + (\kappa_u BC + \alpha dBE_2)yu + cCB_2w^2 - dBC_2u^2 + \text{h.o.t.}
\end{aligned}$$

Note that, at the bifurcation point SN_{Mass} , the constant multiplying y cancels by the zero eigenvalue condition (5.21). Substituting x , y , w , and u , according to the inverse transformation (5.29), and discarding all quadratic and higher order terms except those of the form ξ^2 , we obtain

$$\begin{aligned}
\xi' &= cCB_0 - dBC_0 \\
&\quad + (-ABC + (1-\alpha)(cCD - dBE)) \\
&\quad \times \left(\frac{BC - cCG - dBH}{BC} \xi - \frac{aBC - cCD - dBE}{BC} \psi - \frac{c}{B} \omega + \frac{d}{C} v \right) \\
&\quad\quad + (\kappa_w BC - cCD_2) \frac{BC - cCG - dBH}{BC} G \xi^2 \\
&\quad\quad + dBE_2 \frac{BC - cCG - dBH}{BC} H \xi^2 \\
&\quad\quad + \alpha cCD_2 \frac{BC - cCG - dBH}{BC} G \xi^2 \\
&\quad\quad - (\kappa_u BC + \alpha dBE_2) \frac{BC - cCG - dBH}{BC} H \xi^2
\end{aligned}$$

$$\begin{aligned}
& + cCB_2G^2\xi^2 - bBC_2H^2\xi^2 + \text{other quadratic terms} + \text{h.o.t.} \\
= & cCB_0 - dBC_0 \\
& + (-ABC + (1 - \alpha)(cCD - dBE)) \\
& \times \left(\frac{BC - cCG - dBH}{BC} \xi - \frac{aBC - cCD - dBE}{BC} \psi - \frac{c}{B} \omega + \frac{d}{C} v \right) \\
& + (\kappa_w BC - (1 - \alpha)cCD_2) \frac{BC - cCG - dBH}{BC} G\xi^2 \\
& - (\kappa_u BC - (1 - \alpha)dBE_2) \frac{BC - cCG - dBH}{BC} H\xi^2 \\
& + cCB_2G^2\xi^2 - bBC_2H^2\xi^2 + \text{other quadratic terms} + \text{h.o.t.}
\end{aligned}$$

From equation (5.29c) we know that

$$\omega = w + G\xi,$$

whose derivative, using equation (5.18c) up to linear terms, is

$$\begin{aligned}
\omega' & = w' + G\xi' \\
& = B_0 - Dx - \alpha Dy - Bw + \text{h.o.t.} \\
& + G(cCB_0 - dBC_0) \\
& + G(-ABC + (1 - \alpha)(cCD - dBE)) \\
& \times \left(\frac{BC - cCG - dBH}{BC} \xi - \frac{aBC - cCD - dBE}{BC} \psi - \frac{c}{B} \omega + \frac{d}{C} v \right) \\
& + \text{h.o.t.} \\
= & B_0 + G(cCB_0 - dBC_0) \\
& + G(-ABC + (1 - \alpha)(cCD - dBE)) \\
& \times \left(\frac{BC - cCG - dBH}{BC} \xi - \frac{aBC - cCD - dBE}{BC} \psi - \frac{c}{B} \omega + \frac{d}{C} v \right)
\end{aligned}$$

$$\begin{aligned}
& + \frac{BC - cCG - dBH}{BC} D\xi - \frac{(1+a)BC - cCD - dBE}{BC} D\psi \\
& \quad - \frac{cD}{B}\omega + \frac{dD}{C}v \\
& - \alpha \frac{BC - cCG - dBH}{BC} D\xi + \alpha \frac{(1+a)BC - cCD - dBE}{BC} D\psi \\
& \quad + \alpha \frac{cD}{B}\omega - \alpha \frac{dD}{C}v \\
& + BG\xi - B\omega + \text{h.o.t.} \\
= & B_0 + G(cCB_0 - dBC_0) \\
& + G(-ABC + (1-\alpha)(cCD - dBE)) \\
& \quad \times \left(\frac{BC - cCG - dBH}{BC} \xi - \frac{aBC - cCD - dBE}{BC} \psi - \frac{c}{B}\omega + \frac{d}{C}v \right) \\
& + \left((1-\alpha) \frac{BC - cCG - dBH}{BC} D + BG \right) \xi \\
& - \left((1-\alpha) \frac{aBC - cCD - dBE}{BC} D + D \right) \psi \\
& - \left((1-\alpha) \frac{cD}{B} + B \right) \omega + (1-\alpha) \frac{dD}{C} v + \text{h.o.t.}
\end{aligned}$$

Finally, from equation (5.29d) we know that

$$v = u + H\xi,$$

whose derivative, using equation (5.18d) and up to linear terms, is

$$\begin{aligned}
v' & = u' + H\xi' \\
& = C_0 - Ex - \alpha Ey - Cw + \text{h.o.t.} \\
& + H(cCB_0 - dBC_0) \\
& + H(-ABC + (1-\alpha)(cCD - dBE)) \\
& \quad \times \left(\frac{BC - cCG - dBH}{BC} \xi - \frac{aBC - cCD - dBE}{BC} \psi - \frac{c}{B}\omega + \frac{d}{C}v \right)
\end{aligned}$$

$$\begin{aligned}
& + \text{h.o.t.} \\
= & C_0 + H(cCB_0 - dBC_0) \\
& + H(-ABC + (1 - \alpha)(cCD - dBE)) \\
& \times \left(\frac{BC - cCG - dBH}{BC} \xi - \frac{aBC - cCD - dBE}{BC} \psi - \frac{c}{B} \omega + \frac{d}{C} v \right) \\
& - \frac{BC - cCG - dBH}{BC} E \xi + \frac{(1 + a)BC - cCD - dBE}{BC} E \psi \\
& \quad - \frac{cE}{B} \omega + \frac{dE}{C} v \\
& + \alpha \frac{BC - cCG - dBH}{BC} E \xi - \alpha \frac{(1 + a)BC - cCD - dBE}{BC} E \psi \\
& \quad + \alpha \frac{cE}{B} \omega - \alpha \frac{dE}{C} v \\
& + CH\xi - Cv + \text{h.o.t.} \\
= & C_0 + H(cCB_0 - dBC_0) \\
& + H(-ABC + (1 - \alpha)(cCD - dBE)) \\
& \times \left(\frac{BC - cCG - dBH}{BC} \xi - \frac{aBC - cCD - dBE}{BC} \psi - \frac{c}{B} \omega + \frac{d}{C} v \right) \\
& - \left((1 - \alpha) \frac{BC - cCG - dBH}{BC} E - CH \right) \xi \\
& + \left((1 - \alpha) \frac{aBC - cCD - dBE}{BC} E + E \right) \psi \\
& - (1 - \alpha) \frac{cE}{B} \omega + \left((1 - \alpha) \frac{dE}{C} - C \right) v + \text{h.o.t.}
\end{aligned}$$

Summarizing, the G2 module in the new coordinates becomes

$$\begin{aligned}
\xi' = & cCB_0 - dBC_0 \\
& + (-ABC + (1 - \alpha)(cCD - dBE)) \\
& \times \left(\frac{BC - cCG - dBH}{BC} \xi - \frac{aBC - cCD - dBE}{BC} \psi - \frac{c}{B} \omega + \frac{d}{C} v \right) \\
& + (\kappa_w BC - (1 - \alpha)cCD_2) \frac{BC - cCG - dBH}{BC} G \xi^2
\end{aligned}$$

$$\begin{aligned}
& - (\kappa_u BC - (1 - \alpha)dBE_2) \frac{BC - cCG - dBH}{BC} H\xi^2 \\
& + cCB_2G^2\xi^2 - bBC_2H^2\xi^2 + \text{o.q.t.} + \text{h.o.t.}, \tag{5.30a}
\end{aligned}$$

$$\psi' = -\psi, \tag{5.30b}$$

$$\begin{aligned}
\omega' &= B_0 + G(cCB_0 - dBC_0) \\
& + G(-ABC + (1 - \alpha)(cCD - dBE)) \\
& \times \left(\frac{BC - cCG - dBH}{BC} \xi - \frac{aBC - cCD - dBE}{BC} \psi - \frac{c}{B} \omega + \frac{d}{C} v \right) \\
& + \left((1 - \alpha) \frac{BC - cCG - dBH}{BC} D + BG \right) \xi \\
& - \left((1 - \alpha) \frac{aBC - cCD - dBE}{BC} D + D \right) \psi \\
& - \left((1 - \alpha) \frac{cD}{B} + B \right) \omega + (1 - \alpha) \frac{dD}{C} v + \text{h.o.t.}, \tag{5.30c}
\end{aligned}$$

$$\begin{aligned}
v' &= C_0 + H(cCB_0 - dBC_0) \\
& + H(-ABC + (1 - \alpha)(cCD - dBE)) \\
& \times \left(\frac{BC - cCG - dBH}{BC} \xi - \frac{aBC - cCD - dBE}{BC} \psi - \frac{c}{B} \omega + \frac{d}{C} v \right) \\
& - \left((1 - \alpha) \frac{BC - cCG - dBH}{BC} E - CH \right) \xi \\
& + \left((1 - \alpha) \frac{aBC - cCD - dBE}{BC} E + E \right) \psi \\
& - (1 - \alpha) \frac{cE}{B} \omega + \left((1 - \alpha) \frac{dE}{C} - C \right) v + \text{h.o.t.} \tag{5.30d}
\end{aligned}$$

Now, referring back to equations (5.28), these equations come from forcing the fourth term in equations (5.30c) and (5.30d) to vanish. As per the third term in equations (5.30c) and (5.30d) they must vanish since the zero eigenvalue condition **C.1** (guaranteed by equation (5.21)) implies that the linear term (second term) in equation (5.30a) vanishes. Thus, all ξ -linear terms in equations (5.30b) and (5.30d) vanish.

Equation (5.30a) is almost the one-dimensional form we are looking for. We still have to apply Theorem 4.0.1 to the whole system (5.30) and rewrite equation (5.30a) depending only on ξ .

5.2.4 Reduction to one-dimensional form

The original version of G2 module (5.4) has precisely one zero eigenvalue if equation (5.21),

$$ABC = (1 - \alpha)(cCD + dBE),$$

and inequality (5.23),

$$(A + B + C)^2 + 4(1 - \alpha)(cD + dE) > 4(AB + BC + CA),$$

hold, where the constants therein are defined by (5.17), (5.19), and (5.20). The change of coordinates (5.25) transforms the G2 module into system (5.30). The zero eigenvalue condition implies that the terms of the form

$$\begin{aligned} & (-ABC + (1 - \alpha)(cCD - dBE)) \\ & \times \left(\frac{BC - cCG - dBH}{BC} \xi - \frac{aBC - cCD - dBE}{BC} \psi - \frac{c}{B} \omega + \frac{d}{C} v \right) \end{aligned}$$

in system (5.30) vanish. Equations (5.28) imply that the ξ -linear terms in equations (5.30c) and (5.30d) vanish.

Let $\phi = (\psi, \omega, v)$, $\zeta = (\xi, \phi)$, $g_1(\xi, \phi; p)$ defined by the right-hand side of equation (5.30a), M defined by the linear terms in the right-hand side of equations

(5.30b)–(5.30d)

$$M = \begin{bmatrix} -1 & 0 & 0 \\ -(1-\alpha)\frac{aBC-cCD-dBE}{BC}D - D & -(1-\alpha)\frac{cD}{B} - B & (1-\alpha)\frac{dD}{C} \\ (1-\alpha)\frac{aBC-cCD-dBE}{BC}E + E & -(1-\alpha)\frac{cE}{B} & (1-\alpha)\frac{dE}{C} - C \end{bmatrix},$$

$g_2(\xi, \phi; p)$ defined by the remaining terms in the right-hand side of equations (5.30b)–(5.30d), and $g = (g_1, g_2)$. Then, the G2 module in the new coordinates (5.30) is written

$$\xi' = g_1(\xi, \phi; p),$$

$$\phi' = M\phi + g_2(\xi, \phi; p).$$

At $(\xi, \phi; p) = (0, 0; p^*)$, where $Mass = Mass^*$ at p^* , we have $B_0 = C_0 = 0$ so that $g(0, 0; p^*) = 0$, by construction. Also, $D_\zeta g(0, 0; p^*) = 0$, by construction. If inequality (5.27),

$$B^2C^2 - (1-\alpha)(cC^2D - dB^2E) \neq 0,$$

holds, then M is invertible. This construction guaranties that singularity condition **C.1** is satisfied.

From equation (5.30a), we have

$$\begin{aligned} \sigma_0 = D_{\xi\xi}g_1(\xi, \phi, p^*) &= \frac{BC - cCG - dBH}{BC} \\ &\times ((\kappa_w BC - (1-\alpha)cCD_2)G - (\kappa_u BC - (1-\alpha)dBE_2)H) \\ &\quad + cCB_2G^2 - bBC_2H^2. \end{aligned} \quad (5.31)$$

Note that the transversality condition **C.3** holds since

$$D_{Mass}g_1(0, 0; p^*) = D_{Mass}f(z_{SN}^*; p^*) = k_{m0} \neq 0.$$

If the nondegeneracy conditions **C.2** is satisfied, i.e.,

$$\sigma_0 \neq 0, \tag{5.32}$$

then, by Theorem **4.0.1** and Corollary **4.0.1**, there is a SN_{Mass} bifurcation that takes place when $Mass$ crosses $Mass^*$. Moreover, there is a neighbourhood of $(\xi, p) = (0, p^*)$ where there exists a unique function $\phi = \eta(\xi; p)$ such that $0 = \eta(0; p^*)$. Function $\eta(\xi; p)$ must not have constant terms or terms of the form ξ^{-n} (for $n \geq 0$), otherwise the condition $0 = \eta(0; p^*)$ is not satisfied. Thus, we can assume this function has a polynomial form

$$\phi = \eta(\xi; p) = \begin{bmatrix} \eta_{11}\xi + \eta_{12}\xi^2 + \dots \\ \eta_{21}\xi + \eta_{22}\xi^2 + \dots \\ \eta_{31}\xi + \eta_{32}\xi^2 + \dots \end{bmatrix},$$

in which case we can collect all the quadratic terms in the right-hand side of **(5.30a)** and reduce the G2 module to one-dimensional form

$$\xi' = g_1(\xi, \eta(\xi; p); p) = (cCB_0 - dBC_0) + \sigma\xi^2, \tag{5.33}$$

where $\sigma = \sigma_0 + \sigma_1$ is the sum of the terms of the form ξ^2 (i.e., σ_0) and other quadratic terms of the form $\eta(\xi; p)\xi$ and $(\eta(\xi; p))^2$.

Although the nondegeneracy **(5.32)** can be easily verified numerically by com-

puting

$$\sigma_0 \approx 14974232.7882 \neq 0, \quad (5.34)$$

it is far more difficult to verify this condition theoretically.

5.3 G2 module with variable cell mass: saddle-node bifurcation driven by V_{c2}

In this section, we study the extended G2 module where the parameter $Mass$ is transformed into a state variable. The equations are

$$\begin{aligned} \frac{dMPF}{dt} &= k_{m0}Mass - (k_{m2} + k_{m2a}Wee1)MPF \\ &\quad + (k_{m1} + k_{m1a}Cdc25)MPF_P - k_{m3}MPF, \end{aligned} \quad (5.35a)$$

$$\begin{aligned} \frac{dMPF_P}{dt} &= (k_{m2} + k_{m2a}Wee1)MPF - (k_{m1} + k_{m1a}Cdc25)MPF_P \\ &\quad - k_{m3}MPF_P, \end{aligned} \quad (5.35b)$$

$$\begin{aligned} \frac{dWee1}{dt} &= V_{w1} \frac{Wee1_T - Wee1}{J_{w1} + (Wee1_T - Wee1)} \\ &\quad - k_{w2}(MPF + \alpha MPF_P) \frac{Wee1}{J_{w2} + Wee1}, \end{aligned} \quad (5.35c)$$

$$\begin{aligned} \frac{dCdc25}{dt} &= k_{c1}(MPF + \alpha MPF_P) \frac{Cdc25_T - Cdc25}{J_{c1} + (Cdc25_T - Cdc25)} \\ &\quad - V_{c2} \frac{Cdc25}{J_{c2} + Cdc25}, \end{aligned} \quad (5.35d)$$

$$\frac{dMass}{dt} = \mu Mass \left(1 - \frac{Mass}{K_{Mass}} \right), \quad (5.35e)$$

According to Proposition 4.2.1, we need to show that the nonsingularity condition (4.19) and the transversality condition (4.20) are satisfied in order to prove the existence of a saddle-node bifurcation driven by V_{c2} in the extended G2 module

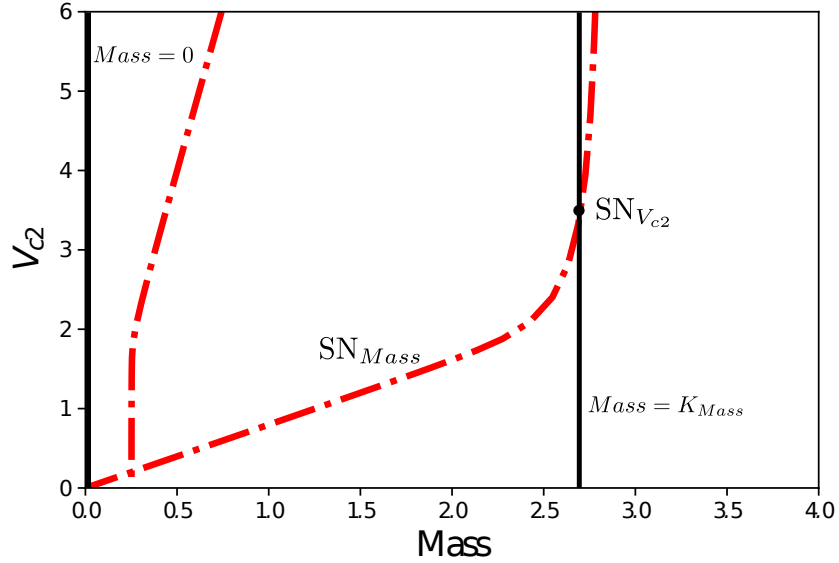


Figure 5.6: Two-parameter bifurcation diagram for the G2 module (5.4) with mass and V_{c2} as bifurcation parameters. The bifurcation curve on the right follows the SN_{Mass} studied in Section 5.2. The nullclines of cell mass (equation (5.35e)) have been superimposed on the diagram. A saddle-node bifurcation is created when the nullcline corresponding to $Mass = K_{Mass}$ is transverse to the SN_{Mass} bifurcation curve. The bifurcation diagram in Figure 5.5 corresponds to a horizontal cross section here when $V_{c2} = 1.4$.

(5.35). According to Proposition 4.2.2, these conditions can be verified graphically by superimposing the nullcline of equation (5.35e) onto the corresponding two-parameter bifurcation diagram for the G2 module (5.4). This bifurcation diagram is shown in Figure 5.6, where we verify that 1) the $Mass$ -nullcline of equation (5.35e) intersects transversally the two-parameter bifurcation curve that follows the SN_{Mass} bifurcation, and 2) the tangent line to the $Mass$ -nullcline of (5.35e) is not parallel the $Mass$ -axis at the intersection. Thus, the extended G2 module (5.35) has a saddle-node bifurcation at the intersection as V_{c2} crosses the bifurcation value V_{c2}^* . We denote this saddle-node bifurcation as $\text{SN}_{V_{c2}}$.

Recall from Section 5.2 that the G2 module (5.4) is reduced to a one-dimensional

form (5.33) around the SN_{Mass} bifurcation for a small ξ . Note that this one-dimensional reduction is valid for a generic SN_{Mass} bifurcation point $(z_{SN}^*; p^*)$, since the calculations are given implicitly in term of the steady states. In particular, it is valid at the intersection of the two-parameter bifurcation curve and the nullcline of g where $Mass = K_{Mass}$. In order to find the normal form for the extended G2 Module (5.35), we still need to consider the contribution of the differential equation for $Mass$ to the one-dimensional form. This can be done through one of two methods: 1) applying Theorem 4.0.1 to the G2 module with variable mass (5.35) analogous to the approach taken in Section 5.2, or 2) taking the one-dimensional reduction of the G2 module, extending it by transforming $Mass$ into variable, and applying Proposition 4.2.1 to this extended model to reduce it to a one dimensional form. Note that the second method is possible because $g(Mass)$ does not depend on any of the other state variables (MPF , etc.). In order to avoid repeating the long calculations carried out in Section 5.2, we apply here the second method.

We rewrite the one-dimensional form (5.33) as

$$f(\xi; Mass, V_{c2}) = (cCB_0 - dBC_0) + \sigma\xi^2,$$

where only the parameters $Mass$ and V_{c2} are considered explicitly for simplicity. By Proposition 4.1.1, there is a unique function $Mass = \nu(V_{c2})$ such that we can reduce the extended G2 module (where mass is a variable) to

$$\xi' = f(\xi + \frac{a}{b}(\nu(V_{c2}) - Mass^*), \nu(V_{c2}); V_{c2}) - \frac{a}{b}g(\nu(V_{c2}); V_{c2}), \quad (5.36)$$

(recall that the nondimensionalized system has a bifurcation point at $(x, y; p) =$

$(0, 0; p^*)$), where

$$b = D_{Mass}g(K_{Mass}; \mu, K_{Mass}) = -\mu,$$

and

$$g(Mass; V_{c2}) = \mu Mass \left(1 - \frac{Mass}{K_{Mass}} \right),$$

from equation (5.35e). Note that the $Mass$ is now a state variable for the function f in (5.36). Note also that the parameters $Mass$ and V_{c2} are present implicitly in all the parameters through the steady state $z^* = (MPF^*, MPF_P^*, Cdc22^*, Wee1^*)$, while $Mass$ is explicitly present in μ , C_0 , and C (see equation (5.14)), and V_{c2} is explicitly present in C_0 and C (since β_u is a multiple of V_{c2}). Therefore, our calculation does not allow us to compute $a = D_{V_{c2}}f_1$ explicitly. However, it is easy to see that

$$\nu(V_{c2}) = K_{Mass} = Mass^*.$$

Hence, a does not need to be computed because both terms $\nu(V_{c2}) - Mass$ and $g(\nu(V_{c2}); V_{c2})$ in (5.36) vanish. Thus, the one-dimensional reduction of the extended G2 module (5.35) is

$$\xi' = f(\xi, K_{Mass}; V_{c2}) = (cCB_0 - dBC_0) + \sigma\xi^2. \quad (5.37)$$

Note that, the only difference between the one-dimensional forms (5.33) and (5.37) is that $Mass = K_{Mass}$ is constant in the latter.

The bifurcation diagram for the G2 module with variable mass (5.35) with V_{c2} taken as bifurcation parameter is shown in Figure 5.7. As expected, there is a saddle-node bifurcation, denoted, $SN_{V_{c2}}$, when $V_{c2} = V_{c2}^* \approx 3.49$. The upper stable node (solid black line) in Figure 5.7 corresponds to the upper stable steady state in Figure 5.5. The $SN_{V_{c2}}$ bifurcation point and corresponding eigenvalues are found

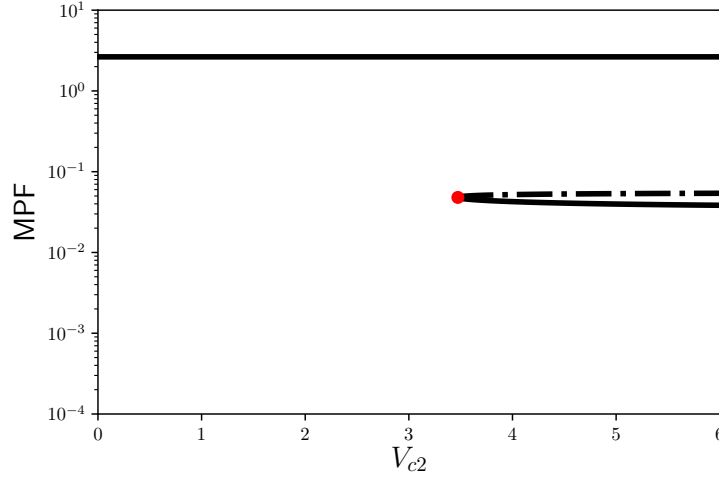


Figure 5.7: Bifurcation diagram of the G2 module with variable mass (5.35) with V_{c2} as varying parameter.

numerically to be given by

$$V_{c2}^* \approx 3.492928, \quad \begin{bmatrix} MPF^* \\ MPF_P^* \\ Wee1^* \\ Cdc25_P^* \\ Mass^* \end{bmatrix} \approx \begin{bmatrix} 0.048031 \\ 2.650923 \\ 0.826130 \\ 0.007779 \\ 2.7 \end{bmatrix}, \quad \vec{\lambda} \approx \begin{bmatrix} 0 \\ -0.0700 \\ -0.2000 \\ -36.974 \\ -115.67 \end{bmatrix}. \quad (5.38)$$

Note that this bifurcation point is approximately equal to that found earlier for the $SNIC_{V_{c2}}$ bifurcation of the full cell cycle model (see (5.3)), i.e., the G2 module with variable mass captures very well the dynamics of the full cell cycle model around the $SNIC_{V_{c2}}$ bifurcation. In the next section, we will see that adding the M module and resetting condition to the G2 module with variable mass does not affect the $SN_{V_{c2}}$ bifurcation point.

5.4 G2 and M modules combined with variable cell mass and resetting condition: SNIC bifurcation driven by V_{c2}

In the previous section, we showed that the G2 module with variable mass has a saddle-node bifurcation driven by V_{c2} . Such saddle-node bifurcation is inherited from the G2 module when the parameter $Mass$ is transformed into a variable. In this section, we further extend the G2 module by adding the M module and mass resetting condition. First, we add the M module, corresponding to equations for APC and IE. Second, we discuss how the addition of the resetting condition closes the cell cycle.

Addition of the M module to the G2 module with variables mass (5.35) results in the model already presented at the beginning of this chapter in equations (5.1)

$$\begin{aligned} \frac{dMPF}{dt} = & k_{m0}Mass - (k_{m2} + k_{m2a}Wee1)MPF \\ & + (k_{m1} + k_{m1a}Cdc25)MPF_P - (k_{m3} + k_{m3a}APC)MPF, \end{aligned} \quad (5.39a)$$

$$\begin{aligned} \frac{dMPF_P}{dt} = & (k_{m2} + k_{m2a}Wee1)MPF - (k_{m1} + k_{m1a}Cdc25)MPF_P \\ & - (k_{m3} + k_{m3a}APC)MPF_P, \end{aligned} \quad (5.39b)$$

$$\begin{aligned} \frac{dWee1}{dt} = & V_{w1} \frac{Wee1_T - Wee1}{J_{w1} + (Wee1_T - Wee1)} \\ & - k_{w2}(MPF + \alpha MPF_P) \frac{Wee1}{J_{w2} + Wee1}, \end{aligned} \quad (5.39c)$$

$$\begin{aligned} \frac{dCdc25}{dt} = & k_{c1}(MPF + \alpha MPF_P) \frac{Cdc25_T - Cdc25}{J_{c1} + (Cdc25_T - Cdc25)} \\ & - V_{c2} \frac{Cdc25}{J_{c2} + Cdc25}, \end{aligned} \quad (5.39d)$$

$$\frac{dIE}{dt} = k_{i1}(MPF + \alpha MPF_P) \frac{IE_T - IE}{J_{i1} + (IE_T - IE)} - V_{i2} \frac{IE}{J_{i2} + IE}, \quad (5.39e)$$

$$\frac{dAPC}{dt} = k_{a1}IE \frac{APC_T - APC}{J_{a1} + (APC_T - APC)} - V_{a2} \frac{APC}{J_{a2} + APC}, \quad (5.39f)$$

$$\frac{dMass}{dt} = \mu Mass \left(1 - \frac{Mass}{K_{Mass}} \right), \quad (5.39g)$$

where variables and parameters are listed in Tables 5.1 and 5.2, respectively. Note that APC and IE are variables in this combined module, whereas they are considered parameters in the G2 module with variable mass.

As in Section 5.3, we consider V_{c2} , the inactivation rate of Cdc25, a varying parameter. The bifurcation diagram is shown in Figure 5.8. There is a saddle-node bifurcation, denoted $SN_{\bar{V}_{c2}}$ to distinguish it from the previous $SN_{V_{c2}}$, when $V_{c2} = \bar{V}_{c2}^* = 3.47$. Note that if we compare this $SN_{\bar{V}_{c2}}$ bifurcation with the $SN_{V_{c2}}$ bifurcation in Figure 5.7, including the branch, they have not changed after the addition of the M module. However, the addition of the M module eliminated the upper stable node (solid black line) in Figure (5.7) and created the upper saddle point (dot dash black line) in Figure 5.8. In fact, the numerical values of the $SN_{V_{c2}}$ bifurcation are approximately equal to those of the $SNIC_{V_{c2}}$ shown at the beginning of this chapter in equation (5.3), i.e.,

$$V_{c2}^* \approx 3.471683, \quad \begin{bmatrix} MPF^* \\ MPF_P^* \\ Wee1^* \\ Cdc25_P^* \\ IE^* \\ APC^* \\ Mass^* \end{bmatrix} \approx \begin{bmatrix} 0.048044 \\ 2.650815 \\ 0.825999 \\ 0.007785 \\ 0.003287 \\ 0.000013 \\ 2.7 \end{bmatrix}, \quad \vec{\lambda} \approx \begin{bmatrix} 0 \\ -0.0700 \\ -0.2000 \\ -21.768 \\ -36.960 \\ -115.58 \\ -1655.6 \end{bmatrix}.$$

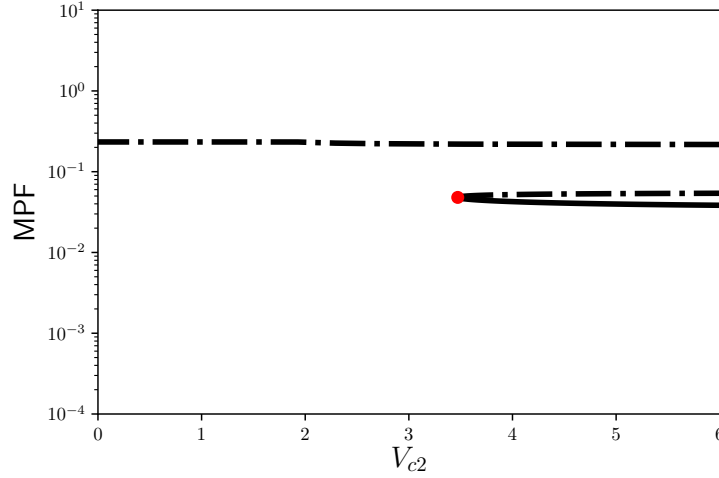


Figure 5.8: Bifurcation diagram of the G2 and M modules with variable mass (5.39) with V_{c2} as varying parameter.

The resetting condition (5.2), i.e.,

$$\text{if } MPF(t) = \theta_M \text{ and } \frac{dMPF}{dt}(t) < 0 \implies Mass(t) \leftarrow \frac{Mass(t)}{2},$$

maps trajectories reaching the upper saddle (dot dashed black line) in Figure 5.8 from the right side (to the right of $Mass^*$) of Figure 5.5 that defines M-phase to the left side (to the left of $Mass^*$) that defines G2-phase. Note that this mapping is done smoothly with respect to all the variables, except $Mass$, since their value does not change at the reset. This defines a branched manifold that closes the cell cycle (i.e., the M-phase to interphase transition) and transforms the $SN_{2V_{c2}}$ bifurcation into a $SNIC_{V_{c2}}$ bifurcation.

Since the $SN_{V_{c2}}$ bifurcation remains unchanged with the addition of the M-phase and the resetting condition, we conjecture that the one-dimensional reduction of the $SNIC_{V_{c2}}$ bifurcation is the same as (5.37).

5.5 Normal form for the SNIC bifurcation driven by V_{c2} : describing the G2/M transition

We now rescale back to the original time scale of t , according to equation, (5.15)

$$\tau = k_{m3}t \implies \frac{d\tau}{dt} = k_{m3}. \quad (5.40)$$

Then,

$$\frac{d\xi}{dt} = \frac{d\xi}{d\tau} \frac{d\tau}{dt} = k_{m3} \frac{d\xi}{d\tau} = k_{m3} (cCB_0 - dBC_0 + \sigma\xi^2),$$

and equation (5.37) is rewritten as

$$\frac{d\xi}{dt} = \rho + \gamma\xi^2, \quad (5.41)$$

where

$$\rho = k_{m3}(cCB_0 - dBC_0), \quad \text{and} \quad \gamma = k_{m3}\sigma. \quad (5.42)$$

Although the constant γ can be eliminated with non-dimensionalization, we prefer to keep this ‘almost’ normal form in order to have the same time scale of the cell cycle. For $V_{c2} = 1.4$, we can estimate

$$\rho \approx -371.466, \quad (5.43)$$

from equations (5.3), (5.17), and (5.19). However, we cannot estimate γ because we do not have a closed expression for $\sigma = \sigma_0 + \sigma_1$ (see equation (5.33)). Since the cell cycle is in the oscillatory regime when $V_{c2} = 1.4$, the normal form should not have steady states when $V_{c2} = 1.4$. Thus, given $\rho < 0$ we can assume that $\gamma < 0$. Equation (5.41) is a normal form for the saddle-node bifurcation that approximates

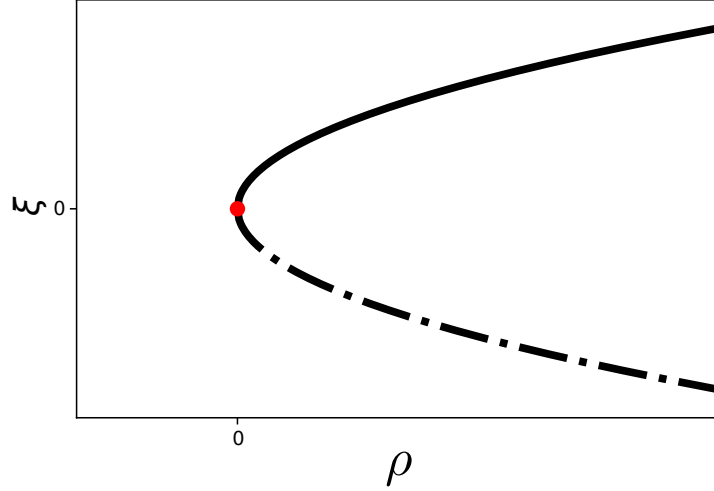


Figure 5.9: Bifurcation diagram of the normal form (5.41) of the saddle-node bifurcation.

locally the $\text{SNIC}_{V_{c2}}$ bifurcation of the cell cycle in a neighbourhood of the bifurcation point $(\xi, p) = (0, p^*)$ (where p is the vector of all parameters in the cell cycle).

We denote the neighbourhood of $\xi = 0$ where the normal form (5.41) approximates the cell cycle around the $\text{SNIC}_{V_{c2}}$ bifurcation as $(\xi_{\text{left}}, \xi_{\text{right}})$. Given the initial condition $\xi(0; p) = 0$, we have $\xi(0; p) \in (\xi_{\text{left}}, \xi_{\text{right}})$. If $V_{c2} = V_{c2}^*$ (i.e., $p = p^*$), then $(\xi, p) = (\xi(0; p^*), p^*) = (0, p^*)$ is exactly the bifurcation point.

When $\rho < 0$, the solution of the normal form (5.41) is always decreasing from ξ_{left} to ξ_{right} . If $\rho = 0$, there is a saddle-node bifurcation at $\xi = 0$. If $\rho > 0$, there are stable and unstable equilibria at $\xi = \sqrt{|\frac{\rho}{\gamma}|}$ and $\xi = -\sqrt{|\frac{\rho}{\gamma}|}$, respectively. See Appendix 5.B for more details. Figure 5.9 shows the corresponding bifurcation diagram.

If we solve the normal form (5.41) for $\rho < 0$ beyond ξ_{left} and ξ_{right} , ξ blows-up in finite time to positive infinity backwards from ξ_{left} , and to positive infinity forwards from ξ_{right} , respectively (see Appendix 5.B). This extension of the normal form (5.41) to positive and negative infinity is illustrated in Figure 5.10c. The time from

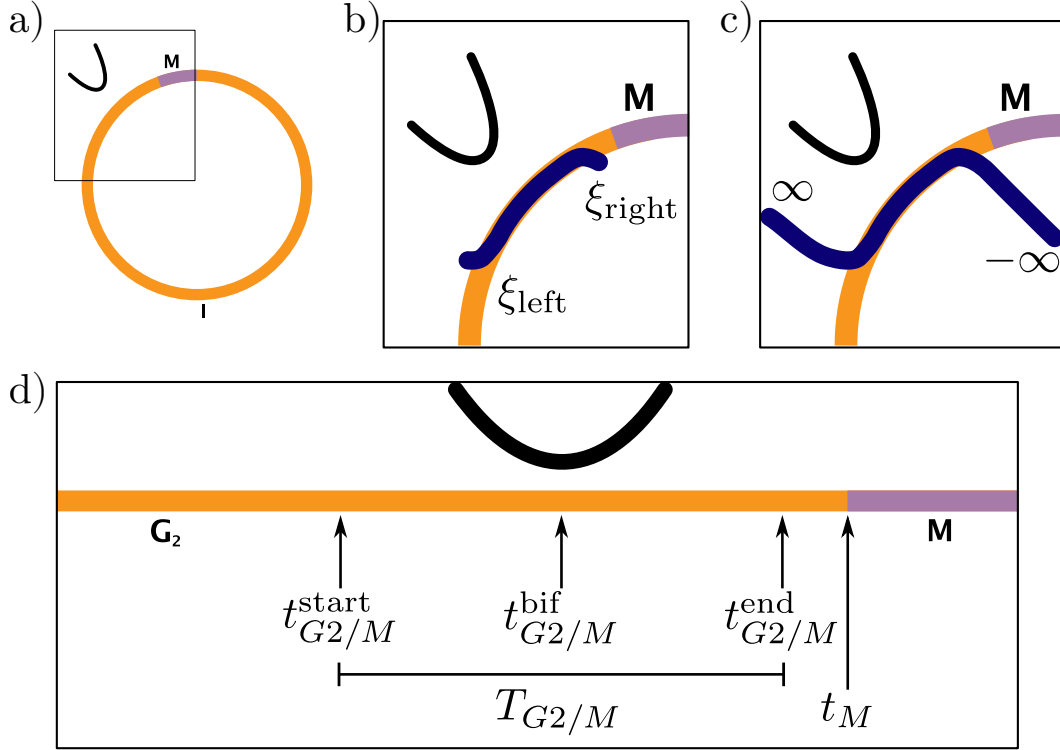


Figure 5.10: Diagram of the one-dimensional approximation of the cell cycle model around the SNIC_{V_{c2}} bifurcation. a) Representation of the cell cycle with a zoom into the G₂/M transition where the SNIC_{V_{c2}} bifurcation takes place (see Figure 2.1). b) Representation of the one-dimensional approximation of the cell cycle (5.41) (blue) in the cell cycle diagram in the neighborhood ($\xi_{\text{left}}, \xi_{\text{right}}$) of $\xi = 0$. c) Representation of the extended normal form (5.41) (blue) by solving it beyond ξ_{left} and ξ_{right} . d) Linear representation of the cell cycle during the G₂/M transition with corresponding times defined in equations (5.44) and (5.46).

negative infinity blow-up to positive infinity blow-up is

$$T_{G2/M} = \frac{\pi}{\sqrt{\rho\gamma}}, \quad (5.44)$$

(see equation (5.52) in Appendix 5.B).

Now consider the full cell cycle model (5.1) with initial condition at the start of the cell cycle and basal value of $V_{c2} = 1.4$. Denote the *time of bifurcation* $t_{G2/M}^{\text{bif}}$ as the time such that the concentration of *MPF* is equal to its concentration at the

bifurcation point (5.3), i.e.,

$$MPF(t_{G2/M}^{\text{bif}}) = MPF^*. \quad (5.45)$$

If V_{c2} is instantaneously set to V_{c2}^* at $t = t_{G2/M}^{\text{bif}}$, the cell cycle model is exactly at the bifurcation point. We define a finite time interval around the time of bifurcation $t_{G2/M}^{\text{bif}}$ as

$$I_{G2/M} = [t_{G2/M}^{\text{start}}, t_{G2/M}^{\text{end}}] = [t_{G2/M}^{\text{bif}} - \frac{1}{2}T_{G2/M}, t_{G2/M}^{\text{bif}} + \frac{1}{2}T_{G2/M}]. \quad (5.46)$$

Identifying the G2/M transition with the $\text{SNIC}_{V_{c2}}$ bifurcation, we say that $t_{G2/M}^{\text{bif}}$ is the time of the $\text{SNIC}_{V_{c2}}$ bifurcation associated with the G2/M transition, $T_{G2/M}$ (equation (5.44)) is the length of the G2/M transition, and $I_{G2/M}$ (equation (5.46)) is the interval of the G2/M transition. These values are illustrated in Figure 5.10d.

5.6 Discussion

We reduced the the cell cycle model (5.1) to normal form (5.41) around the $\text{SNIC}_{V_{c2}}$ bifurcation. Thus, all seven variables in the cell cycle model are reduced to one variable, which concentrates the dynamics of the $\text{SNIC}_{V_{c2}}$ bifurcation. For this reduction, we broke down the cell cycle model into sub-modules, the G2 module and the M module.

In Section 5.2, we considered the G2 module with constant $Mass$ (5.4). We used Theorem 4.0.1 and Corollary 4.0.1 (see Meiss [63] for more details on saddle-node bifurcations in \mathbb{R}^n) to show that this module has a saddle-node bifurcation driven by $Mass$ and to reduce it to the one-dimensional form (5.33). In particular, we found conditions on the parameters of the G2 module that guarantee that the hypotheses

of Theorem 4.0.1 and Corollary 4.0.1 are satisfied.

In Section 5.3, we transformed $Mass$ into a variable to obtain the G2 module with variable $Mass$ (5.35). We used Proposition 4.2.2, proved in Chapter 4, to show that the G2 module with variable $Mass$ (5.35) has a saddle-node bifurcation driven by V_{c2} , which is the carryover of the saddle-node driven by $Mass$ in the G2 module (5.4). Moreover, we used Proposition 4.2.1 and the one-dimensional form (5.33) to reduce the G2 module with variable $Mass$ (5.35) to the one-dimensional form (5.37).

In Section 5.4, we added the M module and resetting condition (5.2) to the G2 module with variable $Mass$ to construct the cell cycle model (5.39). We used numerical results to conclude that the M module remains constant around the saddle-node bifurcation driven by V_{c2} and does not affect the variables of the G2 module or $Mass$. The resetting condition (5.2) defines a branched manifold that closes the cell cycle (see Haderer and Hillen [31] for more details on branched manifolds) and transforms the saddle-node bifurcation into a SNIC bifurcation. Since the reset takes place away from the SNIC bifurcation driven by V_{c2} , the resetting condition does not affect the one-dimensional reduction. Thus, the one-dimensional reduction of the full cell cycle model around SNIC bifurcation driven by V_{c2} is locally the same as the saddle-node reduction (5.37) from the previous section.

In Section 5.5, we standardized our one-dimensional form of the cell cycle model around the SNIC bifurcation driven by V_{c2} to have the same time-scale as the cell cycle model (see equation (5.41)). Moreover, we provided a mathematical definition of the G2/M transition of the cell cycle in terms of the SNIC bifurcation driven by V_{c2} . Specifically, we define the time interval $I_{G2/M} = [t_{G2/M}^{\text{start}}, t_{G2/M}^{\text{end}}]$ of the G2/M transition (see equation (5.46)) around the time of bifurcation $t_{G2/M}^{\text{bif}}$. This implies that the G2/M transition is a finite time interval defined around the SNIC bifurcation

(locally, saddle-node bifurcation) driven by V_{c2} .

We conjecture that the end of the G2/M transition, $t_{G2/M}^{\text{end}}$, determines the threshold for M-phase entry, θ_M , defined by Novák et al. [75] and Gérard et al. [25], and widely used in Chapters 2 and 3. A potential initial approach to support this conjecture is to estimate $t_{G2/M}^{\text{start}}$, $t_{G2/M}^{\text{bif}}$, and $t_{G2/M}^{\text{end}}$ based on Table 5.2. The results might be useful to also define the other transitions in the cell cycle in a similar way.

Some of the steps taken in this chapter were justified numerically (such as providing the nondegeneracy condition (5.34) or showing that the M module remains constant during the saddle-node bifurcation driven by V_{c2}) or unfinished (such as finding the steady states, the unique function $\eta(\xi; p)$, and constant σ in Section 5.2). Taking a more rigorous approach to justify these steps is left as future work.

The one-dimensional reduction of the cell cycle around the SNIC bifurcation driven by V_{c2} (5.41) will be used in the next chapter to derive a survival fraction model based on the ATM-Chk2 pathway.

Appendices

5.A Power series expansions of the Goldbeter-Koshland kinetics

The Goldbeter-Koshland kinetics is given by

$$\dot{x}(t) = v_1 \frac{1-x}{J_1+1-x} - v_2 \frac{x}{J_2+x}, \quad (5.47)$$

where v_1 and v_2 are the maximum reaction velocities and J_1 and J_2 are the Michaelis rates. The two non-linear terms in the Goldbeter-Koshland kinetics have a power

series expansion about $x = 0$

$$\frac{a+x}{J+a+x} = \frac{a}{J+a} + \sum_{n=1}^{\infty} \frac{(-1)^{n+1}J}{(J+a)^{n+1}}x^n, \quad |x| < J. \quad (5.48)$$

That is,

$$\frac{1-x}{J+1-x} = \frac{1}{J+1} - \frac{J}{(J+1)^2}x - \frac{J}{(J+1)^3}x^2 - O(x^3)$$

and

$$\frac{x}{J+x} = \frac{1}{J}x - \frac{1}{J^2}x^2 + O(x^3).$$

Thus we can approximate the right-hand side of (5.47) for small values of x with

$$\dot{x}(t) \approx v_1 \left(\frac{1}{J_1+1} - \frac{J_1}{(J_1+1)^2}x - \frac{J_1}{(J_1+1)^3}x^2 \right) - v_2 \left(\frac{1}{J_2}x - \frac{1}{J_2^2}x^2 \right).$$

Combining terms, we obtain

$$\dot{x}(t) \approx \frac{v_1}{J_1+1} - \left(\frac{v_1 J_1}{(J_1+1)^2} + \frac{v_2}{J_2} \right) x - \left(\frac{v_2 J_1}{(J_1+1)^3} - \frac{v_2}{J_2^2} \right) x^2. \quad (5.49)$$

5.B Normal form for the saddle-node bifurcation

Consider the normal form for the saddle-node bifurcation

$$\frac{dx}{dt} = -b - cx^2, \quad (5.50)$$

where $c > 0$. Note that we keep the constant c in order to avoid scaling time. If $b > 0$, then $\frac{dx}{dt} < 0$ and there are no steady states. If $b < 0$, then there are two steady

states

$$\frac{dx}{dt} = 0 \implies -b - cx^2 = 0 \implies x_{\pm} = \pm \sqrt{\left| \frac{b}{c} \right|}.$$

Denoting $f(x) = -b - cx^2$, we have $f'(x) = -2cx$. Since $f(x_+) < 0$, x_+ is stable.

Conversely, since $f(x_-) > 0$, x_- is unstable.

We are interested on the solution of (5.41) when $b > 0$ given initial condition $x(0) = \infty$. Using the method to solve for separable equations, we have

$$\frac{dx}{dt} = -b \left(1 + \frac{c}{b} x^2 \right) \implies \int \frac{dx}{1 + \left(\sqrt{\frac{c}{b}} x \right)^2} = - \int b dt.$$

Using the substitution $u = \sqrt{\frac{c}{b}} x$ for the integral in the right hand side, we obtain

$$\sqrt{\frac{b}{c}} \operatorname{atan} \left(\sqrt{\frac{c}{b}} x(t) \right) = -bt + C.$$

Using the initial condition $x(0) = \infty$, we find

$$C = \sqrt{\frac{b}{c}} \operatorname{atan}(\infty) = \frac{\pi}{2} \sqrt{\frac{b}{c}}.$$

Substituting back and solving for $x(t)$, we obtain

$$\begin{aligned} \operatorname{atan} \left(\sqrt{\frac{c}{b}} x(t) \right) &= \frac{\pi}{2} - \sqrt{bct}, \\ \implies \sqrt{\frac{c}{b}} x(t) &= \tan \left(\frac{\pi}{2} - \sqrt{bct} \right) = \cot \left(\sqrt{bct} \right) \end{aligned}$$

Thus, the solution to the normal form (5.50) is given by

$$x(t) = \sqrt{\frac{b}{c}} \cot \left(\sqrt{bct} \right). \quad (5.51)$$

This solution blows-up for a finite time T_{blow} . That is,

$$x(T_{\text{blow}}) = \sqrt{\frac{b}{c}} \cot\left(\sqrt{bc}T_{\text{blow}}\right) = \infty \iff \sqrt{bc}T_{\text{blow}} = \pi.$$

Thus, the time of blow-up is

$$T_{\text{blow}} = \frac{\pi}{\sqrt{bc}}. \quad (5.52)$$

5.C Parameters

Table 5.2: Parameter values. Most parameter values have been taken from Gérard et al. [25] or adapted to match cell cycle length in mammalian cells. Parameters related to the radiation pathway come from different sources or were cautiously chosen on the basis of numerical simulations. Details are provided in the footnotes that are referenced in the Source column. Parameters with no units are dimensionless.

Symbol	Definition	Value	Units	Source
k_{m0}	Rate of synthesis of Cdk-cyclin fusion protein, MPF	0.2	hr ⁻¹	¹
k_{m1}	Rate constant for the dephosphorylation of MPF	0.4	hr ⁻¹	²
k_{m1a}	Rate constant for the dephosphorylation of MPF by Cdc25	20.0	hr ⁻¹	²
k_{m2}	Rate constant for the phosphorylation of MPF	0.4	hr ⁻¹	²
k_{m3}	Rate constant for the degradation of MPF and MPF _p	0.2	hr ⁻¹	²

continued...

¹Taken from Gérard et al. [25]; slightly modified to accommodate the correct G2/M transition dynamics.

²Taken from Gérard et al. [25]; scaling factor of 8.5 needed to rescale the length of the cell cycle to approximately 24 hrs.

...continued

Symbol	Definition	Value	Units	Source
k_{m3a}	Rate constant for the degradation of MPF and MPF _P by APC	6.35	hr ⁻¹	2
V_{w1}	Maximum activation rate, by dephosphorylation, of Wee1	1.0	hr ⁻¹	2
k_{w2}	Rate constant for activation of g by MPF	5.3	hr ⁻¹	2
J_{w1}	Michaelis constant for Wee1 activation	0.01		3
J_{w2}	Michaelis constant for Wee1 inactivation	0.01		3
k_{c1}	Rate constant for Cdc25 phosphorylation by MPF	8.5	hr ⁻¹	2
V_{c2}	Maximum inactivation rate, by dephosphorylation, of Cdc25	1.4	hr ⁻¹	1
k_{c2a}	Rate constant for the inactivation of Cdc25 by Chk2	2.4	hr ⁻¹	4
J_{c1}	Michaelis constant for Cdc25 activation	0.01		3
J_{c2}	Michaelis constant for Cdc25 inactivation	0.01		3
k_{i1}	Rate constant for the activation of IE by MPF	1.7	hr ⁻¹	2
V_{i2}	Maximum inactivation rate of IE	0.4	hr ⁻¹	2
J_{i1}	Michaelis constant for IE activation	0.001		3
J_{i2}	Michaelis constant for IE inactivation	0.001		3
k_{a1}	Rate constant for the activation, by phosphorylation, of APC by IE	6.8	hr ⁻¹	2

continued...

³Taken from Gérard et al. [25].

⁴Educated guess.

...continued

Symbol	Definition	Value	Units	Source
V_{a2}	Maximum inactivation rate, by phosphorylation, of APC	1.7	hr^{-1}	2
J_{a1}	Michaelis constant for APC activation	0.001		3
J_{a2}	Michaelis constant for APC inactivation	0.001		3
α	Partial activity of MPF _P	0.05		2
μ	Growth rate of the cell	0.07	hr^{-1}	5
K_{Mass}	Maximum cell mass	2.7		4
$Wee1_T$	Total concentration of kinase Wee1	1.0		2
$Cdc25_T$	Total concentration of phosphatase Cdc25	1.0		2
IE_T	Total concentration of intermediate enzyme IE	1.0		2
APC_T	Total concentration of protein APC	1.0		2

⁵Informed by Park et al. [80].

Chapter 6

Effect of low-dose radiation on the survival fraction through the ATM-Chk2 pathway: a theoretical approach

Throughout Chapters 2 and 3, we analyzed the effect of radiation on the G2/M transition and the survival fraction via the Chk2-ATM pathway, mostly from a numerical perspective. Our results support Marples and Joiner's hypothesis that the G2/M transition plays a major role in the hyper-radiosensitivity and increased radioresistance (HRS/IRR) phenomenon. In this Chapter, we establish the connection between radiation and the cell survival fraction from a theoretical perspective. In order to provide a survival fraction model accounting for our observations, we need to capture the precise mechanism that causes the HRS/IRR. This mechanism is the G2/M transition, which is associated with a saddle-node on an invariant circle (SNIC) bifurcation. The reduction of the cell cycle model to a normal form around

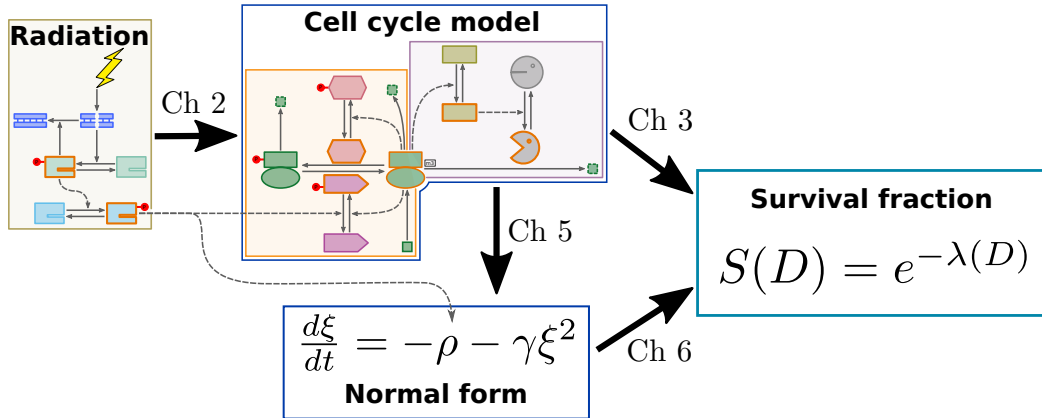


Figure 6.1: Diagram of the approach taken to find a survival fraction model that accounts for the effect of radiation on the G2/M transition of the cell cycle. The diagrams for the cell cycle and radiation pathway are taken from Figure 2.2.

the SNIC bifurcation driven by V_{e2} is done in Chapter 5. In this chapter, we use this normal form to derive an expression for the survival fraction based on the G2/M transition. Figure 6.1 illustrates how this chapter is a follow-up of the previous chapters.

This chapter is structured as follows. In Section 6.1, we summarize the results of previous chapters relevant to the this chapter. In Section 6.2, we motivate the use of the normal form for the SNIC $_{V_{e2}}$ bifurcation in replacement of the cell cycle model to describe the progression of the cell cycle. In Section 6.3, we transform the normal form for the SNIC $_{V_{e2}}$ bifurcation to its corresponding phase model, and provide a theoretical derivation for the time available for repair and the average number of lethal lesions. In Section 6.4, we provide a connection between our formulation of the survival fraction and the Induced Repair model, under certain simplification and assumptions.

6.1 Summary of the previous chapters

Recall the cell cycle model with radiation pathway studied in previous chapters

$$\begin{aligned} \frac{dMPF}{dt} &= k_{m0}Mass - (k_{m2} + k_{m2a}Wee1)MPF \\ &\quad + (k_{m1} + k_{m1a}Cdc25)MPF_P - (k_{m3} + k_{m3a}APC)MPF, \end{aligned} \quad (6.1a)$$

$$\begin{aligned} \frac{dMPF_P}{dt} &= (k_{m2} + k_{m2a}Wee1)MPF - (k_{m1} + k_{m1a}Cdc25)MPF_P \\ &\quad - (k_{m3} + k_{m3a}APC)MPF_P, \end{aligned} \quad (6.1b)$$

$$\begin{aligned} \frac{dWee1}{dt} &= V_{w1} \frac{Wee1_T - Wee1}{J_{w1} + (Wee1_T - Wee1)} \\ &\quad - k_{w2}(MPF + \alpha MPF_P) \frac{Wee1}{J_{w2} + Wee1}, \end{aligned} \quad (6.1c)$$

$$\begin{aligned} \frac{dCdc25}{dt} &= k_{c1}(MPF + \alpha MPF_P) \frac{Cdc25_T - Cdc25}{J_{c1} + (Cdc25_T - Cdc25)} \\ &\quad - (V_{c2} + k_{c2a}Chk2) \frac{Cdc25}{J_{c2} + Cdc25}, \end{aligned} \quad (6.1d)$$

$$\frac{dIE}{dt} = k_{i1}(MPF + \alpha MPF_P) \frac{IE_T - IE}{J_{i1} + (IE_T - IE)} - V_{i2} \frac{IE}{J_{i2} + IE}, \quad (6.1e)$$

$$\frac{dAPC}{dt} = k_{a1}IE \frac{APC_T - APC}{J_{a1} + (APC_T - APC)} - V_{a2} \frac{APC}{J_{a2} + APC}, \quad (6.1f)$$

$$\frac{dMass}{dt} = \mu Mass \left(1 - \frac{Mass}{K_{Mass}} \right), \quad (6.1g)$$

$$\frac{dChk2}{dt} = k_{h1}ATM DSB \frac{Chk2_T - Chk2}{J_{h1} + (Chk2_T - Chk2)} - V_{h2} \frac{Chk2}{J_{h2} + Chk2}, \quad (6.1h)$$

$$\frac{dATM}{dt} = k_{t1}DSB \frac{ATM_T - ATM}{J_{t1} + (ATM_T - ATM)} - V_{t2} \frac{ATM}{J_{t2} + ATM}, \quad (6.1i)$$

$$\frac{dDSB}{dt} = k_{d1}\dot{D}(t) - k_{d2}ATM DSB, \quad (6.1j)$$

subject to the resetting condition

$$\text{if } MPF(t) = \theta_M \text{ and } \frac{dMPF}{dt}(t) < 0 \implies Mass(t) \leftarrow \frac{Mass(t)}{2}, \quad (6.2)$$

Table 6.1: Name and description of variables in Eqs. (6.1a)–(6.1j). All variables represent concentration, except $Mass$ and DSB .

Symbol	Description
MPF	Active Cdk1-cyclin B complex (Mitotic Promoting Factor)
MPF_P	Inactive, phosphorylated form of MPF
$Wee1$	Active dephosphorylated form of kinase Wee1 (MPF inactivator)
$Cdc25$	Active phosphorylated form of the phosphatase Cdc25C (MPF activator)
IE	Active form of an intermediate enzyme [94]
APC	Active phosphorylated form of APC (Anaphase Promoting Complex)
$Chk2$	Active phosphorylated form of Chk2 (Checkpoint kinase 2)
ATM	Active phosphorylated, monomerized and recruited form of ATM
DSB	Recognized Double Strand Brakes formed by Ionizing Radiation
$Mass$	Mass of the cell

where the variables denote the concentration of the most important proteins involved in the G2/M transition and the ATM-Chk2 pathway, the number of DSBs, and the mass of the cell (see Table 6.1). The parameters denote the average rate of reactions between given proteins, cell growth, carrying capacity, and other average rates (see Table 6.3 in Appendix 6.C).

The model has two main components: equations (6.1a)–(6.1g) and (6.2) correspond to cell cycle model, and equations (6.1h)–(6.1j) correspond to the radiation pathway. In Chapter 2, we showed that radiation can trigger G2 checkpoint activation by increasing the maximum inactivation rate of Cdc25, which we denoted

$$\tilde{V}_{c2} = V_{c2} + k_{c2a}Chk2, \quad (6.3)$$

and appears in equation (6.1d). The G2 checkpoint activation is identified with a SNIC bifurcation, denoted $SNIC_{V_{c2}}$, driven by \tilde{V}_{c2} . In the absence of radiation, Chk2 is inactive and \tilde{V}_{c2} equals the basal inactivation rate V_{c2} . In the presence of radiation, Double Strand Breaks (DSBs) are formed, which in turn activates Chk2,

and increases \tilde{V}_{c2} . The $\text{SNIC}_{V_{c2}}$ bifurcation occurs at $\tilde{V}_{c2} = V_{c2}^*$. When $\tilde{V}_{c2} > V_{c2}^*$, the G2 checkpoint can be activated provided that the cell is in late G2-phase. The corresponding bifurcation diagram is shown in Figure 2.3. Repair mechanisms decrease the number of DSBs and the value of \tilde{V}_{c2} until Chk2 becomes inactive again and the cell cycle resumes. As stated in Chapter 2, this Chk2 activation mechanism combined with the SNIC bifurcation driven by V_{c2} are thought to be responsible for the HRS/IRR phenomenon.

The radiation scheme used in Chapter 2 is a radiation pulse of intensity D at time t_0

$$D(t) = D\delta(t - t_0), \quad (6.4)$$

where $\delta(t)$ is the Dirac delta function. If initial conditions are set to be at the start of the cell cycle right after cell division ($t = 0$), then we define t_M (the time of M-phase entry, which is the same as the length of the interphase) as the time when the concentration of MPF reaches $\theta_M = 0.2$ from below ($\frac{dMPF}{dt} > 0$), and we define T (the length of the cell cycle) as the time when MPF reaches $\theta_M = 0.2$ from above ($\frac{dMPF}{dt} < 0$). Our simulations focus on a radiation pulse applied during interphase ($t_0 \in [0, t_M]$) and low intensity of radiation ($D < 1$ Gy). When radiation is applied, the time of M-phase entry is delayed (the extent of the delay depends on the intensity D and time of radiation t_0), defining a new time of M-phase entry $t_M(t_0, D)$. Thus, under no radiation, we simply say $t_M(0, 0) = t_M$.

In Chapter 3, we used numerical simulations to show that G2 checkpoint activation driven by radiation can cause the HRS/IRR phenomenon, especially in cells enriched in G2-phase. Our simulations were consistent with the results of Marples and Joiner [59]. We used the cell cycle with radiation pathway model for an average individual cell to develop a survival fraction model based on a population of cells.

The survival fraction framework, based on the total average number of lethal events, $\lambda(D)$, was defined as the sum of the average number of lethal lesions due to G2 checkpoint failure, $\lambda_{G2/M}(D)$, and all other lesions that are not accounted for in our modelling, $\lambda_{\text{other}}(D)$. Thus,

$$\lambda(D) = \underbrace{\hat{\alpha}D + \hat{\beta}D^2}_{\lambda_{\text{other}}(D)} + \underbrace{\frac{\alpha_0}{t_M} \int_0^{t_M} DSB(t_M(t_0, D))f(t_0)dt_0}_{\lambda_{G2/M}(D)}. \quad (6.5)$$

where $\hat{\alpha}$, $\hat{\beta}$, and α_0 are a proportionality constants, and $f(t)$ is the distribution of cells over the cell cycle. Since the Linear Quadratic (LQ) model is a good model for most survival fraction data, we assume that the linear and quadratic terms are appropriate to model all other lesions not included in our modelling. Assuming a Poisson distribution for the average number of lethal events, the survival fraction becomes

$$S(D) = e^{-\lambda(D)}. \quad (6.6)$$

In Chapter 3, we also identified that ATM becomes active for radiation higher than 5 mGy (very low dose of radiation). Since survival fraction experiments are relevant above this level of radiation, it is reasonable to assume that ATM is always active in experiments. Thus, we set ATM equal to constant one in equation (6.1j) and solved for DSB to find an expression for the integrand in (6.5)

$$DSB(t_M(t_0, D)) = k_{d1}e^{-k_{d2}(t_M(t_0, D)-t_0)}D, \quad (6.7)$$

(see equation (3.10)). Here, we identified the time available for repair

$$t_R(t_0, D) = t_M(t_0, D) - t_0, \quad (6.8)$$

as an important quantity to compute the survival fraction. Substituting (6.7) and (6.8) into (6.5), we find that the average number of lethal lesions due to G2 checkpoint failure becomes

$$\lambda_{G2/M}(D) = \frac{\alpha_0 k_{d1} D}{t_M} \int_0^{t_M} e^{-k_{d2} t_R(t_0, D)} f(t_0) dt_0, \quad (6.9)$$

where k_{d1} and k_{d2} are the rates for formation and repair of DSBs. However, computing $t_R(t_0, D)$ explicitly from the cell cycle model is difficult given the size and non-linearity of the model. Instead, our approach is to reduce the cell cycle model about the $\text{SNIC}_{V_{c2}}$ bifurcation in order to simplify the calculation of the time available for repair.

In Chapter 5, the cell cycle model (corresponding to equations (6.1a)–(6.1g) and (6.2)) is reduced to a one-dimensional form about the $\text{SNIC}_{V_{c2}}$ bifurcation (locally saddle-node bifurcation)

$$\frac{d\xi}{dt} = -\rho - \gamma\xi^2 \quad (6.10)$$

(see equation (5.41)), where ξ is a linear combination of the variables in the cell cycle, and $\rho > 0$ and $\gamma > 0$ are constants that depend on the parameters of the cell cycle. Note that we have flipped the sign of the constants ρ and γ for simplicity. In this chapter, we refer to equation (6.10) as the normal form of the $\text{SNIC}_{V_{c2}}$ bifurcation (locally $\text{SN}_{V_{c2}}$ bifurcation). Using the normal form (6.10), we defined the G2/M transition as the finite time interval (see Figure 6.2)

$$I_{G2/M} = [t_{G2/M}^{\text{start}}, t_{G2/M}^{\text{end}}] = [t_{G2/M}^{\text{start}}, t_M]. \quad (6.11)$$

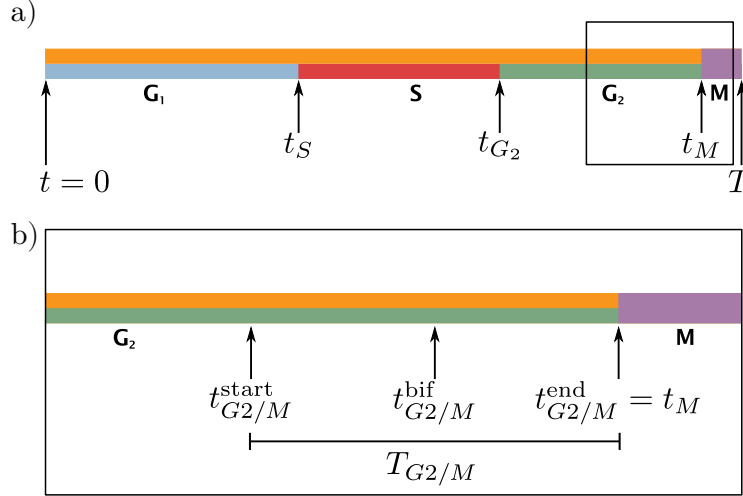


Figure 6.2: Linear representation of the cell cycle. a) Full cell cycle. b) Zoom into the G₂/M transition with corresponding length and start and end times.

Note that the length of this interval determines the duration of the G₂/M transition

$$T_{G_2/M} = t_{G_2/M}^{\text{end}} - t_{G_2/M}^{\text{start}} = \frac{\pi}{\sqrt{\rho\gamma}}. \quad (6.12)$$

We will see that the normal form defined on the whole interval $I_{G_2/M}$ is a good representation of the cell cycle model about the $\text{SNIC}_{V_{c_2}}$ bifurcation.

6.2 Normal form for the cell cycle during the G₂/M transition with the radiation pathway

In this chapter, we assume that ρ , in the normal form (6.10), is proportional to $V_{c_2}^* - V_{c_2}$, i.e.,

$$\rho = \nu(V_{c_2}^* - V_{c_2}), \quad (6.13)$$

for some proportionality constant $\nu > 0$, and γ is constant. Even though it is not evident, from the calculations carried out in Chapter 5 (see equation (5.42)), that

this assumption holds for the normal form (6.10), it is a standard and reasonable assumption to make when studying the normal form of a saddle-node bifurcation [38].

In the presence of radiation, the radiation pathway directly affects the cell cycle model by increasing the basal value of V_{c2} (the bifurcation parameter) through $Chk2$ activation according to the definition of \tilde{V}_{c2} in equation (6.3). Based on assumption (6.13), the radiation pathway modifies the value of the bifurcation parameter in a similar fashion to \tilde{V}_{c2}

$$\tilde{\rho} = \nu(V_{c2}^* - \tilde{V}_{c2}) = \nu(V_{c2}^* - (V_{c2} + k_{c2a}Chk2)). \quad (6.14)$$

This motivates the combination of the normal form (6.10) with the radiation pathway (6.1h)-(6.1j) into one model

$$\frac{d\xi}{dt} = -\nu(V_{c2}^* - V_{c2} - k_{c2a}Chk2) - \gamma\xi^2, \quad (6.15a)$$

$$\frac{dChk2}{dt} = k_{h1}ATM DSB \frac{Chk2_T - Chk2}{J_{h1} + (Chk2_T - Chk2)} - V_{h2} \frac{Chk2}{J_{h2} + Chk2}, \quad (6.15b)$$

$$\frac{dATM}{dt} = k_{t1}DSB \frac{ATM_T - ATM}{J_{t1} + (ATM_T - ATM)} - V_{t2} \frac{ATM}{J_{t2} + ATM}, \quad (6.15c)$$

$$\frac{dDSB}{dt} = k_{d1}\dot{D}(t) - k_{d2}ATM DSB. \quad (6.15d)$$

Figure 6.3 shows the solution of model (6.15) for a radiation pulse given by equation (6.4) as well as the solution of the same model under no radiation. We observe that, as expected, radiation introduces a delay in the evolution of $\xi(t)$.

This delay is similar to that observed in the cell cycle when radiation is applied during the G2/M transition (see, for example, Figure 2.3). In light of this connection, we want to define an analogous time available for repair, equation (6.8), for the

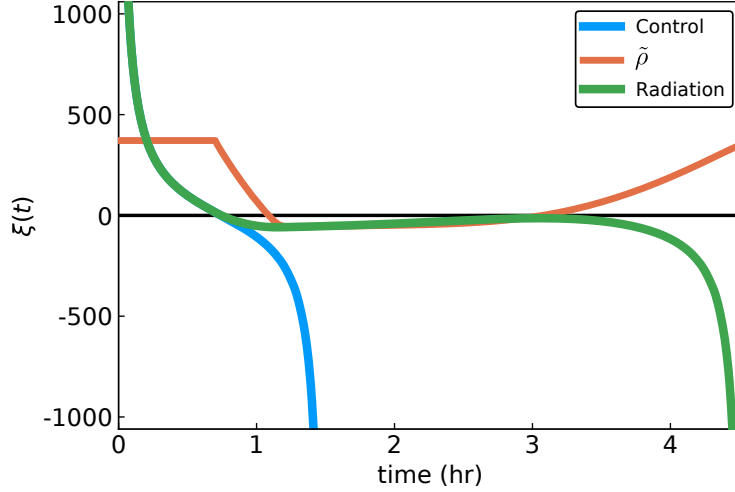


Figure 6.3: Solution of the normal form and radiation pathway model (6.15). A radiation pulse is applied at time $t = 0.8$. This activates $Chk2(t)$ for a short period of time, forces $\tilde{\rho}$ (equation (6.14); orange) to become negative temporarily, and causes a delay in the system (green) compared to the no-radiation case (blue). The parameter values are found in Table 6.3 in Appendix 6.C and Table 6.2, and the initial condition is $\xi(0) = 10^4$.

normal form and radiation pathway model (6.15). For this purpose, we assume that the threshold of MPF for M-phase entry in the cell cycle model, θ_M , occurs at the end of the G2/M transition, defined by the interval in equation (6.11), i.e., at time $t = t_M = t_{G2/M}^{\text{end}}$.

Provided that radiation has intensity D and start time $t_0 \in I_{G2/M}$, we are interested in the approximate time available for repair

$$\tilde{t}_R(t_0, D) = \tilde{t}_M(t_0, D) - t_0, \quad (6.16)$$

where $\tilde{t}_M(t_0, D)$ is the time such that $\xi(\tilde{t}_M(t_0, D)) = -\infty$. Thus, \tilde{t}_R and \tilde{t}_M are analogous quantities to t_R and t_M (see equation (6.8)), respectively. Note that the normal form with radiation pathway (6.15) is a representation of the cell cycle with radiation pathway (6.1) for $t_0 \in I_{G2/M}$. That is, if we want to measure the time

delay to M-phase entry in the cell cycle model for $t_0 \in I_{G2/M}$, we can do so using the normal form with radiation pathway. Then, the state of the cell cycle model at $t_{G2/M}^{\text{start}}$ and $t_M(t_0, D)$ are associated with $\xi = -\infty$ and $\xi = \infty$, respectively, in the normal form (see Figure 5.10).

In order to show the equivalence between equations (6.8) and (6.16), we compute (6.16) numerically using the same radiation scheme used in Chapter 3. In other words, we compute the time available for repair for the normal form and radiation pathway (6.15) to compare it with the time available for repair for the cell cycle and radiation pathway computed in Chapter 3 (see Figure 3.9).

The parameters in the normal form with radiation pathway (6.15) (except for ν , V_{c2}^* and γ) are described in Table 6.3. The parameter $V_{c2}^* \approx 3.47$ is the bifurcation value of V_{c2} estimated in Chapters 2 and 5 (see, for example, equation (5.3)). To estimate the value of the proportionality constant ν assumed in equation (6.13), we solve for ν in this equation and use the estimation of ρ in equation (5.43) under no radiation ($Chk2 = 0$),

$$\nu = \frac{\rho}{V_{c2}^* - V_{c2}} \approx 179.45. \quad (6.17)$$

The constant $\gamma = k_{m3}\sigma = k_{m3}(\sigma_0 + \sigma_1)$ is associated with the reduction of the G2 module to the one-dimensional form in Section 5.2 (see equation (5.33)). The value of σ_0 was computed numerically in equation (5.34), but the value of σ_1 cannot be computed explicitly since it involves the Implicit Function Theorem. However, for the purpose of carrying out the numerical simulations, we choose the value of γ so that the period of the normal form matches the length of the G2/M transition $T_{G2/M}$, equation (6.12). Using assumption (6.13), the period of equation (6.15a)

Table 6.2: Description of variable and parameters new to the normal form with radiation pathway model (6.15) and other parameter used the simulations.

Symbol	Description	Value	Source
γ	Constant associated with all quadratic terms in the one-dimensional reduction of the G2 module (see equation (5.33)).	0.012	Eq. (6.18)
ν	Proportionality constant (see equation (6.13)).	179.45	Eq. (6.17)
V_{c2}^*	Bifurcation value of V_{c2} .	3.47	Eq. (5.3)

under no radiation ($Chk2 \equiv 0$) is given by

$$T_{G2/M} = \frac{\pi}{\sqrt{\gamma\nu(V_{c2}^* - V_{c2})}}.$$

Based on the time-axis of the right plot in Figure 3.9, we estimate that this period should be about $T_{G2/M} = 1.6$ hours. Thus, solving for γ in equation (6.2), we obtain

$$\gamma = \frac{1}{\nu(V_{c2}^* - V_{c2})} \left(\frac{\pi}{T_{G2/M}} \right)^2 \approx 0.012. \quad (6.18)$$

In summary, variables σ , ν , and V_{c2}^* and their values are described in Table 6.2.

For our simulations, we use the initial condition $\xi(0) = 10^5$ (the rest of the variables are set to zero), and integrate until ξ reaches $\xi = -10^5$. Then, we apply a radiation pulse of intensity D at time t_0 (see equation (6.4)) and compute $\tilde{t}_R(t_0, D)$ (see equation (6.16)) for a discretization of the time domain, $[0, T_{G2/M}]$ (measured in hours), and dose domain, $[0, 1]$ (measured in Gy). The resulting graph of $\tilde{t}_R(t_0, D)$ is shown in Figure 6.4a, alongside the corresponding graph of the time available for repair, $t_R(t_0, D)$, found in Chapter 3.

In this figure, we observe that time available for repair for the normal form, equation (6.16) and the time available for repair using the full cell cycle model, equation

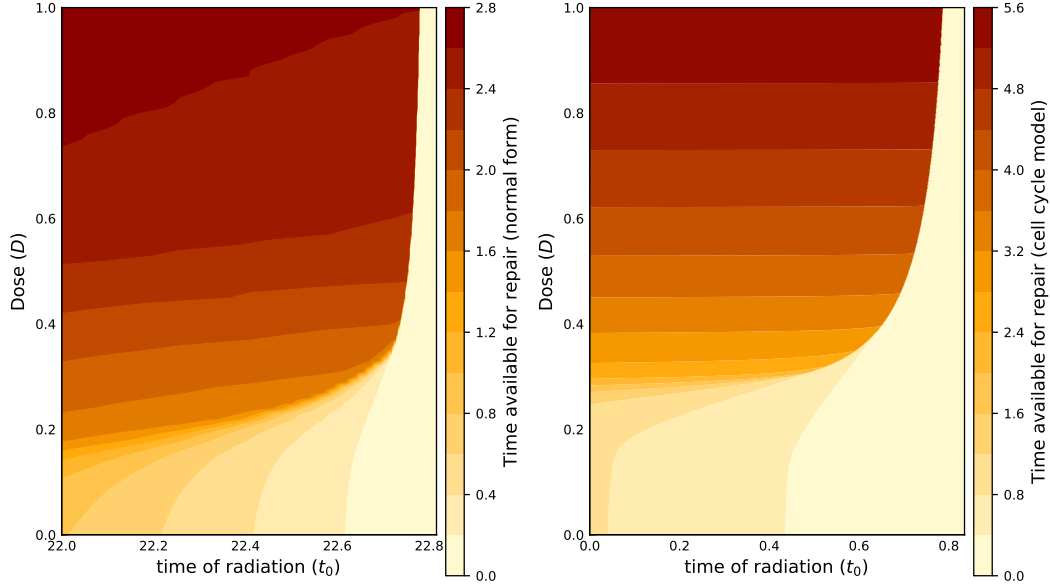


Figure 6.4: Numerical time available for repair for a) the cell cycle and radiation pathway (6.1) with a zoom in the G2/M transition ($t \in (t_{G2/M}^{\text{start}}, t_M)$), and b) the normal form with radiation (6.15).

(6.8) have the same qualitative behaviour. That is, the normal form approximation describes the core behaviour of the cell cycle in response to radiation during the G2/M transition, namely, the two thresholds described in Chapter 2. These results support our assumption on the linear dependence of ρ on V_{c2} , equation (6.13).

6.3 Average number of lethal lesions due to G2 checkpoint failure

In the previous section, we showed that the reduction to normal form for the SNIC bifurcation (6.10) approximates the dynamics of the cell cycle model and describes the time available for repair (6.8) for a pulse of radiation during the late G2-phase. Thus, we can compute the average number of lethal lesions due to checkpoint failure (6.9) by separating the integral into two parts; one prior to the G2/M transition

($t_0 \in [0, t_{G2/M}^{\text{start}}]$), and the other one during the G2/M transition ($t_0 \in I_{G2/M} = [t_{G2/M}^{\text{start}}, t_{G2/M}^{\text{end}}] = [t_{G2/M}^{\text{start}}, t_M]$)

$$\lambda_{G2/M}(D) = \frac{\alpha_0 k_{d1} D}{t_M} \left[\underbrace{\int_0^{t_{G2/M}^{\text{start}}} e^{-k_{d2} t_R(t_0, D)} f(t_0) dt_0}_I + \underbrace{\int_{t_{G2/M}^{\text{start}}}^{t_M} e^{-k_{d2} t_R(t_0, D)} f(t_0) dt_0}_{II} \right]. \quad (6.19)$$

The integral I in (6.19) captures the effect of radiation on the G2/M transition prior to it, while the integral II captures the effect of radiation on the G2/M transition during the G2/M transition itself, as illustrated in Figure 3.9.

The value of $t_{G2/M}^{\text{start}}$ depends on the time required to repair the number of DSBs induced by the radiation treatment ($k_{d1} D$ DSBs in the case of the radiation pulse) and therefore on the dose D .

In Section 6.3.1, we compute I . In Section 6.3.2, we compute II . In Section 6.3.3, we combine these results to obtain the average number of lethal lesions.

6.3.1 Time available for repair prior to the G2/M transition

DSBs formed prior to the M-phase entry have little or no impact on the G2/M transition because they get repaired before they affect the transition. This means that the time of M-phase entry can be approximated with the same time under no radiation

$$t_M(t_0, D) \approx t_M(0, 0) = t_M.$$

Thus, the time available for repair is independent of the intensity D

$$t_R(t_0, D) = t_M - t_0,$$

as well as the integral I in (6.19)

$$\begin{aligned} I &= \int_0^{t_{G2/M}^{\text{start}}} e^{-k_{d2}t_R(t_0, D)} f(t_0) dt_0 \\ &\approx \int_0^{t_{G2/M}^{\text{start}}} e^{-k_{d2}(t_M - t_0)} f(t_0) dt_0 \\ &= e^{-k_{d2}t_M} \int_0^{t_{G2/M}^{\text{start}}} e^{k_{d2}t_0} f(t_0) dt_0. \end{aligned} \quad (6.20)$$

6.3.2 Time available for repair during the G2/M transition

Consider the non-autonomous version of the normal form for the saddle-node bifurcation

$$\frac{d\xi}{dt} = -\rho + g(t) - \gamma\xi^2, \quad (6.21)$$

where ρ and γ are positive constants, $g(t)$ is non-negative with $\text{supp}(g) \subseteq (t_0, \infty)$, and $\xi(0) = \infty$ is the default initial condition.

In our case, ρ is defined as in equation (6.13) and

$$g(t) = \nu k_{c2a} C h k_2(t), \quad (6.22)$$

is the input from the radiation pathway (see equation (6.15a)). Note that $g(t) = g(t; t_0, D)$ depends on the intensity of radiation D and the time of radiation t_0 .

Non-autonomous systems of the form (6.21) have been studied within the theory of non-autonomous dynamical systems [44]. This theory focuses on the existence of pullback and forward attractors, terminology used to refer to time-dependent steady

states for non-autonomous systems analogous to the steady states in autonomous systems. Moreover, the non-autonomous normal form for the saddle-node bifurcation (normal form (6.21) without the resetting condition) has been studied by Li et al. [55] when $g(t)$ is a linear function of time, and by Langa et al. [50] and Kim and O [42] for more general functions $g(t)$.

In our study, we are interested in the effect of the external input $g(t)$ on the evolution of $\xi(t)$. For this purpose, we use an alternative method to analyze the non-autonomous normal form by transforming it into the corresponding phase model

$$\frac{d\vartheta}{dt} = 1 - \frac{1}{\rho} \sin^2(\sqrt{\rho\gamma}\vartheta) g(t), \quad \vartheta \in [0, T_{G2/M}], \quad (6.23)$$

where $T_{G2/M} = \frac{\pi}{\sqrt{\rho\gamma}}$ is the length of the autonomous normal form, and ϑ , called the *phase of ξ* , is the parameter in the interval $[0, T_{G2/M}]$ used for the parameterization of the solution $\xi(t)$ of equation (6.10) (see Appendix 6.A for details on the phase model). Note that we identify the interval $I_{G2/M}$ (equation (6.11)) with $[0, T_{G2/M}]$. The parameterization is the mapping $\vartheta \mapsto \xi(\vartheta)$ from the interval $[0, T_{G2/M}]$ into the phase space \mathbb{R} , which satisfies

$$\xi(\vartheta = 0) = \infty, \quad \text{and} \quad \xi(\vartheta = T_{G2/M}) = -\infty. \quad (6.24)$$

The phase model usually appears in the context of oscillatory systems and SNIC bifurcations, where $\xi = -\infty$ and $\xi = \infty$ are glued together to define a reset. However, here we are only interested in the first phase of ξ without resetting it at $-\infty$.

In the autonomous case, $g(t) \equiv 0$, the phase coincides with time $\frac{d\vartheta}{dt} = 1$, i.e., $\vartheta(t) = t$. In the non-autonomous case, $\vartheta(t)$ changes with $g(t)$, being more sensitive

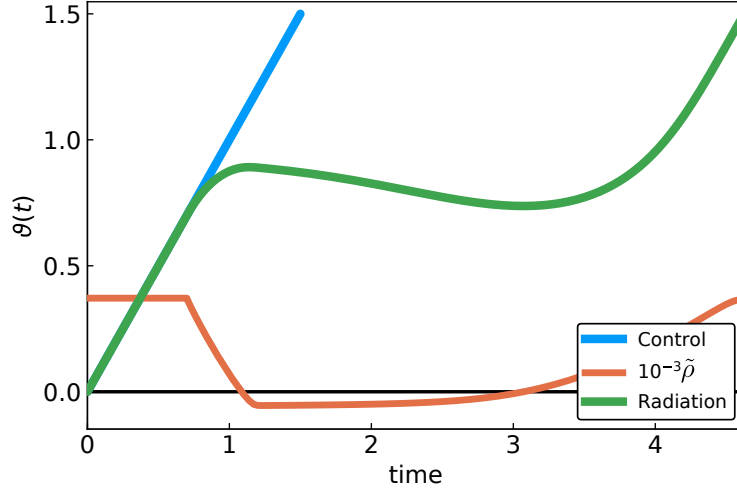


Figure 6.5: Solution of the phase model (6.23). Equation (6.15a) was replaced by (6.23) and the radiation scheme, parameters, and initial conditions match those in Figure 6.3. The y -axis of $\tilde{\rho}$ has been rescaled for the clarity of the graph.

to $g(t)$ at $T_{G2/M}/2$ where $\sin^2(\cdot)$ is maximal, and less sensitive to $g(t)$ at the end points of $[0, T_{G2/M}]$ where $\sin^2(\cdot)$ is minimal. Figure 6.5 shows the solution of the phase model for $g(t) \equiv 0$ and $g(t) \neq 0$ describing the same profile of the radiation pathway as in Figure 6.2. The introduction of a non-zero $g(t)$ causes a delay in the phase in the same way the non-autonomous normal form experiences a delay.

We can use the non-autonomous phase model (6.23) to find an approximation for the time available for repair $t_R(t_0, D)$ for cells exposed to radiation close to the $\text{SNIC}_{V_{c2}}$ bifurcation (locally a saddle-node bifurcation), i.e., between $t_{G2/M}^{\text{start}}$ and $t_{G2/M}^{\text{end}} = t_M$ (see equation (6.19)), as

$$t_R(t_0, D) = T_{G2/M}(t_0, D) - t_0, \quad (6.25)$$

where $T_{G2/M}(t_0, D)$ is defined as the time it takes ϑ to go from 0 to $T_{G2/M}$. Note that $\vartheta(T_{G2/M}(t_0, D)) = T_{G2/M}$.

If we integrate the phase model (6.23) from t_0 to $T_{G2/M}(t_0, D)$ with respect to

t , we obtain

$$\int_{\vartheta(t_0)}^{\vartheta(T_{G2/M}(t_0, D))} d\vartheta = \int_{t_0}^{T_{G2/M}(t_0, D)} \left(1 - \frac{1}{\rho} \sin^2(\sqrt{\rho\gamma}\vartheta) g(t) \right) dt$$

$$\implies \vartheta(T_{G2/M}(t_0, D)) - \vartheta(t_0) = T_{G2/M}(t_0, D) - t_0 - \frac{1}{\rho} \int_{t_0}^{T_{G2/M}(t_0, D)} \sin^2(\sqrt{\rho\gamma}\vartheta) g(t) dt.$$

Therefore,

$$T_{G2/M} - t_0 = T_{G2/M}(t_0, D) - t_0 - \frac{1}{\rho} \int_{t_0}^{T_{G2/M}(t_0, D)} \sin^2(\sqrt{\rho\gamma}\vartheta) g(t) dt.$$

Isolating the term $T_{G2/M}(t_0, D) - t_0$ and using $T_{G2/M} = \frac{\pi}{\sqrt{\rho\gamma}}$, we find an expression for the time available for repair $t_R(t_0, D)$ defined in (6.25)

$$t_R(t_0, D) = T_{G2/M}(t_0, D) - t_0 \approx \underbrace{\frac{\pi}{\sqrt{\rho\gamma}} - t_0}_{\text{time with no radiation}} + \underbrace{\frac{1}{\rho} \int_{t_0}^{T_{G2/M}(t_0, D)} \sin^2(\sqrt{\rho\gamma}\vartheta) g(t) dt}_{\text{delay due to radiation}}. \quad (6.26)$$

Before we substitute (6.26) into integral II in equation (6.19), we note that the time available for repair calculated is with respect to the phase model (i.e., is the time domain of the phase $\vartheta(t)$), whereas the integration time of equation (6.19) is with respect to the cell cycle time of a control cell. Thus, we approximate the integral II in equation (6.19) by changing the limits of integration from $[t_{G2/M}^{\text{start}}, t_M]$ to the corresponding analogous times with respect to the phase domain $[0, T_{G2/M}]$, i.e.,

$$II \approx \int_0^{T_{G2/M}} e^{-k_{d2}t_R(t_0, D)} f(t_0 + t_{G2/M}^{\text{start}}) dt_0$$

$$\begin{aligned}
&= \int_0^{\frac{\pi}{\sqrt{\rho\gamma}}} e^{-k_{d2}(\frac{\pi}{\sqrt{\rho\gamma}}-t_0)} \\
&\quad \times e^{-\frac{k_{d2}}{\rho} \left(\int_{t_0}^{T_{G2/M}(t_0, D)} \sin^2(\sqrt{\rho\gamma}\vartheta) g(t) dt \right)} f(t_0 + t_{G2/M}^{\text{start}}) dt_0. \quad (6.27)
\end{aligned}$$

6.3.3 Combined average number of lethal lesions due to G2 checkpoint failure away and during the G2/M transition

Combining equations (6.20) and (6.27), we obtain an approximation for the average number of lethal lesions due to G2 checkpoint failure (6.19)

$$\begin{aligned}
\lambda_{G2/M}(D) &= \frac{\alpha_0 k_{d1} D}{t_M} I + \frac{\alpha_0 k_{d1} D}{t_M} II \\
&\approx \underbrace{\frac{\alpha_0 k_{d1} e^{-k_{d2} t_M}}{t_M} \left(\int_0^{t_{G2/M}^{\text{start}}} e^{k_{d2} t_0} f(t_0) dt_0 \right)}_{\text{prior to the G2/M transition}} D \\
&\quad + \frac{\alpha_0 k_{d1}}{t_M} \left(\int_0^{\frac{\pi}{\sqrt{\rho\gamma}}} e^{-k_{d2}(\frac{\pi}{\sqrt{\rho\gamma}}-t_0)} \right. \\
&\quad \left. \times e^{-\frac{k_{d2}}{\rho} \left(\int_{t_0}^{T_{G2/M}(t_0, D)} \sin^2(\sqrt{\rho\gamma}\vartheta) g(t) dt \right)} f(t_0 + t_{G2/M}^{\text{start}}) dt_0 \right) D. \quad (6.28) \\
&\quad \underbrace{\hspace{15em}}_{\text{during the G2/M transition}}
\end{aligned}$$

In the expression above, we see that prior to the G2/M transition, the average number of lethal lesions is proportional to the dose D , whereas during the G2/M transition is potentially non-linear in D since the dose affects the integrand.

In the next section, we will see how the explicit expression for the time available for repair (6.26), obtained through the phase model, allows us to come up with an approximated theoretical expression for the survival fraction that can explain the HRS/IRR phenomenon.

6.4 Understanding the effect of an impulse $g(t)$ on the phase model

In this section, we assume a homogeneous distribution of cells over the cell cycle, $f(t) = \frac{1}{T}$. In such a case, equation (6.20) becomes

$$I \approx e^{-k_{d2}t_M} \int_0^{t_{G2/M}^{\text{start}}} e^{k_{d2}t_0} \frac{1}{T} dt_0 = \frac{e^{-k_{d2}t_M}}{k_{d2}T} (e^{k_{d2}t_{G2/M}^{\text{start}}} - 1).$$

and the average number of lethal events due to G2/M checkpoint failure prior to the G2/M transition, given the first term in equation (6.28), becomes

$$\lambda_{G2/M}(D) \approx \frac{\alpha_0 k_{d1} e^{-k_{d2}t_M} (e^{k_{d2}t_{G2/M}^{\text{start}}} - 1)}{k_{d2}t_M T} D. \quad (6.29)$$

Ideally, we would like to solve equation (6.26) with an expression of $g(t)$ as the solution of the radiation pathway (note the dependence of $g(t)$ on $Chk2(t)$ in equation (6.22)) or a window function that approximates the solution (see the dynamical behaviour of Chk2 in Figure 6.4). However, for the sake of simplicity, we will consider the following pulse function to describe the behaviour of the input function

$$g(t) = \rho_0(D) \delta(t - t_0), \quad (6.30)$$

where $\rho_0(D)$ is given by the steady-state solution of $Chk2$ (obtained by applying equation (6.45) to equation (6.15b))

$$\rho_0(D) = k_{c2a} GK(k_{h1} k_{d1} D, V_{h2}, J_{h1}, J_{h2}), \quad (6.31)$$

and $GK(\cdot)$ is the Goldbeter-Koshland function (see Appendix 6.B). Function $\rho_0(D)$

is a steep sigmoidal function of D with minimum value zero at $D = 0$, half value at $D = V_{h2}/(k_{h1}k_{d1})$, and maximum asymptotic value k_{c2a} for $D \gg \frac{V_{h2}}{k_{h1}k_{d1}}$. This choice of $g(t)$ is only relevant for small values of D .

Using the pulse (6.30) in the time available for repair (6.26) for the phase model, we obtain

$$\begin{aligned} t_R(t_0, D) &= \frac{\pi}{\sqrt{\rho\gamma}} - t_0 + \frac{1}{\rho} \int_{t_0}^{T_{G2/M}(t_0, D)} \sin^2(\sqrt{\rho\gamma}\vartheta) \rho_0(D) \delta(t - t_0) dt \\ &= \frac{\pi}{\sqrt{\rho\gamma}} - t_0 + \frac{\rho_0(D)}{\rho} \int_{-\infty}^{\infty} \sin^2(\sqrt{\rho\gamma}\vartheta) \delta(t - t_0) dt \\ &= \frac{\pi}{\sqrt{\rho\gamma}} - t_0 + \frac{\rho_0(D)}{\rho} \sin^2(\sqrt{\rho\gamma}\vartheta(t_0)). \end{aligned}$$

Since $\vartheta(t_0) = t_0$, the time available for repair simplifies to

$$t_R(t_0, D) = \frac{\pi}{\sqrt{\rho\gamma}} - t_0 + \frac{\rho_0(D)}{\rho} \sin^2(\sqrt{\rho\gamma}t_0).$$

Substituting this time available for repair into integral II of equation (6.27), and assuming a homogeneous distribution of cells over the cell cycle $f(t) = \frac{1}{T}$, we obtain

$$\begin{aligned} II &\approx \int_0^{\frac{\pi}{\sqrt{\rho\gamma}}} e^{-k_{d2}\left(\frac{\pi}{\sqrt{\rho\gamma}} - t_0\right)} e^{-\frac{k_{d2}\rho_0(D)}{\rho} \sin^2(\sqrt{\rho\gamma}t_0)} \frac{1}{T} dt_0 \\ &= \frac{1}{T} \int_0^{\frac{\pi}{\sqrt{\rho\gamma}}} e^{-k_{d2}\left(\frac{\pi}{\sqrt{\rho\gamma}} - t_0\right)} e^{-\frac{k_{d2}\rho_0(D)}{2\rho} (1 - \cos(2\sqrt{\rho\gamma}t_0))} dt_0 \\ &= \frac{1}{T} e^{-\frac{k_{d2}\rho_0(D)}{2\rho}} \int_0^{\frac{\pi}{\sqrt{\rho\gamma}}} e^{-k_{d2}\left(\frac{\pi}{\sqrt{\rho\gamma}} - t_0\right)} e^{\frac{k_{d2}\rho_0(D)}{2\rho} \cos(2\sqrt{\rho\gamma}t_0)} dt_0 \\ &= \frac{1}{2\sqrt{\rho\gamma}T} e^{-\frac{k_{d2}\rho_0(D)}{2\rho}} \int_0^{2\sqrt{\rho\gamma}\frac{\pi}{\sqrt{\rho\gamma}}} e^{-k_{d2}\left(\frac{\pi}{\sqrt{\rho\gamma}} - \frac{s}{2\sqrt{\rho\gamma}}\right)} e^{\frac{k_{d2}\rho_0(D)}{2\rho} \cos(s)} ds \\ &= \frac{1}{2\sqrt{\rho\gamma}T} e^{-\frac{k_{d2}\rho_0(D)}{2\rho}} \int_0^{2\pi} e^{-\frac{k_{d2}}{2\sqrt{\rho\gamma}}(2\pi - s)} e^{\frac{k_{d2}\rho_0(D)}{2\rho} \cos(s)} ds, \end{aligned}$$

after using the substitution $s = 2\sqrt{\rho\gamma}t_0$.

Since

$$e^{-\frac{k_{d2}\pi}{\sqrt{\rho\gamma}}} \leq e^{-\frac{k_{d2}}{2\sqrt{\rho\gamma}}(2\pi-s)} \leq 1,$$

for $0 \leq s \leq 2\pi$, we find the following lower and upper bounds for II

$$\frac{1}{2\sqrt{\rho\gamma}T} e^{-\frac{k_{d2}\rho_0(D)}{2\rho}} e^{-\frac{k_{d2}\pi}{\sqrt{\rho\gamma}}} \int_0^{2\pi} e^{\frac{k_{d2}\rho_0(D)}{2\rho} \cos(s)} ds \leq II \leq \frac{1}{2\sqrt{\rho\gamma}T} e^{-\frac{k_{d2}\rho_0(D)}{2\rho}} \int_0^{2\pi} e^{\frac{k_{d2}\rho_0(D)}{2\rho} \cos(s)} ds.$$

Given that

$$\int_0^{2\pi} e^{x \cos(s)} ds = 2\pi I_0(x),$$

where $I_0(x)$ is the modified Bessel function of the first kind ($n = 0$)

$$I_0(x) = \sum_{k=0}^{\infty} \frac{1}{(k!)^2} \left(\frac{x}{2}\right)^{2k},$$

the lower and upper bounds for II can be written as

$$\frac{\pi}{\sqrt{\rho\gamma}T} e^{-\frac{k_{d2}\rho_0(D)}{2\rho}} e^{-\frac{k_{d2}\pi}{\sqrt{\rho\gamma}}} I_0\left(\frac{k_{d2}\rho_0(D)}{2\rho}\right) \leq II \leq \frac{\pi}{\sqrt{\rho\gamma}T} e^{-\frac{k_{d2}\rho_0(D)}{2\rho}} I_0\left(\frac{k_{d2}\rho_0(D)}{2\rho}\right).$$

By continuity, there exists an $a \in [0, 1]$ such that

$$II = \frac{\pi}{\sqrt{\rho\gamma}T} e^{-\frac{ak_{d2}\pi}{\sqrt{\rho\gamma}}} e^{-\frac{k_{d2}\rho_0(D)}{2\rho}} I_0\left(\frac{k_{d2}\rho_0(D)}{2\rho}\right).$$

For small D , we can use the linear approximation (see equation (6.46))

$$\rho_0(D) \approx cD = \frac{k_{c2a}J_{h2}k_{h1}k_{d1}}{(1 + J_{h1})V_{h2}}D, \quad (6.32)$$

to rewrite II as

$$\begin{aligned} II &\approx \frac{\pi}{\sqrt{\rho\gamma}T} e^{-\frac{ak_{d2}\pi}{\sqrt{\rho\gamma}}} e^{-\frac{ck_{d2}}{2\rho}D} I_0\left(\frac{ck_{d2}}{2\rho}D\right) \\ &= \frac{\pi}{\sqrt{\rho\gamma}T} e^{-\frac{ak_{d2}\pi}{\sqrt{\rho\gamma}}} e^{-\frac{ck_{d2}}{2\rho}D} \left(1 + \frac{1}{16}\left(\frac{ck_{d2}}{\rho}\right)^2 D^2 + \frac{1}{1024}\left(\frac{ck_{d2}}{\rho}\right)^4 D^4 + \dots\right). \end{aligned}$$

Multiplying this by the term $\alpha_0 k_{d1} D/t_M$ in equation (6.19), gives us an expression for the average number of lethal lesions during the G2/M transition that depends on the inactivation rate of Chk2 ($\rho = \nu(V_{c2}^* - V_{c2})$) and the DSBs formation and repair rates

$$\begin{aligned} \lambda_{G2/M}(D) &\approx \frac{\alpha_0 k_{d1}}{t_M} \frac{\pi}{\sqrt{\rho\gamma}T} e^{-\frac{ak_{d2}\pi}{\sqrt{\rho\gamma}}} e^{-\frac{ck_{d2}}{2\rho}D} \left(D + \right. \\ &\quad \left. \frac{1}{16}\left(\frac{ck_{d2}}{\rho}\right)^2 D^3 + \frac{1}{1024}\left(\frac{ck_{d2}}{\rho}\right)^4 D^5 + \dots \right). \quad (6.33) \end{aligned}$$

Combining the average number of lethal lesions prior to the G2/M transition (6.29) and during the G2/M transition (6.33), we find

$$\begin{aligned} \lambda_{G2/M}(D) &= \frac{\alpha_0 k_{d1} e^{-k_{d2}t_M} (e^{k_{d2}t_{G2/M}^{\text{start}}} - 1)}{k_{d2}t_M T} D \\ &\quad + \frac{\alpha_0 k_{d1}}{t_M} \frac{\pi}{\sqrt{\rho\gamma}T} e^{-\frac{ak_{d2}\pi}{\sqrt{\rho\gamma}}} e^{-\frac{ck_{d2}}{2\rho}D} \left(D \right. \\ &\quad \left. + \frac{1}{16}\left(\frac{ck_{d2}}{\rho}\right)^2 D^3 + \frac{1}{1024}\left(\frac{ck_{d2}}{\rho}\right)^4 D^5 + \dots \right). \end{aligned}$$

Ignoring higher order terms, the total average number of lethal lesions (6.5) becomes

$$\begin{aligned}\lambda(D) &= \lambda_{\text{other}}(D) + \lambda_{G2/M}(D) \\ &\approx \hat{\alpha}D + \hat{\beta}D^2 + \frac{\alpha_0 k_{d1} e^{-k_{d2} t_M} (e^{k_{d2} t_{G2/M}^{\text{start}}} - 1)}{k_{d2} t_M T} D \\ &\quad + \frac{\alpha_0 k_{d1}}{t_M} \frac{\pi}{\sqrt{\rho\gamma} T} e^{-\frac{\alpha k_{d2} \pi}{\sqrt{\rho\gamma}}} e^{-\frac{c k_{d2}}{2\rho} D} D. \quad (6.34)\end{aligned}$$

Note that the equations above are valid for a small radiation dose (needed to obtain approximations (6.30), (6.32), and assumed to have an active ATM in order to write (6.7) explicitly) and for a uniform distribution of cells over the cell cycle ($f(t) = 1/T$). In Section 3.3, we observed that such assumptions result in a HRS/IRR effect in the survival fraction.

Moreover, the expression of the total number of lethal lesions (6.34) provides an underlying kinetic process for the Induced Repair (IR) model (1.2)

$$-\log(S_{IR}(D)) = (\alpha_r + (\alpha_s - \alpha_r) e^{-\frac{D}{d_c}}) D + \beta D^2,$$

with

$$\begin{aligned}\alpha_r &= \hat{\alpha} + \frac{\alpha_0 k_{d1} e^{-k_{d2} t_M} (e^{k_{d2} t_{G2/M}^{\text{start}}} - 1)}{k_{d2} t_M T}, \\ \alpha_s - \alpha_r &= \frac{\alpha_0 k_{d1}}{t_M} \frac{\pi}{\sqrt{k_{m3} \sigma \nu (V_{c2}^* - V_{c2})} T} e^{-\frac{\alpha k_{d2} \pi}{\sqrt{k_{m3} \sigma \nu (V_{c2}^* - V_{c2})}}}, \\ d_c &= \frac{2\nu V_{h2} (V_{c2}^* - V_{c2}) (1 + J_{h1})}{k_{d1} k_{d2} k_{h1} k_{c2a} J_{h2}} \\ \beta &= \hat{\beta}.\end{aligned}$$

6.5 Discussion

In this chapter, we summarized the results from the previous chapters and used them to derive a theoretical expression for the survival fraction based on the G2/M transition. In Section 6.2, we combined the normal form of the cell cycle around the SNIC bifurcation driven by V_{c2} , derived in Chapter 5, with the radiation pathway. We showed that the normal form captures the effect of radiation on the G2/M transition as studied in Chapter 2. In particular, we showed that we can approximate the time available for repair for the cell cycle model, defined in Chapter 3, using the normal form. Given that parameters in the normal form depend in a complex way on the cell cycle model parameters and could not be determined explicitly, we assumed that the independent term of the normal form depends linearly on the parameter V_{c2} .

In Section 6.3, we derived a theoretical expression for the average number of lethal lesions due to G2 checkpoint failure, developed in Chapter 3, and separated it into two parts. First, a part prior to the G2/M transition where there is enough time to repair radiation damage and the M-phase entry is not affected. This results in a linear term with respect to the dose D in the average number of lethal lesions. Second, a part during the G2/M transition where the moment of M-phase entry is governed by the normal form. We transformed the normal form into its corresponding phase model to derive a theoretical expression that captures how the time available for repair is delayed based on the radiation pathway. This results in a non-linear term with respect to the dose D .

In Section 6.4, we showed that for a simplified radiation pathway (a pulse) and a homogeneous distribution of cells over the cell cycle, the total average number of lethal events, developed in Chapter 3, is equivalent to the yield of lesions of the Induced Repair (IR) model. We derived a novel explicit expression for the

non-linear part of the average number of lethal lesions in terms of the parameters of the cell cycle model and radiation pathway, by considering lethal lesions due to G2 checkpoint failure. Our result provides a biological and mechanistic explanation for the empirical parameters in the IR model, widely used to describe survival fraction data with a hyper-radiosensitivity and increased radioresistance (HRS/IRR) effect. This includes the rates for DSBs formation and repair, the inactivation rate of Cdc25, the theoretical bifurcation value V_{c2}^* , the length of the interphase and the cell cycle, the rate of degradation of MPF, and the Michaelis-Menten rates associated with Chk2 activation, among others.

To our knowledge, this is the first time the IR model is explained in terms of mechanisms regulating the cell cycle and a pathway of kinetic reactions induced by radiation. Moreover, we showed that the non-linear component of the HRS/IRR effect is due to the effect of radiation on the G2/M transition governed by a saddle-node bifurcation driven by Chk2 activation. Olobatuyi et al. [78] provided an explanation for the IR model in terms of the probability of G2 checkpoint activation, the damage induced by radiation during the G2-phase, repair rate, and mitotic catastrophe rate. We believe that our results provide meaningful insights on some of the components in their model. For instance, we believe the function $c(D)$ in equation (5) in Olobatuyi et al. [78] is intrinsically related to function $\rho_o(D)$ in equation (6.32). To explore this further, it would be necessary to study the relationship between their compartmental approach and our mechanistic approach. Bodgi and Foray [5] derived an alternative mechanistic explanation for the IR model based on the monomerization pathway of ATM. However, this approach does not provide insights on the participation of the G2 checkpoint on the HRS/IRR effect. We note that the studying the mechanisms regulating the cell cycle and the pathway of radiation is not the only way to explain the IR model, since it is

known that there are exclusive mechanisms that result in the HRS/IRR phenomenon [66, 67, 47, 45, 104, 77].

For obtaining the average number of lethal lesions due to checkpoint failure, we considered the time available for repair for lesions caused prior to and during the G2/M transition (see equation (6.19)). We note that high radiation causes more damage, which in turn requires more time to repair. Thus, if the time required to repair damage is larger than the duration of the G2/M transition, then radiation begins to affect M-phase entry prior to the G2/M transition.

We are aware of some of the limitations in our approach. For example, we did not account for any other checkpoint that might be triggered by radiation. Also, we neglected ATM activity in order to simplify our calculations.

We believe that the phase model approach introduced in this chapter could be used to describe the effect of radiation on other mechanisms that regulate the cell cycle dynamics and, therefore, to obtain a more general survival fraction model. In Chapter 7, we propose a general phase model for the cell cycle based on the results of this chapter and discuss its potential applications to radiobiology.

Appendices

6.A Phase model for the normal form of the SNIC bifurcation

Consider the normal form for the SNIC bifurcation

$$\frac{dx}{dt} = -b - cx^2, \quad x(0) = \infty, \quad x = -\infty \implies x \leftarrow \infty \text{ (reset)}. \quad (6.35)$$

where $b > 0, c > 0$. Note that this is the normal form for the saddle-node bifurcation, studied in the Appendix 5.B, with a resetting condition that glues together $x = -\infty$ and $x = \infty$. This causes an oscillatory solution of the form

$$x(t) = \sqrt{\frac{b}{c}} \cot(\sqrt{bct}), \quad x = -\infty \implies x \leftarrow \infty \text{ (reset)}, \quad (6.36)$$

with period

$$T_{\text{blow}} = \pi/\sqrt{bc}. \quad (6.37)$$

We can reparametrize this oscillatory solution of period T_{blow} with respect to a new parameter ϑ , called the *phase of the oscillation*, in the circle \mathbb{S}^1 of circumference T_{reset} in the following way:

$$p: \mathbb{S}^1 \rightarrow \mathbb{R},$$

such that $\vartheta \mapsto x(\vartheta)$, where $\vartheta = t \bmod T_{\text{reset}}$. Using the phase of oscillation ϑ , we can transform the normal form of (6.35) to the canonical phase model

$$\frac{d\vartheta}{dt} = 1.$$

Consider now the non-autonomous case of the normal form for the SNIC bifurcation

$$\frac{dx}{dt} = -b + g(t) - cx^2, \quad x(0) = \infty, \quad x = -\infty \implies x \leftarrow \infty \text{ (reset)}, \quad (6.38)$$

where $g(t)$ is a time-dependent input. This system, which describes bursting of neurons, is widely studied in neuroscience [38]. For the non-autonomous case, the phase of oscillation ϑ can also be used to transform the normal form (6.38) to the

phase model

$$\frac{d\vartheta}{dt} = 1 - \frac{1}{b} \sin^2 \left(\sqrt{bc}\vartheta \right) g(t), \quad (6.39)$$

up to terms of order $o(|g(t)|)$ (see Izhikevich [38, Ch. 10] for details). The second term in the right hand side of equation (6.39) is the change in the phase caused by $g(t)$ through the Phase Response Curve (PRC)

$$\text{PRC}(\vartheta) = \frac{1}{b} \sin^2 \left(\sqrt{bc}\vartheta \right).$$

The PRC measures the shift in the phase caused by $g(t)$ depending on the phase of $x(t)$. Since the PRC above is always positive ($0 \leq \vartheta \leq T_{\text{blow}} = \frac{\pi}{\sqrt{bc}}$), a positive input $g(t)$ would cause a delay in the system due to the negative term in (6.39). The PRC can be found using, for example, Kuramoto's approach

$$\begin{aligned} \text{PRC}(\vartheta) &= \frac{1}{\frac{dx}{dt}(\vartheta)} = \frac{1}{-b - cx^2(\vartheta)} = \frac{-1}{b + c \left(\sqrt{\frac{b}{c}} \cot \left(\sqrt{bc}\vartheta \right) \right)^2} \\ &= \frac{-1}{b + c \frac{b}{c} \cot^2 \left(\sqrt{bc}\vartheta \right)} = \frac{-1}{b \left(1 + \cot^2 \left(\sqrt{bc}\vartheta \right) \right)} \\ &= \frac{-1}{b \csc^2 \left(\sqrt{bc}\vartheta \right)} = -\frac{1}{b} \sin^2 \left(\sqrt{bc}\vartheta \right), \end{aligned}$$

where $x(\vartheta)$ is the solution (6.36) to the normal form (6.35) evaluated at ϑ .

Note that the effect of a positive input $g(t)$ is maximal when the phase is half-period ($\vartheta = T_{\text{reset}}/2$) and minimal near the reset where $\sin^2(\sqrt{\rho\gamma}\vartheta)$ reaches a minimum.

6.B Goldbeter-Koshland kinetics

The *Goldbeter-Koshland* kinetics model describes the dynamics of a protein R that is phosphorylated to be transformed into R_P , and where phosphorylation and dephosphorylation are promoted by proteins S_1 and S_2 . The diagram of the reaction is shown in Fig. 6.6.

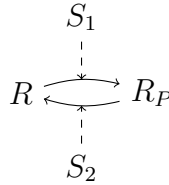


Figure 6.6: Diagram of Goldbeter-Koshland kinetics

The rate of reaction is modelled in a Michaelian form

$$r_1 = \frac{k_1 S_1 R}{J_1 + R}, \quad r_2 = \frac{k_2 S_2 R_P}{J_2 + R_P},$$

where k_1 and k_2 are the rate of phosphorylation by S , and J_1 and J_2 are the Michaelis-Menten constants [86].

If we assume that the total concentration of protein R is constant

$$R_T = R + R_P,$$

then the rate of change of R can be written as

$$\frac{dR_P}{dt} = \underbrace{\frac{k_1 S_1 (R_T - R_P)}{J_1 + (R_T - R_P)}}_{\text{rate of phosphorylation } r_1} - \underbrace{\frac{k_2 S_2 R_P}{J_2 + R_P}}_{\text{rate of dephosphorylation } r_2}, \quad (6.40)$$

or, if the concentration of S_1 and S_2 are not of interest,

$$\frac{dR_P}{dt} = \frac{V_1(R_T - R_P)}{J_1 + (R_T - R_P)} - \frac{V_2 R_P}{J_1 + R_P}, \quad (6.41)$$

where V_1 and V_2 are the maximum rate of phosphorylation and dephosphorylation of R . Equation (6.40) is often written as

$$\dot{x}(t) = v_1 \frac{1 - x}{J_1 + 1 - x} - v_2 \frac{x}{J_2 + x}. \quad (6.42)$$

Steady states

The steady states for the Goldbeter-Koshland kinetics are given by setting Eq. (6.41) equal to zero

$$\begin{aligned} 0 &= \frac{V_1(R_T - R_P)}{J_1 + (R_T - R_P)} - \frac{V_2 R_P}{J_1 + R_P} \\ \Rightarrow \frac{V_1(R_T - R_P)}{J_1 + (R_T - R_P)} &= \frac{V_2 R_P}{J_1 + R_P}. \end{aligned}$$

Dividing both sides by R_T and setting $z = \frac{R_P}{R_T}$ we obtain

$$\frac{V_1(1 - z)}{J_1 + (1 - z)} = \frac{V_2 z}{J_1 + z}.$$

Solving this equation we obtain the second degree polynomial on z

$$(V_2 - V_1)z^2 - (V_2 - V_1 + V_2 J_1 + V_1 J_2)z + V_1 J_2 = 0. \quad (6.43)$$

Eq. (6.43) has two roots of the form

$$z = \frac{B \pm \sqrt{B^2 - 4(V_2 - V_1)V_1 J_2}}{2(V_2 - V_1)}$$

where

$$B = V_2 - V_1 + V_2 J_1 + V_1 J_2.$$

After rationalization, we can write

$$z = \frac{2V_1 J_2}{B \mp \sqrt{B^2 - 4(V_2 - V_1)V_1 J_2}}.$$

It can be shown that the positive case gives a root that is always between 0 and 1.

Thus, the steady state value is

$$\frac{R_P^*}{R_T} = GK(V_1, V_2, J_1, J_2) = \frac{2V_1 J_2}{B + \sqrt{B^2 - 4(V_2 - V_1)V_1 J_2}}. \quad (6.44)$$

The function $GK(V_1, V_2, J_1, J_2)$ is known as the Goldbeter-Koshland function [94].

If we divide Eq. (6.44) by V_2 and use the value of B , we can make explicit the value of the steady state in terms of the quotient $\frac{V_1}{V_2}$,

$$\begin{aligned} \frac{R_P^*}{R_T} = GK(V_1, V_2, J_1, J_2) = & \\ & \frac{2\frac{V_1}{V_2} J_2}{\left(1 - \frac{V_1}{V_2}\right) + J_1 + J_2 \frac{V_1}{V_2} + \sqrt{\left[\left(1 - \frac{V_1}{V_2}\right) + J_1 + J_2 \frac{V_1}{V_2}\right]^2 - 4\left(1 - \frac{V_1}{V_2}\right) \frac{V_1}{V_2} J_2}}. \end{aligned} \quad (6.45)$$

Note that since $V_1 = k_1 S_1$, the quotient $\frac{V_1}{V_2}$ gives a measure of the concentration of the phosphorylating protein S_1 . A plot of the steady states in terms of the quotient $\frac{V_1}{V_2}$ is shown in Fig. 6.7. Here we observe that the protein R is dephosphorylated when $\frac{V_1}{V_2} < 1$ ($\frac{R_P}{R_T} \sim 0$ and $\frac{R}{R_T} \sim 1$) and is phosphorylated when $\frac{V_1}{V_2} > 1$ ($\frac{R_P}{R_T} \sim 1$ and $\frac{R}{R_T} \sim 0$). If R is dephosphorylated and V_1 increases (because S_1 increase) the transition to phosphorylation state happens close to $\frac{V_1}{V_2} \approx 1$, and the smaller

the values of J_1 and J_2 are the faster the transition is. Compare the slope when $J_1 = J_2 = 10^{-1}$ with the steeper slope when $J_1 = J_2 = 10^{-2}$. This feature is known as *ultra-sensitivity* of the phosphorylation of R by S_1 .

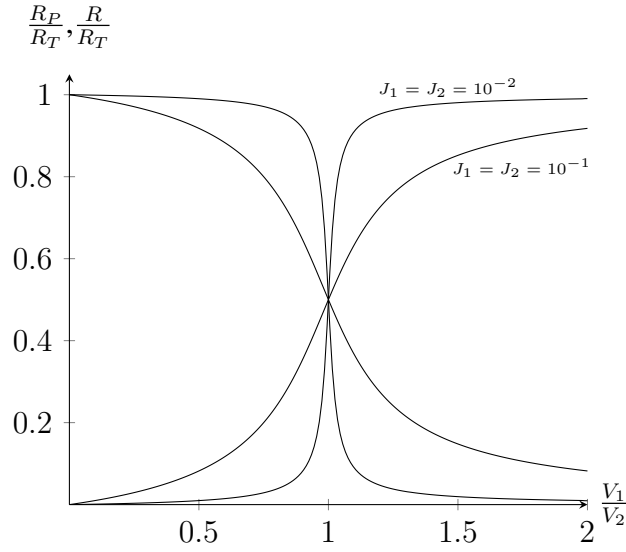


Figure 6.7: Goldbeter-Koshland function. The ultrasensitivity is refers to the steep slope at the inflection point $V_1/V_2 = 1$ for small Michaelis-Menten rates J_1 and J_2 .

The asymptotic expansion of (6.45) about $\frac{V_1}{V_2} = 0$ is given by

$$GK(V_1, V_2, J_1, J_2) \sim \frac{J_2}{1 + J_1} \frac{V_1}{V_2} + \frac{2(1 + J_1 - J_1 J_2) J_2}{(1 + J_1)^2} \left(\frac{V_1}{V_2} \right)^2. \quad (6.46)$$

6.C Table of parameter values

Table 6.3: Parameter values. Most parameter values have been taken from Gérard et al. [25] or adapted to match the cell cycle length in mammalian cells. Parameters related to the radiation pathway come from different sources or were cautiously chosen on the basis of numerical simulations. Details are provided in the footnotes that are referenced in the Source column. Parameters with no units are dimensionless.

Symbol	Definition	Value	Units	Source
k_{m0}	Rate of synthesis of Cdk-cyclin fusion protein, MPF	0.2	hr ⁻¹	¹
k_{m1}	Rate constant for the dephosphorylation of MPF	0.4	hr ⁻¹	²
k_{m1a}	Rate constant for the dephosphorylation of MPF by Cdc25	20.0	hr ⁻¹	2
k_{m2}	Rate constant for the phosphorylation of MPF	0.4	hr ⁻¹	2
k_{m2a}	Rate constant for the phosphorylation of MPF by Wee1	50.0	hr ⁻¹	1
k_{m3}	Rate constant for the degradation of MPF and MPF _P	0.2	hr ⁻¹	2
k_{m3a}	Rate constant for the degradation of MPF and MPF _P by APC	6.35	hr ⁻¹	2
V_{w1}	Maximum activation rate, by dephosphorylation, of Wee1	1.0	hr ⁻¹	2
k_{w2}	Rate constant for activation of Wee1 by MPF	5.3	hr ⁻¹	2
J_{w1}	Michaelis constant for Wee1 activation	0.01		³

continued...

¹Taken from Gérard et al. [25]; slightly modified to accommodate the correct G2/M transition dynamics.

²Taken from Gérard et al. [25]; scaling factor of 8.5 needed to rescale the length of the cell cycle to approximately 24 hrs.

³Taken from Gérard et al. [25].

...continued

Symbol	Definition	Value	Units	Source
J_{w2}	Michaelis constant for Wee1 inactivation	0.01		3
k_{c1}	Rate constant for Cdc25 phosphorylation by MPF	8.5	hr ⁻¹	2
V_{c2}	Maximum inactivation rate, by dephosphorylation, of Cdc25	1.4	hr ⁻¹	1
k_{c2a}	Rate constant for the inactivation of Cdc25 by Chk2	2.4	hr ⁻¹	4
J_{c1}	Michaelis constant for Cdc25 activation	0.01		3
J_{c2}	Michaelis constant for Cdc25 inactivation	0.01		3
k_{i1}	Rate constant for the activation of IE by MPF	1.7	hr ⁻¹	2
V_{i2}	Maximum inactivation rate of IE	0.4	hr ⁻¹	2
J_{i1}	Michaelis constant for IE activation	0.001		3
J_{i2}	Michaelis constant for IE inactivation	0.001		3
k_{a1}	Rate constant for the activation, by phosphorylation, of APC by IE	6.8	hr ⁻¹	2
V_{a2}	Maximum inactivation rate, by phosphorylation, of APC	1.7	hr ⁻¹	2
J_{a1}	Michaelis constant for APC activation	0.001		3
J_{a2}	Michaelis constant for APC inactivation	0.001		3
k_{h1}	Rate constant for the activation, by phosphorylation, of Chk2 by ATM	0.32	hr ⁻¹	5

continued...

⁴Educated guess.

⁵Chosen to fit activation time presented by Buscemi et al. [11].

...continued

Symbol	Definition	Value	Units	Source
V_{h2}	Maximum inactivation rate, by dephosphorylation, of Chk2	1.9	hr^{-1}	6
J_{h1}	Michaelis constant for Chk2 activation	0.01		4
J_{h2}	Michaelis constant for Chk2 inactivation	0.01		4
k_{t1}	Rate constant for the activation (recruitment and autophosphorylation) of ATM around DSB repair foci	30	$\text{dsb}^{-1}\text{hr}^{-1}$	7
V_{t2}	Maximum inactivation rate of ATM	3.8	hr^{-1}	2
J_{t1}	Michaelis constant for ATM auto-phosphorylation	0.01		4
J_{t2}	Michaelis constant for ATM deactivation	0.01		4
k_{d1}	Rate constant for DSBs damage formation	35.0	$\text{dsb} \cdot \text{Gy}^{-1}$	8
k_{d2}	Rate constant for DSBs repair	0.4	hr^{-1}	9
α	Partial activity of MPF _P	0.05		2
μ	Growth rate of the cell	0.07	hr^{-1}	10
K_{Mass}	Maximum cell mass	2.7		4
$Wee1_T$	Total concentration of kinase Wee1	1.0		2
$Cdc25_T$	Total concentration of phosphatase Cdc25	1.0		2
IE_T	Total concentration of intermediate enzyme IE	1.0		2

continued...

⁶Chosen to fit Chk2 activation threshold after radiation [37].

⁷Taken from Kozlov et al. [45].

⁸Taken from Rothkamm and Löbrich [83].

⁹Taken from Scott [85].

¹⁰Informed by Park et al. [80].

...continued

Symbol	Definition	Value	Units	Source
APC_T	Total concentration of protein APC	1.0		2
$Chk2_T$	Total concentration of Checkpoint kinase 2	1.0		4
ATM_T	Total concentration of ATM	1.0		4

Chapter 7

Discussion and future work

7.1 Summary and discussion

The mechanisms governing the hyper-radiosensitivity and increased radioresistance (HRS/IRR) phenomenon remain unclear [57, 92, 3]. There has been important progress in this area during recent years, which has required advanced mathematical modelling of the cellular mechanisms affected by radiation [5, 78]. Bodgi et al. [6] consider that a mathematically sophisticated approach is necessary to understand the effect of radiation on cells. Despite being widely accepted and used in cell survival data, the Linear Quadratic (LQ) model [40, 41], suitable for most cell survival data [8], and the Induced Repair (IR) model, suitable for cell survival data showing HRS/IRR [92], are empirical models without a clear interpretation of the parameters therein [6].

In this thesis, we seek a mechanistic explanation for the HRS/IRR phenomenon based on the hypothesis that the G2 checkpoint plays a key role in the HRS/IRR [58]. We consider a multi-level modelling approach. At the individual level, we modelled the cell cycle and the kinetic pathway triggered by radiation to study the

effect of radiation on the G2/M transition of the cell cycle. At the population level, we reduced the dynamics of the cell cycle during the G2/M transition and assumed a distribution of cells over the cell cycle to study the effect of radiation on a population of cells. Our approach is broken down into Chapters 2 to 6 as follows:

- In Chapter 2, we modelled the cell cycle and radiation pathway with focus on the G2/M transition and the ATM-Chk2 pathway. Our cell cycle model is based on the research of Novák and Tyson on the cell cycle control networks for yeast cells [71, 97]. Our proposed model for radiation pathway describes formation and repair of Double Strand Breaks (DSBs) and fast activation/inactivation of the kinases ATM and Chk2 with Goldbeter-Koshland kinetics [27].

We showed that radiation can trigger the G2 checkpoint via a saddle-node on an invariant circle (SNIC) bifurcation driven by parameter V_{c2} (denoted $\text{SNIC}_{V_{c2}}$). We also showed that radiation must be high enough (> 0.3 Gy) and long enough before M-phase entry in order to activate the G2 checkpoint.

A few questions arise from our results in Chapter 2. How does failure of G2 checkpoint activation translate into HRS/IRR? How does our $\text{SNIC}_{V_{c2}}$ bifurcation relate to a SNIC_{Mass} bifurcation studied by Novák et al. [74]? These questions are addressed in Chapters 3 and 5, respectively.

- In Chapter 3, we modelled the cell survival fraction based on the time available for repair of DSBs before M-phase entry and lethal events affecting the cell survival. We assumed a distribution of cells over the cell cycle and Poisson's Law for the average number of lethal events. Our model for the survival fraction is based on the assumption that the first lethal events triggered by radiation determine the fate of a cell and affect the capability of cells to

reproduce. In the case of G2 checkpoint failure, it is known that DSBs during M-phase lead to events that affect future generations [102].

We simulated the cell cycle model and radiation pathway to obtain a numerical survival fraction curve. We observed that the effect of radiation on the G2/M transition studied in Chapter 2 produces an HRS/IRR effect in the survival fraction. Moreover, this effect is more pronounced for synchronous cells in G2-phase, less pronounced for asynchronous cells, and absent for synchronous cells in G1- and S-phases. These results are consistent with experimental observations [59].

Our results support the hypothesis that the HRS/IRR phenomenon is caused by the ability of cells to respond to DNA damage during the G2/M transition [59]. This motivates a theoretical exploration of our survival fraction model. However, that would require a simplification of the cell cycle model about the $\text{SNIC}_{V_{c2}}$ bifurcation that governs the G2/M transition and a theoretical expression of the time available for repair. Such theoretical derivations are carried out in Chapters 5 and 6, respectively.

- Chapter 4 is a theoretical interlude to study a generic problem in dynamical systems introduced by us: the carryover of a saddle-node bifurcation. We define the carryover of a saddle-node bifurcation as the manifestation of an existing saddle-node bifurcation after transforming one of the parameters into a variable. We considered the case where the new differential equation associated with the parameter transformed into variable does not depend on the rest of the variables.

We proved that additional singularity and transversality conditions are sufficient for the carryover of the saddle-node bifurcation. Moreover, such con-

ditions can be verified graphically with a two-parameter bifurcation diagram involving the parameter of interest.

This study of the carryover of a saddle-node bifurcation originates from the question posed in Chapter 2 regarding the connection between the $\text{SNIC}_{V_{c2}}$ and the SNIC_{Mass} bifurcations, the former being the carryover of the latter. This result is used in Chapter 5.

- In Chapter 5, we reduced the cell cycle model to a normal form about the $\text{SNIC}_{V_{c2}}$ bifurcation.

We broke down the cell cycle model into modules, the G2 and M modules. First, we looked at the G2 module, showed that it has a saddle-node bifurcation driven by cell mass, and reduced the module to one-dimensional form about the saddle-node bifurcation. Second, we transformed the cell mass into a variable and applied our propositions in Chapter 4 to derive a one-dimensional form about the saddle-node bifurcation, now driven by V_{c2} . Third, we showed that adding the M module and resetting condition for cell division transforms the saddle-node bifurcation into a SNIC bifurcation without the one-dimensional form. Finally, we used the one-dimensional form (which we now refer to as normal form) to define the G2/M transition in mathematical terms.

The normal form and the definition of the G2/M transition are used in Chapter 6.

- In Chapter 6, we used the reduction of the cell cycle model to normal form about the $\text{SNIC}_{V_{c2}}$ (locally a saddle-node bifurcation) bifurcation obtained in Chapter 5 to derive an expression for the cell survival fraction based on the framework proposed and simulated in Chapter 3. We transformed the normal

form to a phase model and provided a theoretical form for the average number of lethal lesions. Assuming low dose of radiation and active ATM, we showed that our formulation of the survival fraction reproduces the IR model.

It is known that the HRS/IRR effect is produced by different and independent mechanisms [66, 67, 47, 45, 104, 77]. Here we explore the HRS/IRR phenomenon associated with the G2/M transition. We established numerical and theoretical arguments to support the hypothesis that the G2/M transition plays a major role in the HRS/IRR phenomenon. Moreover, we provided a preliminary theoretical explanation for the parameters in the IR model.

Our exploration of the involvement of the radiation pathway and the cell cycle on the survival fraction allows us to summarize two main biological mechanisms: 1) the G2 checkpoint or G2/M transition is identified with a saddle-node (SNIC, globally) bifurcation driven by the inactivation rate of Cdc25, and 2) the fast switch-like activation of Chk2 dictates the activation of the G2 checkpoint in response to radiation. Combining these two mechanisms with the assumption that DSBs during M-phase affect the ability of cells to reproduce, we provided a biological explanation for the participation of the G2 phase in the HRS/IRR phenomenon.

Our theoretical and numerical results rely on several simplifications of our modelling. In particular, we modelled the radiation pathway with Goldbeter-Koshland kinetics for the kinases ATM and Chk2, we only considered one type of DSBs, we have neglected the dynamics of the G1- and S-phases in our model for the cell cycle, we set ATM to active form in order to solve for the DSBs, and the radiation pathway has been simplified to a pulse in the study of the phase model.

7.2 Future work

In the development of this thesis, we gained insights on the effect of radiation on the G2/M transition and the survival fraction. We learned that the G2/M transition is governed by a SNIC bifurcation. We also learned that a combination of temporal conditions and high kinase activity lead to the proper activation of the G2 checkpoint. We realized that the phase model becomes convenient to describe the progression of the cell cycle accounting for the G2/M transition. We also provided a way to define the survival fraction based of lethal events that explicitly account for the response of cells to radiation. Based on these insights, we propose the following future work.

Carryover of bifurcations

The study of the carryover of a bifurcation in this thesis was limited to the saddle-node bifurcation with two parameters and the new equation associated with the transformed parameter independent of the rest of the variables. This case was enough for our particular interest. However, it would be interesting to study the carryover of other types of bifurcations (transcritical, pitchfork, Hopf, etc), k -dimensional parameters, and general form for the equation associated with the parameter transformed into a variable.

The phase model of the cell cycle

We believe that the phase model (6.23) should be extended for the whole cell cycle to account for the G1 (or restriction) and Metaphase (or spindle) checkpoints, in addition to the G2/M checkpoint. We believe that each checkpoint is identified with a type of bifurcation driven by a given parameter in the cell cycle network.

Therefore, we propose a phase model for the cell cycle of the form

$$\frac{d\vartheta}{dt} = 1 - \sum_i \text{PRC}_i(\vartheta)g_i(t), \quad \vartheta \in [0, T], \quad (7.1)$$

where $i \in \{G1, G2/M, Meta\}$, $\text{PRC}_i(\vartheta)$ is the Phase Response Curve (PRC) of checkpoint i , $g_i(t)$ is the output of the corresponding radiation pathway affecting the bifurcation parameter of checkpoint i , and T is the length of the cell cycle.

In the case of the G2/M checkpoint governed by a SNIC bifurcation, the PRC has the form

$$\text{PRC}_{G2/M}(\vartheta) = \frac{1}{b} \sin^2 \left(\sqrt{bc} \langle \vartheta \rangle_{I_{G2/M}} \right), \quad (7.2)$$

where b, c depend on the parameters of the cell cycle (β and γ in equation (5.42)), $I_{G2/M} = [t_{G2/M}^{\text{start}}, t_{G2/M}^{\text{end}}]$ is the finite interval of the G2/M transition (see equation (5.46)), and the angle bracket notation $\langle \cdot \rangle_I$ is a generalization of Maculay's brackets notation given by

$$\langle x \rangle_{[a,b]} = \begin{cases} x - a, & x \in [a, b], \\ 0, & \text{otherwise.} \end{cases}$$

The angle bracket notation guarantees that the PRC (7.2) only affects the phase during the G2/M transition. It is still left to investigate the validity of our assumptions on b and c made in Chapter 6 and to explore their dependence on the parameters of the cell cycle. In the case where b is proportional to $V_{c2}^* - V_{c2}$ and c is constant, we have that

$$g_{G2/M}(t) = k_{c2a} \text{Chk2}(t), \quad (7.3)$$

where k_{c2a} is the inactivation rate of Cdc25 by Chk2. Below we discuss possible improvements to the DSBs-ATM-Chk2 radiation pathway.

The PRC of the other checkpoints is material for research. We speculate that the

G1 checkpoint is governed by a saddle-node bifurcation as well, while the Metaphase checkpoint might be associated with a Hopf bifurcation, based on Tyson et al. [97]. With regards to the “early” and “Sinclair” (also known as G2 accumulation [70]) G2 checkpoints discussed by Marples [59], we believe that they correspond to the same saddle-node mechanism activated via different radiation pathways. We believe that the early G2 checkpoint corresponds to the ATM-Chk2 pathway studied here, which is fast but active above a threshold, while the G2 accumulation checkpoint corresponds to a different slow but sensitive pathway. It would be necessary to study these ideas and to identify the corresponding bifurcation parameters.

This general formulation of the phase model has the potential to investigate the effect of radiation on the cell cycle without explicitly accounting for the complex network of the cell cycle. One of the challenges we faced in this thesis was the complexity of the cell cycle model and the identifiability of the parameters within, even when we neglected other cell cycle regulatory mechanisms other than the G2/M transition. Reducing the G2/M transition to its corresponding PRC allows to represent specific cell lines with parameters b and c , although their biological interpretation is left to explore. If one is interested in the progression of the cell cycle, the phase model for the cell cycle allows to focus on the radiation pathway instead.

The DSB-ATM-Chk2 radiation pathway

We consider that the radiation pathway requires further investigation. First, we have only considered one type of DSBs and only one mechanism of DSBs repair. However, a distinction between recognized, unrecognized, repairable, unrepairable, and misrepaired DSBs should be considered [93, 84, 92]. Moreover, a distinction

between non-homologous end joining (NHEJ) and homologous recombination (HR) should also be considered as these repair processes have different times and have different consequences [89].

Second, the ATM pathway should be revised. We have simplified ATM activation to fast sensitive activation at very low-dose with Goldbeter-Koshland kinetics. However, it is known that other mechanisms, including monomerization, ubiquitination, and self-activation are highly involved in ATM activity [45, 20, 5, 79, 53]. Since ATM is key in the distinction between normal and mutant cells, it is imperative to further explore the modelling of ATM.

Cell Fate Mechanism model

Our main assumption to derive the survival fraction model is that the early response of a cell to radiation determines the fate of the cell, therefore affecting the ability of the population of cells to reproduce. More specifically, our model for the survival fraction follows this logic: radiation triggers a kinetic pathway (the ATM-Chk2 pathway), which affects possible lethal lesions (DSBs during M-phase entry) in an individual cell and this has an effect on a population of cells (average number of lethal lesions due to G2 checkpoint failure) that is reflected on the clonogenic survival (survival fraction). The average number of lethal events due to G2 checkpoint failure contributes to a form of cell death known as mitotic catastrophe [102]. However, we believe that our approach should be extended to include all forms of cell death.

Cell death after radiation consists of five main mechanisms: apoptosis, autophagy, mitotic catastrophe, necrosis and senescence [69]. Those mechanisms differ in their morphological features [for review see 46, 24, 69]. Here, we understand that *mitotic catastrophe* occurs as a consequence of mitotic failure and

deficit of cell cycle checkpoints [21]. Whether or not mitotic catastrophe should be considered a form of cell death [100, 102], it is a mechanism that affects the fate of the cell and contributes to clonogenic survival [69]. For this reason, we prefer to refer to those mechanisms as cell fate mechanisms.

We propose a Cell Fate Mechanism (CFM) model for the cell survival that accounts explicitly for every form of cell fate. The CFM model is based on lethal events as the outcome of lethal lesions. Denote $\lambda(D)$ as the average number of lethal events in an average cell, where D is the total dose delivered in Grays (Gy). Assuming Poisson's Law for lethal events, we find the survival fraction to be

$$S(D) = P(K = 0; \lambda(D)) = e^{-\lambda(D)}, \quad (7.4)$$

where P is the probability density function for the Poisson distribution. We split the average number of lethal events into the different cell fates, i.e., average number of lethal events due to apoptosis to be $\lambda_{\text{apop}}(D)$, autophagy to be $\lambda_{\text{auto}}(D)$, mitotic catastrophe to be $\lambda_{\text{mito}}(D)$, necrosis to be $\lambda_{\text{necro}}(D)$, and senescence to be $\lambda_{\text{senes}}(D)$. If these quantities are independent, we can write the survival fraction for the CFM model as

$$S(D) = e^{-\lambda(D)} = e^{-\lambda_{\text{apop}}(D) - \lambda_{\text{auto}}(D) - \lambda_{\text{mito}}(D) - \lambda_{\text{necro}}(D) - \lambda_{\text{senes}}(D)}. \quad (7.5)$$

We believe that all of the cell fate mechanisms can be approximated with linear and quadratic terms for most of survival fraction data, resulting in the LQ model

$$\lambda(D) \approx \alpha D + \beta D^2.$$

However, in experiments where the LQ model fails to describe the data, we think

that some of the terms in the CFM model (7.5) deviate from the linear-quadratic approximation. For instance, in this thesis we defined

$$\lambda_{\text{mito}}(D) = \frac{\alpha_{\text{mito}}}{T} \int_0^T DSB_{\text{lethal}}(t_0, D) f(t_0) dt_0. \quad (7.6)$$

where α_{mito} is a proportionality constant and $DSB_{\text{lethal}}(t_0, D)$ is the solution of the ATM-Chk2 radiation pathway.

The CFM model has tremendous potential from the numerical point of view. For instance, if we want to study the effect of Chk2 on the survival fraction, we could simulate a given radiation pathway and use the phase model (7.1) for the progression of the cell cycle.

7.3 Final remarks

The study of the effect of radiation on cells is based on the clonogenic experiment and the survival fraction curve. The analysis of cell survival fraction data has been done over the last 80 years using the Linear Quadratic model and, more recently, the Induced Repair model. Despite being excellent models, they fail to provide meaningful information regarding the underlying mechanisms of cellular response to radiation. To study underlying mechanisms, we need to incorporate complex mathematical modelling. The trade-off here is to give away simplicity for biological understanding. In this thesis, we explored the effect of radiation on the cell cycle and cell survival fraction via the ATM-Chk2 pathway. This exploration provided meaningful explanations for the HRS/IRR phenomenon and opened opportunities to further explore the effect of radiation on cells.

Bibliography

- [1] Edward L. Alpen. *Radiation Biophysics*. Prentice Hall, 1990.
- [2] Jiri Bartek, Jacob Falck, and Jiri Lukas. CHK2 kinase—a busy messenger. *Nature Reviews Molecular Cell Biology*, 2(12):877–86, 2001.
- [3] Elise Berthel, Nicolas Foray, and Mélanie L. Ferlazzo. The nucleoshuttling of the ATM protein: A unified model to describe the individual response to high and low-dose of radiation? *Cancers*, 11(7), 2019.
- [4] Jeff Bezanson, Alan Edelman, Stefan Karpinski, and Viral B. Shah. Julia: A Fresh Approach to Numerical Computing. *SIAM Review*, 59(1):65–98, 2017.
- [5] Larry Bodgi and Nicolas Foray. The nucleo-shuttling of the ATM protein as a basis for a novel theory of radiation response: resolution of the linear-quadratic model*. *International Journal of Radiation Biology*, 92(3):117–131, 2016.
- [6] Larry Bodgi, Aurélien Canet, Laurent Pujo-menjouet, and Annick Lesne. Mathematical models of radiation action on living cells: From the target theory to the modern approaches. A historical and critical review. *Journal of Theoretical Biology*, 394:93–101, 2016.

- [7] D J Brenner, L R Hlatky, P J Hahnfeldt, Y Huang, and R K Sachs. The linear-quadratic model and most other common radiobiological models result in similar predictions of time-dose relationships. *Radiation research*, 150(1): 83–91, 1998.
- [8] David J. Brenner. The Linear-Quadratic Model Is an Appropriate Methodology for Determining Isoeffective Doses at Large Doses Per Fraction. *Seminars in Radiation Oncology*, 18(4):234–239, 2008.
- [9] David J. Brenner, Rainer K. Sachs, Lester J. Peters, H. Rodney Withers, and Eric J. Hall. We forget at our peril the lessons built into the α/β model. *International Journal of Radiation Oncology Biology Physics*, 82(4):1312–1314, 2012.
- [10] Sandeep Burma, Benjamin P. Chen, Michael Murphy, Akihiro Kurimasa, and David J Chen. ATM Phosphorylates Histone H2AX in Response to DNA Double-strand Breaks. *Journal of Biological Chemistry*, 276(45):42462–42467, 2001.
- [11] G. Buscemi, C. Savio, L. Zannini, F. Miccichè, D. Masnada, M. Nakanishi, H. Tauchi, K. Komatsu, S. Mizutani, K. Khanna, P. Chen, P. Concannon, L. Chessa, and D. Delia. Chk2 activation dependence on Nbs1 after DNA damage. *Molecular and Cellular Biology*, 21(15):5214–5222, 2001.
- [12] K H Chadwick and H P Leenhouts. A molecular theory of cell survival. *Physics in medicine and biology*, 18(1):78–87, 1973.
- [13] Carlos Contreras, Gustavo Carrero, and Gerda de Vries. A Mathematical Model for the Effect of Low-Dose Radiation on the G2/M Transition. *Bulletin of Mathematical Biology*, 2019.

- [14] Stanley B Curtis. Lethal and potentially lethal lesions induced by radiation—a unified repair model. *Radiation research*, 106(2):252–70, 1986.
- [15] Dorothee Deckbar, Julie Birraux, Andrea Krempler, Leopoldine Tchouandong, Andrea Beucher, Sarah Walker, Tom Stiff, Penny Jeggo, and Markus Löbrich. Chromosome breakage after G2 checkpoint release. *Journal of Cell Biology*, 2007.
- [16] Dorothee Deckbar, Penny A Jeggo, and Markus Löbrich. Understanding the limitations of radiation-induced cell cycle checkpoints. *Critical reviews in biochemistry and molecular biology*, 46(4):271–283, 2011.
- [17] Maddalena Donzelli and Giulio F Draetta. Regulating mammalian checkpoints through Cdc25 inactivation. *EMBO reports*, 4(4):671–677, 2003.
- [18] B G Douglas and J F Fowler. The effect of multiple small doses of x rays on skin reactions in the mouse and a basic interpretation. *Radiation research*, 66(2):401–426, 1976.
- [19] M M Elkind and G F Whitmore. *The radiobiology of cultured mammalian cells*. Gordon and Breach, New York., 1967.
- [20] L Enns, A Rasouli-Nia, M Hendzel, B Marples, and M Weinfeld. Association of ATM activation and DNA repair with induced radioresistance after low-dose irradiation. *Radiation protection dosimetry*, 166(1-4):131–6, 2015.
- [21] David Eriksson and Torgny Stigbrand. Radiation-induced cell death mechanisms. *Tumor Biology*, 31(4):363–372, 2010.
- [22] G. B. Ermentrout and N. Kopell. Parabolic Bursting in an Excitable System

Coupled with a Slow Oscillation. *SIAM Journal on Applied Mathematics*, 46 (2):233–253, 1986.

- [23] B Fertil, I Reydellet, and P J Deschavanne. A benchmark of cell survival models using survival curves for human cells after completion of repair of potentially lethal damage. *Radiation research*, 138(1):61–69, 1994.
- [24] L Galluzzi, M C Maiuri, I Vitale, H Zischka, Maria Castedo, L Zitvogel, and Guido Kroemer. Cell death modalities: classification and pathophysiological implications. *Cell death and differentiation*, 14(7):1237–1243, 2007.
- [25] Claude Gérard, John J Tyson, Damien Coudreuse, and Béla Novák. Cell Cycle Control by a Minimal Cdk Network. *PLOS Computational Biology*, 11(2):e1004056, 2015.
- [26] Michel Godin, Francisco Feijó Delgado, Sungmin Son, William H. Grover, Andrea K. Bryan, Amit Tzur, Paul Jorgensen, Kris Payer, Alan D. Grossman, Marc W. Kirschner, and Scott R. Manalis. Using buoyant mass to measure the growth of single cells. *Nature Methods*, 7(5):387–390, 2010.
- [27] A Goldbeter and DE Koshland. An amplified sensitivity arising from covalent modification in biological systems. *Proceedings of the National Academy of Sciences of the United States of America*, 78(11):6840–6844, 1981.
- [28] Aaron A Goodarzi, Angela T Noon, Dorothee Deckbar, Yael Ziv, Yosef Shiloh, Markus Löbrich, and Penny A Jeggo. ATM Signaling Facilitates Repair of DNA Double-Strand Breaks Associated with Heterochromatin. *Molecular Cell*, 31(2):167–177, 2008.

- [29] D T Goodhead. The initial physical damage produced by ionizing radiations. *International Journal of Radiation Biology*, 56(5):623–634, 1989.
- [30] Dudley T. Goodhead. Saturable Repair Models of Radiation Action in Mammalian Cells. *Radiation Research Supplement*, 8:S58–S67, 1985.
- [31] K P Hadeler and Thomas Hillen. Differential Equations on Branched Manifolds. In P Clement and G Lumer, editors, *Evolution Equations, Control Theory and Biomathematics*, pages 241–258. 1994.
- [32] Jean François Haince, Sergei Kozlov, Valina L Dawson, Ted M Dawson, Michael J Hendzel, Martin F Lavin, and Guy G Poirier. Ataxia telangiectasia mutated (ATM) signaling network is modulated by a novel poly(ADP-ribose)-dependent pathway in the early response to DNA-damaging agents. *Journal of Biological Chemistry*, 282(22):16441–16453, 2007.
- [33] Douglas Hanahan and Robert A Weinberg. The Hallmarks of Cancer. *Cell*, 100(1):57–70, 2000.
- [34] LH Hartwell and TA Weinert. Checkpoints: controls that ensure the order of cell cycle events. *Science*, 246(4930):629–634, 1989.
- [35] Roland B Hawkins. A microdosimetric-kinetic model for the effect of non-Poisson distribution of lethal lesions on the variation of RBE with LET. *Radiation research*, 160(1):61–69, 2003.
- [36] George Iliakis, Ya Wang, Jun Guan, and Huichen Wang. DNA damage checkpoint control in cells exposed to ionizing radiation. *Oncogene*, 22: 5834–5847, 2003.

- [37] Aya Ishikawa, Motohiro Yamauchi, Keiji Suzuki, and Shunichi Yamashita. Image-based quantitative determination of DNA damage signal reveals a threshold for G2 checkpoint activation in response to ionizing radiation. *Genome Integrity*, 1:1–10, 2010.
- [38] Eugene M. Izhikevich. *Dynamical Systems in Neuroscience: The Geometry of Excitability and Bursting*. MIT Press, 2007.
- [39] Michael C. Joiner, Brian Marples, Philippe Lambin, Susan C. Short, and Ingela Turesson. Low-dose hypersensitivity: Current status and possible mechanisms. *International Journal of Radiation Oncology Biology Physics*, 49(2):379–389, 2001.
- [40] A. M. Kellerer and H. H. Rossi. The theory of dual radiation action. *Current topics in radiation research*, 8:85–158, 1972.
- [41] Albrecht M Kellerer and Harald H Rossi. A Generalized Formulation of Dual Radiation Action. *Radiation Research*, 75(3):471, 1978.
- [42] Sang-Mun Kim and Hyong-Chol O. Conditions for Bifurcations in a Non-Autonomous Scalar Differential Equation. 2013. URL <http://arxiv.org/abs/1311.1812>.
- [43] John P Kirkpatrick, Jeffrey J Meyer, and Lawrence B Marks. The linear-quadratic model is inappropriate to model high dose per fraction effects in radiosurgery. *Seminars in radiation oncology*, 18(4):240–3, 2008.
- [44] Peter Kloeden and Christian Pötzsche. *Nonautonomous Dynamical Systems in the Life Sciences*. Springer International Publishing, 2013.

- [45] Sergei V. Kozlov, Mark E. Graham, Burkhard Jakob, Frank Tobias, Amanda W. Kijas, Marcel Tanuji, Philip Chen, Phillip J. Robinson, Gisela Taucher-Scholz, Keiji Suzuki, Sairai So, David Chen, and Martin F. Lavin. Autophosphorylation and ATM activation: Additional sites add to the complexity. *Journal of Biological Chemistry*, 286(11):9107–9119, 2011.
- [46] G Kroemer, L Galluzzi, P Vandenabeele, J Abrams, E S Alnemri, E H Baehrecke, M V Blagosklonny, W S El-Deiry, P Golstein, D R Green, M Hengartner, R A Knight, S Kumar, S A Lipton, W Malorni, G Nuñez, M E Peter, J Tschopp, J Yuan, M Piacentini, B Zhivotovsky, and G Melino. Classification of cell death: recommendations of the Nomenclature Committee on Cell Death 2009. *Cell Death and Differentiation*, 16(1):3–11, 2009.
- [47] Sarah A Krueger, Spencer J Collis, Michael C Joiner, George D Wilson, and Brian Marples. Transition in Survival From Low-Dose Hyper-Radiosensitivity to Increased Radioresistance Is Independent of Activation of ATM SER1981 Activity. *International Journal of Radiation Oncology*Biophysics*, 69(4):1262–1271, 2007.
- [48] Yuri A. Kuznetsov. *Elements Of Applied Bifurcation Theory*. Springer, 2004.
- [49] P Lambin, E P Malaise, and Michael C Joiner. Might intrinsic radioresistance of human tumour cells be induced by radiation? *International journal of radiation biology*, 69(3):279–290, 1996.
- [50] J.A. Langa, J.C. Robinson, and A. Suñer. Bifurcations in non-autonomous scalar equations. *Journal of Differential Equations*, 221(1):1–35, 2006.
- [51] D E Lea and D G Catcheside. The mechanism of the induction by radiation of

- chromosome aberrations in *Tradescantia*. *Journal of Genetics*, 44:216–245, 1942.
- [52] Douglas Edward Lea. *Actions of radiations on living cells*. Cambridge: University Press, 1955.
- [53] Brian L. Lee, Anamika Singh, J.N. Mark Glover, Michael J. Hendzel, and Leo Spyropoulos. Molecular Basis for K63-Linked Ubiquitination Processes in Double-Strand DNA Break Repair: A Focus on Kinetics and Dynamics. *Journal of Molecular Biology*, 429(22):3409–3429, 2017.
- [54] Glass Leon and Michael C. Mackey. *From Clocks to Chaos: The Rhythms of Life*. Princeton University Press, 1988.
- [55] Jeremiah H. Li, Felix X.-F. Ye, Hong Qian, and Sui Huang. Time-dependent saddle-node bifurcation: Breaking time and the point of no return in a non-autonomous model of critical transitions. *Physica D: Nonlinear Phenomena*, 395:7 – 14, 2019.
- [56] Markus Löbrich and Penny A Jeggo. The impact of a negligent G2/M checkpoint on genomic instability and cancer induction. *Nature Reviews Cancer*, 7(11):861–869, 2007.
- [57] B Marples and M C Joiner. The response of Chinese hamster V79 cells to low radiation doses: evidence of enhanced sensitivity of the whole cell population. *Radiation research*, 133(1):41–51, 1993.
- [58] B Marples, B G Wouters, S J Collis, A J Chalmers, and M C Joiner. Low-dose hyper-radiosensitivity: a consequence of ineffective cell cycle arrest

- of radiation-damaged G2-phase cells. *Radiation research*, 161(3):247–55, 2004.
- [59] Brian Marples. Is low-dose hyper-radiosensitivity a measure of G2-phase cell radiosensitivity? *Cancer and Metastasis Reviews*, 23(3-4):197–207, 2004.
- [60] Brian Marples and Spencer J Collis. Low-Dose Hyper-Radiosensitivity: Past, Present, and Future. *International Journal of Radiation Oncology Biology Physics*, 70(5):1310–1318, 2008.
- [61] S Matsuoka, M Huang, and S J Elledge. Linkage of ATM to cell cycle regulation by the Chk2 protein kinase. *Science (New York, N.Y.)*, 282(5395):1893–1897, 1998.
- [62] R H Medema and L Macûrek. Checkpoint control and cancer. *Oncogene*, 31(21):2601–13, 2012.
- [63] James D Meiss. *Differential Dynamical Systems*. SIAM, 2007.
- [64] Jessica Miciak and Fred Bunz. Understanding the pluses of pulses. *Cell Cycle*, 16(14):1325, 2017.
- [65] David O Morgan. *The Cell Cycle: Principles of Control*. New Science Press Ltd, 2007.
- [66] C. Mothersill and C. Seymour. Medium from irradiated human epithelial cells but not human fibroblasts reduces the clonogenic survival of unirradiated cells. *International Journal of Radiation Biology*, 71(4):421–427, 1997.
- [67] Carmel Mothersill, C. B. Seymour, and M. C. Joiner. Relationship between Radiation-Induced Low-Dose Hypersensitivity and the Bystander Effect. *Radiation Research*, 157(5):526–532, 2002.

- [68] David Murray and Alexander J McEwan. Radiobiology of systemic radiation therapy. *Cancer biotherapy & radiopharmaceuticals*, 22(1):1–23, 2007.
- [69] David Murray and Razmik Mirzayans. Role of Therapy-Induced Cellular Senescence in Tumor Cells and its Modification in Radiotherapy: The Good, The Bad and The Ugly. *Journal of Nuclear Medicine & Radiation Therapy*, s6(01), 2013.
- [70] Shinichiro Nakada, Yoko Katsuki, Issei Imoto, Tetsuji Yokoyama, Masayuki Nagasawa, Johji Inazawa, and Shuki Mizutani. Early G2/M checkpoint failure as a molecular mechanism underlying etoposide-induced chromosomal aberrations. *Journal of Clinical Investigation*, 116(1):80–89, 2006.
- [71] Béla Novák and John J Tyson. Numerical analysis of a comprehensive model of M-phase control in *Xenopus* oocyte extracts and intact embryos. *Journal of cell science*, 106:1153–1168, 1993.
- [72] Béla Novák and John J Tyson. Modeling the Cell Division Cycle: M-phase Trigger, Oscillations, and Size Control, 1993.
- [73] Béla Novák and John J Tyson. Design principles of biochemical oscillators. *Nature reviews. Molecular cell biology*, 9(12):981–991, 2008.
- [74] Béla Novák, Zsuzsa Pataki, Andrea Ciliberto, and John J Tyson. Mathematical model of the cell division cycle of fission yeast. *Chaos*, 11(1):277–286, 2001.
- [75] Béla Novák, John J Tyson, Bela Gyorffy, and Attila Csikasz-Nagy. Irreversible cell-cycle transitions are due to systems-level feedback. *Nature Cell Biology*, 9(7):724–728, 2007.

- [76] G. M. Obaturov, V. V. Moiseenko, and A. S. Filimonov. Model of mammalian cell reproductive death. I. Basic assumptions and general equations. *Radiation and Environmental Biophysics*, 32(4):285–294, 1993.
- [77] Oluwole Olobatuyi, Gerda de Vries, and Thomas Hillen. A reaction–diffusion model for radiation-induced bystander effects. *Journal of Mathematical Biology*, 75(2):341–372, 2017.
- [78] Oluwole Olobatuyi, Gerda de Vries, and Thomas Hillen. Effects of G2-checkpoint dynamics on low-dose hyper-radiosensitivity. *Journal of Mathematical Biology*, 77(6-7):1969–1997, 2018.
- [79] Faissal Ouenzar, Michael J Hendzel, and Michael Weinfeld. Shuttling towards a predictive assay for radiotherapy. *Translational Cancer Research*, 5(S4):S742–S746, 2016.
- [80] K. Park, L. J. Millet, N. Kim, H. Li, X. Jin, G. Popescu, N. R. Aluru, K. J. Hsia, and R. Bashir. Measurement of adherent cell mass and growth. *Proceedings of the National Academy of Sciences*, 107(48):20691–20696, 2010.
- [81] Christopher Rackauckas and Qing Nie. DifferentialEquations.jl – A Performant and Feature-Rich Ecosystem for Solving Differential Equations in Julia. *Journal of Open Research Software*, 5(15):15, 2017.
- [82] Harald H Rossi and Marco Zaider. Compound Dual Radiation Action: I. General Aspects. *Radiation Research*, 132(2):178, 1992.
- [83] Kai Rothkamm and Markus Löbrich. Evidence for a lack of DNA double-strand break repair in human cells exposed to very low x-ray doses. *Proceed-*

ings of the National Academy of Sciences of the United States of America, 100(9):5057–62, 2003.

- [84] Rainer K Sachs, P Hahnfeld, and David J Brenner. The link between low-LET dose-response relations and the underlying kinetics of damage production/repair/misrepair. *International journal of radiation biology*, 72(4): 351–74, 1997.
- [85] Bobby R. Scott. Multicellular signalling model for DNA double-strand break repair kinetics after low-dose radiation. *International Journal of Low Radiation*, 7(5):347–358, 2010.
- [86] Lee A Segel and Leah Edelstein-Keshet. *A Primer on Mathematical Models in Biology*. SIAM, 2013.
- [87] Wei Sha, Jonathan Moore, Katherine Chen, Antonio D Lassaletta, C.-S. Yi, John J Tyson, and Jill C Sible. Hysteresis drives cell-cycle transitions in *Xenopus laevis* egg extracts. *Proceedings of the National Academy of Sciences*, 100(3):975–980, 2003.
- [88] S Short, C Mayes, M Woodcock, H Johns, and Michael C Joiner. Low dose hypersensitivity in the T98G human glioblastoma cell line. *International journal of radiation biology*, 75(7):847–55, 1999.
- [89] Reza Taleei. Modelling Dsb Repair Kinetics for Dna Damage Induced By Proton and Carbon Ions. *Radiation Protection Dosimetry*, pages 1–4, 2018.
- [90] Reza Taleei and Hooshang Nikjoo. The non-homologous end-joining (NHEJ) pathway for the repair of DNA double-strand breaks: I. A mathematical model. *Radiation research*, 179(5):530–9, 2013.

- [91] H D Thames. An 'incomplete-repair' model for survival after fractionated and continuous irradiations. *International journal of radiation biology and related studies in physics, chemistry, and medicine*, 47(3):319–39, 1985.
- [92] Charles Thomas, Jennifer Martin, Clément Devic, Elke Bräuer-Krisch, Michel Diserbo, Juliette Thariat, and Nicolas Foray. Impact of dose-rate on the low-dose hyper-radiosensitivity and induced radioresistance (HRS/IRR) response. *International Journal of Radiation Biology*, 89(10):813–822, 2013.
- [93] C A Tobias. The repair-misrepair model in radiobiology: comparison to other models. *Radiation research. Supplement*, 8:S77–S95, 1985.
- [94] John J Tyson and Béla Novák. Regulation of the Eukaryotic Cell Cycle: Molecular Antagonism, Hysteresis, and Irreversible Transitions. *Journal of Theoretical Biology*, 210(2):249–263, 2001.
- [95] John J Tyson and Béla Novák. Chapter 14 - Irreversible Transitions, Bistability and Checkpoint Controls in the Eukaryotic Cell Cycle: A Systems-Level Understanding. *Handbook of Systems Biology*, pages 265–285, 2012.
- [96] John J Tyson and Béla Novák. Models in biology: lessons from modeling regulation of the eukaryotic cell cycle. *BMC Biology*, 13(1):46, 2015.
- [97] John J Tyson, Katherine C Chen, and Béla Novák. Network dynamics and cell physiology. *Nature reviews. Molecular cell biology*, 2(12):908–916, 2001.
- [98] John J Tyson, Attila Csikasz-Nagy, and Béla Novák. The dynamics of cell cycle regulation. *BioEssays*, 24(12):1095–1109, 2002.
- [99] John J Tyson, Katherine C Chen, and Béla Novák. Sniffers, buzzers, toggles

and blinkers: Dynamics of regulatory and signaling pathways in the cell. *Current Opinion in Cell Biology*, 15(2):221–231, 2003.

- [100] H Vakifahmetoglu, M Olsson, and B Zhivotovsky. Death through a tragedy: mitotic catastrophe. *Cell death and differentiation*, 15(7):1153–62, 2008.
- [101] C. M. van Leeuwen, A. L. Oei, J. Crezee, A. Bel, N. A. P. Franken, L. J. A. Stalpers, and H. P. Kok. The alfa and beta of tumours: a review of parameters of the linear-quadratic model, derived from clinical radiotherapy studies. *Radiation Oncology*, 13(1):96, 2018.
- [102] I Vitale, L Galluzzi, M Castedo, and G Kroemer. Mitotic catastrophe: a mechanism for avoiding genomic instability. *Nat Rev Mol Cell Biol*, 12(6): 385–392, 2011.
- [103] M V Williams, J Denekamp, and J F Fowler. A review of alpha/beta ratios for experimental tumors: implications for clinical studies of altered fractionation. *International journal of radiation oncology, biology, physics*, 11(1):87–96, 1985.
- [104] Peng Zhang, Bin Wang, Xiaoming Chen, Dusica Cvetkovic, Lili Chen, Jinyi Lang, and C.-M Ma. Local Tumor Control and Normal Tissue Toxicity of Pulsed Low-Dose Rate Radiotherapy for Recurrent Lung Cancer. *Dose-Response*, 13(2):155932581558850, 2015.